

# Dynamic Single–Chain Nanoparticles

Zur Erlangung des akademischen Grades eines  
DOKTORS DER NATURWISSENSCHAFTEN

(Dr. rer. nat)

Von der KIT-Fakultät für Chemie und Biowissenschaften  
des Karlsruher Instituts für Technologie (KIT)

genehmigte

DISSERTATION

von

M.Sc. Tobias Sebastian Fischer

aus

Leutkirch im Allgäu, Deutschland

1. Referent: Prof. Christopher Barner-Kowollik

2. Referent: Prof. Patrick Théato

Tag der mündlichen Prüfung: 16.07.2018



Die vorliegende Arbeit wurde von November 2015 bis Juni 2018 unter Anleitung von Prof. Dr. Christopher Barner-Kowollik am Karlsruher Institut für Technologie (KIT) – Universitätsbereich angefertigt.





*“Persönlichkeiten werden nicht durch schöne Reden geformt, sondern durch Arbeit  
und eigene Leistung.”*

- Albert Einstein



*Für  
Sandra und Elaine*



# ZUSAMMENFASSUNG

Die vorliegende Arbeit befasst sich mit der Entwicklung neuer Konzepte im Bereich der Einzelkettennanopartikel hin zu dem endgültigen Ziel der Darstellung künstlich hergestellter Enzyme. Der Hauptteil dieser Arbeit beschreibt die Entwicklung und Synthese neuer Konzepte zur Herstellung von reversibel faltbaren Einzelkettennanopartikeln (engl. single-chain nanoparticles, SCNPs) basierend auf Nitroxidchemie, sowie der Kombination von zwei orthogonalen Faltungsmotiven, die durch intramolekulare Wechselwirkungen dual gefaltete SCNPs erzeugen. Die entwickelten Konzepte lassen sich in den sogenannten selektiven Punktfaltungsansatz und das Prinzip der Wiederholeinheit-Methode unterteilen. Des Weiteren wurden Polymere, die freie Nitroxidradikale tragen mittels hochauflösender Elektrospray-Ionisation (ESI) Massenspektrometrie durch eine neu entwickelte ESI-MS Methode untersucht, um die analytische Grundlage für die Charakterisierung Nitroxid-haltiger SCNPs zu etablieren.

Im Rahmen der selektiven Punktfaltung wurde das Wasserstoffbrückenbindungssystem aus Hamilton Wedge (HW)/Cyanursäure (CA) an die Kettenenden eines Polymergerüsts angebracht. Des Weiteren wurde ein Spinmarker (Nitroxid) an vorletzter Stelle, nahe der HW Funktionalität angebracht, um mittels Kernresonanzspektroskopie (engl. nuclear magnetic resonance, NMR) Rückschlüsse über den Faltungsprozess zu erhalten. Zudem wurde die Kettenlänge des funktionellen Polymers variiert, um den Einfluss des Molekulargewichtes auf das Faltungsverhalten zu untersuchen. Die Faltung und Entfaltung des entwickelten Systems wurde mittels  $^1\text{H}$  NMR und DOSY (engl. diffusion ordered NMR spectroscopy) analysiert. Im Anschluss daran wurden Nitroxid haltige Polymere mit verschiedenen Kettenlängen und unterschiedlich hohen Anteilen an stabilen freien Nitroxidradikalen hergestellt und deren Einfluss auf das experimentell ermittelte Massenspektrum mittels hochauflösender ESI Massenspektrometrie untersucht. Des Weiteren wurde das Verfahren der selektiven Punktfaltung vermöge des HW/CA Wasserstoffbrückenbindungssystems mit dem Prinzip der Metallkomplexierung eines phosphanhaltigen Polymers durch ein Palladium (II) Salz kombiniert. Die HW/CA Faltungsmotive wurden in  $\alpha$ - und  $\omega$ -Position angebracht, während die Triarylphosphane an zuvor bestimmte Stellen entlang des Polymerrückgrats angebracht wurden. Die synthetisierten partiell

reversibel faltbaren SCNPs wurden anschließend mittels  $^1\text{H}$  und  $^{31}\text{P}$  NMR, dynamischer Lichtstreuung (engl. dynamic light scattering) und DOSY charakterisiert, um deren dynamisches und statisches Faltungsverhalten zu belegen.

Der zweite Teil der vorliegenden Promotionsschrift beschreibt die Herstellung von Einzelkettennanopartikeln über die Wiederholeinheit-Methode. In einem ersten System wurde das HW/CA Wasserstoffbrückenbindungskonzept mit dem Wirt-Gast Komplex, bestehend aus Benzo-21-Krone-7 (B21C7, Wirt) und einem sekundären Ammoniumsalz (AS, Gast), welches aus der supramakromolekularen Chemie adaptiert wurde, kombiniert. In einer Kontrollstudie wurde das B21C7/AS System erfolgreich im Bereich der Einzelkettenfaltung etabliert. Anschließend wurde die orthogonale Wechselwirkung der Wasserstoffbrückenbindungseinheit und des Wirt-Gast Komplexes in einem Methacrylat-basierten Tetrablockcopolymer gezeigt. Des Weiteren wurde die orthogonale, schrittweise und richtungsunabhängige Entfaltung mit Hilfe von  $^1\text{H}$  NMR, DOSY und DLS Messungen untersucht. Im letzten Teil der Arbeit sind photo-induzierte, dynamisch faltbare sowie selbstberichtende SCNPs beschrieben. Hierfür wurde ein photo-aktiver bifunktionaler Vernetzer hergestellt, der die 2-Hydroxy-4'-(2-hydroxyethoxy)-2-methylpropiophenon (Irgacure 2959) Funktionalität an beiden Kettenenden trägt. Dieser induziert sodann die lichtinduzierte ( $\lambda_{\text{max}} = 320 \text{ nm}$ ) Faltungsreaktion. Die dynamischen Eigenschaften der gebildeten SCNPs wurden durch deren Entfaltung unter oxidativen Bedingungen und der Regenerierung der ursprünglichen offenen Polymerkette gezeigt. In einem nächsten Schritt wurde das entfaltete Polymer erneut der UV-Licht induzierten ( $\lambda_{\text{max}} = 320 \text{ nm}$ ) Faltungsreaktion, bei gleichen Bedingungen wie die ursprüngliche Faltung, unterworfen. Die gefalteten SCNPs zeigen hierbei selbstberichtende Merkmale in Form von Fluoreszenz, wohingegen die Fluoreszenz in der offenkettigen Form, durch die Präsenz des Nitroxidradikals, unterdrückt wird. Die Faltung und Entfaltung des entwickelten Systems wurde mittels Größenausschlusschromatographie (engl. size-exclusion chromatography, SEC),  $^1\text{H}$  NMR, Elektronenspinresonanz und Fluoreszenzspektroskopie, sowie DLS und DOSY belegt. Die vorliegende Arbeit hat gezeigt, dass neue Konzepte im Bereich der dynamischen Einzelkettennanopartikel etabliert wurden, auf dem Weg hin zu dem übergeordneten Ziel von synthetisch dargestellten Enzymen.

# ABSTRACT

The current thesis reports new concepts in the field of single-chain folding en route to the ultimate goal of the synthesis of artificial enzymes. The main part focuses on the formation of new platform technologies for the formation of single-chain polymeric nanoparticles (SCNP) based on nitroxide chemistry as well as the combination of two complementary orthogonal recognition units to establish intramolecularly dual reversibly folded nanoparticles. These concepts are separated into the so-called selective point folding avenue and the repeat unit approach. Furthermore, nitroxide radical containing polymers were investigated by high resolution mass spectrometry to establish the analytical basis for the characterization of nitroxide containing SCNPs.

In the selective point folding section, the hydrogen bonding motifs termed Hamilton's Wedge (HW) and cyanuric acid (CA) are attached to the chain ends of a polystyrene polymeric backbone. Critically, the penultimate position is decorated with a nitroxide spin-label close to the HW moiety in order to investigate the folding mechanism of the system *via* nuclear magnetic resonance (NMR) measurements. Further, to investigate the chain-length dependency of the folding, polymers with different molecular weights were synthesized. The folding and unfolding of the system is followed by  $^1\text{H}$  NMR spectroscopy and diffusion ordered NMR spectroscopy. Next, the high resolution mass spectrometric access towards polymers featuring free stable nitroxide radicals are presented, investigating the influence of the chain-length as well as the nitroxide content within the polymer on the experimentally obtained electrospray ionization (ESI) mass spectra, to access molecular information of nitroxide containing SCNPs, as proper NMR analysis is prohibited by the paramagnetic nitroxide radical. The last section of the selective point folding avenue presents the preparation of a dual folding system combining the HW/CA hydrogen bonding motif with the existing concept of metal complexation of a phosphorous containing polymer through a palladium (II) salt. The CA/HW motifs are attached to the  $\alpha$ - and  $\omega$ -position, respectively, while the triarylphosphanes are attached at preselected points along the polymeric backbone. The formation of the SCNPs is characterized by  $^1\text{H}$  and  $^{31}\text{P}$  NMR spectroscopy, diffusion ordered spectroscopy (DOSY) and dynamic light scattering (DLS) measurements.

The second part of the current thesis describes the formation of single-chain polymeric nanoparticles by the repeating unit approach. Initially, a dual folding system combining the hydrogen bonding concept of HW/CA and the host-guest system consisting of benzo-21-crown-7 (B21C7, host) and a secondary ammonium salt (AS, guest) adopted from supramacromolecular chemistry was established. A proof of principle study verifies the formation of SCNPs induced by the host-guest system. Accordingly, the orthogonal interaction of the hydrogen bonding motifs and the host-guest system is demonstrated in a methacrylate based tetrablock copolymer. Furthermore, the stepwise, orthogonal and pathway independent unfolding was investigated by means of  $^1\text{H}$  NMR, DLS and DOSY. Further, the formation of photo-induced refoldable and self-reporting SCNPs is reported. A photo-active bifunctional crosslinker featuring the 2-hydroxy-4'-(2-hydroxyethoxy)-2-methylpropiophenone (Irgacure 2959) unit on both chain termini induces the photo-triggered single-chain collapse of nitroxide containing polymers. The formed SCNPs display dynamic characteristics and are readily unfolded under oxidative conditions to re-establish the initial state of the polymer. Subsequently, the linear polymers are refolded, utilizing the same conditions as for the initial UV-light induced ( $\lambda_{\text{max}} = 320 \text{ nm}$ ) folding reaction. The established system is self-reporting in the folded state by fluorescence, while the fluorescence is quenched in the open linear polymer in presence of the nitroxide radical. The folding and unfolding of the system is characterized by size-exclusion chromatography (SEC),  $^1\text{H}$  NMR, electron paramagnetic resonance (EPR) and fluorescence spectroscopy as well as DLS and DOSY. The current thesis describes new methodologies in the field of single-chain folding on the way to the ultimate goal of preparing fully synthetic enzymes.



# TABLE OF CONTENTS

|  |            |
|--|------------|
| <b>ZUSAMMENFASSUNG .....</b>   | <b>I</b>   |
| <b>ABSTRACT .....</b>  | <b>III</b> |
| <b>1. INTRODUCTION.....</b>  | <b>1</b>   |
| <b>2. SINGLE-CHAIN FOLDING .....</b>   | <b>5</b>   |
| 2.1 Radical Polymerization Techniques.....   | 5          |
| 2.2 Selective Point Folding vs. Repeat Unit Folding.....   | 13         |
| 2.3 Covalent Crosslinking.....   | 16         |
| 2.4 Non-Covalent Interactions .....  | 22         |
| 2.5 Characterization Methods.....  | 32         |
| <b>3. DYNAMIC SINGLE-CHAIN NANOPARTICLES .....</b>   | <b>51</b>  |
| 3.1 Selective Point Folding Approach.....  | 51         |
| 3.1.1 Spin Labelling of a Hydrogen Bonding System .....  | 53         |
| 3.1.2 Analyzing Nitroxide Containing Polymers by High Resolution Electrospray<br>Ionisation Mass Spectrometry..... | 69         |
| 3.1.3 Metal Complexation and Hydrogen Bond Driven Single-Chain Folding .   | 79         |
| 3.2 The Repeat Unit Approach.....  | 91         |
| 3.2.1 Reversible Dual Folding Driven by Hydrogen Bonds and Host-Guest<br>Chemistry.....                            | 93         |
| 3.2.2 Self-Reporting Refoldable Dynamic-Covalent Fluorescent Single-Chain<br>Nanoparticles.....                    | 115        |
| <b>4. CONCLUSIONS AND OUTLOOK .....</b>  | <b>135</b> |

|  |            |
|--|------------|
| <b>5. EXPERIMENTAL SECTION .....</b>               | <b>141</b> |
| <b>5.1 Materials .....</b>                         | <b>141</b> |
| <b>5.2 Instrumentation.....</b>                    | <b>143</b> |
| <b>5.3 Experimental Procedures .....</b>           | <b>149</b> |
| <b>6. BIBLIOGRAPHY .....</b>                       | <b>193</b> |
| <b>7. APPENDIX.....</b>                            | <b>211</b> |
| <b>PUBLICATIONS ARISING FROM THIS THESIS .....</b> | <b>243</b> |
| <b>ABBREVIATIONS .....</b>                         | <b>244</b> |
| <b>ACKNOWLEDGEMENTS.....</b>                       | <b>249</b> |

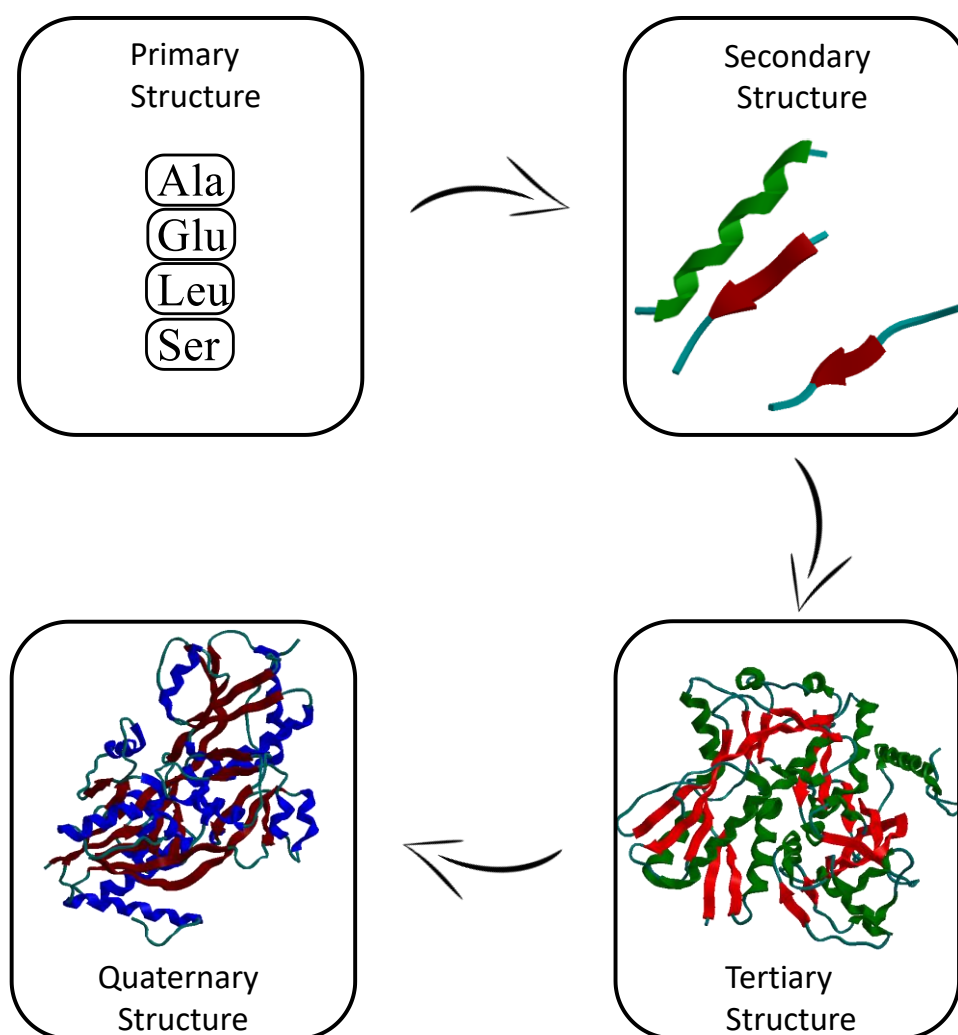
# 1

## INTRODUCTION

It is part of the human nature to mimic what they see in nature. In Greek mythology, *Daidalos* tries to counterfeit birds and builds wings with real feathers to fly. The mimicry of nature not is only evident in myths and drafts. Taking inspiration from nature is as old as 3000 years, when the Chinese tried to produce artificial silk.<sup>[1]</sup> The process of transferring natural functions and structures into functional artificial materials is also called *biomimetics*,<sup>[2]</sup> and has rapidly emerged over the last decades. Many materials have been developed that influence our daily life such as the lotus effect for self-cleaning surfaces, dry adhesive tape mimicking the adhesive features of gecko feet, spidersilk for generating fibers that are even tougher than Kevlar, and the tooth like scales of shark skin to lower the hydrodynamic resistance of ships and in pipelines are only a few examples among others.<sup>[1,3]</sup>

Although scientist made significant efforts to emulate nature, the degree of control in natural biopolymers is still unmatched by synthetic chemists. Nature is capable of controlling the synthesis of biopolymers and thus creates highly-defined monodisperse biomacromolecules such as proteins and enzymes, which essentially enable life. Despite recent progress in sequence-defined synthesis, the commonly prepared synthetic polymers are still low molecular weight species compared to high molecular weight proteins and enzymes synthesized by nature.<sup>[4-8]</sup> The sequence-defined structure, which is also the termed primary structure of *e.g.* a protein, arranges itself into higher ordered three dimensional secondary, tertiary and even quaternary structures (refer to Scheme 1). For example, proteins can dynamically fold into complex architectures such as  $\alpha$ -helices or  $\beta$ -sheets through self-assembling

processes. Nature stabilizes these three dimensional structures by either (dynamic) covalent or non-covalent interactions. To ensure the reversibility of the natural self-assembled structures, nature uses disulphide bridges as dynamic covalent bond, for instance, and van-der-Waals interactions, hydrogen bonding, aromatic or hydrophobic stacking, host-guest interactions or metal complexation in case of non-covalent interactions.<sup>[9-11]</sup>



**Scheme 1.** The structure of proteins is divided into four structures. The primary structure represents the amino acid sequence. The secondary structure, which is usually the  $\alpha$  helix and the  $\beta$  pleated sheet. The  $\beta$  pleated sheet is taken from a 3-stranded parallel  $\beta$ -sheet. RCSB: 2N4N.<sup>[12]</sup> The substructures fold into complex architectures represented by the tertiary structure. Several peptide sequences can be part of the complex; the three dimensional structure is also known as quaternary structure. The structures shown for the tertiary and quaternary structure are taken from BenM effector binding domain. RCSB: 2F6G.<sup>[13]</sup>

Although preparing artificial macromolecules as precise as nature remains the 'holy grail' of synthetic chemistry, efforts have been made in the field of reversible deactivation radical polymerization (RDRP) techniques to obtain well-defined synthetic polymers to mimic nature's complex materials.<sup>[14]</sup> Especially, the field of single-chain folding aims at mimicking complex architectures inspired by natural proteins and enzymes by making use of RDRP protocols. By combining RDRP protocols with orthogonal polymer ligation techniques, the folding of distinct units along the polymer chain can be enabled.<sup>[15]</sup> The recognition units can, for example, be placed at preselected points along the polymeric backbone and thus fold into well-defined single-chain nanoparticles. In the field of single-chain folding, this route is the so-called selective point folding. Alternatively, in the repeat unit approach, the folding units are placed statistically along the polymeric backbone or in specific polymer blocks, hence the intramolecular collapse is statistical and not as well-defined as in the selective point avenue. Nevertheless, the aim of both strategies is to impart a certain structure to the resulting nanoparticle, emulating the tertiary structure of proteins. In simulations it has been proven that – at least with the selective point folding – a certain geometry is maintained after reversible folding processes until a certain polymer chain-length.<sup>[16]</sup> The envisioned long-term aim in the field of single-chain technology is to prepare fully synthetic proteins which are able to execute simple tasks. Possible applications of the so-called single-chain nanoparticles could be in nanomedicine, as sensors or in catalysis.

Thus, the aim of the current thesis is to establish new dynamic folding technologies in the field of single-chain folding.

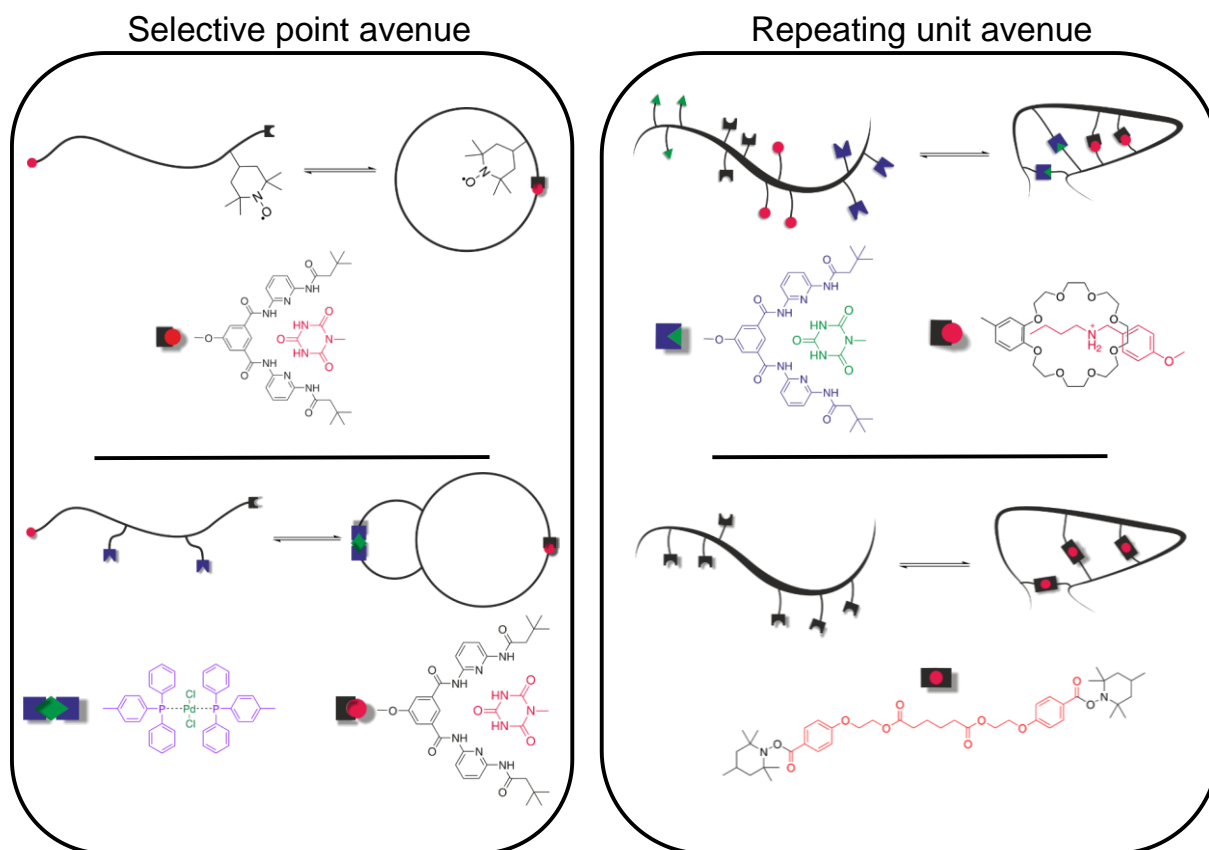


**Figure 1.** Overview over the projects explored in the current thesis, divided in the fields of selective point folding and repeat unit folding.

## SINGLE-CHAIN FOLDING

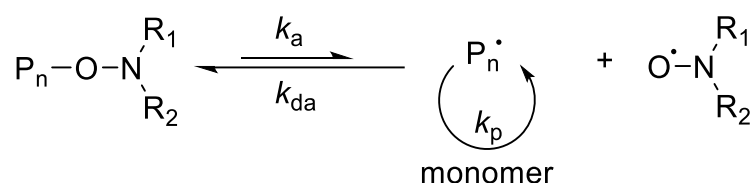
The following section provides the theoretical background relevant for the thesis. An overview over reversible deactivation radical polymerization (RDRP) techniques is provided and the field of single-chain folding is introduced, enabling the reader to follow the subsequent scientific discussions.

### 2.1 Radical Polymerization Techniques

The field of single-chain technology, which commonly applies reversible deactivation radical polymerization (RDRP) techniques, is trying to mimic natural biomolecules such as proteins, although nature's degree of control is yet unreached. The following paragraphs provide an overview over the so-called controlled or living/controlled polymerization methods (or more correctly, RDRP) that were applied in the course of the current thesis to produce well-defined polymers featuring narrow molecular weight distributions, such as nitroxide-mediated radical polymerization (NMP), atom transfer radical polymerization (ATRP) and reversible addition-fragmentation chain transfer (RAFT) polymerization.

### 2.1.1 Nitroxide-Mediated Radical Polymerization (NMP)

Among the RDRP methods, nitroxide-mediated radical polymerization was developed first, despite the power of ionic polymerization methods that were discovered by *Szwarc* in 1956.<sup>[17,18]</sup> The first example was the NMP polymerization of styrene, reported by the group of *Hamer* in 1993.<sup>[19]</sup> Here, styrene was polymerized using dibenzoyl peroxide (DBP) as initiator in the presence of 2,2,6,6-tetramethyl-1-piperidynyl-*N*-oxy (TEMPO). The linear increase of the molecular weight with time suggested a quasi-living nature of the polymerization with constant polydispersities of below 1.3. In fact, the living characteristics of the polymerization can be explained by its polymerization mechanism (refer to Scheme 2).



**Scheme 2.** Fundamental polymerization mechanism underpinning the NMP process. The propagating polymer chains are reversibly trapped by the nitroxide persistent radicals. The reaction equilibrium lies on the side of the deactivated (dormant, left) alkoxyamine.<sup>[20]</sup>

The key feature of the NMP mechanism is the reversible C-O bond cleavage of the (polymeric) alkoxyamine under thermal conditions. The propagation process in NMP is controlled by the so-called persistent radical effect (PRE).<sup>[21]</sup> The activated propagating polymeric species reacts with the nitroxide radical in a deactivation process to form the dormant alkoxyamine. Importantly, the equilibrium lies on the deactivated or dormant side, which is necessary to strongly reduce termination reactions between the propagating species. Consequently, the deactivation coefficient rate ( $k_{\text{da}}$ ) must be much larger than the activation coefficient ( $k_{\text{a}}$ ), leading to a significant decrease of the radical concentration compared to free radical polymerization.

Furthermore, the polymerization can be induced by alkoxyamines, next to employing free nitroxide radicals as initiator.<sup>[20,22]</sup> The chemical structure of alkoxyamines need to fulfil certain criteria, in order to enable a polymerization with living characteristics. First,



## 2.1 Radical Polymerization Techniques

---

they should not self-terminate as well as not initiate the polymerization process. Second, the structure of the alkoxyamine should prevent  $\beta$ -hydrogen abstraction. In addition, a fast C-O bond cleavage of the alkoxyamine at the polymerization temperature is essential.<sup>[18,22,23]</sup> The synthesis of such alkoxyamines is described in different reviews, and the interested reader is referred to literature.<sup>[18,20]</sup> The chemical structure of different commonly used NMP nitroxides is depicted in Figure 2. Generally, NMP is apparently the least-demanding RDRP technique, since it is metal-free and possesses a relatively high functional group tolerance, at least when specialized alkoxyamines are employed.

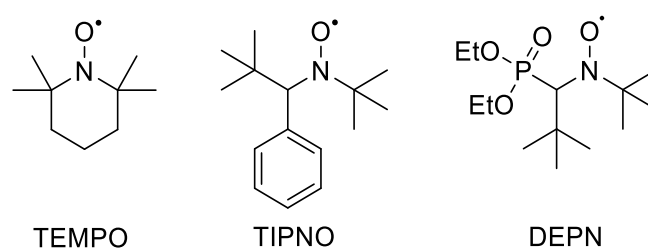
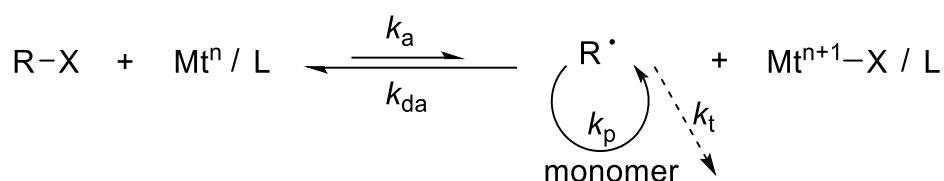


**Figure 2.** Commonly applied nitroxides in NMP.

### 2.1.2 Atom Transfer Radical Polymerization (ATRP)

Besides NMP technology, atom transfer radical polymerization also delivers well-defined polymeric structures. ATRP is based on the principle of atom transfer radical addition (ATRA), and was independently developed in 1995 by *Matyjaszewski* and *Sawamoto*.<sup>[24,25]</sup> To gain control over the radical polymerization process, a fast initiation as well as the generation of dormant species should be dominant to reduce the radical concentration throughout the polymerization process. ATRP meets those criteria by the addition of a transition metal complex in combination with a suitable ligand. The catalytic redox system, consisting of the above mentioned transition metal complex and a ligand, invokes the reversible equilibrium (refer to Scheme 3) between the propagating chain and the deactivated species.<sup>[26]</sup>



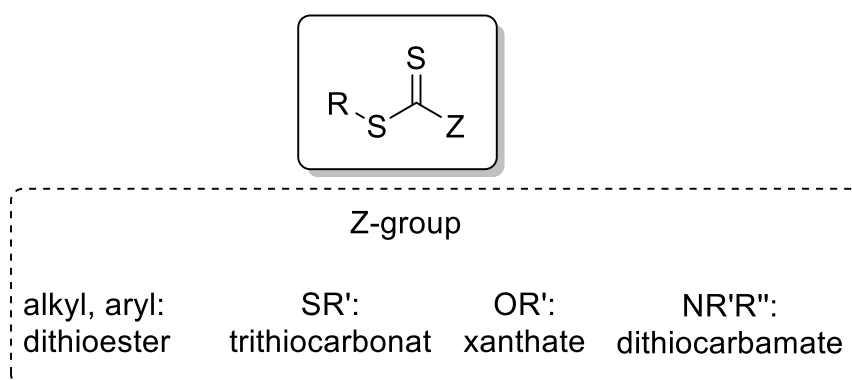
**Scheme 3.** General mechanism of atom transfer radical polymerization. Propagating chains are reversibly trapped with a halide from a transition metal complex to generate the dormant species to prevent termination reactions. Mt: transition metal, L: ligand, X: halide.

In the activation step, the halide which is typically bromine, is transferred to the transition metal, which is oxidized and the generation of a radical occurs simultaneously. The formed radical can subsequently initiate the polymerization. Next, the macroradical is deactivated by the reaction with the halide from the oxidized transition metal complex. The equilibrium is a fast and dynamic process and as for NMP, the equilibrium in ATRP must lie predominantly on the side of deactivated dormant species. In order to reduce the number of radicals present in the system and to hence strongly reduce termination reactions, the propagating radical concentration should typically be around  $10^{-9}$  to  $10^{-8}$  M.<sup>[26,27]</sup> The presence of the halide end group also enables the possibility to directly functionalize the resulting polymer by applying standard organic protocols.<sup>[28]</sup> While several transition metals were applied in ATRP, e.g. Ti, Ru, Co or Re amongst others,<sup>[29–37]</sup> copper based systems appear to provide the most efficient and versatile transition metal complexes.<sup>[38]</sup> In addition to the transition metal derivatives, the ligand plays also an important role in the activation step and therefore has to be selected carefully.<sup>[14]</sup>

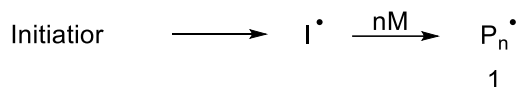
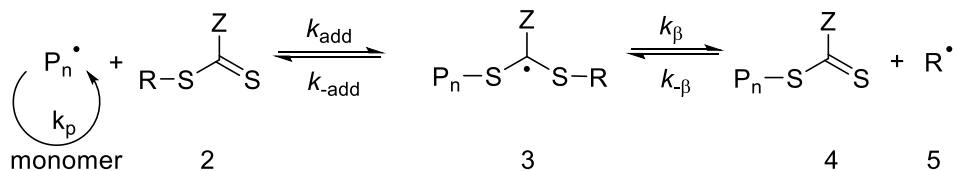
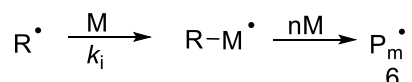
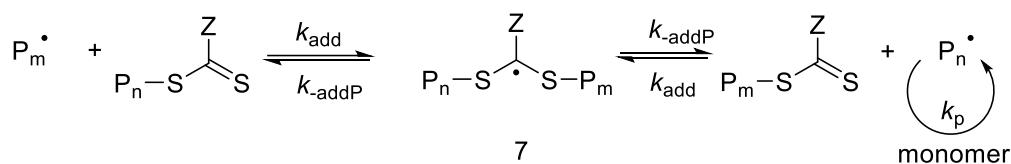
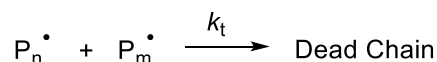
One of the reasons ATRP is frequently used, is the fact that all reagents are commercially available, which is a major advantage compared to the other RDRP techniques. However, there are also some disadvantages present. Since transition metals are used, the system is sensitive towards oxidants such as oxygen, for instance. Furthermore, the removal of the metal complex can be challenging. Progress in the field of ATRP addressed these challenges further. For example, in order to make the system more robust towards oxidation, activators regenerated by electron transfer (ARGET) ATRP has been developed.<sup>[39,40]</sup> Here, the additionally added reducing agent continuously regenerates the catalytic species and reduces the amount of copper in the system to a minimum. In terms of purification of the system towards the metal, a sophisticated protocol has been established.<sup>[41]</sup>

### 2.1.3 Reversible Addition-Fragmentation Chain Transfer (RAFT) Polymerization

The third and last RDRP technique that has been employed within the current thesis to obtain well-defined polymeric structures is the reversible addition-fragmentation chain transfer polymerization technique. Twenty years ago, RAFT was developed by the Commonwealth Scientific and Industrial Research Organization (CSIRO) in Melbourne and has evolved as one of the most powerful and versatile polymerization techniques towards the synthesis complex macromolecular architectures.<sup>[42,43]</sup> Critically, the RAFT process differs from the above discussed NMP and ATRP mechanisms. In the RAFT process, a so-called chain transfer agent (CTA), or the so-called RAFT agent reacts with a propagating chain and generates another radical that can reinitiate macromolecular growth. Thereafter, the growing chain reacts with the CTA and the initially temporarily terminated chain is released again. This reversible step allows for the synthesis of well-defined polymers with high end group fidelity, without a reduction in the radical concentration and thus without (ideally) rate retardation effects.<sup>[42]</sup> Typical RAFT agents are dithioester, trithiocarbonates or xanthates (refer to Figure 3).



**Figure 3.** General structure of a RAFT agent.

**Initiation****Reversible chain transfer****Reinitiation****Chain equilibrium****Termination**

**Scheme 4.** Scheme of the mechanism of the RAFT polymerization displaying the main steps of initiation, reversible chain transfer, reinitiation, chain equilibrium and termination.<sup>[44,45]</sup>

The general RAFT mechanism is depicted in Scheme 4. Identical to conventional free radical polymerization, the initiation of the RAFT polymerization is induced by a classical initiator such as AIBN.<sup>[42,44]</sup> This radical reacts with monomer and forms a polymeric species (1). The polymeric species 1 reacts with the RAFT agent in a preequilibrium step, yielding the dormant species 3. This deactivation step is followed by the release of new radical species (5) that can readily initiate polymerization of a new chain (6), while the (macro-)RAFT agent 4 is regenerated. The polymeric chain 6 subsequently reacts with the macro-RAFT agent and forms the dormant species 7 in the chain- or main equilibrium. As in the preequilibrium, the dormant species 7 can release one of the polymeric chains for further growth. To obtain living characteristics, the dormant species has to be present at high concentrations.<sup>[45]</sup>

The growing chain and the dormant species are in rapid equilibrium, which balances the probability for both chains to grow equally. Hence, the RAFT agent also needs to fulfil certain criteria. First, the C=S double bond needs to be reactive and both – the R and Z group – activate the double bond towards radical addition as well as stabilizing the resulting radical adduct. The S-R bond needs to be a weak single bond, so R can be homolytically cleaved to reinitiate the polymerization, which also needs to hold valid for the later formed bond between the polymeric species ( $P_n$  or  $P_m$ ) attached to the CTA.

The monomers are inserted between the R- and Z-C(=S)S-groups of the respectively used RAFT agent. Consequently, the polymer chains commonly feature the fragmented RAFT agent as end groups.<sup>[43]</sup> Furthermore, the fast and reversible transition between the propagating and dormant chain results in low polydispersities. During the RAFT polymerization, radical-radical coupling is not excluded, and forms – to a limited extent – dead polymer chains. The termination rate directly depends on the radicals that are initially introduced to the system and thus can be limited by lowering the radical concentration, albeit at the cost of polymerization rate.<sup>[43,46,47]</sup>

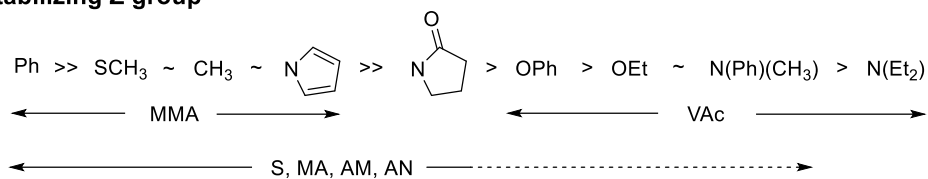
An ideal RAFT process has – as noted above – a similar polymerization rate as conventional free radical polymerization, and hence can be described by following equation:

$$R_p(t) = k_p[M] \sqrt{\frac{fk_d[I]_0 e^{-k_d t}}{k_t}} \quad (1)$$

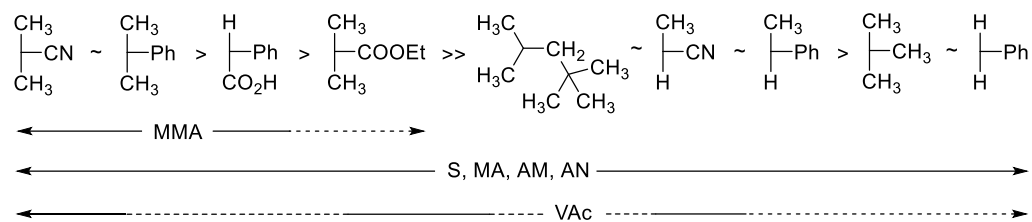
Here,  $R_p$  is the polymerization rate,  $k_p$  represents the propagation rate coefficient,  $k_d$  the decomposition rate coefficient of the initiator,  $k_t$  the termination rate coefficient,  $[M]$  and  $[I]_0$  are the monomer and initial initiator concentration, respectively, and  $f$  indicates the initiator efficiency.<sup>[43]</sup>

Most of the commonly employed monomers in FRP are also accessible in RAFT polymerization with the right choice of the RAFT agent. As indicated above, variable RAFT agents are used for RAFT polymerizations and have to be selected individually for each monomer type. A general guideline for the selection of the R- and Z- group in the CTA is provided in Scheme 5.

## Stabilizing Z group



## Leaving R group



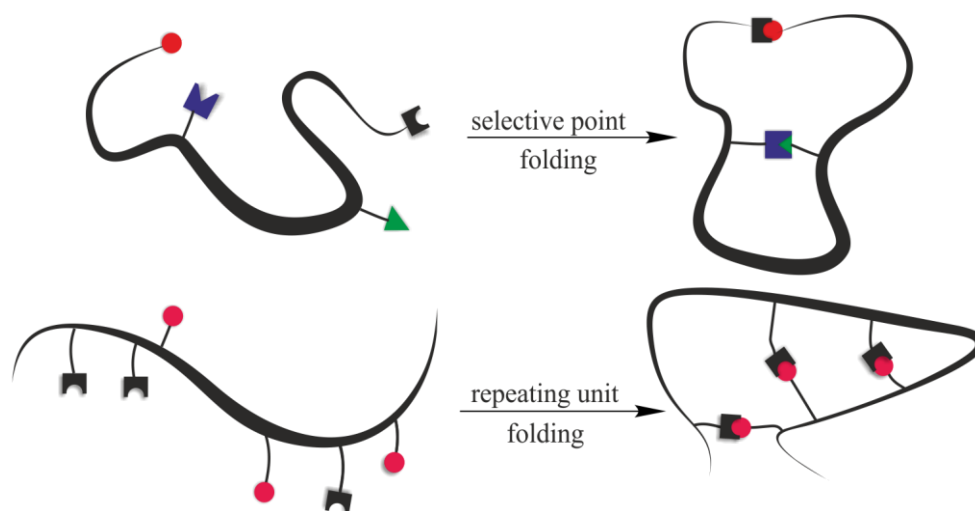
**Scheme 5.** Guideline for RAFT agent selection based on Ref <sup>[44]</sup>. Dashed lines indicate poor polymerization control. MMA: methyl methacrylate, MA: methacrylate, S: styrene, AM: acrylamide, AN: acrylonitrile, VAc: vinylacetate.

### 2.2 Selective Point Folding vs. Repeat Unit Folding

Commonly, single-chain folded architectures can be classified into two main classes according to the method they are synthesized. On the one side, there is the selective point folding avenue: here, the synthetic chemist has to tether the orthogonal folding motifs at pre-selected points along the polymeric backbone (refer to Scheme 6). Consequently, the resulting single-chain nanoparticles, obtained by applying the selective point folding route, are well-defined as a result of a controlled collapse that is induced. The straightforward way is to attach the recognition units at the reactive chain ends of the parent polymer in  $\alpha$ - and  $\omega$ -position, respectively.

In the selective point folding approach, the group of *Barner-Kowollik* used the so-called Hamilton Wedge/cyanuric acid and the thymine/diaminopyridine motifs to prepare well-defined single-chain folded architectures (refer to Figure 4a and c).<sup>[48,49]</sup> In their earliest example, the orthogonal folding motifs were attached in  $\alpha$ - and  $\omega$ - position to result in a SCNP that is cyclic.<sup>[48]</sup> In another study, they were able to fuse these orthogonal recognition units,<sup>[50,51]</sup> and utilize the selective point folding avenue to yield a well-defined dual folding system.<sup>[52]</sup> By tethering the folding entities at preselected points along the polymeric backbone, an 8-shaped architecture was achieved. The resulting structure was subsequently characterized by dynamic light scattering (DLS), diffusion ordered NMR spectroscopy (DOSY) and atomic force microscopy (AFM). In the presented studies, the hydrogen bonds are cleavable by adding a competitive solvent, e.g. methanol. One of the projects investigated in the current thesis is the addition of a spin-label to an  $\alpha$  cyanuric acid and  $\omega$  Hamilton Wedge functional polymer. The spin-label is grafted to the polymer close to the Hamilton Wedge functionality in order to obtain structural information about the polymer in the folded and unfolded state *via* NMR spectroscopy, respectively (refer to Section 3.1.1).

*Lutz* and coworkers prepared well-defined copolymers of styrene and an *N*-propargyl maleimid in bulk *via* ATRP. The varying positioning of the alkyne protected maleimid-based monomer was accomplished by a controlled addition procedure during the polymerization process. Before collapsing the polymers into several macromolecular



**Scheme 6:** Schematic illustration of the selective point folding avenue (upper scheme) and the repeat unit approach (lower scheme), resulting in single-chain folded architectures.

shapes, such as P-, Q-, 8- and  $\alpha$ -shaped, the endgroups of the polymers were modified as well as the protection groups of the maleimides were removed. The folding of the precursor polymers was then executed by intramolecular copper-azide alkyne cycloaddition (CuAAC) under high dilution conditions. The above mentioned structures were subsequently characterized by  $^1\text{H}$  NMR spectroscopy, Fourier-transform infrared spectroscopy (FT-IR) as well as size exclusion chromatography (SEC).<sup>[53]</sup>

In a relevant study, the group of *Barner-Kowollik* prepared a well-defined homotelechelic polymer by ATRP, which featured triphenylphosphines as end groups. The subsequent addition of a palladium (II) metal complex induces the chain collapse. The formation of the single-chain metal complexes were evidenced by  $^1\text{H}$ ,  $^{31}\text{P}\{^1\text{H}\}$  NMR spectroscopy, SEC and DLS.<sup>[54]</sup> Within the course of the current thesis, the concept of metal complexation using a Pd (II) complex is fused with the Hamilton Wedge/cyanuric acid hydrogen bonding motif (refer to Section 3.1.3).

The complementary way to fold single-polymer chains into SCNPs is the repeat unit approach (refer to Scheme 6). By adopting this methodology, the resulting SCNPs are less well-defined in comparison to the selective point folding approach. Often, block and statistical copolymers are utilized in the repeat unit approach. The orthogonal folding moieties are attached along the polymeric backbone, which consequently leads to statistically folded architectures. The drawback is the statistical folding reaction and thus less well-defined SCNPs are obtained *via* the repeat unit approach compared to



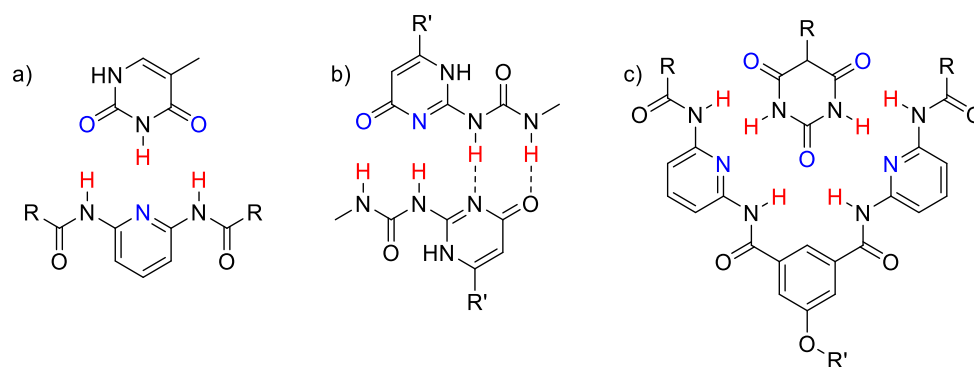


**Figure 4.** The hydrogen bonding motifs thymine/diaminopyridine (a) leading to three hydrogen bonds through DAD/ADA moieties. 2-Ureido pyrimidinone (b) with four hydrogen bonds in a DDAA/AADD interaction and Hamilton Wedge/cyanuric acid (c), forming six hydrogen bonds in a DADDAD/ADAADA interaction.

selective point folding. However, the repeat unit approach, is often synthetically less demanding, as no folding units have to be placed at exact positions within the polymer backbone. The functional polymers can either be directly copolymerized or the recognition motifs are attached to the polymer in post-polymerization modifications. In the literature, examples for SCNPs prepared *via* the repeat unit approach dominate as a result of the more simple synthetic access to SCNPs and their precursor polymers.<sup>[55]</sup>

As above mentioned, metal complexation leads to single-chain metal complexes. Inspired by natural occurring metalloenzymes, *Sanchez-Sanchez et al.* synthesized a water soluble amphiphilic poly(oligoethylene glycol methyl ether methacrylate-*co*-2-acetoacetoxy ethyl methacrylate) (OEGMA-*co*-AEMA) *via* RAFT polymerization to control the molecular weight and obtained narrow dispersities of the polymers.<sup>[56]</sup> The collapse of the polymer strands was induced by the addition of copper (II) acetate in highly diluted aqueous conditions. The progress of the chain compaction was monitored *via* SEC by periodically withdrawing samples. An increasing retention time was observed indicating the successful formation of SCNPs. In addition, the compaction of the single-polymer chains was followed by DLS, small angle neutron scattering (SANS) and <sup>1</sup>H NMR spectroscopy. Accordingly, these authors compared the synthesized SCNPs with the readily available metalloenzymes and draw the conclusion that their metal containing nanoparticles show an increased stability towards thermal changes as well as reduced degradability by hydrolytic enzymes.

On the other hand, the group of *Meijer* prepared a copolymer by the ring opening metathesis polymerization (ROMP) of a 2-ureido-pyrimidinon (UPy) substituted

norbornene,<sup>[57]</sup> which Upy moieties are known to dimerize (refer to Figure 4b) and form hydrogen bonds.<sup>[58–63]</sup> Therefore, the Upy moieties were protected with an UV labile *o*-nitrobenzyl chloride to prevent the dimerization of the Upy motif, and hence provide control on the folding process. Irradiation of the polymers with light at 350 nm cleaves the protecting groups and consequently single-chain folding is induced at high dilutions (below 1 mg mL<sup>-1</sup>). Reversibility of the system is observed when formic acid is added to disrupt the hydrogen bonds, which was justified by SEC, demonstrating a shift towards higher retention times for the intramolecularly collapsed SCNPs.<sup>[57]</sup>

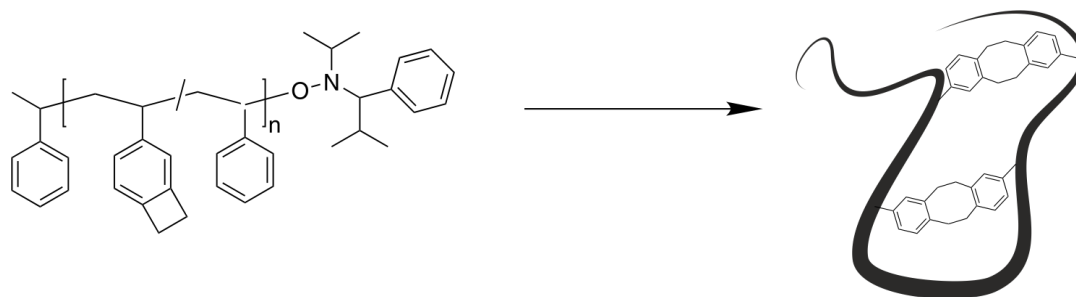
## 2.3 Covalent Crosslinking

A vast variety of covalent crosslinking approaches are known to produce single-chain folded architectures.<sup>[64]</sup> The folding mechanism can be divided into several categories. Generally, it is distinguished between covalent and non-covalent crosslinks to produce the collapsed polymer nanoparticles. The non-covalent folding approaches can be further divided into hydrogen bonds, host-guest interactions and metal complexation (refer to section 2.4). The current section provides a short overview on some selected examples for the covalent crosslinking strategies employed in the field of single-chain folding.

*Hawker* and coworkers introduced the benzocyclobutene (BCB) as a covalent crosslinking unit into the field of single-chain folding.<sup>[65–67]</sup> Until 2002, when they adopted the BCB motif in the single-chain folding realm, the BCB unit was used as a component in latent Diels-Alder reactions in organic chemistry.<sup>[68]</sup> In their study, the precursor block copolymer consisting of styrene-*stat*-4 vinylbenzocyclobutene was prepared *via* NMP. The resulting copolymers feature molecular weights up to 235 kDa and dispersities in the range of 1.08-1.26 along with various BCB mol% within the copolymers (2.5-30 mol%). Nanoparticle formation was exclusively observed by adding the polymer to a boiling solvent such as dibenzyl ether at 250 °C (refer to Scheme 7). Otherwise, even under ultrahigh dilution conditions (5.0×10<sup>-5</sup> M BCB

## 2.3 Covalent Crosslinking

---



**Scheme 7.** Intramolecular crosslinking of a single polymer chain *via* the benzocyclobutene (BCB) unit. Folding is induced by continuous addition of the precursor polymer to benzyl ether at 250 °C, as demonstrated by *Harth et al.*<sup>[65]</sup>

groups), intermolecular crosslinking was pronounced. Nevertheless, the formed crosslinks in the SCNPs are permanent and remain unreactive under the reaction conditions. Respectively, the folded polymers were characterized *via* SEC, DLS and NMR spectroscopy, further suggesting the formation of intramolecular crosslinks.

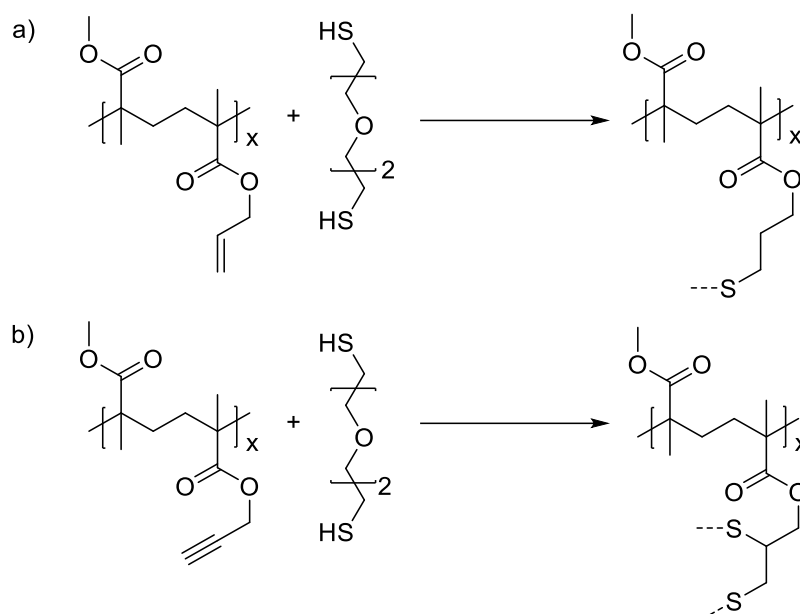
Copper(I) catalyzed azide-alkyne 1,3 dipolar cycloaddition (CuAAC) is a powerful tool for creating conjugated polymers and has been reviewed in detail.<sup>[69–75]</sup> The CuAAC was demonstrated to be applicable during the synthesis of single-chain folded aggregates.<sup>[76–78]</sup> *De Luzuriaga et al.* reported the synthesis of SCNPs that are crosslinked through the CuAAC.<sup>[76]</sup> Here, a terpolymer featuring the monomers methyl methacrylate, 3-azidopropyl methacrylate and 3-trimethylsilyl-propyn-1-yl methacrylate was polymerized by RAFT, in order to obtain good control over the molecular weight as well as the distribution. Polymers with different functional concentrations of the functional monomers were prepared with 4, 7 and 10 mol%, respectively, prior to collapsing the systems. After the polymerization, the trimethylsilyl (TMS) protected alkyne functionality was deprotected followed by the CuAAC reaction. The formation of the intramolecular 1,2,3 triazole, generated during the crosslinking reaction, was confirmed by FT-IR and <sup>1</sup>H NMR spectroscopy. In the IR spectrum, the azide asymmetric stretch at 2102 cm<sup>-1</sup> as well as the TMS protecting group at 2181 cm<sup>-1</sup> indicate the successful folding reaction. The successful reaction is additionally supported by <sup>1</sup>H NMR spectroscopy. The <sup>1</sup>H NMR spectrum displays a new resonance at 5.36 ppm associated with the triazole ring, in addition to the vanished resonances from the TMS protecting group at 0.2 ppm. Further, SEC measurements indicated a decrease of the apparent number average molecular weight ( $M_n$ ) of 40–46%, the latter arising from the fact that the SCNPs are known for their reduced

hydrodynamic volume in comparison to the unfolded precursor polymers. Furthermore, the nanoparticles were also visualized by TEM, depicting sub 10 nm particles, providing additional proof for the formation of intramolecularly folded nanoparticles.

*Pomposo* and coworkers applied the Glaser-Hay coupling for self-ligating homofunctional polymer chains internally.<sup>[79]</sup> Synthetically, MMA was copolymerized with propargyl acrylate (PgA) in a redox initiated RAFT polymerization process. The intramolecular crosslinking was realized by the Glaser-Hay coupling, which is a copper-catalyzed carbon-carbon coupling.<sup>[80,81]</sup> The intramolecular folding was conducted in high dilution under inert atmosphere, due to the oxygen labile CuI catalyst. Tetramethylethylenediamine (TMEDA) was used as ligand for the copper(I) complex. The diyne functional SNCPs were obtained in the range of 80-92% and characterized by SEC, the latter showing the shift of the retention time.

In another study from the group of *Pomposo*, the photo activated thiol-ene as well as the thiol-yne coupling (TYC, refer to Scheme 8) was explored in the field of single-chain folding.<sup>[82]</sup> Copolymers with unprotected alkene and alkyne functionalities were prepared *via* redox-initiated RAFT polymerization for fine control over the molecular weight and dispersities of the copolymers. Molecular weights of the alkene/alkyne functional polymers were targeted to a molecular weight of around 125 kDa and close to 20 mol% of the functionality within the random copolymer. A mixture of dimethylaniline (DMA) and benzoyl peroxide (BPO) was used as redox-initiator, while 2-cyano-2-propyl-benzodithioate (CPBD) was selected as a chain transfer agent (CTA), MMA and allyl methacrylate were utilized as monomers. For the alkyne functional copolymer, the allylic acrylate was substituted by propargyl acrylate. The resulting precursor polymers were folded by photoactivated thiol-ene coupling (TEC) and TYC ( $\lambda = 300-400$  nm), respectively, using 3,6-dioxa-1,8-octane-dithiol (DODT) as homobifunctional crosslinker. The resulting single-chain aggregates were characterized by means of SEC, SAXS and DLS to unambiguously underpin the assumption of intramolecular collapsed polymeric nanoparticles.

## 2.3 Covalent Crosslinking



**Scheme 8.** Photoactivated crosslinking of an alkene functional polymer by thiol-ene coupling (a) and an alkyne functional polymer via thiol-yne coupling (b) using 3,6-dioxa-1,8-octane-dithiol (DODT) as crosslinker reported by Pomposo and coworkers.<sup>[82]</sup>

In the group of *Barner-Kowollik*, the covalent crosslinking of single polymer chains was accomplished by using hetero Diels-Alder (HDA) chemistry.<sup>[83]</sup> Initially, a cyclopentadiene (Cp)-protected cyanodithioester (CDTE) monomer was copolymerized with MMA by either RAFT polymerization or conventional free radical polymerization. The polymers feature different chain length and molar ratios of the functional monomer and were subsequently folded by heating the dilute solution of the polymer in presence of a sorbic bilinker, which substituted the Cp of the protected CDTE. The presented HDA system can be reversed by heating the SCNP in a solution with an excess of sorbic alcohol, which consequently leads to the unfolded nanoparticles. The folding and unfolding of the polymers was monitored by SEC and DLS, both showing the characteristic features of single-chain nanoparticles, *i.e.* a shift towards higher retention times in SEC, due to the compaction of the polymer chain and smaller DLS derived hydrodynamic diameters (from 3.9 nm of the parent polymer to 3.3 nm for the folded SCNP). In addition, the folding and unfolding character of the system was monitored by <sup>1</sup>H NMR spectroscopy. The comparison of the CDTE resonances of remaining Cp-protected species and for the open chain (in the range of 6-7 ppm) with the adduct resonances at approximately 5.5-6.0 ppm indicate the formation of crosslinks of close to 86% after the crosslinking reaction. The group of *Berda* used the thermally triggered DA reaction for the intra-chain crosslinking of a

furan and maleimide containing copolymer.<sup>[84]</sup> Synthetically, the intramolecular folding was induced by reaction of a maleimide and pendant furan groups. In their study, two methods to fold the linear polymer chains were pursued: (i) the internal folding reaction by synthesizing a terpolymer of MMA, furfuryl methacrylate (FMA) and a maleimide functional methacrylate and (ii) induction of the intra-chain crosslinking reaction of a MMA and FMA copolymer by adding an external maleimide functional crosslinker.

Besides the thermally induced Diels-Alder (DA) reactions presented above, DA reactions can also be triggered by light to induce the folding reaction of functional polymers, as demonstrated by *Altintas et al.*<sup>[85]</sup> The precursor block copolymer was prepared from styrene and 4-chloromethylstyrene (CMS) *via* the NMP technique to control the functional group density (from 9 to 34 mol%) along with narrow polydispersities. The photo responsive DA motifs – 4-hydroxy-2,5-dimethylbenzophenone and a maleimide analogue – were attached to the polymer in a post-polymerization modification manner, which is a one-pot two-step procedure. The quantitative functionalization of the block copolymer was confirmed by <sup>1</sup>H NMR spectroscopy. The intramolecular crosslinking was subsequently induced by UV light ( $\lambda_{\max} = 320$  nm) in DCM under highly diluted concentrations ( $c = 0.0117$  mg mL<sup>-1</sup>). Here, SEC was indicative of intermolecular crosslinking at higher concentrations. In addition, a kinetic study of the folding process was conducted, suggesting completed single-chain folding after 30 min of irradiation. The size of the SCNPs could be tuned by the functional group density of the folding motifs. Monotethered nanoparticles were obtained by CuAAC of the precursor polymers with an azide functional polyethylene glycol. The folding of the precursor polymers was followed by SEC, DLS, <sup>1</sup>H NMR spectroscopy and atomic force microscopy (AFM).

The group of *Barner-Kowollik* pioneered the synthesis of fluorescent single-chain nanoparticles induced by UV light.<sup>[86]</sup> The folding reaction is based on tetrazole chemistry<sup>[87,88]</sup> in – the natural occurring medium – water. The use of water corresponds to the working medium of proteins and enzymes. Poly(acrylic acid) (PAA) was selected as water soluble polymer, due to its well-known properties, such as non-toxicity and biocompatibility.<sup>[89]</sup> The linear PAA were synthesized by RAFT and subsequently modified by esterification with the tetrazole (Tet), furan-protected maleimide and triethylene glycol monomethyl ether for better biocompatibility in a ratio of 1:2.5:5.3 and 1:2.3:3.3. Both polymers still possess unreacted carboxylic acid

## 2.3 Covalent Crosslinking

functionalities. However, these unreacted acid functionalities can react efficiently with photogenerated nitrile imines, as was also shown by *Li* and coworkers.<sup>[90]</sup> The single-chain architectures were synthesized by the photo induced nitrile imine-mediated tetrazole-ene cycloaddition (NITEC). In order to verify the nitrile imine- carboxylic acid ligation (NICAL), which occurs simultaneously, due to the presence of unreacted carboxylic acid functionalities within the polymers, an additional polymer only featuring the Tet units was prepared. After irradiating the highly diluted solution of the unfolded polymers at  $\lambda_{\text{max}} = 320 \text{ nm}$  for 17 h, the resulting SCNPs were readily characterized by  $^1\text{H}$  NMR, UV-vis, fluorescence spectroscopy, DLS and SEC, all indicating the successful formation of single-chain nanoparticles.

The dimerization of anthracene is often discussed alongside with the dimerization of coumarin and cinnamates in the field of single-chain folding, exploited to photochemically induce the chain collapse.<sup>[91–94]</sup> The group of *Berda* used the known photochemical dimerization behaviour of anthracenes<sup>[95]</sup> and adopted it in the realm of single-chain folding. Hence, they utilized the dimerization ability of anthracene in a [4+4] cycloaddition manner upon irradiation with  $\lambda_{\text{max}} = 350 \text{ nm}$  (refer to Figure 5a).<sup>[96]</sup> A copolymer of MMA was copolymerized with 9-anthracene methacrylate by RAFT to control the composition as well as the molecular weight and its distribution. The SCNPs containing the lowest functional group density (10 mol%) showed the smallest change of the hydrodynamic volume in SEC, whereas the SCNP derived from the precursor with 46% anthracene units shows the largest shift in SEC towards higher retention times, indicative of SCNP formation.

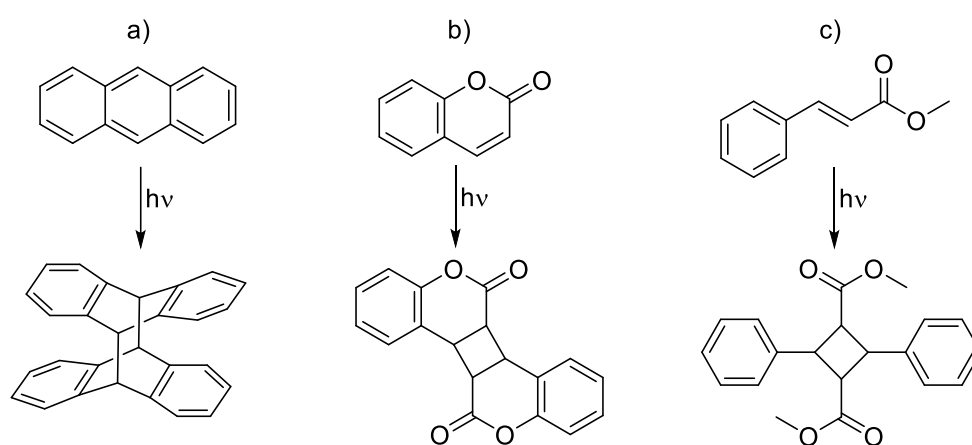


**Figure 5.** Photochemical dimerization of a) anthracene, b) coumarin and c) cinnamates in the realm of single chain folding.<sup>[91–94,96]</sup>

The multi-angle light scattering (MALLS) detector adopted in the triple detection SEC system for characterization unveiled a small shoulder at shorter retention times for the folded polymers with increasing reaction time, indicating intermolecular crosslinking. This higher molecular weight shoulder becomes more and more pronounced with increasing anthracene content.

There are many more possibilities and functionalities to access single-chain nanoparticles, such as photo induced Bergman cyclization<sup>[97]</sup>, Michael addition<sup>[98,99]</sup> or intramolecular metathesis<sup>[100,101]</sup>, among many others.<sup>[55,64,102–104]</sup>

## 2.4 Non-Covalent Interactions

In order to emulate naturally occurring structures such as proteins, non-covalent chemistry – namely hydrogen bonds, aromatic stacking and hydrophobic interactions – are used in the realm of single-chain folding along covalent folding chemistry, which was discussed in the previous section. The following section focuses on non-covalent interactions that induce single-chain folding and stabilize the resulting SCNP architectures.

### 2.4.1 Hydrogen Bonds

The class of hydrogen bonds is the most applied and studied design to stabilize single-chain nanoparticles. Several orthogonal motifs are known in literature such as the benzene-tricarboxamide (BTA),<sup>[105,106]</sup> 2-ureidopyrimidinone (Upy),<sup>[57,107]</sup> or Hamilton's Wedge/cyanuric acid (HW/CA),<sup>[48]</sup> ranging from two to six hydrogen bonds. Some selected examples will be introduced in the following section.

An important motif in the class of hydrogen bonding is the so-called benzene-tricarboxamide (BTA), which forms three hydrogen bonds to stabilize the collapsed architecture. The group of *Meijer* intensively studied the BTA folding motif.<sup>[105,106,108–118]</sup> The self-assembly of the BTA units, to develop a helical internal secondary



## 2.4 Non-Covalent Interactions

structure within the SCNP (refer to Figure 6a), can be controlled by introducing the photolabile *o*-nitrobenzyl group that can be cleaved by irradiation of the polymer at  $\lambda_{\max} = 354 \text{ nm}$ .<sup>[106]</sup> The investigated polymers consisted of propargyl methacrylate and isobornyl methacrylate in the ratio of 80:20, which were copolymerized *via* ATRP. The resulting polymers contained close to 25% propargyl groups and subsequently about half of the accessible propargyl groups were converted with an azide functional BTA-moiety in a copper(I) catalyzed azide-alkyne cycloaddition reaction affording a copolymer with about 20 BTA units per chain. After the UV light induced deprotection of the BTA moiety in high dilution ( $c = 3 \text{ mg mL}^{-1}$ ), the intramolecular self-assembly was observed in a mixture of 1,2 dichloroethane and methylcyclohexane (65:35 vol%) and readily characterized by circular dichroism (CD) spectroscopy. CD spectroscopy illustrates a negative Cotton effect at  $\lambda = 225 \text{ nm}$  and suggests the collapse.

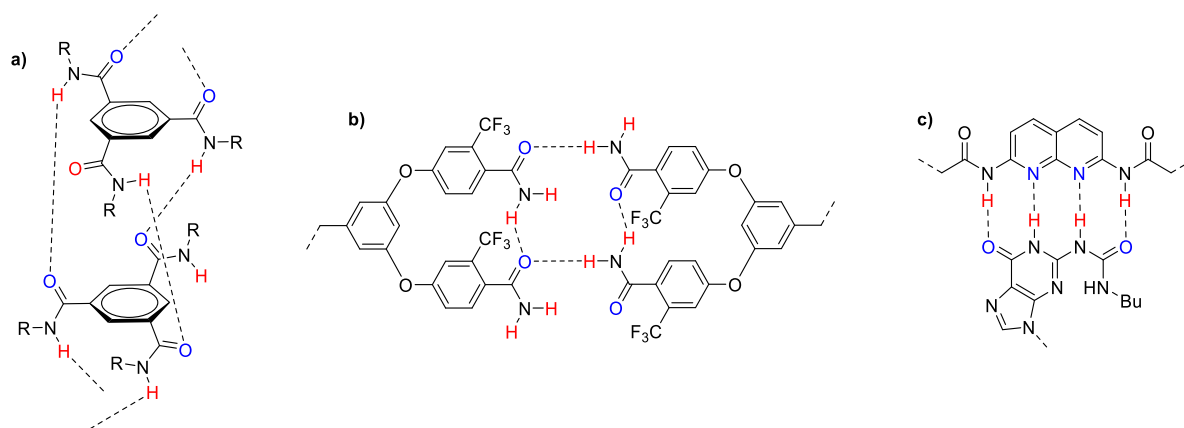


**Figure 6.** Hydrogen bonding motifs a) benzene-tricarboxamide (BTA) building up three hydrogen bonds. b) the quadruple hydrogen bonding motif of the dimerizing benzamide and c) the ureidoguanosine and diaminonaphthyridine (UG-DAN) quadruple hydrogen bonding motif.

The orthogonality of the BTA was shown in another study by the group of *Meijer* in which the dual folding was induced by exploiting the self-assembly of the BTA unit and additionally the dimerization of the Upy hydrogen bonding motif.<sup>[110]</sup>

The second literature known example that leads to three hydrogen bonds is the thymine/diaminopyridine recognition motif, which has been discussed in Section 2.2.

The 2-ureidopyrimidinone (Upy) functionality leads to four hydrogen bonds by the dimerization of the Upy motif and was presented in Section 2.2 and thus will not be discussed in further detail in the current section.

Seo et al. caused the intramolecular non-covalent crosslinking with a benzamide containing polymer.<sup>[119]</sup> The functional polymer was prepared by the copolymerization of methyl methacrylate (MMA) and a MMA based monomer featuring a benzamide dendron (refer to Figure 6b) *via* RAFT. The folded state was reached by dissolving the polymers in a mixture of THF and toluene with subsequent evaporation of the more volatile THF. The intramolecular folded structures were characterized *via* scanning force microscopy showing well dispersed, uniform, spherical nanoparticles. These results were confirmed by dynamic light scattering (DLS) measurements.

Weck and coworkers used the recognition motif of ureidoguanosine and daminonaphthyridine (UG-DAN) for quadruple hydrogen bonds (refer to Figure 6c).<sup>[120]</sup> A triblock copolymer was synthesized by ring opening metathesis polymerization (ROMP) featuring the DAN, UG functionalities on the outer block A and C, respectively, while a flexible middle block (norbornene octyl ester) served as spacer. The sheet-type single-chain structures were characterized and verified *via* DLS and <sup>1</sup>H NMR spectroscopy.

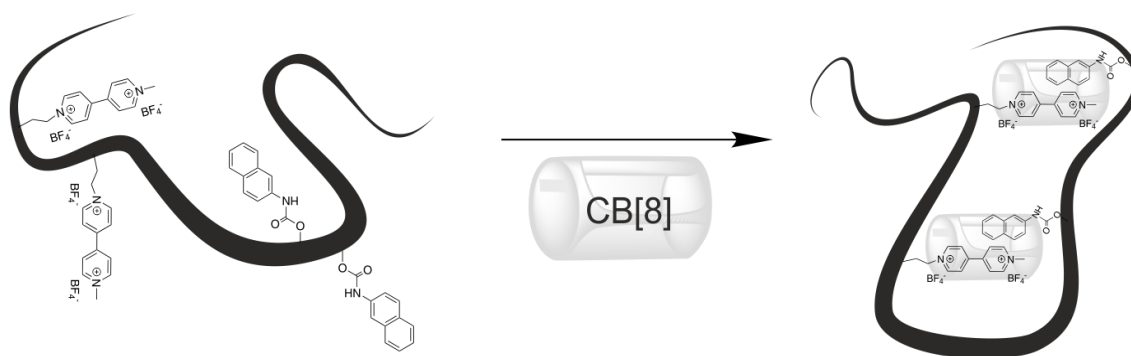
As indicated in Section 2.2, the Hamilton Wedge/cyanuric acid (refer to Figure 4c) recognition pair can be applied in the single-chain realm to stabilize the SCNPs by six hydrogen bonds.<sup>[48–50,52,108]</sup> In a collaborative study of the *Meijer* and *Barner-Kowollik* groups,<sup>[108]</sup> a PMMA based copolymer polymer featuring a primary bromine functional monomer, a trimethylsilyl protected alkyne as well as a trimethylsilyl protected hydroxyl functionality, was prepared. The ABC-type block copolymer was synthesized through chain-extension *via* RAFT polymerization. Each functional monomer was copolymerized with ethyl hexyl methacrylate and the final polymer contains close to 5% of each functional monomer. In post-polymerization modifications, the HW/CA pair was grafted to the outer blocks A and C, whereas the BTA moiety was attached to the middle block B. The motifs were orthogonally linked *via* etherification, CuAAC and Steglich esterification, respectively.<sup>[108]</sup> The recognition motifs fold selectively as was shown with various characterization techniques. CD measurements of the SCNP show no interference of the HW/CA folding motif on the BTA self-assembly. Furthermore, NMR studies show no influence of the BTA motif of the folding of the HW/CA pair. To evidence the single-chain nature of the resulting structures, light scattering measurements were carried out resulting in particle sizes between 11.7 and 24.4 nm. Here, the size of the SCNPs is depending on the size of the precursor polymers.

### 2.4.2 Host-Guest Interactions

As it is one of the overall aims in the field of single-chain folding to emulate nature's structures and to be able to ultimately synthesize a synthetic protein, it is important to explore several classes of binding motifs. A second class of reversible binding motifs that will be discussed are host-guest systems. Host systems applied in the field of single-chain folding are cyclodextrins<sup>[121]</sup> or cucurbit[n]uril,<sup>[122]</sup> for instance.

Cyclodextrins are well studied hosts and were successfully applied in single-chain technology.<sup>[121,123,124]</sup> In order to emulate the natural occurring working medium of proteins, *Willenbacher* et al. prepared a water soluble polymer with the cyclodextrin (CD)/Adamantyl (Ada) host-guest system in  $\alpha$  and  $\omega$  position, respectively. The Ada moiety is known to be strongly complexed by  $\beta$ -cyclodextrins in aqueous media with association constants up to  $10^5 \text{ M}^{-1}$ .<sup>[124]</sup> The resulting SCNPs were followed by DLS as well as nuclear Overhauser enhancement spectroscopy (NOESY). The group of *Che* used the  $\beta$ -CD host in another system with a bridged bis(ferrocene) guest to prepare electrically responsive single-chain nanoparticles.<sup>[121]</sup>

Another commonly used host-guest system is the family of cucurbit[n]uril (CB[n]). Here, the number of glycoluril units is given by the number [n]. The most commonly used CB[n] are CB[5]-CB[8].<sup>[125,126]</sup> The cucurbiturils are mostly used to prepare supramolecular assemblies as well as networks.<sup>[127-131]</sup> Generally, cucurbituril hosts complex hydrocarbons, for example, CB[8] is capable of binding two aromatic rings simultaneously, such as biphenyl or naphthalene derivatives.<sup>[125,132]</sup> *Sherman* and coworkers took advantage of this feature and used the CB[8] host to complex a substituted bipyridine and a substituted naphthyl moiety to induce the single-chain collapse by the formation of a host-guest complex in water (refer to Scheme 9).<sup>[133]</sup> Another advantage of the host-guest interaction is that it can be disrupted by different external stimuli such as pH, light or temperature. The applicability in water demonstrates another step towards the overall aim in mimicking natural proteins, since



**Scheme 9.** Schematic illustration for the host-guest complexation of a bipyridine and naphthyl moiety by the CB[8] complex.<sup>[133]</sup>

they are operating in aqueous media. Furthermore, the same group used the larger *nor-seco*-CB[10] (*ns*-CB[10]) to prepare a ternary 2:1 complex. The *ns*-CB[10] has two identical cavities and binds a substituted bipyridine as a guest inducing single-chain folding, yielding a ternary 2:1 complex.<sup>[122]</sup> The (reversible) SCNPs were monitored by DLS and AFM measurements.

In the current thesis, a dual folding system consisting of the hydrogen bonding system Hamilton Wedge/cyanuric acid (refer to Section 2.3.1) and the host guest system benzo-21-crown-7 and a secondary ammonium salt (refer to Section 3.2.1) has been prepared to increase the system complexity and move towards the next level in order to mimic the high complexity of natural biomacromolecules. In addition, the dynamic nature of the folding/unfolding has been investigated.

### 2.4.3 Metal Complexation

In nature, the higher ordered structures are not only stabilized by non-covalent hydrogen bonds but also other techniques to maintain and stabilize their structure such as hydrophobic interactions, aromatic stacking or metal complexation.<sup>[134]</sup> In the following section, some of the established methods for metal complexation that are applied in the single-chain folding realm are presented.

Several metals can be used to induce the collapse of single polymer chains such as copper (II),<sup>[56,135–139]</sup> rhodium (I),<sup>[140–142]</sup> iridium (I),<sup>[141]</sup> nickel (0),<sup>[141]</sup> palladium (II),<sup>[54,143]</sup>

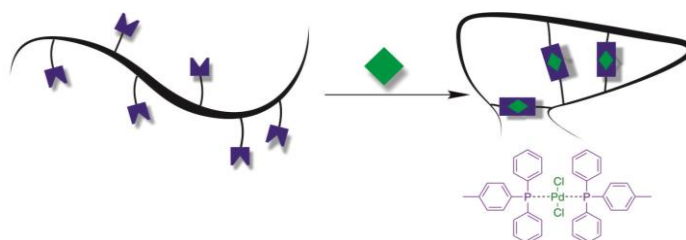
## 2.4 Non-Covalent Interactions

---

ferrous (II)<sup>[144,145]</sup> or platinum (II).<sup>[146]</sup> Although copper is known to be toxic in high amounts,<sup>[147,148]</sup> several examples can be found in literature with respect to single-chain folding. *Bai et al.* synthesized a polyolefin containing aspartate, which was internally crosslinked by the addition of Cu (II) in water, mimicking natural metalloenzymes. The so-called metal-organic nanoparticles (MONP) were further used in a CuAAC click reaction for the ligation of terminal functional alkynes and azides with low catalyst concentration of the Cu catalyst (parts per million) in water. Importantly, the MONP display low toxicity.<sup>[139]</sup>

The group of *Lemcoff* prepared a poly(cyclooctadiene). The ethylene ligands of a rhodium (Rh) complex were exchanged with the double bonds of the cyclooctadiene (COD) and thus led to the compaction of the single-polymer chain by metal complexation. In a proof of concept study, the complexation was first shown in a small molecule study. For the SCNP, the size reduction of the polymer was monitored *via* DLS, SEC and TEM, all suggesting the formation intramolecular linked SCNPs.<sup>[140]</sup> The same group was also able to expand that principle to the iridium (I) and Ni (0) metals as well as the combination of Rh (I) and Ir (I) to bimetallic nanoparticles.<sup>[141]</sup>

In our group, the single-chain folding induced by the complexation of platinum (II) ions was investigated along with the catalytic activity for the amination of allyl alcohol of the prepared single-chain nanoparticles. The polymer was prepared by NMP, copolymerizing styrene and 4-(diphenylphosphino)styrene employing different feedstock ratios. The phosphine can form 2:1 complexes with Pt (II) and thus leads to the compaction as a result of the intramolecular crosslinking as demonstrated by DLS and DOSY (refer to Scheme 10).<sup>[146]</sup> The incorporation of the Pt ions was verified by <sup>31</sup>P as well as <sup>195</sup>Pt NMR spectroscopy. A catalytic study for the amination of allyl alcohols displays better or similar results of the Pt-SCNPs compared to [Pt(PPH)<sub>3</sub>Cl<sub>2</sub>] catalyst.



**Scheme 10.** Schematic illustration of the SCNP collapse induced by metal complexation of triarylphosphane containing polymers using Pt (II) ions.

### 2.4.4 $\pi - \pi$ Interactions

Nature stabilizes its formed higher architecture structures by hydrogen bonds, hydrophobic interactions or aromatic stacking. As a result, the field of single-chain polymer nanoparticles also knows some examples exploiting aromatic  $\pi - \pi$  stacking. An example for aromatic stacking was provided by the group of *Weck*. In their study, a triblock copolymer consisting of pentafluorostyrene (PFS), *N,N* dimethylacrylamide and styrene on the blocks A, B and C, respectively, was prepared using the RAFT protocol. The folding of the system was induced by the  $\pi - \pi$  interactions between the A and C blocks of the electron deficient PFS block A and the electron rich styrene block C. The middle block B of the copolymer serves as a spacer block consisting of poly(acrylamide). The SCNP is suggested to form  $\beta$ -hairpin structure.<sup>[149]</sup>

*Gillissen* et al. prepared polynorbornene based polymers featuring (*N*-dodecyl)-5-norbornene-exo-2,3-dicarboximide and 3,3'-bis(acylamino)-2,2'-bipyridine substituted benzene-1,3,5-tricarboxamide (BiPy-BTA) *via* ring opening metathesis polymerization.<sup>[150]</sup> Polymers with 5 and 10% BiPy-BTA were prepared. In high dilution, the BiPy-BTA units lead to the intramolecular collapse of the polymers, stabilized by  $\pi - \pi$  interactions. Interestingly, after the collapse the formed SCNPs show fluorescent, compartmentalized characteristics. 2,2' Bipyridines are known for their affinity to metal ions such as copper,<sup>[151–153]</sup> making the SCNPs interesting for applications such as sensing of Cu(II) ions. When metal ions such as Fe(III), Cr(III), V(III), Mn(III), Zr(III) or Cu(II) are added the fluorescence is quenched, whereas Cu(II) ions were shown to be most effective in decreasing the fluorescence.

Within the current thesis, luminescent, *i.e* fluorescent, single-chain nanoparticles have been prepared. Hence, in the following paragraphs the concept of luminescence and their application within the field of single-chain folding will be discussed.

### Fluorescent Single-Chain Nanoparticles

Generally, upon light impact, an electron is excited from its electronic ground state, which is usually a singlet state and called  $S_0$ , to the excited (singlet) state  $S_1$ ,  $S_2$  and so on, possessing higher energies. The excitation process is also referred to as absorption. The excited states undergo different competing deactivation mechanisms. The activation and deactivation processes can be illustrated in the so-called Jablonski diagram (refer to Figure 7). The deactivation process can either occur non-irradiative (vibrational relaxation and internal conversion) or irradiative, resulting in fluorescence or phosphorescence. In non-irradiative processes, the energy is thermally dissipated by the transition from higher (excited) states to levels of lower energy. By the transition from the excited  $S_1$  state to the ground state  $S_0$ , fluorescence is generated (irradiative deactivation). Compared to non-irradiative processes, fluorescence is a rather slow process. In addition to fluorescence, phosphorescence can be observed when intersystem crossing (ISC) occurs from the excited singlet state to an excited triplet state, although being spin forbidden. The non-radiative transition of the ISC can only take place between excited states of different spin multiplicity.<sup>[154]</sup> Here, the emission of radiation from the ground level of the excited triplet state to the ground state  $S_0$  causes the phosphorescence. ISC is a slow process, resulting in an even slower process for phosphorescence, which makes the phenomenon of phosphorescence rather unlikely.<sup>[155–157]</sup>

The concept of fluorescent single-chain nanoparticles is relatively new, nevertheless the way to implement fluorescent properties to the respective nanoparticles can be divided into four strategies: (i) the precursor is pre-functionalized with a fluorophore; (ii) post-polymerization functionalization of the SCNP with the fluorophore; (iii) the fluorophore entrapment/*in situ* generation or (iv) fluorophore generation through SCNP collapse. For the routes (i) and (ii) the fluorescent moiety is attached before or after the single-chain collapse, respectively.<sup>[76,158]</sup> Within the third route, a fluorescent moiety such as pyrene is attached to the polymer to e.g. determine the polarity in locally packed zones in the folded SCNP.<sup>[159,160]</sup> The example from *Gillissen et al.*<sup>[150]</sup> exploits the fourth pathway to fluorescent SCNPs: the fluorophore is generated *via* the collapse of the single polymer chains.

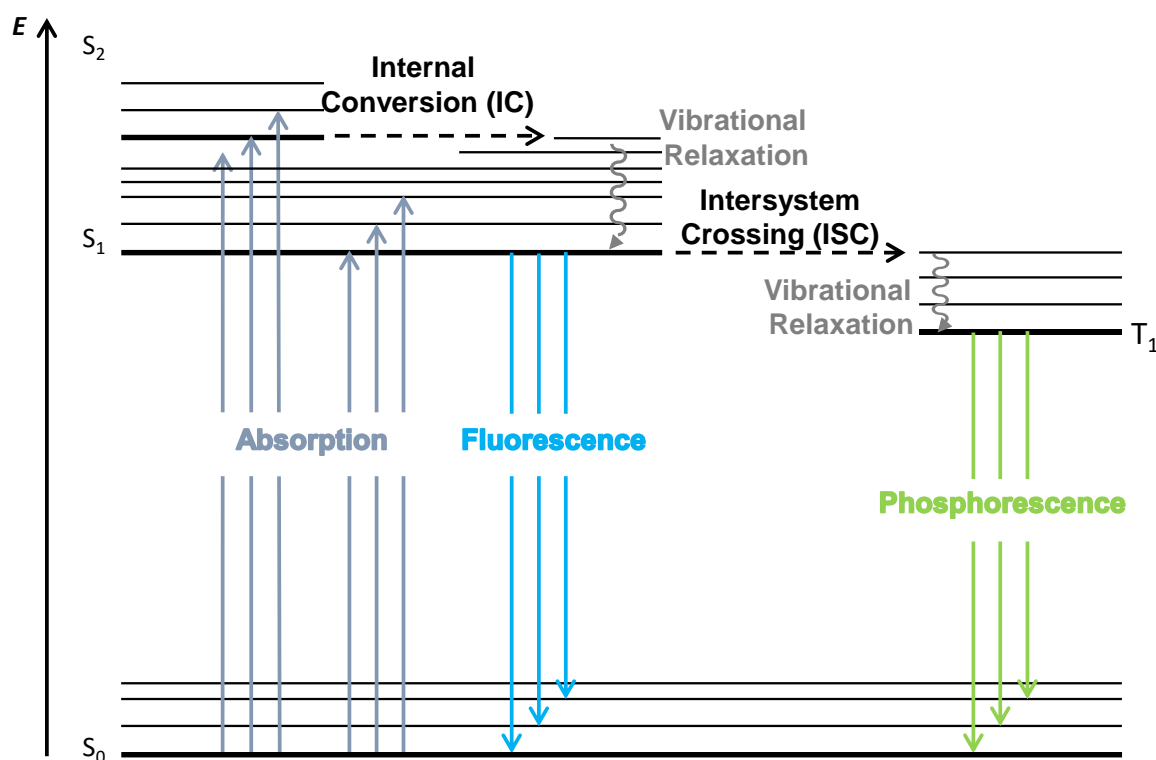


**Figure 7.** Schematic Jablonski diagram. The ground electronic singlet state  $S_0$ , excited singlet state  $S_1$ , and triplet state  $T_1$  energies (together with vibrational states) are indicated by horizontal lines. Fluorescence and phosphorescence (radiative) vibrational transitions, internal conversions and intersystem crossing (non-radiative) processes are indicated by arrows. The levels of vibrational energy and the position of the electronic states are not drawn to scale.<sup>[155]</sup>

### 2.4.5 Hydrophobic Interactions

As mentioned in the section above higher degree architectures by nature are also stabilized by hydrophobic interactions.<sup>[134]</sup> Inspired by nature, the field of single-chain polymeric nanoparticles adopted the concept of hydrophobic interactions to produce single-chain nano-objects.<sup>[161–165]</sup>

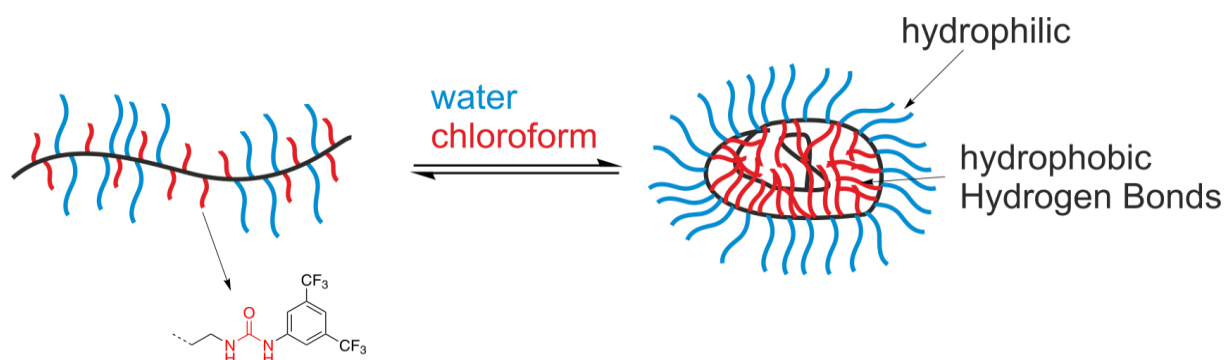
Sawamoto and coworkers synthesized single-chain aggregates by producing water soluble amphiphilic copolymers based on methacrylates through the course of ruthenium-catalyzed RDRP.<sup>[161]</sup> The water solubility arises from the poly(ethylene glycol)methyl ester methacrylate (PEGMA), whereas the hydrophobic alkyl methacrylates, e.g. MMA, *n*-butyl methacrylate or *n*-octyl methacrylate, lead to the formation of single-chain aggregates in water under highly diluted conditions. Interestingly, the molecular weight of the unfolded polymer should be identical to the



## 2.4 Non-Covalent Interactions

estimated SCNP in water, while the size should be smaller in aqueous medium in comparison to good organic solvents. Single-chain folding is observed for up to 40 mol% of hydrophobic functionalities within the polymer. When the concentration is further increased to 50 mol%, intermolecular interactions are observed. These results were also observed in SEC-MALLS measurements as well as DLS. Due to repulsion effects in water, single-chain aggregates are stable to concentrations up to 60 mg mL<sup>-1</sup>. As mentioned above, the hydrodynamic radii obtained by DLS are larger compared to the obtained  $R_h$  in water. The fairly high concentrations as well as the aqueous medium used for the hydrophobic interactions represents a step towards mimicking natural (bio-)macromolecules such as enzymes and proteins.

In another study by the same group, the authors were able to combine hydrophobic folding with intramolecular hydrogen bonding (refer to Scheme 11).<sup>[164]</sup> The feature was realized by preparing a poly(ethylene glycol) and urea functionalized amphiphilic random copolymer, which was again synthesized by ruthenium-catalyzed RDRP. The folding was followed by SEC-MALLS and DLS measurements in water as well as in chloroform as organic solvent.



**Scheme 11** Schematic illustration of the hydrophobic/hydrogen bonding system by *Sawamoto* and coworkers. The hydrophilic side chains (blue) are on the outer part of the SCNP, the hydrophobic (red) side chains are in the core of the SCNP building up hydrogen bonds based on urea. Adapted with permission from ref [164]. Copyright (2016) American Chemical Society.

## 2.5 Characterization Methods

The characterization of polymeric materials, especially single-chain nanoparticles, is a challenging task. The most evident and critical task is to prove single-chain folding and exclude intermolecular interactions/crosslinking. Several methods for the characterization of SCNPs are currently used such as size exclusion chromatography (SEC), NMR spectroscopy or light scattering experiments. In probably all cases of single-chain nanoparticles, there is no unique method that provides all necessary proof for the SCNP formation in one experiment. Consequently, only one characterization method is insufficient for the analysis and characterization of single-chain nanoparticles and, usually, several analytical methods are combined to allow the conclusion that SCNPs are formed.

### 2.5.1 Size Exclusion Chromatography (SEC)

Size exclusion chromatography (SEC) is the most widely used method for characterizing polymers and was introduced by *Moore* in 1964. SEC separates the molecules by size or – more accurately – by its hydrodynamic volume and is the standard analytical method to obtain the molecular weight as well as the molecular weight distribution (MWD) of a polymeric sample.<sup>[104,166,167]</sup>

Specifically, a diluted solution of the analyte is pumped through a column system that is typically filled with macroporous gels such as crosslinked polystyrene, dextran, polyacrylamide, cellulose or silica particles. The separating process is expected by applying sufficiently low flow rates. The inner volume of the gel  $V_i$  and the outer volume  $V_0$  between the gel particles of the gel-scaffold define the total volume of the column. As shown in Figure 8, large (macro)molecules cannot access the pores of the gel and elute first. Here, the elution volume  $V_e$  is equal to the outer volume  $V_0$  given by equation 2:

$$V_e = V_0 \quad (2)$$

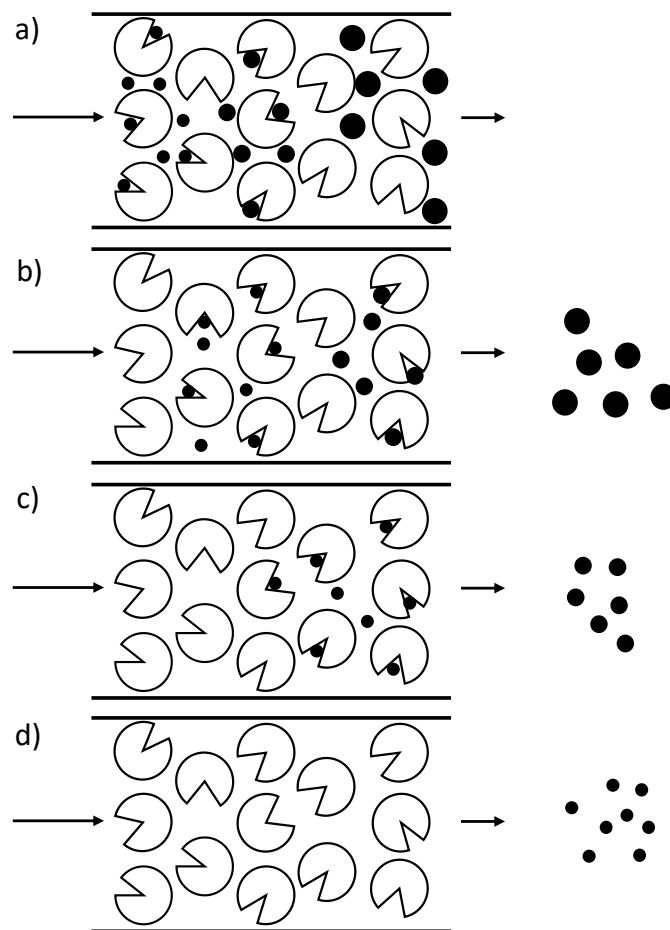


**Figure 8.** Schematic illustration of the separation mechanism during size exclusion chromatography (SEC) of different sized molecules. a) Larger molecules diffuse faster through porous particles. b) The largest particles access only few pores and elute first. c) Medium sized particles can access some pores and elute after the largest molecules. d) Small sized molecules can access all pores and elute last.

With decreasing size of the molecules, they can diffuse freely into the pores and have access to the total pore volume, thus the elution volume is given by equation 3.

$$V_e = V_0 + V_i \quad (3)$$

In case the (macro)molecules can access only a fraction  $K_d$  of the pores ( $0 < K_d < 1$ ) the elution volume is described by the SEC equation 4.

$$V_e = V_0 + K_d V_i \quad (4)$$

The constant  $K_d$  is a thermodynamic parameter and depends on the size or the hydrodynamic volume of the molecule, the pore-size of the gel and the gel itself as well as the solvent, temperature and the degree of branching of the analyte. Since  $K_d$

depends on many parameters, it is not possible to calculate the molecular weight from it. Hence, the system has to be calibrated with well-known, narrowly distributed standards. How calibrations are established for SEC systems as well as the deflection of the molecular weight distributions will not be discussed here and the interested reader is referred to standard text books.<sup>[168–170]</sup>

As already mentioned the SEC separation mechanism is based on the hydrodynamic volume  $V_h$ . The elution volume for branched polymers is smaller compared to linear polymers with the same molecular weight ( $V_{e,branched} < V_{e,linear}$ , with  $M_{branched} = M_{linear}$ ). This phenomenon can be explained by the fact that  $V_h$  of the linear polymer is larger for branched analogues and  $V_h$  is given by equation 5:

$$V_h = \frac{4\pi}{3} R_h^3 \quad (5)$$

where  $R_h$  is the hydrodynamic radius. The hydrodynamic radius can be related to the molecular weight of the sample by the Flory-Fox equation 6, where  $[\eta]$  is the intrinsic viscosity and  $\Phi'$  is the Flory constant.

$$R_h^3 = \Phi' [\eta] M \quad (6)$$

At this point it is obvious that SEC is a suitable analysis method for the characterization of single-chain nanoparticles. The collapsed and often crosslinked SCNPs can be seen as (intramolecular) branched polymers with a smaller hydrodynamic radius and consequently a smaller  $V_h$ . Thus, the SEC chromatogram should show a shift towards higher retention times, due to the fact that smaller particles can access more pores of the gel material in the SEC columns and elute later compared to the linear precursor polymer.

*Pomposo* and coworkers derived an expression for the expected apparent molecular weight ( $M_{app}$ ) of uniform SCNPs that were synthesized from linear precursors through the intramolecular crosslinking.

$$M_{app} = cM^\beta \quad (7)$$

In equation 7,  $c$  is a constant and the power-law exponent is given by

$$\beta = \frac{1+\alpha_F}{1+\alpha_L} \quad (8)$$

where  $\alpha_F \geq 0$  and is related to the fractal nature of the SCNP, measuring its variation from the ideal “hard-sphere” state, while  $\alpha_L$  is one of the Mark-Houwink-Sakurada constants. Generally, it is expected that  $0.56 \leq \beta \leq 1$ , because a value of  $\beta \approx 0.56$  is estimated for compact uniform nanoparticles and  $\beta \approx 1$  for particles with fractal behaviour similar to swollen flexible chains.<sup>[171]</sup>

The polydispersity of the sample can be calculated by

$$\mathcal{D}_{app} = \mathcal{D}^{\beta^2} \quad (9)$$

The power-law for the dispersity is based on the assumption that the MWD follows a log-normal function. The equations 7 and 9 enable the determination of the reduction of the apparent molecular weight and dispersity of the formed SCNPs from their linear precursors based on SEC data.

In addition, the size or hydrodynamic radius  $R_h$  can be calculated from SEC, which is given by the power-law of *Fetters* et al.

$$R_h = 1.44 \times 10^{-2} M_w^{0.561} \quad (10)$$

The expression is valid for samples measured in THF with PS standards.<sup>[172]</sup> With expression 10, the  $R_h$  of the initial polymer as well as the resulting SCNP can be predicted. *Pomposo* et al. used equation 10 for the calculation of the linear precursor and developed formula 11 to estimate the size reduction of the polymer upon folding:<sup>[173]</sup>

$$R = R_0(1 - x)^{0.6} \quad (11)$$

Here,  $R_0$  is the size of the initial polymer sample based on equation 10 and  $x$  is the functional group density. For the formula, a Flory-like argument was used to deduce the equation. Further, the SCNPs dissolved in good solvents are assumed. For the complete deduction of equation 11, the interested reader is referred to the original literature.<sup>[173]</sup> With this formula it is possible to empirically estimate the size reduction of the SCNP by only having measured the SEC chromatogram of the parent polymer. From equation 11 it is obvious that there are some shortcomings. In the case of  $x = 1$ , the SCNP would have a resulting radius of 0 nm and thus an infinite density, which definitely would not hold true. Accordingly, the reported equation must be wrong. Nevertheless, the reported equation 11 helps to empirically estimate the size reduction

prior to the single-chain collapse, which is also reflected by successfully employing the formula to numerous examples reported in literature.

## 2.5.2 Nuclear Magnetic Resonance (NMR) Spectroscopy

Generally, nuclear magnetic resonance (NMR) spectroscopy is practiced as the standard method for the determination of the molecular structure of molecules and to verify the existence of certain functionalities within the molecular structure. Here, the most commonly used techniques are proton and carbon NMR experiments. In the course of single-chain folding, these methods are not sufficient, since they only provide information about the success of a (crosslinking) reaction or the interaction of non-covalent functional groups, resulting in a shift or the appearance of new resonances. Evidence about the intra- or intermolecular nature of the folding event cannot be determined by the proton or carbon NMR spectra. However, some more specialized NMR techniques exist for the assessment of the nature of crosslinking effects. The most employed technique here is diffusion ordered spectroscopy (DOSY), which will be discussed in the following paragraphs.

### 2.5.2.1 Diffusion Ordered Spectroscopy (DOSY)

Diffusion ordered spectroscopy (DOSY) measures – as indicated by the name itself – the diffusion of a molecule in solution and thus provides the diffusion coefficient of the measured sample. The diffusion coefficients,  $D$ , can be determined for every resonance – and thus functional group – in the proton ( $^1\text{H}$ ) NMR spectrum.<sup>[174–176]</sup> The diffusion coefficient of a spherical molecule is related to its hydrodynamic radius,  $R_h$ , and can be expressed by the Stokes-Einstein equation (refer to equation 12):

$$D = \frac{k_B T}{6\pi\eta R_h} \quad (12)$$

## 2.5 Characterization Methods

---

In the formula,  $k_B$ , is the Boltzman constant,  $T$  the temperature,  $\eta$  gives the viscosity of the solution and  $R_h$  is the hydrodynamic radius of the molecule.

As indicated above, DOSY indirectly is able to provide the size of the measured sample and is thus is a widely used characterization method in polymer chemistry, if the hydrodynamic size of a polymer is of interest. Especially in the realm of single-chain folding the size reduction plays an important role, since the size reduction of the SCNP compared to its parent polymer leads to an increase of the diffusion coefficient of the individually compacted chains within the chain ensemble. Consequently, the diameters of the precursor polymers and the resulting SCNPs are different and can be estimated by applying the Stokes-Einstein equation.<sup>[104,176–179]</sup> DOSY experiments can also help to understand the formation of single-chain architectures. Measuring different concentrations, DOSY helps to differentiate between inter- and intramolecular aggregations due to different diffusion coefficients.

In the following paragraph some theoretical knowledge about the DOSY experiment is provided. In Figure 9, the coordinate system that is referred to in the following paragraphs is illustrated, with the magnetic field  $B_0$  along the z-axis.

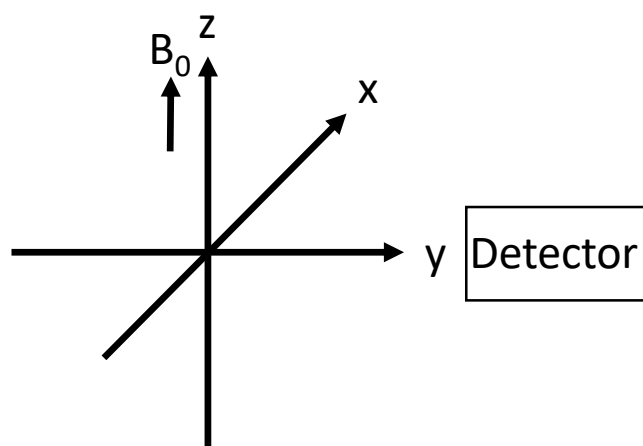


**Figure 9.** Coordinate system for the discussion of diffusion ordered spectroscopy (DOSY). The static magnetic field  $B_0$  is applied along the z-axis, the detector is along the y-axis and the pulses are applied from the x-axis.

The measurement of diffusion is based on the fact that the position of a spin can be spatially labelled (indirectly) by application of a pulsed magnetic field gradient, changing the spins Larmor frequency. A first gradient pulse encodes the previously aligned magnetization and causes a corkscrew effect, which is followed by the time  $\Delta$ ,

where the molecules are allowed to diffuse. A second gradient pulse decodes and realigns the magnetization. The strength of the corkscrew effect is dependent on gradient strength as well as the gradient pulse length  $\delta$ . The signal intensity is given by equation 13 and was developed by *Stejskal* and *Tanner*, where  $\gamma$  is the gyromagnetic ratio,  $G$  represents the strength of the gradient pulse,  $\Delta$  is the mixing time between the pulsed gradients,  $\delta$  is the duration of the pulse and  $D$  is the diffusion coefficient.<sup>[176,180,181]</sup> The complete mathematical derivation will not be discussed here. The interested reader is referred to other reviews in this field.<sup>[182–184]</sup>

$$I = I_0 \exp[-\gamma^2 G^2 \delta^2 \left(\Delta - \frac{\delta}{3}\right) D] \quad (13)$$

*Stejskal* and *Tanner* developed the pulsed magnetic field gradient (PMFG) methods (refer to Scheme 12). The Larmor equation (equation 14) describes the effects of the gradient on nuclear spins.

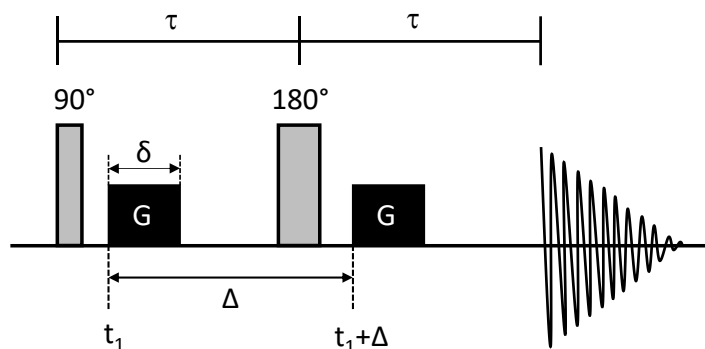
$$\omega_0 = \gamma B_0 \quad (14)$$

$\omega_0$  is the Larmor frequency and  $B_0$  the static magnetic field strength in z direction and  $\gamma$  is the before mentioned gyromagnetic ratio.  $B_0$  is assumed to be spatially homogeneous and consequently  $\omega$  of the sample is the same. Nonetheless, if there is another spatially magnetic field gradient,  $\omega$  becomes spatially dependent. The  $B_0$  field is typically in z direction and thus DOSY measures diffusion along the z-axis, although the x and y directions would also be possible. When only one gradient orientated along the z-axis is applied, the magnitude of  $G$  is a function of the position of the z-axis only. The cumulative phase shift for a single spin is given by equation 15.

$$\Phi(t) = \gamma B_0 t + \int_0^t G(t') + z(t') dt' \quad (15)$$

The first part of the right-handed term represents the phase shift due to the static field and the second part of the term is the phase shift due to the applied gradient. The second part of the term is proportional to the type of nucleus (linear dependence on  $\gamma$ ) as well as the strength of the gradient, the duration of the gradient and the displacement of the spin along the gradient direction.





**Scheme 12.** Schematic illustration of the *Stejskal and Tanner* or pulsed magnetic field (PGF) sequence. Adapted from ref [184]. © 1999 with permission from Elsevier.

The PFG or *Stejskal and Tanner* sequence circumvents several limitations compared to steady gradient experiments. First, the lines are not broadened due to the fact that the gradients are off during acquisition, which allows for the measurement of diffusion. Second, the radiofrequency (rf) power must not be raised to interpret a gradient-broadened spectrum. Next, by the use of larger gradients smaller diffusion coefficients can be measured. Another advantage include the use of gradient pulses, resulting in a well-defined time where diffusion is measured. Finally, gradient pulses make it possible to separate diffusion effects from spin-spin relaxation.

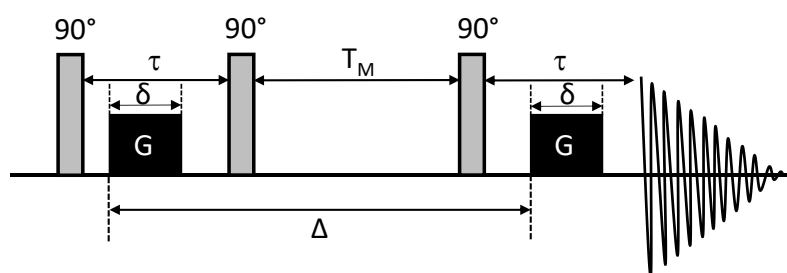
Qualitatively, the ensemble of diffusion spins in thermal equilibrium are rotated from the z-axis in the x,y-plane by 90° pulse (refer to Scheme 12). Next, a gradient pulse of the duration  $\delta$  and magnitude  $G$  is applied in the first period  $\tau$  at time  $t_1$ , resulting in a phase shift of the spins  $i$  at the end of the first  $\tau$  period. The shift of spin  $i$  is expressed by the following equation:

$$\Phi_i(\tau) = \gamma B_0 \tau + \gamma G \int_{t_1}^{t_1+\delta} z_i(t) dt \quad (16)$$

Here, the first term phase shift results from the main static field and the second part of the term results from the applied gradient. Due to the assumption of a constant amplitude gradient,  $G$  is taken out of the integral. After the first  $\tau$  period, a 180° rf pulse is applied to reverse the sign of the phase. A second gradient pulse of equal magnitude and duration is applied at time  $t_1+\Delta$ . In case the spins did not diffuse along the z direction, the spins refocus if the applied gradient pulses are aborted. In this case, a maximum signal will be detected. In the other case – if the spins have moved – the

degree of dephasing is proportional to the displacement in the direction of the gradient in the time period  $\Delta$ , which is caused by the applied gradient. Hence, the recorded signal is attenuated and with increasing diffusion the signal becomes more and more attenuated. Some advantages have already been stated above, e.g. the PFG methods has also a drawback, which is the long period in the  $x,y$  (transverse) plane. The transverse magnetization is then subjected to  $J$ -modulation effects as well as transversal relaxation. The transversal relaxation can be especially short for macromolecules, which then results in a loss of signal. Complete refocusing is prevented by  $J$ -modulation, if hard pulses exchange the spin states of nuclei that are attached to the nucleus of concern.<sup>[182,184]</sup>

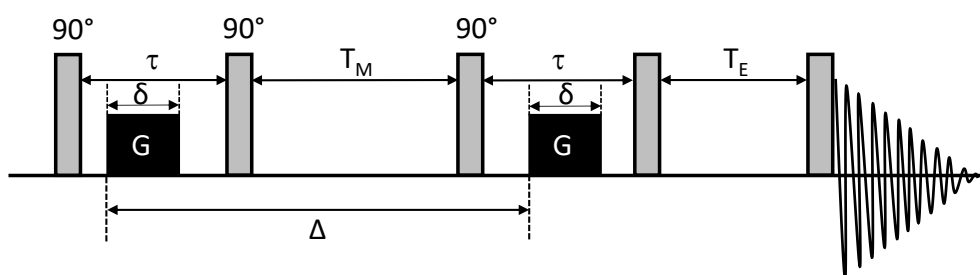
The disadvantage of the transverse magnetization can be overcome by the so-called stimulated echo (STE) sequence that was investigated by Hahn in 1950.<sup>[185]</sup> The STE sequence contains three  $90^\circ$  pulses (refer to Scheme 13) and the signal or echo is recorded after the last pulse and is called stimulated echo. The STE sequence can generate up to five echoes and can be used for measuring the effects of diffusion. The second  $90^\circ$  pulse stores the magnetization by rotating the spins in  $y$ -direction back into the  $z$ -direction, while the spins in  $x$  direction remain unaltered (transverse) and contribute to the first and second echo. After a storage time  $T_M$ , the third  $90^\circ$  pulse flips the  $z$ -components back into the  $y$ -direction, where they are refocused by a second gradient pulse and a STE signal is detected.



**Scheme 13.** Schematic illustration of the stimulated echo (STE) sequence. Adapted from ref [184]. © 1999 with permission from Elsevier.

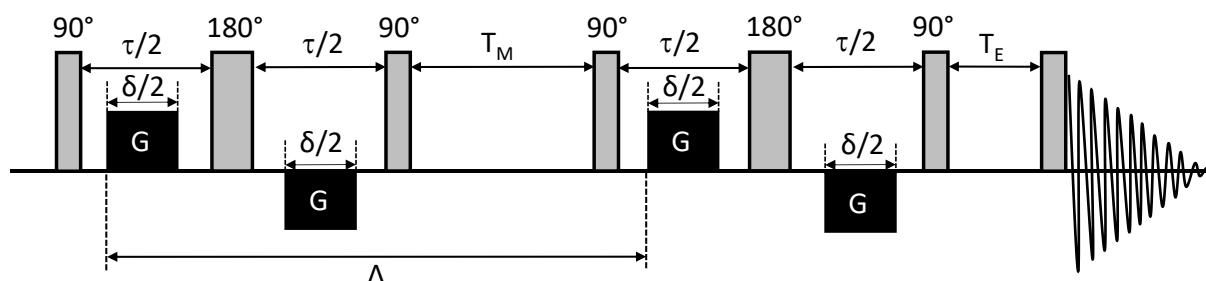
The advantage of the STE sequence is that the evolution time  $\tau$  for the transverse magnetization can be limited. The relaxation depends primarily on  $T_1$ , which is significantly longer than the  $T_2$ , resulting in the enhancement of the signal. Those characteristics mark an improvement compared to the PFG sequence with the short  $\tau$  values, which are only slightly longer than the gradient pulse duration  $\delta$ . However, the developed improvements of the PFG sequence lead to the problem of eddy currents.

The eddy current in the STE sequence arises after the final gradient pulse and since  $\tau$  has to be kept short in this method the effects are significant and dependent on the gradient pulse strength. Some changes to the STE sequence have been made to suppress the eddy current effects, resulting in the improved longitudinal eddy current delay (LED) sequence. In the LED sequence, two more pulses are inserted (refer to Scheme 14). Here, a fourth  $90^\circ$  pulse stores the magnetization in longitudinal direction while the eddy current decays during the eddy current settling period  $T_E$ . The magnetization is then recalled with the fifth and last  $90^\circ$  pulse, after which the echo can be measured.



**Scheme 14.** Schematic illustration of the longitudinal eddy current (LED) delay. Adapted from ref [184]. © 1999 with permission from Elsevier.

Alternatively, the best way to overcome the effects of eddy currents is to use the bi-polar LED (BPLED) sequence that was introduced by *Wu et al.*<sup>[186]</sup> Here, each gradient pulse of the LED sequence is replaced by two pulses of contrasting polarity (G and  $-G$ ). In addition, these two pulses are separated by a  $180^\circ$  pulse (refer to Scheme 15). Hence, the applied G- $180$ -( $-G$ ) sequence diminish the eddy currents.<sup>[180,184,187]</sup>



**Scheme 15.** Schematic illustration of the bi-polar longitudinal eddy current delay (BPLED). Adapted from ref [184]. © 1999 with permission from Elsevier.

Typically, eddy currents have settling times of hundreds of milliseconds, hence the eddy currents generated by the first (positive polarity) pulse can be eliminated by a second (negative polarity) pulse that follows a few milliseconds after the first pulse.<sup>[183]</sup> Similar to the *Stejskal* and *Tanner* signal attenuation given by equation 2, the signal attenuation in the BPLED sequence due to diffusion can be expressed by equation 17.

$$I = I_0 \exp[-\gamma^2 G^2 \delta^2 \left( \Delta - \frac{\delta}{3} - \frac{\tau g}{2} \right) D] \quad (17)$$

### 2.5.3 Electron Paramagnetic Resonance (EPR) Spectroscopy

Electron paramagnetic resonance spectroscopy (EPR) has not been used for the characterization of single-chain nanoparticles in the literature, yet it was used for the characterization of radical polymers within this thesis as well as for the characterization of the SCNP folding/unfolding of nitroxide containing polymers (refer to Section 3.1.2 and Section 3.2.2). Thus, EPR will be discussed in the following paragraphs.

Electron paramagnetic resonance spectroscopy is similar to NMR spectroscopy, but more specific and not as widely applicable. In EPR spectroscopy, the sample must contain unpaired electrons, so a signal can be detected.<sup>[188,189]</sup> Generally, an EPR spectrometer consists of a source for microwave radiation, a sample chamber, detector and an electromagnet with fields of about 0.3 T. A free electron has a magnetic dipole moment, which is given by equation 18.

$$\mu = g\mu_B S \quad (18)$$

Here,  $S$  is the spin quantum number for the rotation and  $\mu_B$  is a constants. The Landé-factor  $g$  is also a constant. The energy of the relevant magnetic dipoles in an external field with a magnetic field strength  $B_0$  is expressed by

$$E = \mu B = g\mu_B S B_0 \quad (19)$$

Electrons can either be in the  $m_s = +\frac{1}{2}$  or  $m_s = -\frac{1}{2}$  state. The transition between the two states depends on  $g$  and the requirement for the resonance and the transition is given by:

$$h\nu = g\mu_B B_0 \quad (20)$$

The resonance condition for an external field with the strength of one Gauss a frequency of 2.8 MHz is required. If the magnetic fields have several thousand Gauss the frequency increases into the realm of microwaves (about 10 GHz).

The  $g$ -factor gives information about the electronic structure of the system and is similar to the shielding constant in NMR, yet provides information about how applied fields can induce streams in the molecule and which magnetic fields cause these streams.<sup>[189,190]</sup> The deviation of  $g$  from the free electron is proportional to  $\xi/\Delta E$ , where  $\xi$  is the spin-orbit interaction constant. The  $g$ -factor is also anisotropic and depends on the orientation of the radical with regard to the applied field and only detectable in solid state, since it is averaged in solution.

In case the resonance conditions are fulfilled, parts of the microwave energy is absorbed and electron spin resonance occurs and the wave is damped. Practically, the absorption maximum is reached by variation of the magnetic field strength. Unpaired electrons such as radicals are not only in the external field of the magnet, but also in the magnetic field of neighbouring nuclei, if they have a nuclear spin  $I \neq 0$ , leading to complex splitting of the energy levels and thus to numerous energy transitions. The splitting is also called hyperfine structure, giving information about the chemical structure of the radical. If a radical has  $N$  equivalent nuclei with the spin quantum number  $I$  the hyperfine structure shows  $2NI+1$  lines in the spectrum. For further information about EPR as well as hyperfine splitting, the interested reader is referred to standard text books and reviews.<sup>[189,191]</sup>

### 2.5.4 Dynamic Light Scattering (DLS)

Dynamic light scattering (DLS), also referred to as photon-correlation spectroscopy, measures time-dependent properties such as the hydrodynamic radius or the translational diffusion coefficient.<sup>[169,192,193]</sup>

In DLS measurements a monochromatic, coherent laser is typically used as light source. Through optical mirrors and lenses the light beam is focused on the sample.

The laser emits light of a certain polarization, which determines the scattering intensity. For small samples, where particle sizes are smaller than  $\lambda/20$ , light is scattered in all directions. For particles larger than 20 nm, oscillating dipoles are generated and the emitted light waves possess a phase difference. The interference of emitted light of the “large” particles leads to a nonisotropic angular dependency of the scattered light intensity. The interference patterns of the scattered light is characteristic for the size and shape of the particles.<sup>[194]</sup>

Some fundamental principles of DLS will be discussed in the following paragraphs. For more detailed information and mathematical derivation the interested reader is referred to text books.<sup>[193–195]</sup>

The basic principle of DLS is the so-called *Doppler*-effect. Here, a source that emits sound or light with a certain speed,  $v$ , moves relative to the detector, thus the wave getting to the detector has a shift, the so-called *Doppler*-shift. Dissolved molecules can rotate in all directions and may have different velocities. In addition, the molecule can rotate altogether or only some parts of them, resulting in many differently shifted frequencies regarding the originating frequency. The resulting spectrum is called optical *Doppler*-shift spectrum  $S(q, \omega)$  and is the sum of many *Lorentz*-functions that contain the Form-factor  $P_{k,m}(X, m)$  and the argument of the *Doppler*-shift spectrum  $G_{k,m}(q, M)$  among others. Both are dependent on the pattern of the scattering molecule and hence are different for spheres, coils or rods. For instance, for a sphere  $X = R$ ;  $G_{k,m} = q^2 D$  and  $P_{k,m} = k = m = 0$ . Here  $q = (4\pi n/\lambda)\sin(\theta/2)$ , where  $\theta$  is the angle of the detected scattered light,  $n$  the refractive index of the used solvent and  $D$  is the translational diffusion coefficient.

Experimentally, the autocorrelation function is determined because there are difficulties in the determination of the optical spectrum  $S(q, \omega)$ . The difficulties are caused by the speed of motion of the molecules, which is small compared to the velocity of light. Thus, not the optical spectrum is detected but the autocorrelation function  $g_1(t)$ , which is expressed in equation 21

$$g_1(q, t) \equiv g_1(t) = \langle X(\tau)X^*(\tau + t) \rangle = \lim_{T \rightarrow \infty} \left( \frac{1}{2T} \right) \int_{-T}^T X(\tau)X^*(\tau + t) d\tau \quad (21)$$

Here, a photon-counter is necessary to measure the incoming photons of the signal source to define the autocorrelation function.  $X(\tau)$  gives the signal at the time  $\tau$  and

$X(\tau + t)$  the signal intensity of the same signal at  $\Delta t$  and  $g_1(t)$  is the arithmetic mean of the product of  $X(\tau)$  and  $X(\tau + t)$ .

The *Wiener-Khinchine*-theorem (refer to equation 22) correlates the autocorrelation function and the optical spectrum  $S(q, \omega)$ .

$$S(q, \omega) = \int_0^{\infty} g_1(t) \exp(-i\omega t) dt \quad (22)$$

After Fourier transformation,  $g_1(t)$  is deduced:

$$g_1(t) = \sum_{k,m} P_{k,m}(X, m) \exp(-G_{k,m}(q, M)t) \quad (23)$$

In case of only translational diffusion, equation 24 is simplified to:

$$g_1(t) = P_{0,0}(X) \exp(-q^2 Dt) \quad (24)$$

Here,  $D$  is the diffusion coefficient and *via* the *Stokes-Einstein* equation 25 the hydrodynamic radius is accessible.

$$D = \frac{k_b T}{6\pi\eta R_h} \quad (25)$$

The above discussed equations are only valid for monodisperse systems. When polydisperse systems are considered, a probability-density-function  $G(\Gamma)$  is defined:

$$g_1(t) = \int_0^{\infty} G(\Gamma) \exp(-\Gamma t) d\Gamma \quad (26)$$

To determine the diffusion coefficient, several mathematically demanding methods can be applied to determine the autocorrelation function. One way to get access to the autocorrelation function,  $g_1(t)$ , is to use a homodyne-procedure and *via* the *Stiegert*-relation  $g_1(t)$  can be determined:

$$g_2(t) = A + B[g_1(t)]^2 \quad (27)$$

### 2.5.5 Mass Spectrometry

Mass spectrometry evolved as a powerful tool to analyse chemical and polymeric substances and to characterize their molecular structure as well as providing information about the molar mass distribution.<sup>[196,197]</sup> In mass spectrometry, the mass-to-charge ( $m/z$ ) ratio of the analyte is detected in the gas phase. An important parameter in mass spectrometry is the resolution  $R$ . The resolution is defined by the resolving power of the spectrometer as  $M/\Delta M$  according to the 5% peak height definition, where  $M$  is the mass of a peak and  $\Delta M$  the width of the peak at 5% of its height.<sup>[198,199]</sup> Moreover, the analyte must be charged to be detected in a mass spectrometer. The pathway of the gaseous ions is controlled by electric and/or magnetic fields.<sup>[200,201]</sup>

A mass spectrometer consists of a sample injection device, an ion source for ionization, an ionization system, a detector and a computer. Initially, the sample is injected by the inlet device, followed by the ionization in an ion source, since non-charged species cannot be detected. The mass spectrometer functions under (ultra) high vacuum to avoid collisions of the analytes with atmospheric gas molecules. There exist different techniques for the ionization and these can be categorized into hard and soft ionization methodologies. Soft ionization techniques such as matrix assisted laser desorption ionization (MALDI),<sup>[202]</sup> in which a laser vaporises the analyte that is embedded in a matrix or electrospray ionization (ESI), allow for the structural elucidation due to the intact non-fragmented ionization of the sample.<sup>[203–205]</sup> On the other hand, there are the hard ionization methods, in which the analyte is destroyed and fragments are detected such as fast atom bombardment (FAB)<sup>[206]</sup> or electron-impact ionization (EI).<sup>[207]</sup> ESI MS has been used within the course of this thesis and will be discussed in the following paragraph.

After ionizing the analyte in the gaseous phase, the ions are separated in the mass analyser. The most popular analysers are: (i) the *time-of-flight* (TOF) analyser that separates the ions by their velocity within a field free path; (ii) the *quadrupole* mass analyser in which ions with a certain  $m/z$  ratio oscillate on specific trajectories through the electrodes and are subsequently detected; (iii) the *quadrupole ion trap* that holds ions with particular  $m/z$  values on a three dimensional electrical field, while



unwanted ions are removed and (iv) *Fourier Transform Ion Cyclotron Resonance* (FT-ICR) analyzers. Here, a strong homogeneous magnetic field separates the ions according to their orbital frequency. Finally, (v) the *Orbitrap* analyser traps the ions by electrostatic attraction of a spindle-shaped electrode. The ions circulate around the electrode as well as along the axis of the electrode simultaneously. FT leads to the frequency of the ions, which can subsequently be used to calculate the  $m/z$  ratio of the sample.<sup>[208]</sup> Thereafter, the dispersed ions reach the detector, which processes the signals to digital data that are subsequently converted to a mass spectrum by a computer.

### **Electrospray Ionization Mass Spectrometry (ESI MS)**

Given their analytical power, mass spectrometric methods have recently been applied by the *Barner-Kowollik* team to single-chain nanoparticles for their characterization on the molecular level, exploiting electrospray ionization (ESI MS). The field of mass spectrometry evolved as an important and powerful tool to analyze polymers and biomacromolecules over the last decades to gain information about their structure. Soft ionization methods such as ESI MS have been introduced by the group of *Mack* and coworkers<sup>[209,210]</sup> and further developed by *Fenn* and colleagues.<sup>[196,211]</sup>

As indicated above, ESI MS provides a mild method to bring the synthetic polymers to the gaseous phase unfragmented and is mainly applied to biopolymers such as peptides, or proteins, because mostly multiple charged species are generated.<sup>[212,213]</sup> Systematically, a dilute solution of the sample is injected into a small diameter capillary or needle at a constant flow. A high voltage is applied to the capillary, which is typically between 0.5-5 kV. By passing through the capillary, excess charges are accumulated resulting from the high potential, creating a Taylor cone at the outlet, where the solution is sprayed. After spraying, the solvent begins to evaporate and an aerosol of highly charged droplets is generated. The droplets are divided due to the high charge density on the droplet surface and the resulting Coulomb repulsive forces. Successive fission leads to droplets that only incorporate a single molecule, which can be detected.<sup>[200,214,215]</sup> For synthetic polymers multiple signals are detected in the mass spectrum, which is correlated to the polydispersity compared to monodisperse

biopolymers that only give one peak at a certain  $m/z$  ratio for one species. The detected signals are always from analyte molecules that are bound to an ion. Typical ions that are used for ionization are  $H^+$ ,  $Na^+$ ,  $K^+$  or  $NH_4^+$ .

*Steinkönig* et al. used high resolution ESI MS to characterize the formation of single-chain nanoparticles on a molecular level coupled with size exclusion chromatography.<sup>[216]</sup> Here, a statistically copolymerized polymer consisting of methyl methacrylate (MMA) and glycidyl methacrylate (GMA) has been prepared. The collapse was induced by intra-chain ring opening metathesis polymerization (ROP) using  $B(C_6F_5)_3$  as catalyst. The resulting SCNPs are stable during the ionization process and thus were characterized by ESI MS. For the collapse, two main scenarios were observed: First, the bimolecular coupling and second: propagation. During bimolecular coupling, two GMA units react, which is entropically favoured. The assumption is supported by SEC ESI MS measurements, showing predominantly the bimolecular coupling compared to the propagation. Second, during the propagation mechanism at least three GMA units react, as described for ROP. In addition, the formation of single-chain architectures was underpinned by the characteristic SEC shift towards higher retention times.

### **2.5.6 Atomic Force Microscopy (AFM) and Transmission Electron Microscopy (TEM)**

The above discussed methods for characterizing single-chain nanoparticles are performed in solution. However, in the literature solvent-free imaging techniques such as atomic force microscopy (AFM) and transmission electron microscopy (TEM) are employed to characterize single-chain architectures. Through the imaging methods, conclusions about the size and shape of the polymeric nanoparticles can be drawn.

AFM is a form of scanning tunnelling microscopy (STM) with high resolution.<sup>[217–219]</sup> In force microscopy, a cantilever-type spring is equipped with a probing tip, which is moved across the sample surface during measurement. During the scanning process the tip-sample interactions lead to position dependent deflections of the cantilever

following *Hooke's law*.<sup>[217,220]</sup> The deflections are caused by forces such as van der Waals, electrostatic, magnetic or capillary and other forces giving information about e.g. the surface topography. Typically, the cantilever deflection is measured by optical methods. Here, a light beam is reflected from the top of the cantilever. The force is kept small by applying a feedback mechanism and to prevent collisions of the tip with the sample. The adjustment of the distance between tip and sample is realized by small piezoelectric elements.<sup>[218,219,221,222]</sup> Thus, the tip follows the contour of the measured sample, leading to a point-by-point picture of the surface. The resolution of AFM depends on the radius of curvature of the tips (typically 10-30 nm), the thickness of the tip and roughness of the sample amongst others. AFM resolution can be as precise as 0.1 to 10 nm.

Plenty of studies investigating SCNPs employed AFM to characterize their structures.<sup>[110,223–226]</sup> Aggregation of the nanoparticles during the evaporation process as well as dewetting effects need to be prevented by careful preparation of the sample for AFM analysis.<sup>[227–229]</sup> The *Meijer* group used the AFM technique in various studies for the characterization and visualization of polymeric SCNPs. The formation of nanoparticles by the dimerization of Upy moieties has been visualized, for instance.<sup>[107]</sup> The AFM monitored particles show smaller diameters compared to the initial parent polymers and showing a “fried-egg” structure. In addition, they were able to monitor the time dependent decrease of the diameter resulting from the degree of deprotection. The Upy moieties were protected, so the parent polymer is stable and not immediately dimerizing. AFM measurements confirmed the SEC results, revealing a more pronounced shift to smaller diameters. In another study, the same group found that the Upy dimerization lead to aggregates after slow evaporation of a diluted solution, similar to other synthetic nanoparticles and even proteins.<sup>[57]</sup> Furthermore, *Hosono* et al. used an AFM-based single-molecule force spectroscopy to gain information on the internal structure of the folded polymer. Here, no AFM scans were performed, but a AFM cantilever was used to stretch the polymeric chain of a SCNPs and to mechanically induce the unfolding of the BTA or Upy folding motifs.<sup>[118]</sup> The stretching leads to rupture events, resulting in force-extension profiles, giving insight into the internal conformation of the SCNPs.

Besides AFM, single-chain polymeric nanoparticles can be visualized by transmission electron microscopy (TEM). In doing so, an electron beam is directed onto a conductive sample and the transmitted electrons are used for imaging. The resolution of TEM microscopes is sufficiently high in the nanometre scale to depict the formed nanoparticles. In addition, contrasting agents such as ruthenium oxides can be applied to enhance the contrast between the surface and the sample. Since TEM does not need any contact with the surface during the measurement particle distortion is prevented, it is a useful technique to get information about the dimensions of SCNPs. Furthermore, the shape of the particles is revealed and numerous studies used TEM for imaging of prepared intramolecular folded structures.<sup>[76,91,104,105,230–232]</sup>

AFM and TEM both have some disadvantages. The sample preparation in AFM and TEM needs to be carefully accomplished, nonetheless the evaporation of the solvent is potentially leading to deviating results. The SCNPs might form “pancake” structures, which is not representative of the SCNP in solution. Here, after drop casting the samples onto the surface, the SCNPs can flat out on the outer parts of the SCNP, while the inner part might be unchanged. Further, the visualized SCNP might consist of more than one polymer chain. Moreover, in TEM the sample must be conductive, which is certainly not the case for most polymers. The coating of the polymers as well as the addition of contrasting agents potentially leads to changed structures of the SCNP or even aggregation of multiple chains. In addition, the structure in the solid state could significantly differ from the configuration in solution, which is necessary for most of the other characterization techniques such as SEC or NMR. Thus, AFM and TEM potentially lead to deviations to other characterization methods.

# 3

## DYNAMIC SINGLE-CHAIN NANOPARTICLES

### 3.1 Selective Point Folding Approach

Section 2.2 outlines variable approaches to realize dynamic intramolecularly collapsed three dimensional single-chain nanostructures, with the selective point folding avenue being one of them. Placing the orthogonal folding motifs at precisely (pre)selected points along the polymeric backbone is often a synthetic challenge, requiring demanding synthetic efforts. Thus, only few examples of single-chain nanoparticles prepared *via* the selective point avenue are found in the literature to date. Within the current section, the systems developed within the present PhD thesis in the realm of the selective point folding are presented. Generally, the folded structures are presented as loops, although more complex structures such as entanglements within the polymeric backbone, are most probably obtained, leading to architectures that deviate from the assumed cyclic structure for the single-chain nanoparticles (SCNPs). Synthetically, the loop is the simplest way of folding and thus representative of the single-chain folded structures in the selective point folding approach. Figure 10 provides a schematic illustration of the developed methodologies towards well-defined single-chain collapsed structures. Further, the high resolution electrospray ionisation mass (ESI MS) analysis of polymers containing different amount of nitroxide radicals is presented. Within the project of the spin-labelled system (refer to Figure 10A) the analytical gap of employing ESI MS to nitroxide containing polymers was thus closed by synthesizing polymers featuring different amounts of nitroxide radicals within the

polymeric backbone. The polymers featuring the nitroxides were characterized by high resolution ESI mass spectrometry to access the molecular information such as chemical structure and composition of the prepared polymeric structures and thus found the analytical basis for the structural characterization of nitroxide containing SCNPs.

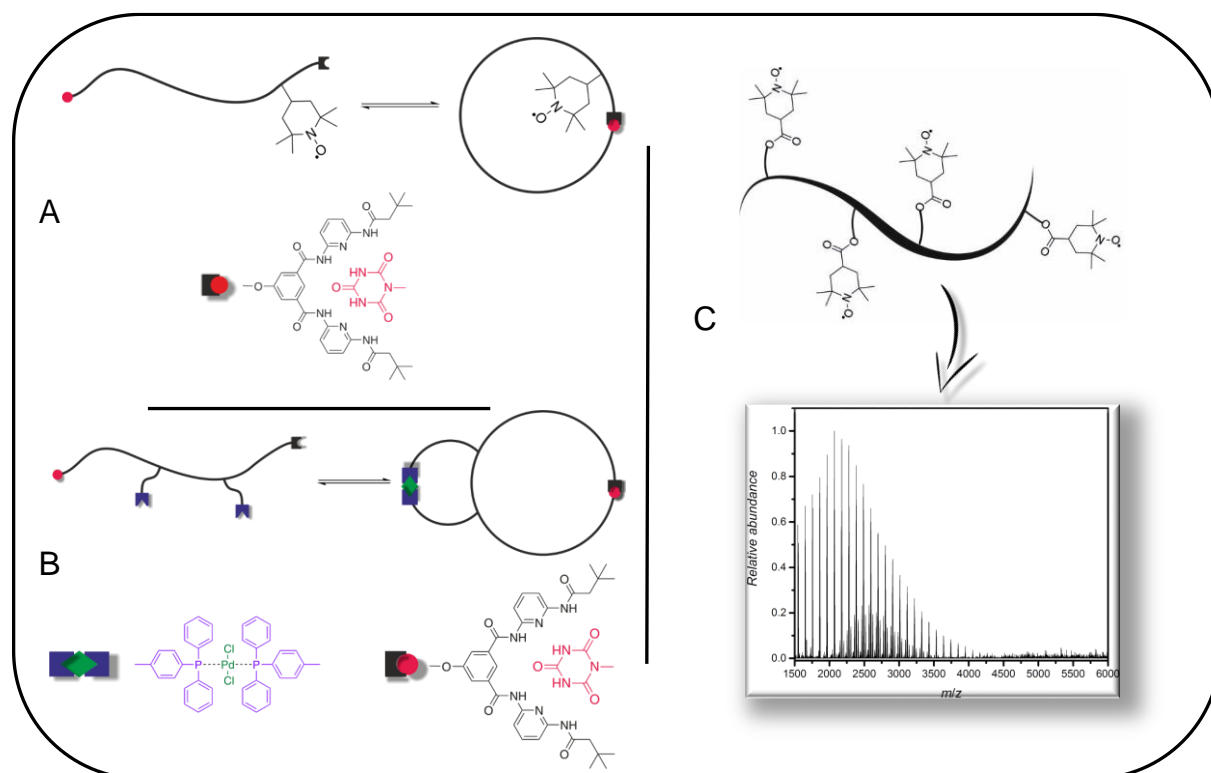


**Figure 10.** Schematic illustration of the selective point folding methodologies presented in the current section. (A) the single polymer chains folded *via* a hydrogen bonding system in  $\alpha$ - and  $\omega$ -position. (B) the selective point folding induced by a dual folding system consisting of a hydrogen bonding system (Hamilton Wedge/cyanuric acid) and metal complexation and (C) the analysis of nitroxide containing polymers with high resolution mass spectrometry as an analytical concept to image folding systems containing nitroxide radicals.

#### 3.1.1 Spin Labelling of a Hydrogen Bonding System

In previous studies, the hydrogen bonding motif of Hamilton Wedge (HW) and cyanuric acid (CA) was investigated by our group in the selective point folding approach and successfully implemented into the field of single-chain folding. Further, SCNPs were designed combining the HW/CA recognition unit with the benzene-tricaboxamide (BTA, refer to Section 2.4.1) in the repeat unit methodology.<sup>[48–50,108]</sup> In addition, theoretical simulations investigated characteristic features of the interacting HW/CA hydrogen bonding motif such as the distance of between the motifs after the hydrogen bonds are established.<sup>[233]</sup> The following paragraphs describe the synthesis of the linear precursor polymers, featuring the HW/CA motif and to further enhance the system compared to the already existing examples, a spin-label is attached close to the HW moiety. Here, the spin-label enables multidimensional nuclear magnetic resonance (NMR) measurements to investigate the folding behaviour and experimentally determine the distance of the established hydrogen bonds upon single-chain collapse.\*<sup>§</sup> In order to achieve the folding, a heterotelechelic styrene based polymer has been prepared that features the cyanuric acid and Hamilton Wedge on the respective chain ends. After the attachment of the spin-label, *i.e.* 2,2,6,6-tetramethylpiperidinyloxy (TEMPO) in penultimate position, close to the HW moiety, the collapse is induced in highly diluted solutions.

---

\*The current project was carried out in collaboration with the NMR group of Prof. B. Luy (KIT). All small molecule compounds and polymers were designed and prepared by T. S. Fischer unless otherwise stated. NMR experiments other than <sup>1</sup>H and <sup>13</sup>C NMR experiments were conducted by S. Spann in the group of Prof. B. Luy.

<sup>§</sup>Parts of the section are adapted or reproduced from T. S. Fischer, J. Steinkönig, H. Woehl, J. P. Blinco, K. Fairfull-Smith, C. Barner-Kowollik, *Polym. Chem.*, **2017**, *8*, 5269-5274. with permission of the Royal Society of Chemistry. T. S. Fischer designed and conducted the synthesis of the polymers as well as the evaluation of the mass spectra and wrote the manuscript. J. Steinkönig conducted the mass spectrometric measurements, H. Woehl, measured EPR, J. P. Blinco, K. Fairfull-Smith were involved in scientific discussions and C. Barner-Kowollik motivated and supervised the project.

Thereafter, the folding is investigated by multidimensional NMR experiments accessible by the spin-label such as nuclear Overhauser enhancement (NOE). The TEMPO spin-label influences the relaxation rate dependent on the distance of the protons to the paramagnetic centre, which can be exploited to determine the distance of the folding motifs in the collapsed state. In order to investigate the influence of the chain-length on the folding behaviour, polymers with different molecular weights were synthesized. In addition, the folding of the polymers was characterized by  $^1\text{H}$  NMR as well as diffusion ordered spectroscopy (DOSY).

#### **Synthesis of the Hamilton Wedge and Cyanuric Acid Functional Folding Motifs**

Initially, the Hamilton Wedge functionality that is to be attached to the polymer *via* copper azide-alkyne cycloaddition (CuAAC) was prepared in a multi-step synthesis (refer to Scheme 16). In addition, the HW moiety has to feature a free hydroxyl functionality to which the spin-label (TEMPO) can be attached after the HW functionality is tethered to the polymeric backbone. In a first step, the monosubstituted diaminopyridine (**3**) was prepared by reacting 2,6-diaminopyridine and *tert*-butylacetylchloride (**17**). Secondly, in an esterification, the protected hydroxydiisophthalic acid (**4**) was synthesized and subsequently reacted with **3** to yield the protected HW species **5**. The  $^1\text{H}$  NMR of **5** shows the characteristic amine proton resonances at 5.68 ppm, thus indicating the success of the reaction. The deprotection of **5** was achieved under basic conditions using 1.2 M NaOH, affording the hydroxyl functional HW **6**. The  $^1\text{H}$  NMR spectrum of **6** as well as the assignment of the resonances is shown in Figure 11. All intermediate structures were confirmed *via* proton and carbon NMR spectroscopy. The synthetic protocols as well as the characterization of all structures are collated in the Experimental Section 5.3.1.



### 3.1.1 Spin Labelling of a Hydrogen Bonding System

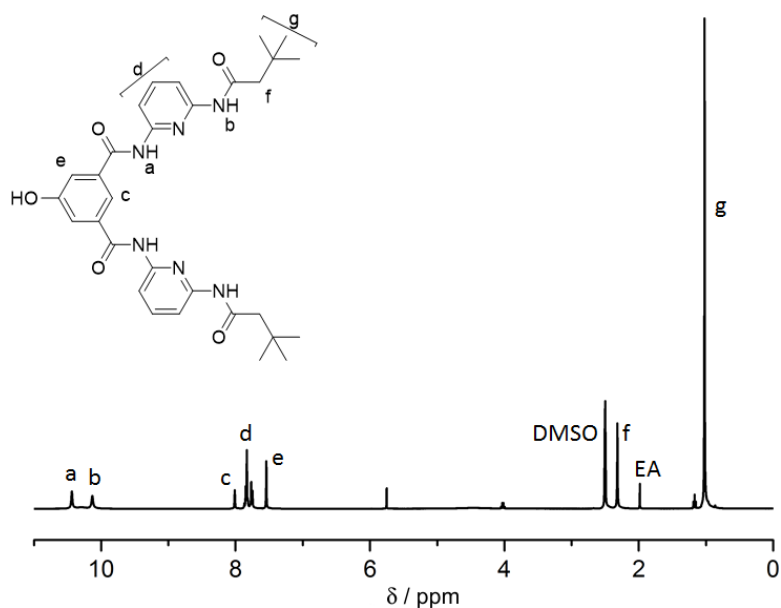
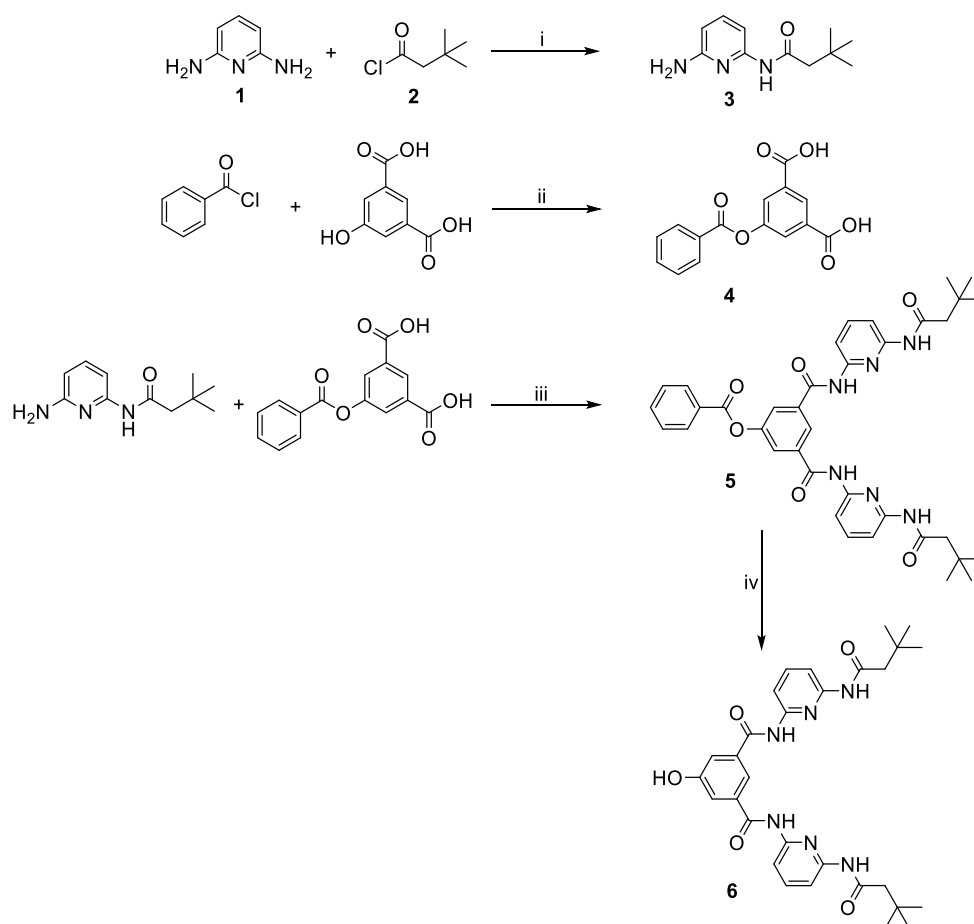


**Figure 11.**  $^1\text{H}$  NMR spectrum of the hydroxyl functional Hamilton Wedge **6**, measured in  $\text{DMSO-}d_6$  (298 K).



**Scheme 16.** Synthetic strategy for the preparation of the HW functionality. (i) dioxane, ambient temperature, 24 h. (ii) NaOH,  $\text{H}_2\text{O}$ ,  $\text{Et}_2\text{O}$ , ambient temperature, 4 h. (iii) 1. THF/DMF. 2. THF, 16 h. (iv) 1.2 M NaOH, ambient temperature, 5 h.

In order to couple the HW compound to the polymer, **6** was further modified resulting in the final compound **11** featuring the required HW moiety as well as the free hydroxyl functionality (refer to Scheme 17). Here, initially the acetal protected 2,2-bis-(hydroxymethyl)-propionic acid **7** was prepared. The acid functionality was esterified with propargyl alcohol to obtain the alkyne functionality that can undergo CuAAC. Next, the acetal protected compound **8** was deprotected, affording the free hydroxyl functionalities of which one was modified in an esterification with bromo acetylchloride to install a bromine functionality that can readily be modified with **6**. Subsequently, in an etherification **10** was reacted with **6** using potassium carbonate to yield the final organic compound **11** that can be tethered to the polymer *via* CuAAC and further features the required functionalities, *i.e.* HW for the folding reaction and an additional hydroxyl functionality to be reacted with 4-hydroxy TEMPO serving as a spin-label. The formation of **11** was confirmed by  $^1\text{H}$  NMR spectroscopy (refer to Figure 12).

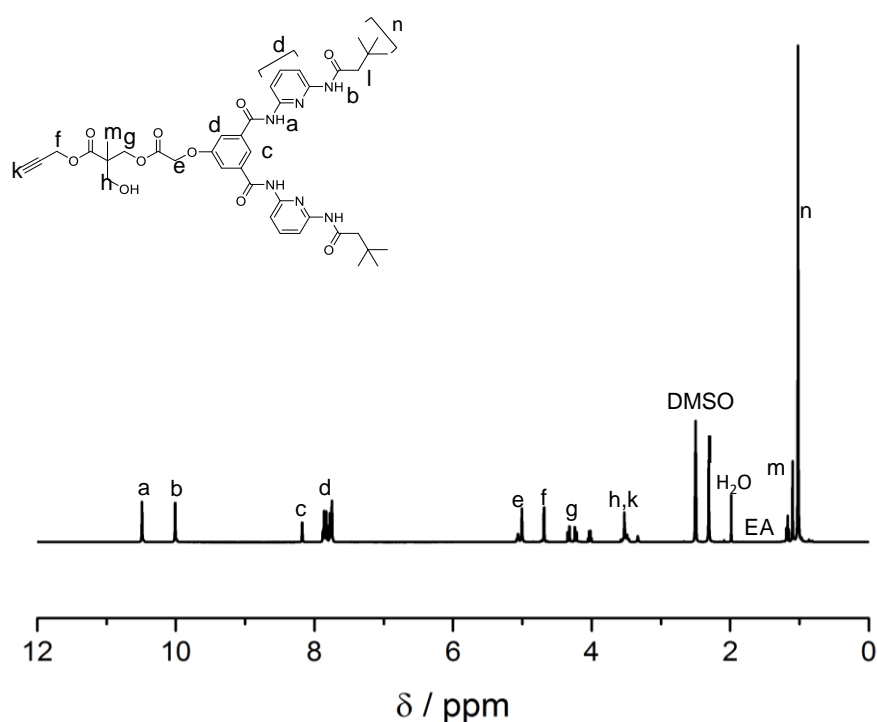
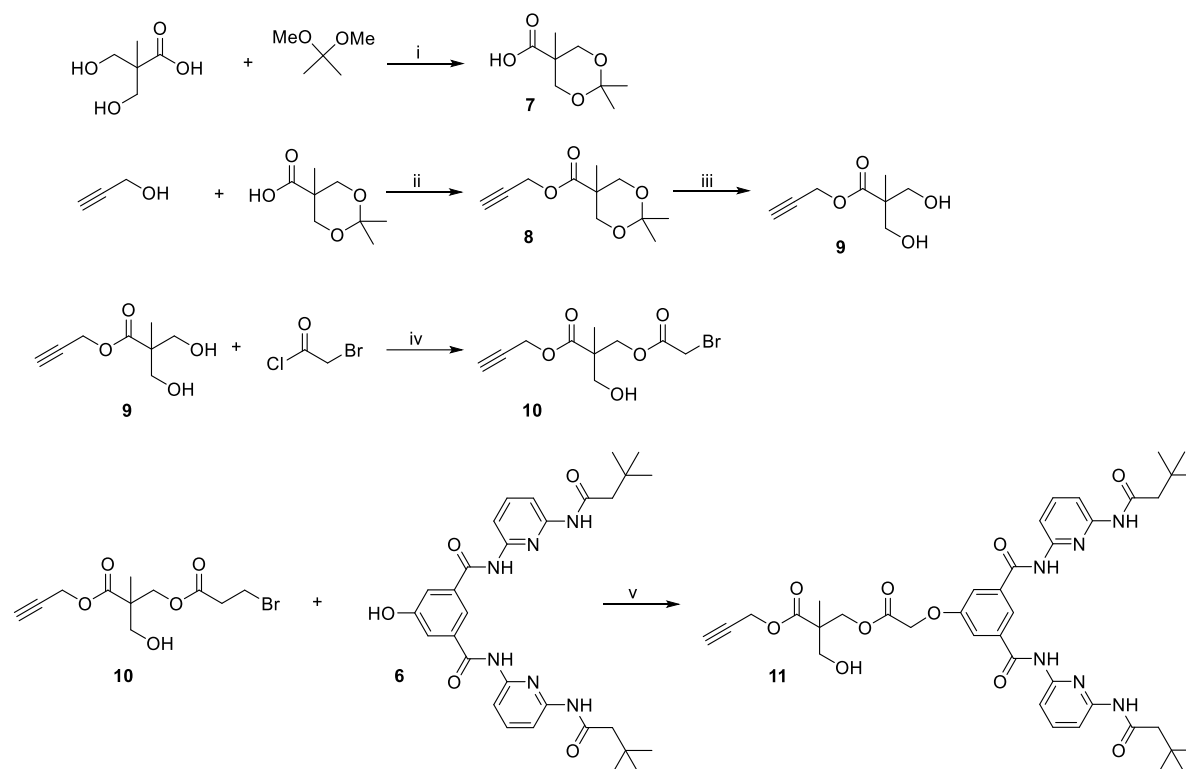


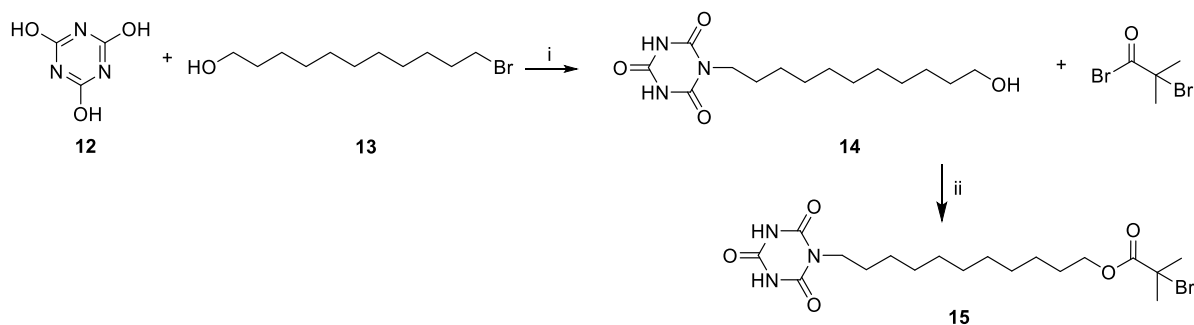
**Figure 12.**  $^1\text{H}$  NMR spectrum of the alkyne functional HW compound **11** featuring an additional hydroxyl functionality, measured in  $\text{DMSO}-d_6$  (298 K).

### 3.1.1 Spin Labelling of a Hydrogen Bonding System



**Scheme 17.** Synthetic pathway to the HW functional organic compound **11**. (i) *p*-TsOH monohydrate, acetone, ambient temperature, 2 h. (ii) DMAP, DCC, DCM, ambient temperature, 24 h. (iii) Dowex H<sup>+</sup>-resin, MeOH, ambient temperature, 12 h. (iv) TEA, THF, ambient temperature, 12 h. (v) K<sub>2</sub>CO<sub>3</sub>, ambient temperature, 72 h.

Concomitantly, an initiator able to induce activator regenerated by electron transfer (ARGET) atom transfer radical polymerization (ATRP) to obtain well-defined polymers was prepared in a two-step procedure (refer to Scheme 18). Simultaneously, the initiator features the complementary motif to the HW functionality – cyanuric acid – to induce the single-chain collapse. In the first step, compound **14** was prepared by substitution of the bromine functionality of the 11-bromoundecanoic acid (**13**) with cyanuric acid (**12**). Next, the hydroxyl functionality of **14** was modified in an esterification with  $\alpha$ -bromoisobutyryl bromide to yield the cyanuric acid functional ATRP initiator **15**. The structure of **15** was confirmed by <sup>1</sup>H as well as <sup>13</sup>C NMR spectroscopy, the <sup>1</sup>H NMR spectrum is depicted in Figure 13. The <sup>1</sup>H NMR spectrum displays the characteristic amide proton resonances at 11.37 ppm and the methyl resonances at 1.88 ppm.



**Scheme 18.** Synthetic strategy for the preparation of the cyanuric acid functional ATRP initiator **15**. (i) DBU, DMF, 70 °C, 24 h. (ii) TEA, DMAP, THF, ambient temperature, 24 h.

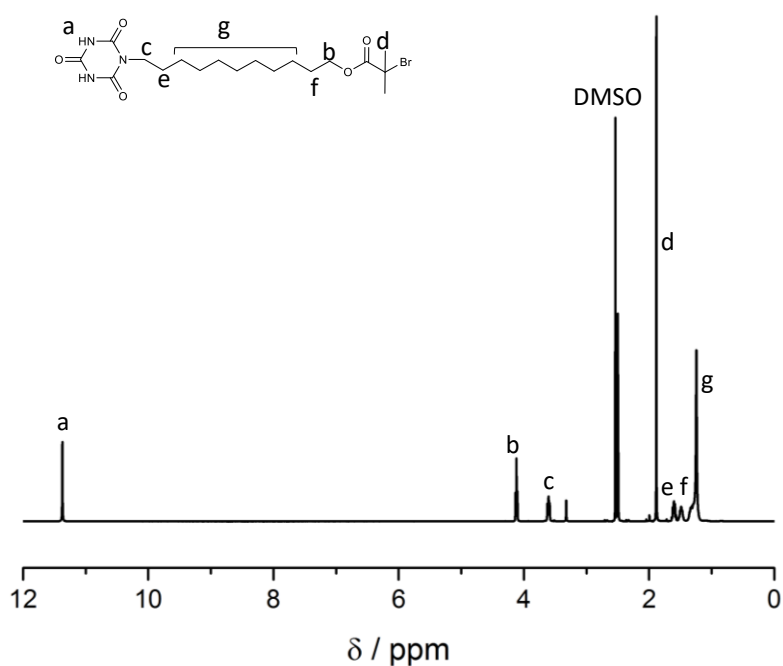


**Figure 13.**  $^1\text{H}$  NMR spectrum of the cyanuric acid functional ARGET ATRP initiator **15**, measured in  $\text{DMSO}-d_6$  (298 K).

### Synthesis of the $\alpha,\omega$ -Functional Polymers

For the synthesis of the heterotelechelic polymer the strategy presented in Scheme 19 was designed. Polymer **P1** was synthesized using the previously synthesized cyanuric acid functional ARGET ATRP initiator **15** and styrene under ARGET ATRP conditions. Three polymers (**P1-P3**) differing in molecular weights and thus chain lengths were

### 3.1.1 Spin Labelling of a Hydrogen Bonding System

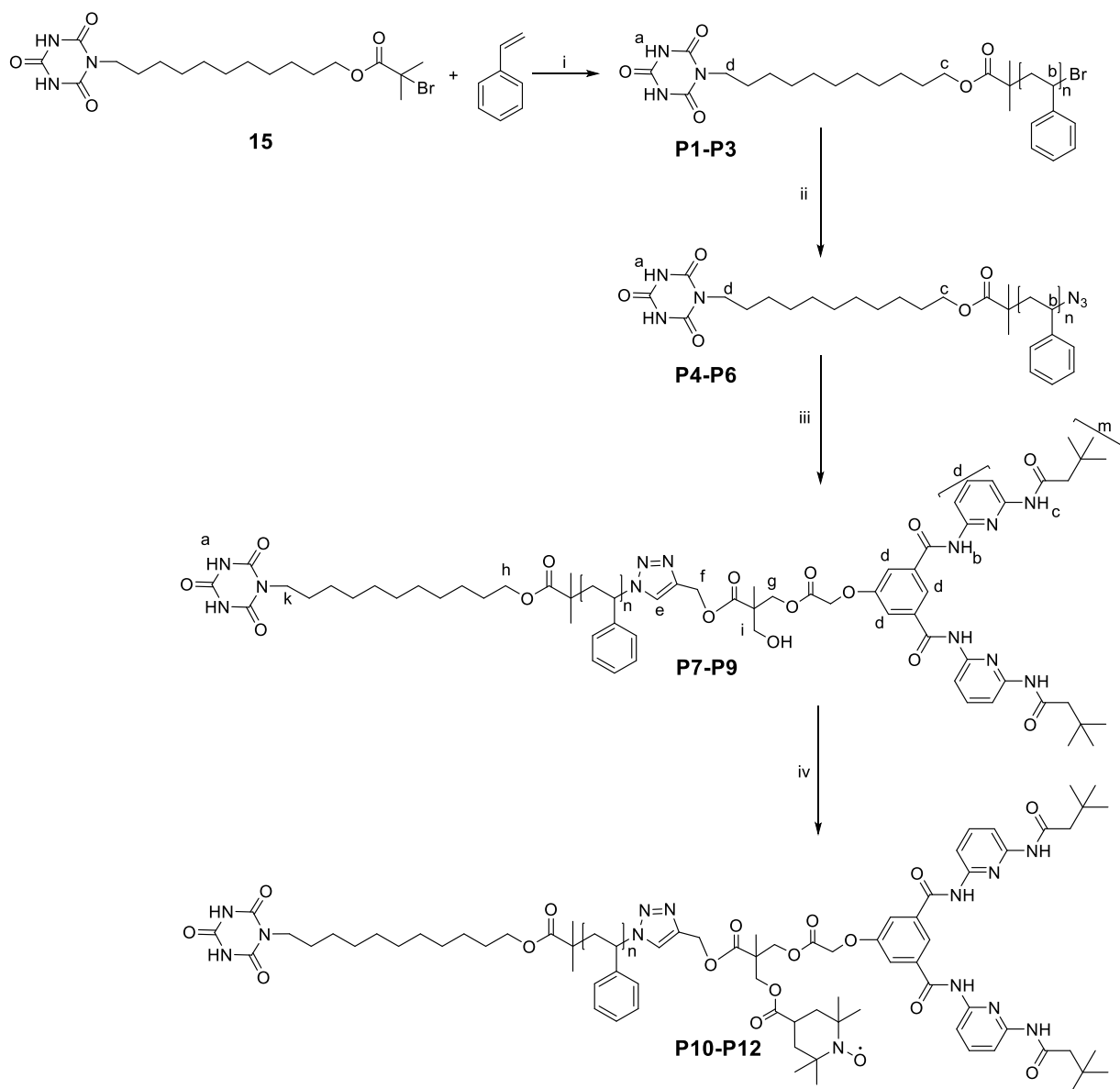
---

**Table 1.** Molecular characteristics of the prepared polymers. The molecular weights and polydispersities of the polymer samples **P1-P12** are depicted.

| ID         | $M_n / \text{g mol}^{-1}$ | $\mathcal{D}$ |
|------------|---------------------------|---------------|
| <b>P1</b>  | 4400                      | 1.08          |
| <b>P2</b>  | 12400                     | 1.10          |
| <b>P3</b>  | 28600                     | 1.09          |
| <b>P4</b>  | 4400                      | 1.07          |
| <b>P5</b>  | 13600                     | 1.04          |
| <b>P6</b>  | 28700                     | 1.10          |
| <b>P7</b>  | 5500                      | 1.06          |
| <b>P8</b>  | 14400                     | 1.04          |
| <b>P9</b>  | 29500                     | 1.09          |
| <b>P10</b> | 5600                      | 1.05          |
| <b>P11</b> | 15200                     | 1.05          |
| <b>P12</b> | 30200                     | 1.09          |

prepared. The molecular characteristics of the polymers are collated in Table 1 (entries 2-4). The initially synthesized polymers display narrow molecular weight distributions and low polydispersities that are characteristic for ATRP polymers. Subsequently, the bromine functionality was replaced by an azide functionality in a nucleophilic substitution reaction. The azide functionality is installed in  $\omega$ -position for further modification *via* CuAAC, which requires an azide moiety. The modification of the polymers was followed by  $^1\text{H}$  NMR to verify the successful and quantitative transformation of the bromine functionality, resulting in a shift from 4.4 ppm to 3.9 ppm.

The second post-polymerization modification was the above mentioned CuAAC click reaction of the azide functional polymers **P4-P6** with the alkyne functional HW moiety **11**. As catalytic system,  $\text{CuSO}_4 \times 5\text{H}_2\text{O}$  and sodium ascorbate were employed in DMF. Within the scope of  $^1\text{H}$  NMR spectroscopy, the quantitative modification of the polymers was confirmed. The  $\text{CH-N}_3$  resonance at approximately 3.9 ppm disappeared and the  $\text{CH}_2$ -triazole proton resonances emerge after the reaction at approximately 5.2 ppm. In addition, the characteristic  $\text{NH}$  resonances at 9.9 and 9.5 ppm attributed to the HW appear (refer to Figure 14).



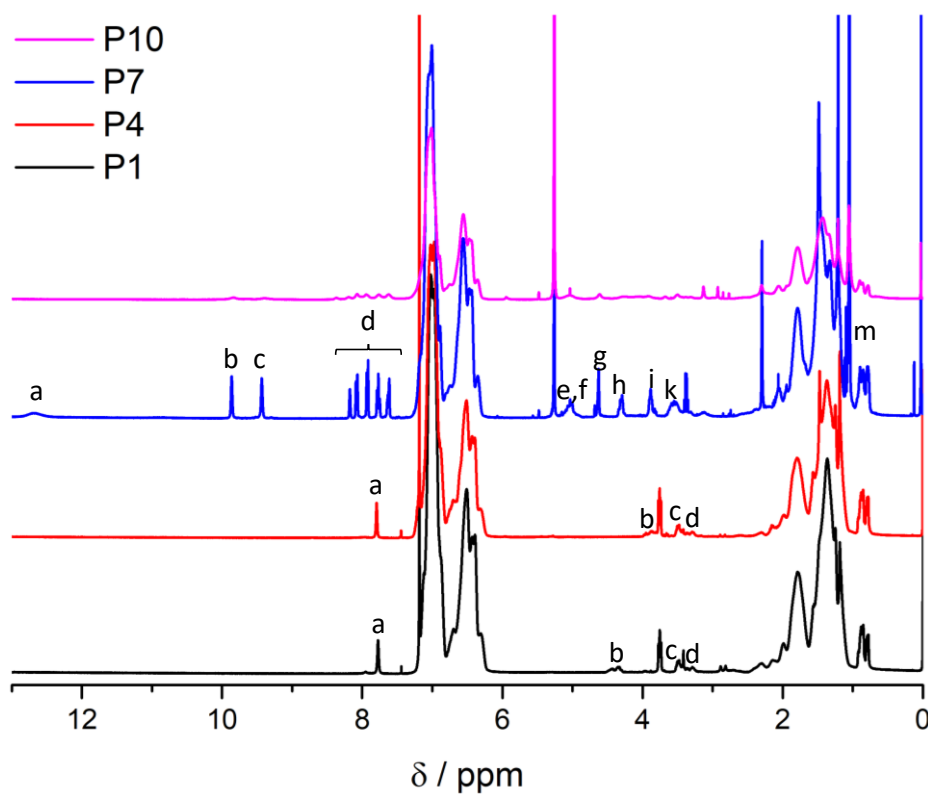
**Scheme 19.** Synthetic route towards the  $\alpha$ -,  $\omega$ -functional heterotelechelic polymers featuring a nitroxide spin-label in penultimate position to the HW moiety. (i) styrene,  $\text{CuBr}_2$ ,  $\text{Me}_6\text{TREN}$ ,  $\text{Sn}(\text{EH})_2$ , anisole,  $90^\circ\text{C}$ . (ii)  $\text{NaN}_3$ , DMF, ambient temperature, 72 h. (iii)  $\text{CuSO}_4 \times 5 \text{H}_2\text{O}$ , sodium ascorbate, DMF, ambient temperature, 24 h. (iv) DCC, DMAP, DCM, ambient temperature, 48 h.

### 3.1.1 Spin Labelling of a Hydrogen Bonding System

---

Furthermore, in sample **P7**, the *NH* resonances of the CA moiety at approximately 13 ppm are visible (refer to Figure 14). Already at this stage the hydrogen bonds are established and shifted compared to the small molecules, yet most probably the interaction detected by NMR takes place intermolecularly since intramolecular interactions are only dominant in highly diluted conditions. In addition, the SEC displays a shift towards higher retention volumes and thus lower molecular weights due to the linking of the HW moiety to the polymer (refer to Figure 15 a-c)

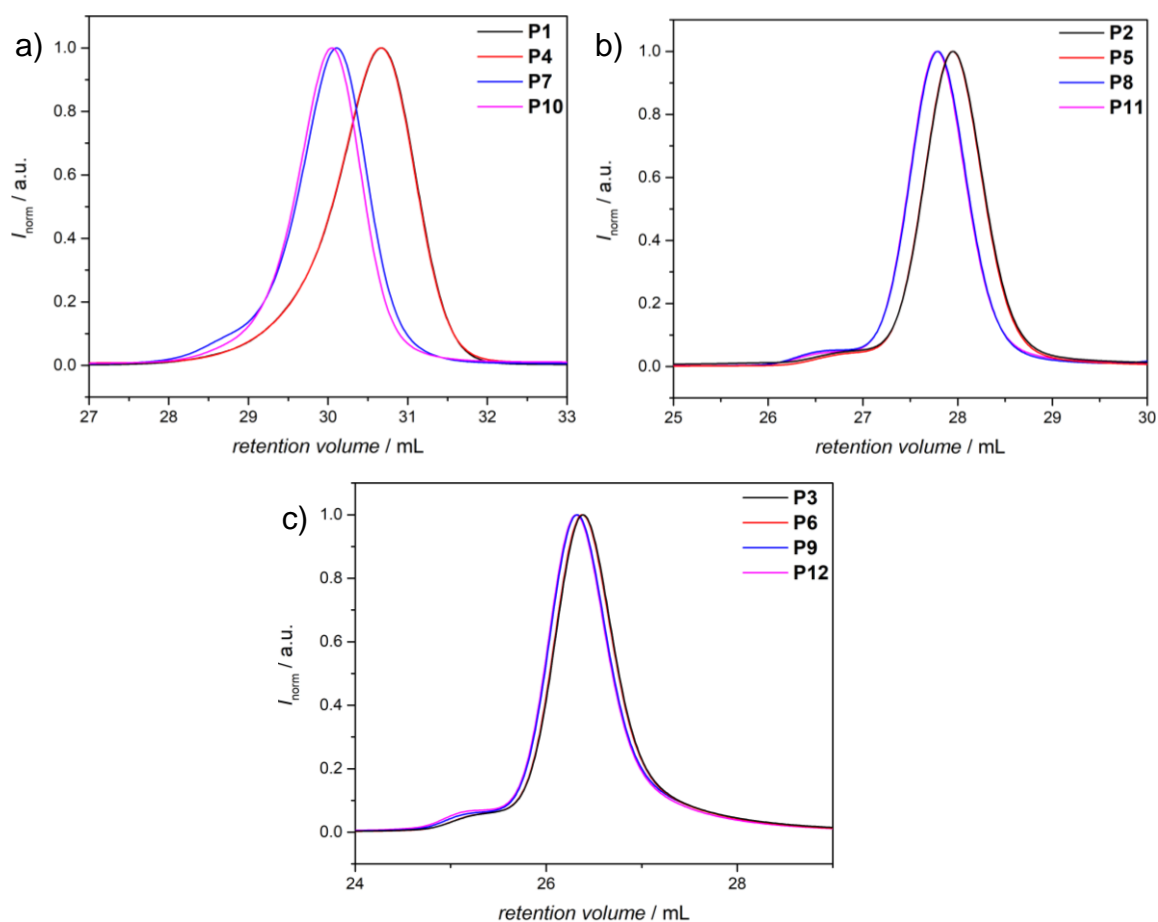
In the final post-polymerization modification, the spin label – *i.e.* 4-carboxy-2,2,6,6-tetramethylpiperidine 1-oxyl (4-carboxy TEMPO) – was introduced to the polymers in penultimate position next to the HW functionality. *Steglich* conditions<sup>[234]</sup> were chosen to attach the TEMPO moiety. In particular, 4-carboxy TEMPO, *N,N'*-dicyclohexylcarbodiimid (DCC) and 4-dimethylaminopyridine (DMAP) in DCM at ambient temperature for 48 h were applied (for full synthetic details refer to the Experimental Procedures in Section 5.3.2). After the attachment of the paramagnetic nitroxide radical in penultimate position to the polymer, NMR analysis becomes rather difficult due to line broadening effects of the paramagnetic centre present in the system (refer to Figure 14). Commonly, <sup>1</sup>H NMR analysis is carried out prior to the attachment or preparation of the paramagnetic species.<sup>[235,236]</sup> Nonetheless, the effect of line broadening itself in the measured <sup>1</sup>H NMR spectra of the polymers **P10-P12** indicate the successful grafting of the nitroxide to the polymer. Further, SEC shows a slight increase of the molecular weights ( $M_n$ ) underpinning the successful nitroxide grafting (refer to Table 1). Furthermore, the modification from **P7** to **P10** was followed by electrospray mass spectrometry in negative ion mode. The styrene based polymers within the current study are generally nonpolar and poorly ionisable through positive charges such as protons or alkali metal ions using the positive ion mode. Therefore, the previously established negative ion mode ionization protocol for polymers pioneered by our team was applied for the detection of the synthesized polymers in ESI MS.<sup>[237]</sup> Here, the polymers are negatively charged using chlorine anions. Compared to the positive ion mode, the PS can be multiply be charged in negative ion mode compared to only singly charged species in positive ion mode. The overview mass spectrum as well as a zoomed in section with the assignments of the structures is given in Figure 16.



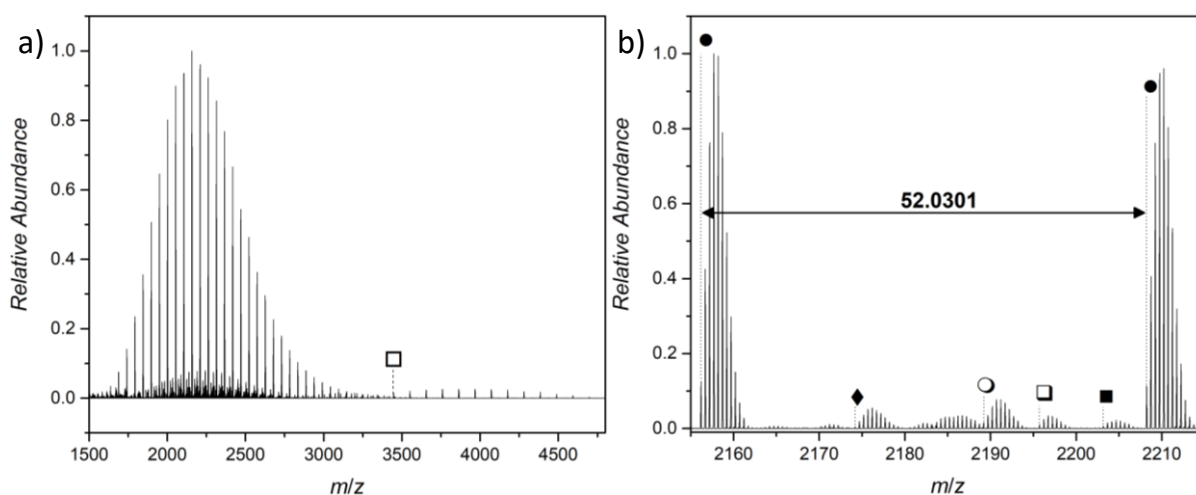
**Figure 14.**  $^1\text{H}$  NMR spectra of the CA and bromine functional ARGET ATRP polymer **P1** (black curve), the CA and azide functional polymer **P4** (red curve), the CA and HW/OH functional polymer **P7** (blue curve) as well as the CA and HW/TEMPO functional polymer **P10** (pink curve). The spectra for **P1** and **P4** were recorded in  $\text{CDCl}_3$  at 298 K. The polymers **P7** and **P10** were measured in  $\text{DCM-}d_2$  at 298 K. Adapted from ref [238] with permission of the Royal Society of Chemistry.



### 3.1.1 Spin Labelling of a Hydrogen Bonding System



**Figure 15.** SEC chromatograms of the synthesized CA/HW functional polymers featuring an nitroxide spin label with different molecular weights (refer to Table 1) measured in THF, 35 °C, 1 mL min<sup>-1</sup> using PS standards for calibration. Graph a) is adapted from ref [238] with permission of the Royal Society of Chemistry.

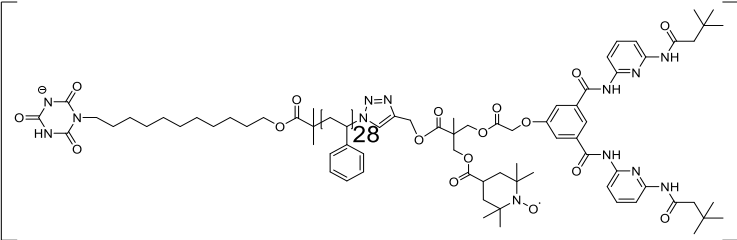
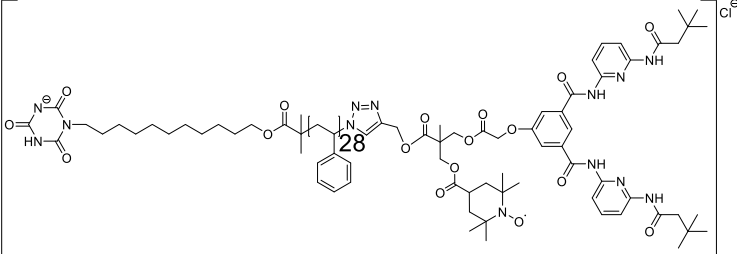
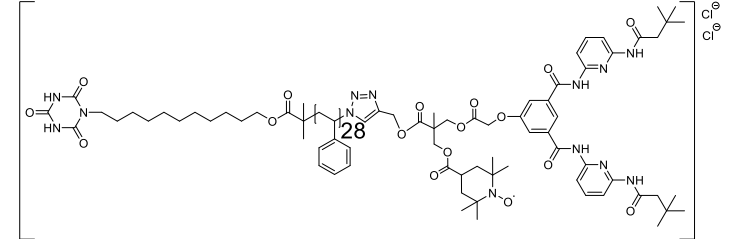


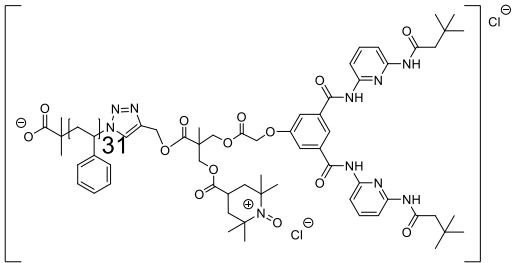
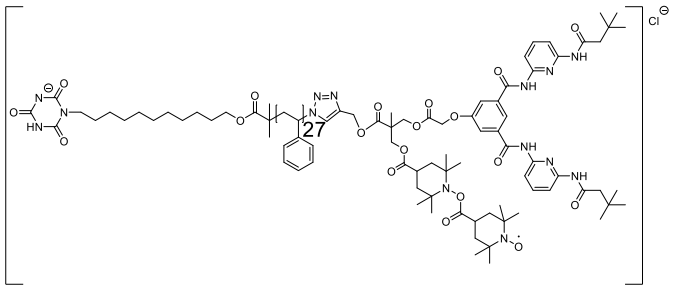
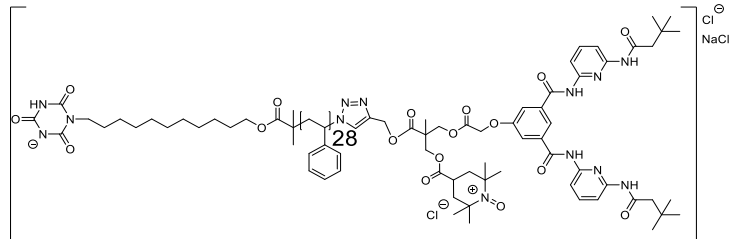
**Figure 16.** a) Overview ESI mass spectrum of P10 from  $m/z$  1500 to 4800 recorded in negative ion mode. (c) Expanded region of the ESI mass spectrum of polymer P5 in the doubly charged area between  $m/z$  2155 and 2215. The most abundant species are labelled as well as the repeating unit of PS. The assignment of the labelled patterns is provided in Table 2, all assignments are discussed in the text. Adapted from ref [238] with permission of the Royal Society of Chemistry.

Based on the structural assignments in the mass spectra (refer to Table 2), it is very likely that the target structure, *i.e.* **P10**, has been prepared (refer to structure □ and ● in Table 2, entries 1 and 2). It should be mentioned, however, that only **P10** is accessible in mass analysis with ESI MS, since the molecular weights of **P11** and **P12** are too high to fall within the detection limit of the employed Orbitrap mass analyser.<sup>[237]</sup> Nonetheless, **P11** and **P12** are assumed to be similar in composition and structure to **P10** despite the larger  $M_n$ , due to the fact that the NMR spectra display the same resonances for the polymers. Interestingly, the mass spectrum of **P10** reveals four additional species. The most abundant species (refer to Figure 16b and Table 2) is the doubly charged species of **P10**. In addition, four low abundant species were assigned in the mass spectrum. Two species where the nitroxide was oxidized to the oxoammonium species were also detected (labelled with ○ and ■, refer also to Figure 16b and Table 2). The oxoammonium salts can be generated by applying voltage in the range of 2.5-4 V or synthetically.<sup>[239–241]</sup> The ionization process in electrospray ionization uses high redox potential, which may cause the formation of the detected oxoammonium species. Further, the synthetic conditions employed for **P10** or a prolonged storing period could lead to the formation of the oxoammonium salt. In addition, in the case of ○, the cleavage of the CA moiety was observed.

### 3.1.1 Spin Labelling of a Hydrogen Bonding System

**Table 2.** Peak assignment of the ESI Orbitrap mass spectrum of **P10** showing the labels (corresponding to the species in Figure 16b), the resolution (obtained by the Xcalibur software), the experimental  $m/z$  and theoretical  $m/z$  values,  $\Delta m/z$  and the proposed chemical structures. Adapted from ref [238] with permission of the Royal Society of Chemistry.

| Label | Resolution | $m/z(\text{exp})$ | $m/z(\text{theo})$ | $\Delta m/z$ | Structure   |
|-------|------------|-------------------|--------------------|--------------|---|
| □     | 35000      | 4278.3730         | 4278.4379          | 0.0649       |    |
| ●     | 45000      | 2156.2037         | 2156.2020          | 0.0017       |    |
| ◆     | 42000      | 2174.1942         | 2174.1903          | 0.0039       |  |

|   |       |           |           |        |  |
|---|-------|-----------|-----------|--------|--|
| ○ | 43000 | 2189.2056 | 2189.1934 | 0.0122 |   |
| □ | 45000 | 2195.7291 | 2195.7337 | 0.0046 |   |
| ■ | 42000 | 2203.1659 | 2203.1674 | 0.0015 |  |

### Single-Chain Collapse

The folding of **P10-P12** to the corresponding single-chain nanoparticles was realized in high dilution conditions (in the range of 1.4 – 2.3 mg mL<sup>-1</sup>) and characterized by DOSY measurements. Generally, DOSY provides the diffusion coefficients of the molecules in solution, based on which the hydrodynamic radius/diameter of the species can be deduced *via* the Stokes-Einstein equation 12 (refer to Section 2.4.2.1). Thus, DOSY measurements provide a suitable platform technology to access information about changes in the diffusion coefficient upon the single-chain collapse. The DOSY measurements were performed by the cooperation partner S. Spann (Luy group, KIT). An overview of the DOSY results is provided in Table 3. It is evident that with increasing molecular weight, the shift of the hydrodynamic diameter from the open linear precursor polymer to the SCNP becomes more and more pronounced. In addition, the larger polymers tend to have higher diameters for the unfolded state. The smallest polymer **P10** displays a shift from 2.7 nm to 4.3 nm, which corresponds to a collapse of the hydrodynamic diameter by close to 37 % (refer to Table 3, entry 1 and 2). For **P11**, the  $D_h$  increases from 4.0 nm in the folded state to 7.5 nm after the addition of MeOH to disrupt the hydrogen bonds, corresponding a collapse of close to 47% (refer to Table 3, entry 3 and 4). Interestingly, for polymer **P12** with the highest molecular weight of 30.0 kDa, a hydrodynamic volume reduction of 61% is observed between the open unfolded state and the SCNPs.

**Table 3.** Overview of the single-chain folding and unfolding (diffusion coefficients  $D$  and the calculated hydrodynamic diameter  $D_h$  *via* the Stokes-Einstein equation 12) as well as the resulting intramolecular collapse measured by DOSY. The DOSY data will be discussed in detail in the forthcoming PhD thesis of S. Spann, KIT, 2019.

| ID                             | Diffusion coefficient $D^a$ / m <sup>2</sup> s | $D_h^b$ / nm | Collapse / % |
|--------------------------------|--|--------------|--------------|
| <b>P10</b> <sub>SCNP</sub>     | $3.91 \times 10^{-10}$                         | 2.7          | 37           |
| <b>P10</b> <sub>unfolded</sub> | $2.42 \times 10^{-10}$                         | 4.3          |              |
| <b>P11</b> <sub>SCNP</sub>     | $2.69 \times 10^{-10}$                         | 4.0          | 47           |
| <b>P11</b> <sub>unfolded</sub> | $1.40 \times 10^{-10}$                         | 7.5          |              |
| <b>P12</b> <sub>SCNP</sub>     | $3.55 \times 10^{-10}$                         | 2.9          | 61           |
| <b>P12</b> <sub>unfolded</sub> | $1.13 \times 10^{-10}$                         | 7.5          |              |

The increasing collapse may be associated with the fact that the polymeric backbone of the larger **P11** and **P12** could be partly aligned through aromatic stacking of the aromatic styrene backbone, whereas **P10** with a  $M_n$  of 5600 Da is not sufficiently long for the alignment through  $\pi$ - $\pi$ -interactions. Accordingly, the combination of  $\pi$ - $\pi$ -stacking of the polymeric backbone and the hydrogen bonding motif at the chain ends leads to a higher degree of compaction and thus a more pronounced shift between the open chain and the resulting SCNP.

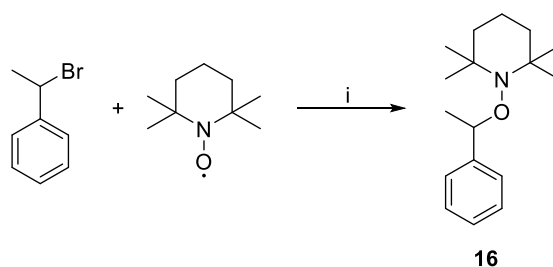
Currently, further multidimensional NMR experiments are under investigation by S. Spann to gain information about the distance of the chain ends during folding. The distance of the recognition motifs in the folded state can be determined by spin-labelling the system to influence the relaxation time in NMR analysis. The relaxation rate depends on the distance of the proton to the spin-marker. Accordingly, the closer protons are to the nitroxide spin-label, the larger the relaxation rate will be influenced. In the end, the integration of nuclear Overhauser enhancement spectroscopy (NOESY) cross-signals or by determination of exact NOEs the distance between the recognition motifs in the folded state can be deduced.

In summary, a heterotelechelic  $\alpha$ -,  $\omega$ -functional polystyrene polymer has been prepared for single-chain folding, featuring the hydrogen bonding motif CA/HW at the chain ends. Further, a spin-label, *i.e.* 4-carboxy-TEMPO, was tethered in penultimate position close to the HW functionality. The spin-label serves as marker for multidimensional NMR measurements to ultimately gain information about the folding distance between the recognition units. To investigate the influence of the chain-length on the folding event, well-defined polymers with different molecular weights, ranging from 5.5 kDa to 30.2 kDa featuring low polydispersities (below 1.1) were prepared *via* ARGET ATRP. The polymers were characterized by  $^1\text{H}$  NMR spectroscopy, high resolution ESI MS spectrometry as well as SEC. The folding and unfolding of the polymers was subsequently followed by DOSY. Currently, NMR measurements are performed to gain the aforementioned folding distance between the HW and CA moieties as a function of temperature.

### 3.1.2 Analyzing Nitroxide Containing Polymers by High Resolution Electrospray Ionisation Mass Spectrometry

After the structure of **P10** had been confirmed by high resolution mass spectrometry, inspection of the literature suggested that nitroxide containing polymers were previously not characterized by mass spectrometry.<sup>[242]</sup> To address the lack of mass spectrometric analytical data on nitroxide containing polymers, a set of polymers featuring different contents of free stable nitroxide radicals within the backbone of the polymer were prepared. The influence of the nitroxide radical content and the chain length on the mass spectra was investigated by increasing the amount of incorporated radicals.\* Well-defined block copolymers are accessible by nitroxide-mediated polymerization (NMP). Here, a TEMPO based initiator starts the polymerization (refer to Section 2.1.1) and is present as end group in the polymers. Hence, the free nitroxide radicals are tethered to the block copolymer in a post-polymerization modification (refer to Scheme 21).

First, the initiator for the nitroxide-mediated polymerization (NMP) was synthesized in a one-step procedure according to literature (refer to Scheme 20).<sup>[243]</sup>



**Scheme 20.** Synthesis of the NMP initiator **16** in an one-step procedure. (i) CuBr, PMDETA, toluene, 50 °C, 1 h.

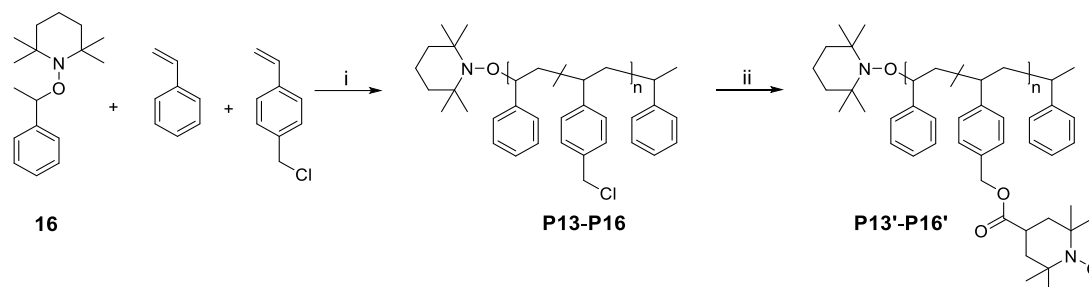
---

\*Parts of the section are adapted or reproduced from T. S. Fischer, J. Steinkönig, H. Woehl, J. P. Blinco, K. Fairfull-Smith, C. Barner-Kowollik, *Polym. Chem.*, **2017**, *8*, 5269-5274. with permission of the Royal Society of Chemistry. T. S. Fischer designed and conducted the synthesis of the polymers as well as the evaluation of the mass spectra and wrote the manuscript. J. Steinkönig conducted the mass spectrometry measurements, H. Woehl, measured EPR, J. P. Blinco, K. Fairfull-Smith helped with scientific discussions and C. Barner-Kowollik motivated and supervised the project.

### 3.1 Selective Point Folding

The structure of **16** was confirmed by  $^1\text{H}$  NMR (refer to Figure 63, Section 5.3.1).

Subsequently, the NMP initiator was used for NMP copolymerization of styrene and 4-(chloromethyl)styrene (CMS, refer to Scheme 21) to afford statistical copolymers poly(styrene-*stat*-4-(chloromethyl)styrene) (p(S-*stat*-CMS, **P13-P16**) with varying amounts of incorporated CMS units within the polymeric backbone, which are 9.3, 15.3, 35.7 and 34.9 mol%, respectively. The polymers **P13-P16** were further characterized by high resolution mass spectrometry as well as SEC (refer to Figure 17 and Figure 18 for the overall and expanded mass spectra as well as Figure 19 for SEC traces). As indicated above, the chain-length was additionally increased from 4300 Da for **P13** to 8400 Da for polymer **P16** (refer to Table 4).



**Scheme 21.** Synthetic procedure for the preparation of the nitroxide functional polymers **P13'-P16'**. (i) **P13, P14**: 2 h at 125 °C in bulk. **P15**: 0.5 h at 125 °C in bulk. **P16**: 1 h at 125 °C in bulk. (ii)  $\text{K}_2\text{CO}_3$ , 4-carboxy TEMPO in DMF for 72 h at 50 °C. Adapted from ref [238] with permission of the Royal Society of Chemistry.

**Table 4.** Molecular characteristics of the synthesized **P13-P16** and **P13'-P16'** polymers. The molecular weights, dispersity and percentage of incorporated CMS and TEMPO are provided. Reproduced from ref [238] with permission of the Royal Society of Chemistry.

| ID          | $M_n^a$ / g mol $^{-1}$ | $\mathcal{D}^a$ | % CMS $^b$ | % TEMPO $^c$ |
|-------------|-------------------------|-----------------|------------|--------------|
| <b>P13</b>  | 4300                    | 1.20            | 9.3        |              |
| <b>P14</b>  | 6000                    | 1.24            | 15.3       |              |
| <b>P15</b>  | 6000                    | 1.37            | 35.7       |              |
| <b>P16</b>  | 8400                    | 1.31            | 34.9       |              |
| <b>P13'</b> | 4800                    | 1.19            |            | 11.3         |
| <b>P14'</b> | 6900                    | 1.23            |            | 16.3         |
| <b>P15'</b> | 8600                    | 1.29            |            | 27.8         |
| <b>P16'</b> | 11100                   | 1.26            |            | 29.1         |

<sup>a</sup> Determined by SEC. <sup>b</sup> Calculated by NMR, using the reported equation from literature.<sup>[85]</sup> <sup>c</sup> Determined by EPR.



### 3.1.2 Analyzing Nitroxide Containing Polymers by High Resolution Mass Spectrometry

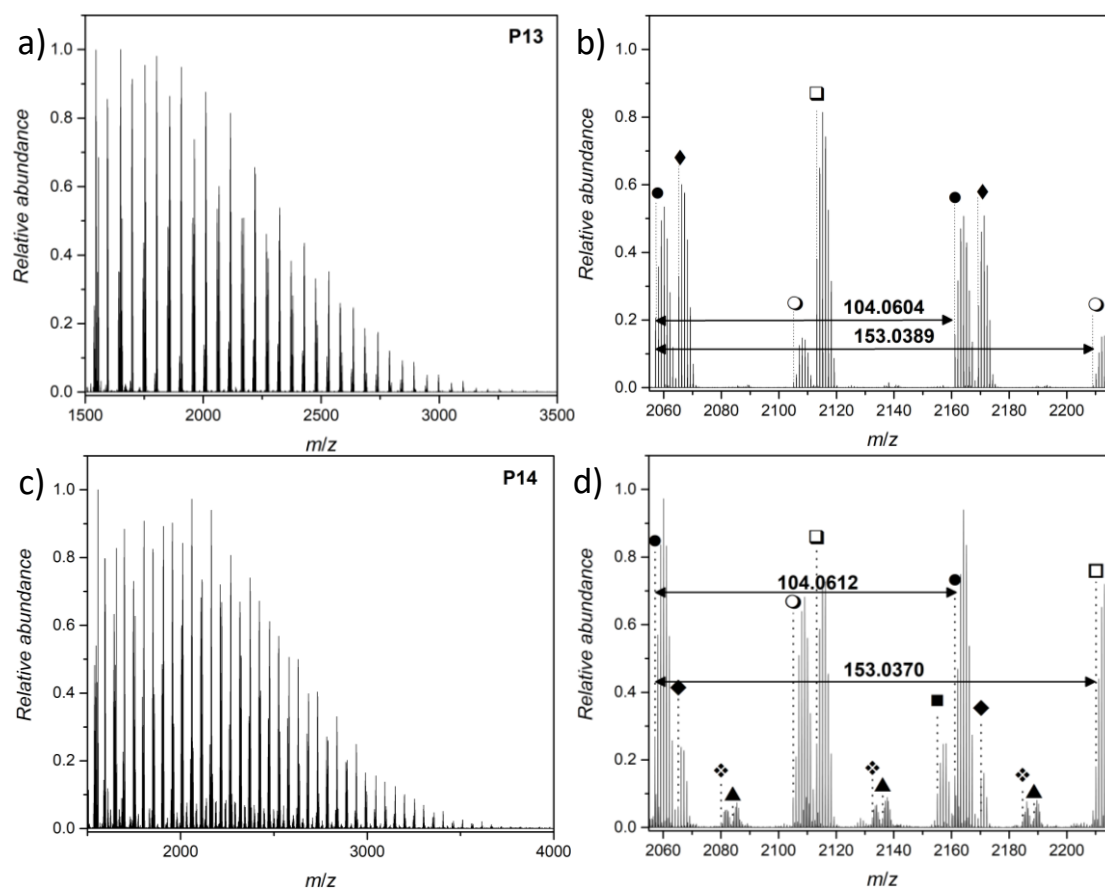


**Figure 17.** Overview and expanded mass spectra of the p(S-*stat*-CMS, **P13** and **P14** recorded in negative ion mode. a) Overview ESI mass spectrum of **P13** recorded from  $m/z$  1500 to 3500. b) Expanded region of the ESI mass spectrum of **P13** recorded from  $m/z$  2055 to 2217. c) Overview ESI mass spectrum of **P14** recorded from  $m/z$  1500 to 4000. d) Expanded region of the ESI mass spectrum of **P14** recorded from  $m/z$  2055 to 2217. Adapted from ref [238] with permission of the Royal Society of Chemistry.

The overall mass spectra of the copolymers **P13-P16** are highly resolved and show no formation of high molecular aggregates at about  $m/z$  3000-3500 or above (refer to Figure 17a and c and Figure 18a and c). For each polymer in the expanded region several structures were assigned and could be identified. The assignment of all assigned species is provided in the Appendix Table A1-Table A4.

### 3.1 Selective Point Folding

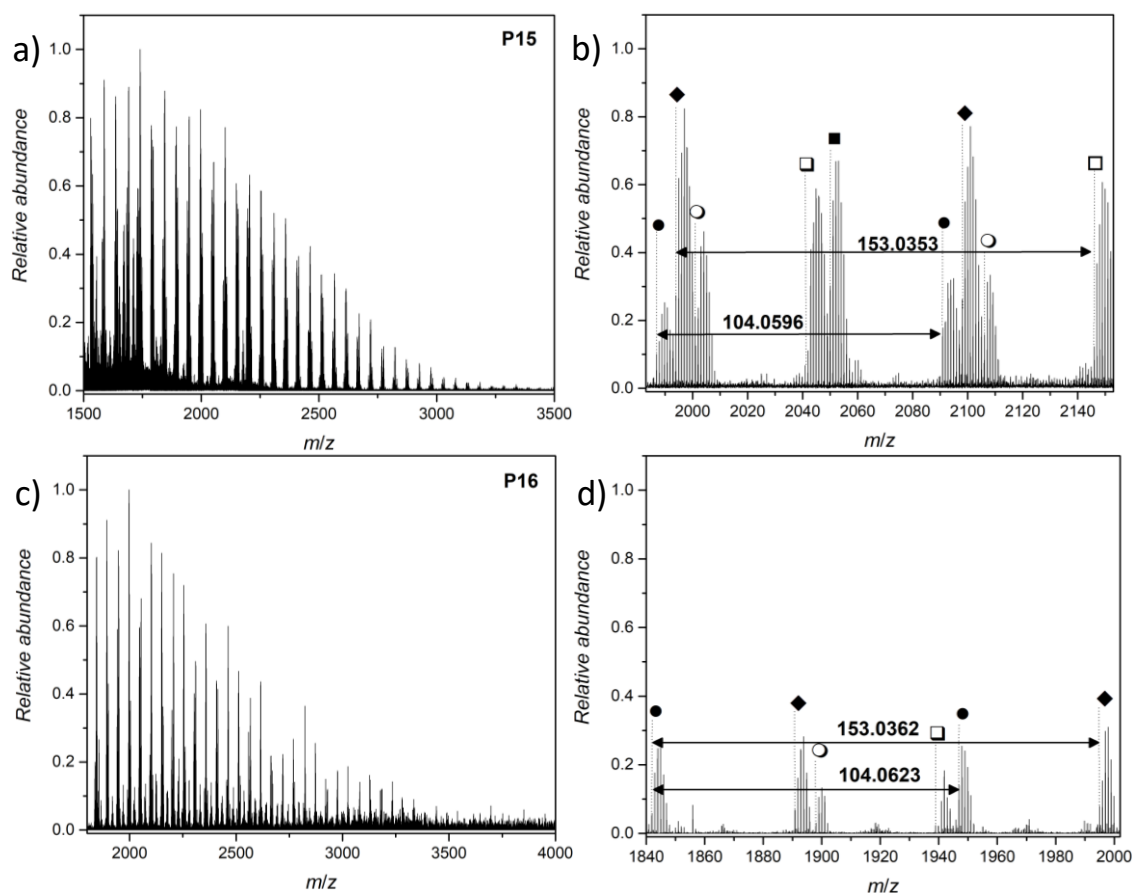


**Figure 18.** Overview and expanded mass spectra of the p(S-*stat*-CMS, **P15** and **P16** recorded in negative ion mode. a) Overview ESI mass spectrum of **P15** recorded from  $m/z$  1500 to 3500. b) Expanded region of the ESI mass spectrum of **P15** recorded from  $m/z$  1983 to 2153. c) Overview ESI mass spectrum of **P16** recorded from  $m/z$  1800 to 4000. d) Expanded region of the ESI mass spectrum of **P16** recorded from  $m/z$  1840 to 2010. Adapted from ref [238] with permission of the Royal Society of Chemistry.

Subsequently, all polymers were modified in a post-polymerization modification by reacting the chlorine group in a nucleophilic substitution reaction with 4-carboxy-2,2,6,6-tetramethylpiperidine 1-oxyl (4-carboxy TEMPO), affording the polymers **P13'**-**P16'**. NMR analysis of paramagnetic compounds, especially molecules containing a persistent nitroxide radical, is challenging and often hampered when the radical is generated, due to effects such as line broadening. Thus, nitroxide containing compounds are generally characterized by  $^1\text{H}$  NMR before the paramagnetic radical centre is generated. Moreover, characterization *via* SEC does not provide any molecular information with regard to the polymer microstructure and only provides the average molecular weights.<sup>[235,236,244]</sup> Nevertheless, the grafting of 4-carboxy TEMPO to the polymers **P13-P16** was analysed by  $^1\text{H}$  NMR spectroscopy, to qualitatively evaluate the post-polymerization modification.

### 3.1.2 Analyzing Nitroxide Containing Polymers by High Resolution Mass Spectrometry

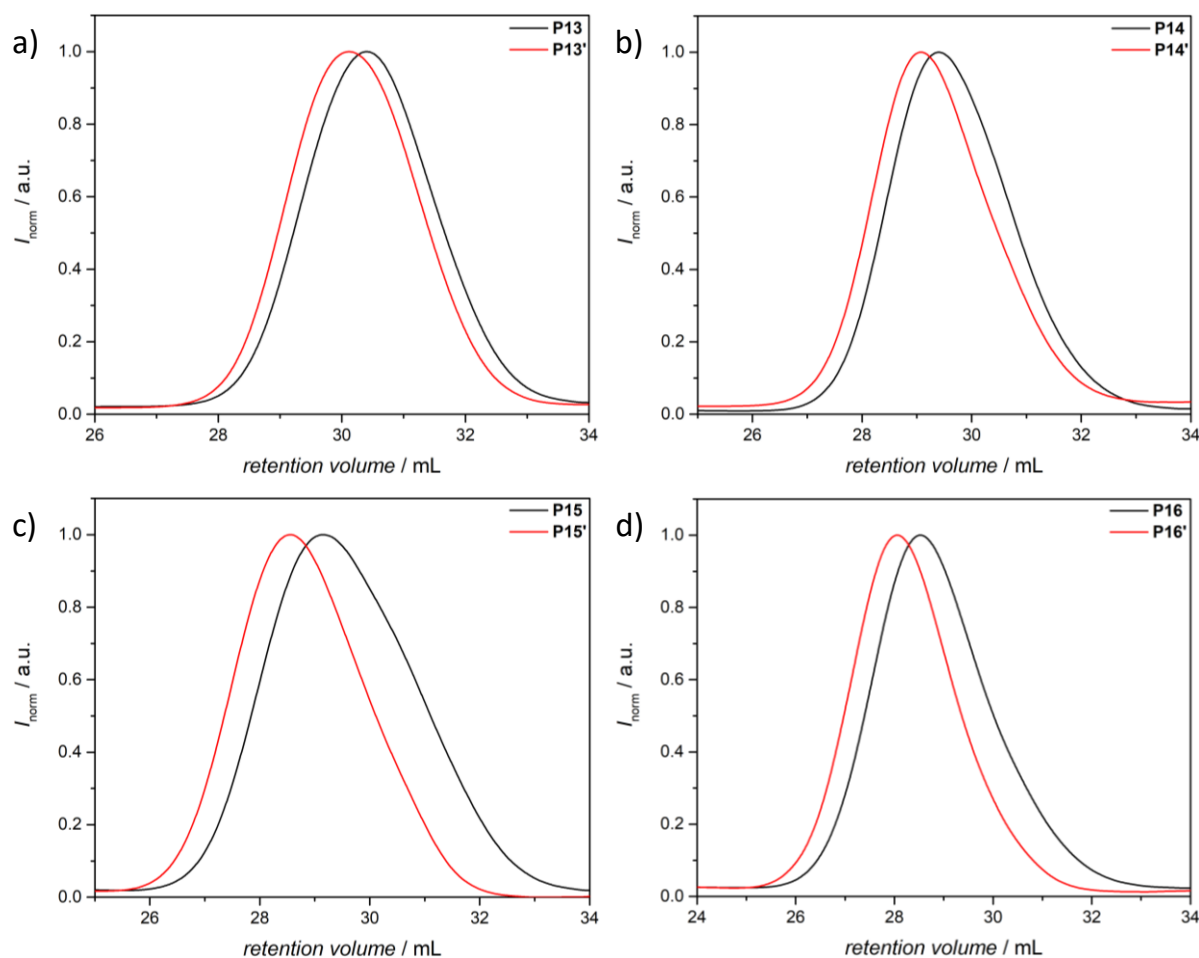


**Figure 19.** SEC traces of the polymers **P13-P16** and **P13'-P16'**, measured in THF, 35 °C, 1 mL min<sup>-1</sup> using PS standards for calibration. Adapted from ref [238] with permission of the Royal Society of Chemistry.

The shift of the  $CH_2$  resonance adjacent to the chlorine functionality from 4.52 ppm to 5.16 ppm, indicates the successful attachment of the radical species (refer to Appendix Figure 79-Figure 81 for the recorded <sup>1</sup>H NMR spectra for **P13-P15** and **P13'-P16'**), without providing any structural information, due to line broadening associated with the persistent nitroxide radical. The SEC chromatogram displays the expected shift towards higher molecular weights after the ligation (refer to Figure 19), thus confirming the formation of **P13'-P16'**. Further proof for the installed nitroxide radicals was obtained by electron paramagnetic resonance (EPR) spectroscopy (refer to Table 4). The density of TEMPO can be determined by EPR by establishing a calibration curve for pure TEMPO and integrating the measured EPR signal of the sample. The EPR measurements and the obtained results are in excellent agreement with the beforehand determined CMS content of the polymers from NMR measurements. The slight discrepancy between the calculated amount of CMS and the obtained nitroxide

content (9.3 mol% CMS in **P13** compared 11.3 mol% TEMPO in **P13'**, 15.3 mol% CMS in **P14** compared to 16.3 mol% TEMPO in **P14'**, 35.7 mol% CMS in **P15** compared to 27.8 mol% TEMPO in **P15'** and 34.9 mol% CMS in **P16** compared to 29.1 mol% TEMPO in **P16'**) may be due to the accuracy of (i) the calculation of the CMS content, which is dependent on the precise determination of the integral values and the NMR spectra themselves and (ii) the EPR measurements and the preparation of the EPR samples. Nevertheless, EPR confirms the modification of the precursor polymers **P13-P16** to the nitroxide radical containing polymer **P13'-P16'**.

The so far employed characterization methods did not afford any information about the structure and chemical composition of the prepared polymers. The molecular and structural proof for **P13'-P16'** was obtained by high resolution mass spectrometry, after subjecting all nitroxide containing polymers to mass analysis, using the reported negative ion mode chlorine attachment.<sup>[237]</sup> By applying the reported method, well resolved mass spectra were recorded up to approximately  $m/z = 3500$  (refer to Figure 20) even with the non-polar nature of the polymeric samples **P13'-P16'**.

Inspecting the overview mass spectra, some general observations can be made: (i) with increasing nitroxide content within the polymeric sample, the mass spectra display an increasing abundance of high molecular weight species. Already in the ESI MS spectrum of **P13'** that contains the lowest amount of nitroxide radicals some minor aggregates at approximately  $m/z = 4500$  are observed, although with low abundance. Interestingly, the sample with approximately 30 mol% TEMPO shows a drift of the baseline, probably due to the formation of high molecular weight aggregates. As reported in literature, the TEMPO radicals can form hydrogen bonds with an H-bond donor. In addition, the dimerization of nitroxides has been reported.<sup>[245,246]</sup> The effect of the baseline drift becomes even more pronounced with increasing molecular weight from **P15'** ( $M_n = 8600 \text{ g mol}^{-1}$ ) to **P16'** ( $M_n = 11100 \text{ g mol}^{-1}$ ). Despite the formation of the high molecular weight aggregates for all polymers, several structures were unambiguously assigned (refer to Figure 21 and Appendix Table A5-Table A8).

### 3.1.2 Analyzing Nitroxide Containing Polymers by High Resolution Mass Spectrometry

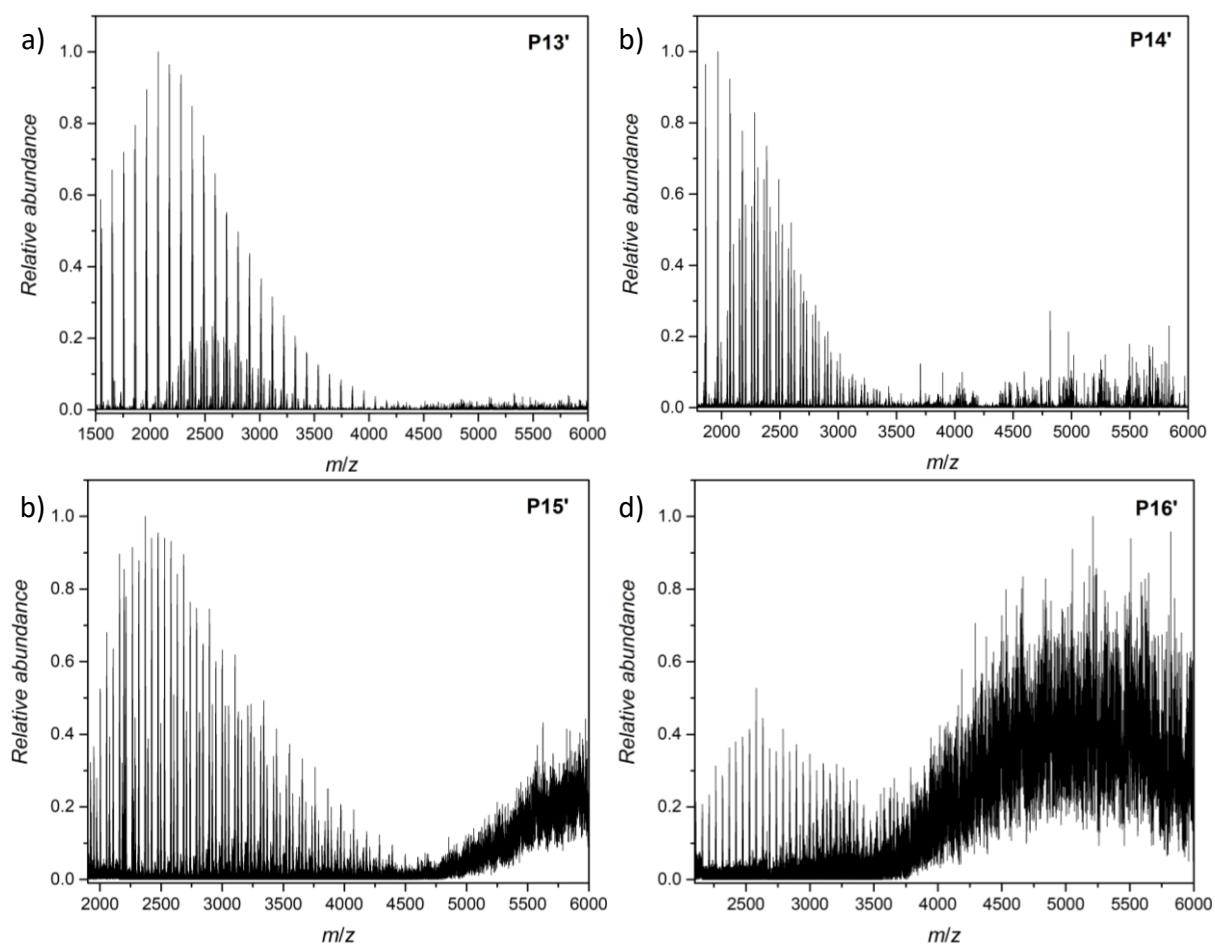


**Figure 20.** Overview ESI mass spectra of the nitroxide containing polymers **P13'**-**P16'** recorded in negative ion mode. (a) Overview ESI mass spectrum of **P13'** from  $m/z$  1500 to 6000, showing some minor high molecular weight species between  $m/z$  4000 to  $m/z$  6000. (b) Overview ESI Orbitrap mass spectrum of **P14'** from  $m/z$  1800 to 6000 with increasing ion abundance of higher molecular weight species compared to (a). (c) Overview ESI Orbitrap mass spectrum of **P15'** from  $m/z$  1900 to 6000, showing a significant increase of ion abundance of higher molecular weight species compared to (a) and (b). (d) Overview ESI Orbitrap mass spectrum of **P16'** from  $m/z$  1800 to 6000. Clusters detected in the mass range between  $m/z$  3500 and  $m/z$  6000 cannot be identified due to insufficient resolution. Such high-molecular weight species are out of range for higher-energy collision dissociation tandem MS experiments ( $<2500$   $m/z$ ). Adapted from ref [238] with permission of the Royal Society of Chemistry.

From Figure 21a-c) it can be seen that for the polymers **P13'**-**P16'** the mass spectrum consists of two species identified in the negative ion mode: (i) a singly-charged species, labelled with ● and (ii) the doubly-charged species that is labelled with ◆. The ESI MS spectrum of the polymer **P16'** that exhibits an increased molecular weight compared to **P13'**-**P15'**, indicates the formation of only doubly-charged species ionized in negative ion mode (labelled with ◆). The obtained isotopic patterns consist of several almost isobaric species, which possess an intact nitroxide radical. In Figure 22, the assignment of the ● labelled pattern of **P13'** at  $m/z$  2481 is depicted. Here, the singly-

### 3.1 Selective Point Folding

charged pattern consists of four species with different styrene:nitroxide ratios. First, there is the homopolymerized PS species that contains no incorporated nitroxide (labelled with ●). The detection of the non-functional PS probably arises from the low concentration of the copolymerized CMS monomer the reaction mixture. Further detected species display different styrene:nitroxide ratios, *i.e.* 18:1 (label ◆), 15:2 (label □) and 12:3 (label ■). The comparison of the radical grafting obtained by the different analytical methods are in good agreement. NMR suggests 9.3%, EPR 11.3% and mass spectrometry 13.3% (label □). In the doubly-charged isotopic pattern (label ◆) of **P13'**, no homopolymerized species are detected and thus only species featuring a free nitroxide radical are found (refer to Figure 23). The detected styrene:nitroxide is in the range of 39:0 to 27:6. The assignment for the isotopic patterns of **P14'**-**P16'** can be found in the Appendix (Figure 82-Figure 86 and Table A5-Table A8).

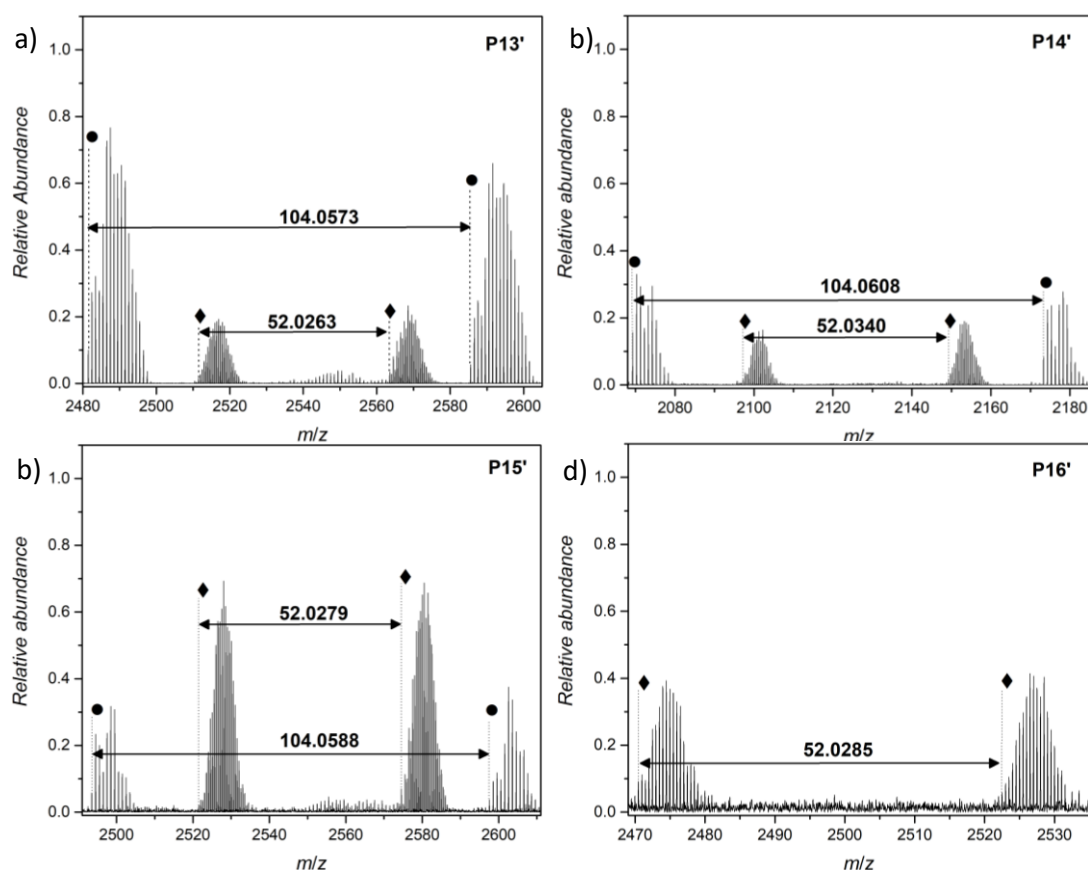


**Figure 21.** Expanded region of the ESI mass spectrum of **P13'**-**P16'** measured in negative ion mode. a) Expanded region of the ESI MS spectrum of polymer **P13'** between  $m/z$  2480 and 2605. b) Expanded region of the ESI mass spectrum of **P14'** recorded from  $m/z$  2068 to 2185. c) Expanded region of the ESI mass spectrum of **P15'** recorded from  $m/z$  2491 to 2611. d) Expanded region of the ESI mass spectrum of **P16'** recorded from  $m/z$  2469 to 2535. Adapted from ref [238] with permission of the Royal Society of Chemistry.

### 3.1.2 Analyzing Nitroxide Containing Polymers by High Resolution Mass Spectrometry

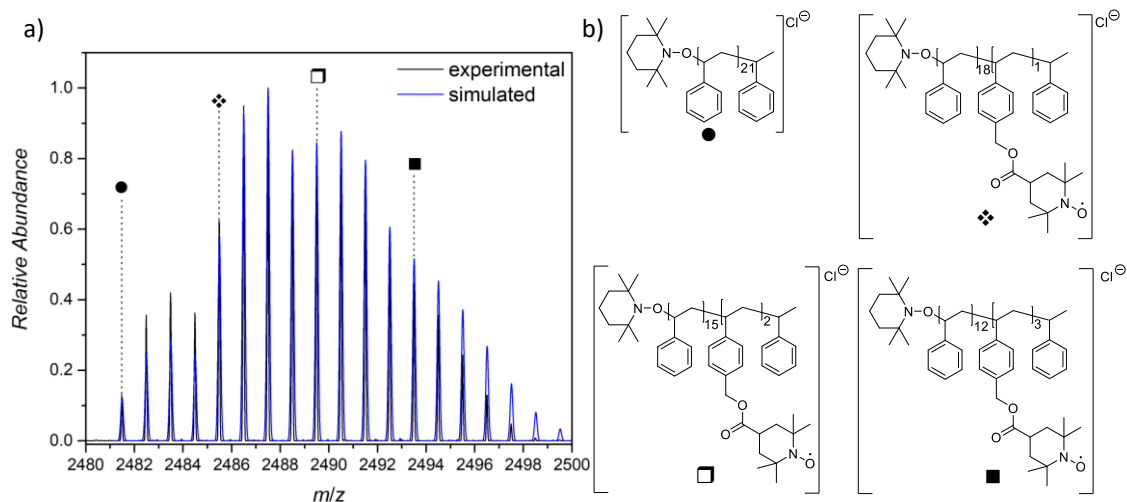


**Figure 22.** Isotopic pattern assignment of peak ● of **P13'**  $m/z$  2481. The most abundant species are labelled. The ratio for the polymeric species in (a) is 0.3 (label ●): 1.0 (label ❖): 0.7 (label □): 0.3 (label ■). Adapted from ref [238] with permission of the Royal Society of Chemistry.

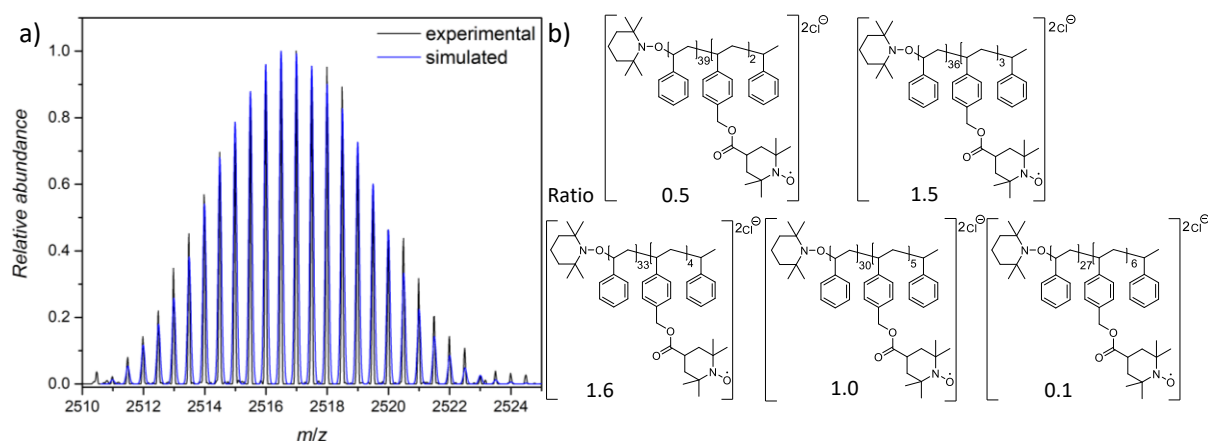


**Figure 23.** a) Isotopic simulation of a selected doubly charged pattern from  $m/z$  2510 to 2525 of **P13'** (◆) comparing the experiment (black line) with the simulation (grey line) b) Identified structures and their ratio within the pattern. Adapted from ref [238] with permission of the Royal Society of Chemistry.

In summary, the current section describes the synthesis of nitroxide containing polymers and a powerful characterization method for such polymers *via* high resolution ESI mass spectrometry. The analytical gap in the structural analysis of polymers that feature nitroxides was revealed by the mass analysis of **P10** (refer to previous Section 3.1.1) and after inspecting the literature with regard to the characterization of nitroxide containing polymers. Thus, the present section of the present dissertation closes this existing critical analytical gap and lies the analytical basis for the characterization of nitroxide containing SCNPs. Accordingly, polymers varying in amount of nitroxide

### 3.1 Selective Point Folding

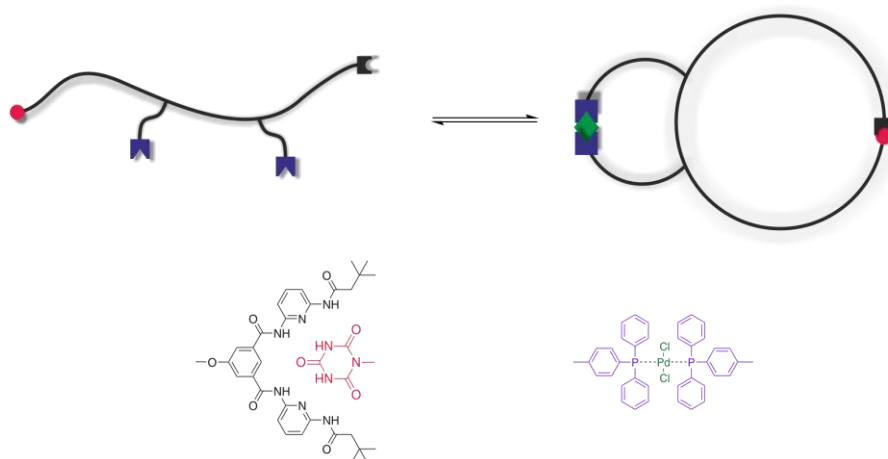
---

within the polymeric backbone in the range of 11.3 and 29.1 mol% as well as chain length ( $4800 \geq M_n/g \text{ mol}^{-1} \geq 11\ 100$ ) were synthesized. The subsequent ESI mass analysis unambiguously confirms the existence of nitroxide radicals along the polymeric backbone. Further, the mass spectra display an increasing amount of high molecular weight aggregates with increasing nitroxide content. In addition, a baseline drift is detected for samples with an amount of nitroxides close to 30 mol% and becomes even more pronounced with increasing molecular weight.



### 3.1.3 Metal Complexation and Hydrogen Bond Driven Single-Chain Folding

Natural macromolecules such as enzymes often contain metals that are directly linked to the protein.<sup>[56]</sup> Proteins in turn are internally stabilized by hydrogen bonds, aromatic stacking or hydrophobic interactions.<sup>[110,134]</sup> Taking inspiration from these concepts, the ensuing step is to combine two methodologies, in order to enhance the system complexity and to pursue the ultimate goal of preparing an artificial protein/enzyme step-by-step. In particular, the above presented concept of Hamilton Wedge and cyanuric acid (refer to Section 3.1.1) hydrogen bonding, is combined with the already established methodology of metal complexation to prepare an orthogonal dual folding system (refer to Scheme 22).<sup>[54,143]</sup> A well-defined polymer was prepared by ARGET ATRP using a cyanuric acid (CA) functional ATRP initiator and subsequently functionalized in multiple steps. The orthogonal recognition motifs were placed at preselected points along the polymeric chain to induce a well-defined collapse of the polymer, which is the characteristic feature of the selective point folding approach.



**Scheme 22.** Schematic illustration of the combination of the hydrogen bonding motif (HW/CA) and metal complexation to prepare dual compacted single-chain nanoparticles.

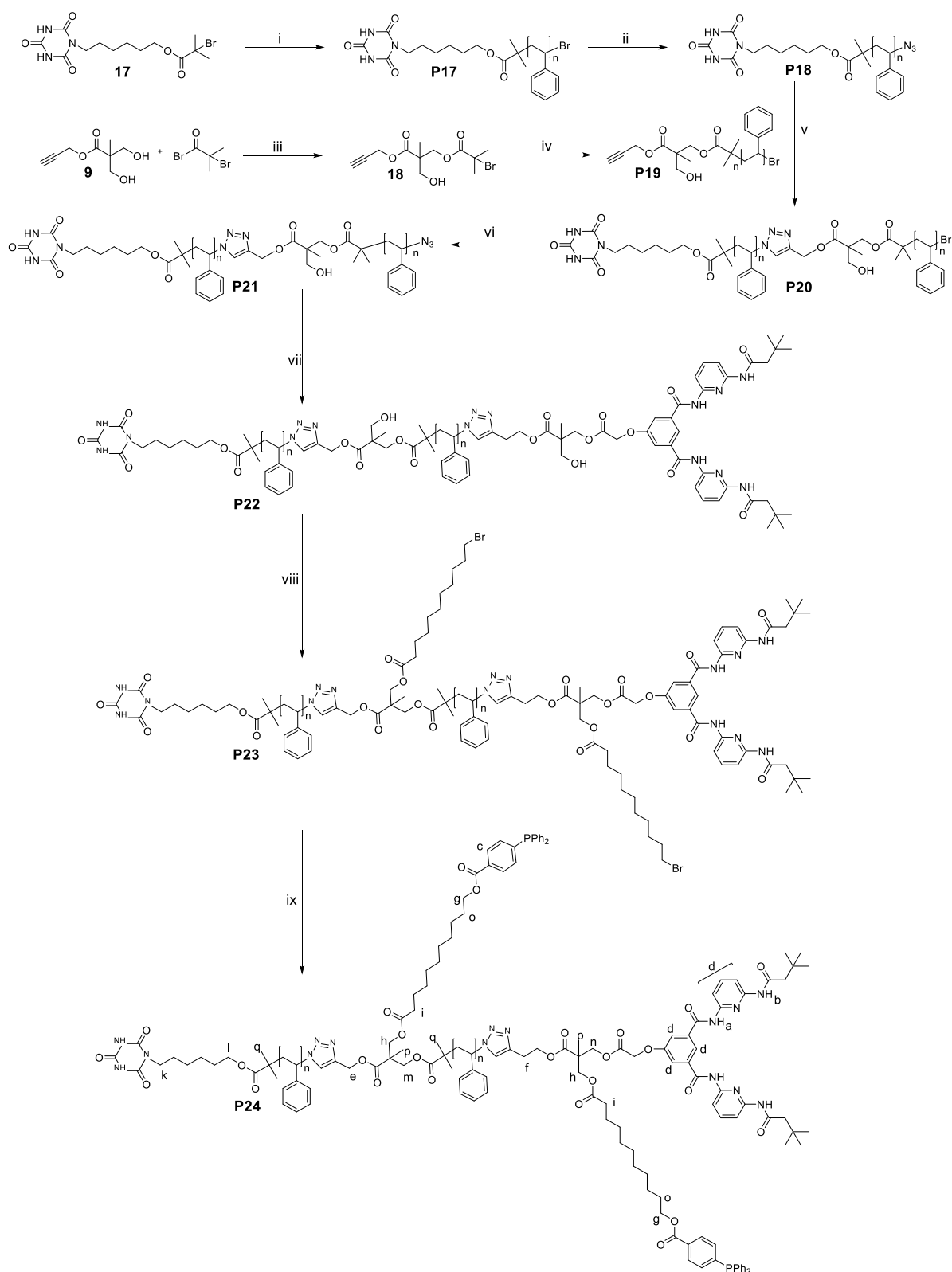
In the following section the preparation of the cyanuric acid functional ATRP polymerization initiator as well as the Hamilton Wedge functionality is not reiterated as it can be found in the previous Section 3.1.1. For the CA functional ATRP initiator **16** bromohexanol was used instead of 11-bromo undecanol and was prepared according to literature.<sup>[48]</sup> Synthetic details and the characterization of **16** are provided in the Experimental Section 5.3.1.

### Synthesis of the Multi-Functional Linear Precursor Polymers

The synthetic route for the polymer carrying the hydrogen bonding motifs – Hamilton Wedge (HW) and CA – as well as the phosphine for metal complexation presented in Scheme 23 has been designed. The CA/HW functionalities are tethered to the  $\alpha$ - and  $\omega$ -position, whereas the phosphines are attached at preselected points along the lateral polymer chain.

The cyanuric acid functional ATRP initiator **17** was utilized for the polymerization of styrene in an initial step to generate the linear precursor polymers that were modified step by step (refer to Scheme 23). The bromine end group of the synthesized polymers was modified to an azide functionality at the chain terminus. Both polymers display narrow molecular weight distributions in SEC (refer to Figure 24). Next to the CA functional polymer **P18**, a further polymer that incorporates an alkyne end group as well as a free hydroxyl functionality (**P19**) was prepared (refer to Experimental Section 5.3.2 for synthetic details) with the intention to be ligated to **P18** in the next step. The macromolecular characteristics for **P19** are a dispersity of 1.06 along with a molecular weight of 5900 Da. As mentioned above, the polymers **P18** and **P19** were grafted by employing CuI as catalyst and DIPEA as ligand in the CuAAC reaction. The <sup>1</sup>H NMR spectrum of **P20** (refer to Figure 25) shows the characteristic resonances at close to 5.1 ppm associated with the CH<sub>2</sub> next to the triazole as well as the CH of the triazole itself, suggesting the success of the grafting reaction. The resonance at 4.4 – 4.5 ppm is attributed to the CH-Br proton and suggests an intact bromine functionality in the newly obtained polymer **P20**. Next, the bromine functionality was directly substituted with the azide to prepare **P21**, which is accessible for a second CuAAC click reaction. The <sup>1</sup>H NMR spectrum provides evidence of the modification by the shift of the CH-Br

### 3.1.3 Metal Complexation and Hydrogen Bond Driven Single-Chain Folding



**Scheme 23.** Synthetic pathway for the synthesis of the multifunctional polymer **P24**. (i) styrene, CuBr<sub>2</sub>, Me<sub>6</sub>TREN, Sn(EH)<sub>2</sub>, anisole, 90 °C. (ii) NaN<sub>3</sub>, DMF, ambient temperature, 24 h. (iii) TEA, ambient temperature, 16 h. (iv) styrene, CuBr<sub>2</sub>, Me<sub>6</sub>TREN, Sn(EH)<sub>2</sub>, anisole, 90 °C (v) CuI, DIPEA, DMF, ambient temperature, 24 h, inert atmosphere. (vi) NaN<sub>3</sub>, DMF, ambient temperature, 24 h. (vii) **11**, CuSO<sub>4</sub>·5 H<sub>2</sub>O, sodium ascorbate, DMF, ambient temperature, 24 h. (viii) bromo-undecanoic acid, DCC, DMAP, DCM, ambient temperature, 72 h. (ix) 4-(diphenylphosphino)bezoic acid, K<sub>2</sub>CO<sub>3</sub>, DMF, 50 °C, 24 h.

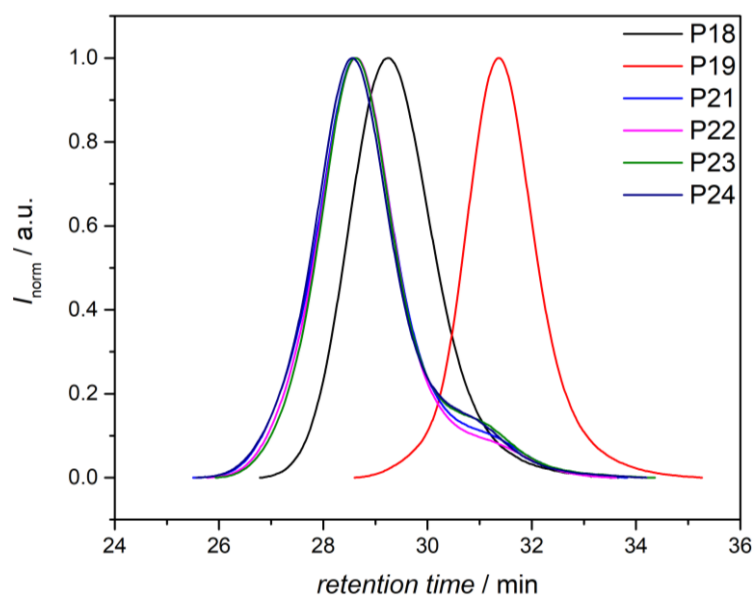


**Figure 24.** SEC chromatograms of the ATRP polymers (**P18-P24**) after the bromine-azide exchange (**P18**), the alkyne- and hydroxyl functional polymer **P19**, the azide functional polymer **P21**, the CA-HW functional polymer **P22** (which carries an additional two hydroxyl functionalities along the backbone), the polymer **P23** (with modified OH functionalities) and the final CA-phosphine-HW polymer **P24**. All samples were measured in THF (35 °C, using PS standards for calibration).

**Table 5.** Overview over the macromolecular characteristics for the polymer **P18-P24**, collating their molecular weights and dispersities obtained by THF SEC.

| ID         | $M_n / \text{g mol}^{-1}$ | $\mathcal{D}$ |
|------------|---------------------------|---------------|
| <b>P18</b> | 14800                     | 1.19          |
| <b>P19</b> | 6200                      | 1.12          |
| <b>P21</b> | 18100                     | 1.34          |
| <b>P22</b> | 18400                     | 1.30          |
| <b>P23</b> | 17200                     | 1.34          |
| <b>P24</b> | 19600                     | 1.32          |

### 3.1.3 Metal Complexation and Hydrogen Bond Driven Single-Chain Folding

---

resonance from 4.4–4.5 ppm to close to 3.9 ppm. In addition, the SEC chromatogram of **P21** depicts the modification of **P18** with the grafted alkyne polymer **P19**, visible in the shift to lower retention times, due to the larger hydrodynamic volume of **P20**. Furthermore, the SEC chromatogram illustrates an intact polymer distribution after the bromine-azide exchange of **P21** (refer to Figure 24), suggesting a narrow dispersity of the system. After the click reaction of **P18** and **P19**, the SEC chromatogram shows a small shoulder at lower retention times, which most probably originates from **P19**. Unfortunately, the shoulder could not be circumvented by alternative synthetic protocols or purification procedures. Neither dialysis nor adding an azide functional resin could remove the species at lower retention times.

The subsequent post-polymerization modification was carried out by CuAAC of **P21** with the alkyne functional HW moiety **11**. Here, the copper click reaction using copper sulfate was selected, due to the fact that a 1,2,3 triazolium quaternization is likely to occur.<sup>[247–249]</sup> By employing  $\text{CuSO}_4 \times 5\text{H}_2\text{O}$ /sodium ascorbate as catalytic system, the CuAAC reaction was confirmed *via*  $^1\text{H}$  NMR spectroscopy. In the  $^1\text{H}$  NMR spectrum of **P22**, the resonances at 9.9 and 9.3 ppm (refer to Figure 25), are indicative for the hydrogen bond interaction between the cyanuric acid moiety and the HW functionality, although at this stage the interaction most probably is intermolecular, due to the higher concentration compared to SCNP folding concentrations of close to  $1 \text{ mg mL}^{-1}$ . In addition, the aromatic HW protons in the range of 7.7 to 8.2 ppm are present, underpinning the modification reaction of the polymer. Furthermore, the SEC trace of **P22** features the same shape as the precursor polymer **P21**, with a slightly increased molecular weight, indicating the ligation of the HW moiety to the polymer. The shift towards lower molecular weights is probably due to the shoulder that increases partly after the reaction and influences the resulting  $M_n$  obtained by SEC. The penultimate modification is the esterification of the free hydroxyl functionalities with bromoundecanoic acid to yield **P23**. The small aliphatic molecule was added to insert a spacer between the polymeric backbone and the phosphine that is attached in the next step to reduce the steric hindrance as well as make the phosphine more flexible in case of the intramolecular collapse upon metal complexation. Finally, the phosphine was attached in a final modification to reduce the probability of oxidization of the phosphine to the phosphine oxide. The phosphine was attached by esterification using potassium carbonate at elevated temperatures. Formation of **P24** featuring the free phosphine was confirmed by SEC,  $^1\text{H}$  and  $^{31}\text{P}\{\text{H}\}$  NMR spectroscopy. The phosphine

NMR spectrum depicts a single resonance at -5.2 ppm, which is associated with the free phosphine, whereas the oxidized phosphine would yield a resonance around 30 ppm. The SEC trace of **P24** is shifted to higher molecular weights, illustrating the same shape as the previous polymers **P20-P23**, alongside with a reasonable narrow dispersity. The  $^1\text{H}$  NMR spectrum (refer to Figure 25) shows the characteristic CA-HW protons at 9.8 and 9.4 ppm, labelled with **a** and **b**, respectively, indicating the interaction of the folding motifs and indicating that the functionalities are attached to the polymer and are intact. In the aromatic region of the NMR spectrum of **P24** between 7.5 and 8.5 ppm, the aromatic protons of the HW as well as the aromatic resonances from the phenyl rings of the triarylphosphine are found, indicating the attachment of the phosphine to the polymer.

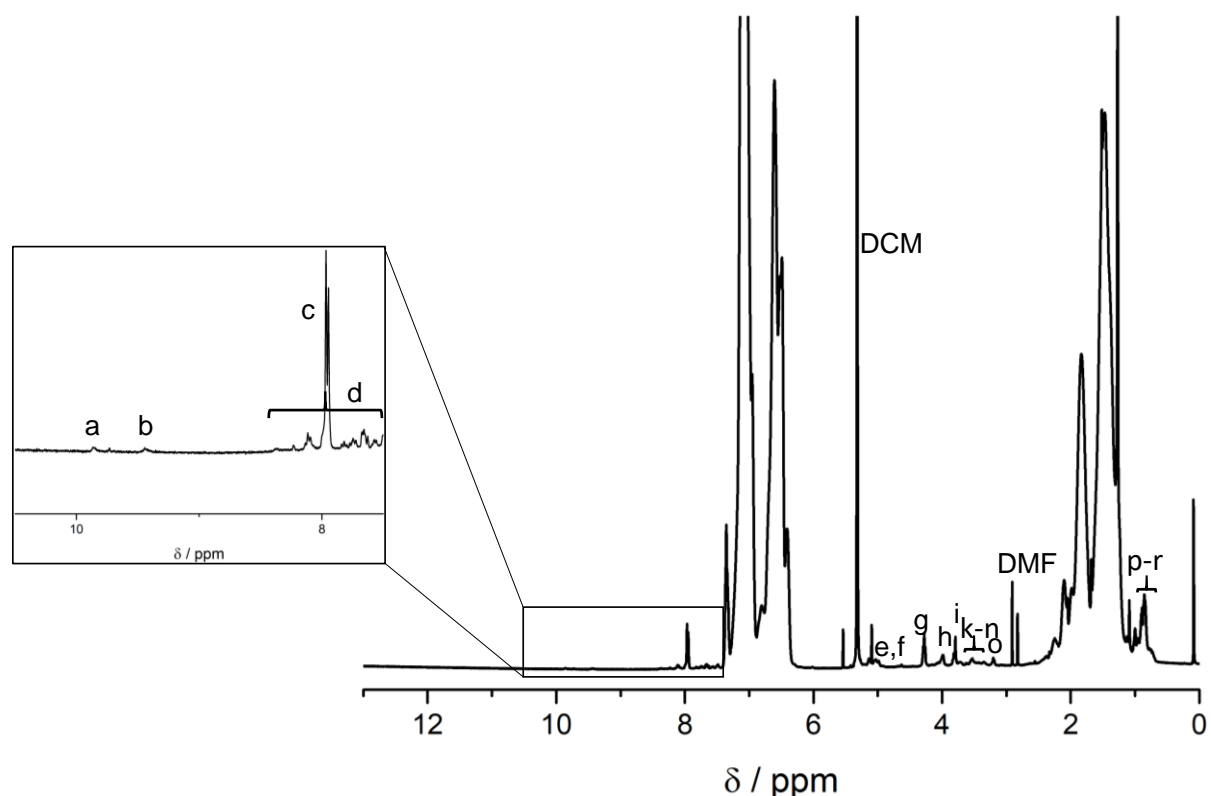
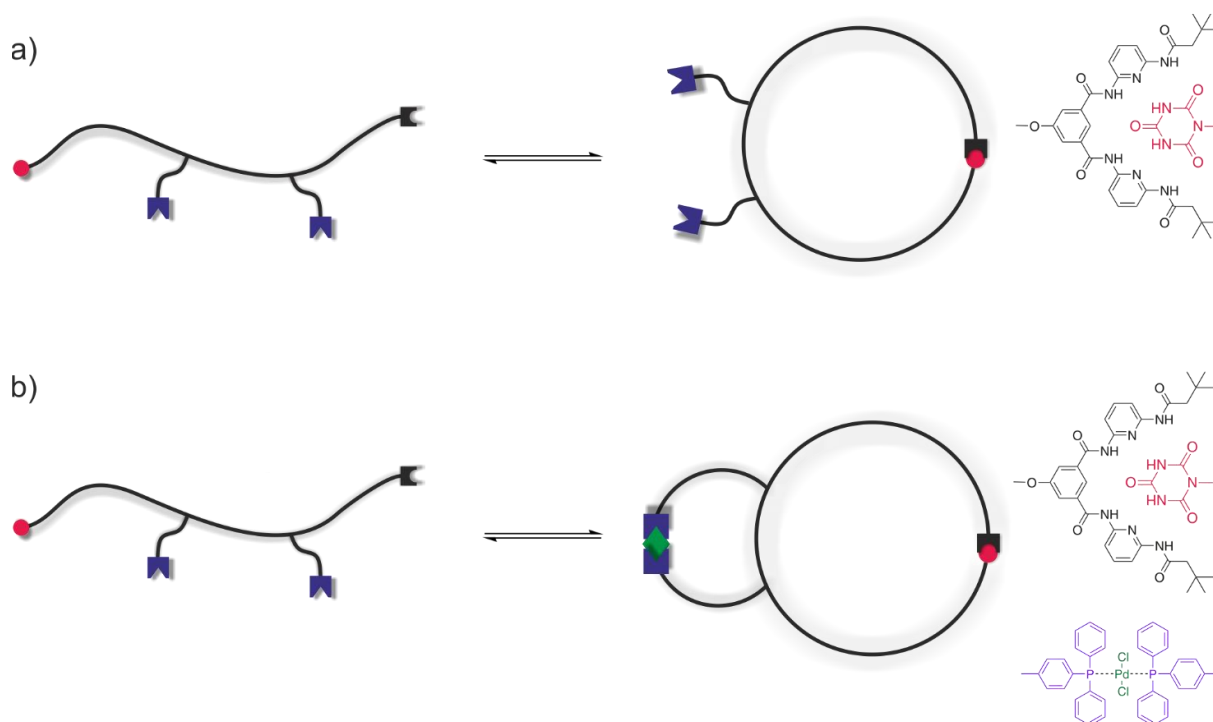


**Figure 25.**  $^1\text{H}$  NMR spectrum of **P24**, measured in  $\text{DCM-d}_2$  and 298 K. The resonance assignments can be found in Scheme 23.

### Dual Compaction of Single Polymer Chains

After the synthesis of polymer **P24**, featuring the CA and HW recognition motifs in  $\alpha$ - and  $\omega$ -position as well as the phosphines at preselected points along the polymeric backbone, some initial attempts for the single-chain folding were performed.

The folding of **P24** is induced both by the formation of the hydrogen bonds between the HW and the CA moiety and the addition of the palladium (II) salt complexing the two triphenylphosphine units (refer to Scheme 24). In case the palladium complex is absent, only the hydrogen bond formation is expected under high dilution conditions.



**Scheme 24.** Schematic illustration of the single-chain collapse induced by a) the hydrogen bonding motif HW/CA and b) the dual compaction after metal complexation and hydrogen bonds.

Second, if the Pd compound is added, both the HW-CA and the metal complexation occur. To induce metal complexation, the dissolved polymer in degassed DCM was slowly added *via* a syringe pump with a flow rate of 1 mL h<sup>-1</sup>, in order to prevent intermolecular crosslinking. In addition, the collapse was conducted under highly diluted conditions ( $4.6 \times 10^{-5}$  M). The resulting Pd-SCNPs were subjected to SEC analysis (refer to Figure 26). The SEC chromatogram shows the anticipated shift

towards higher retention times, although a broadening upon Pd complexation is observed. Here, the polydispersity increases from 1.33 to 1.49, whereas the molecular weight decreases by close to 3000 Da from 19600 Da to 16400 Da, resulting in a decrease of 16.3%.

Information about the dynamic nature of the SCNPs based on hydrogen bonds as well as the combination of hydrogen bonds and metal complexation, were obtained by dynamic light scattering (refer to Figure 27). The DLS measurements were performed in DCM at the concentration of  $1 \text{ mg mL}^{-1}$  to ensure that the intramolecular collapse regime is reached. The DLS measurements\* (refer to Figure 27) underpin the successful folding. Particularly, after the addition of  $10 \text{ }\mu\text{L}$  methanol the hydrogen bonds of the HW/CA pair are disrupted. The disruption leads to an increase of the hydrodynamic diameter from 7.6 nm from the folded state to 8.6 nm for the unfolded polymer **P24** (refer to Table 6).

In comparison to the SCNP that only contains hydrogen bonds, the dual folded Pd-SCNP displays the expected smaller hydrodynamic diameter  $D_h$  of 5.6 nm – compared to 7.6 nm of the H-bond SCNP – upon the dual compaction of the single polymer chain (refer to Table 6).

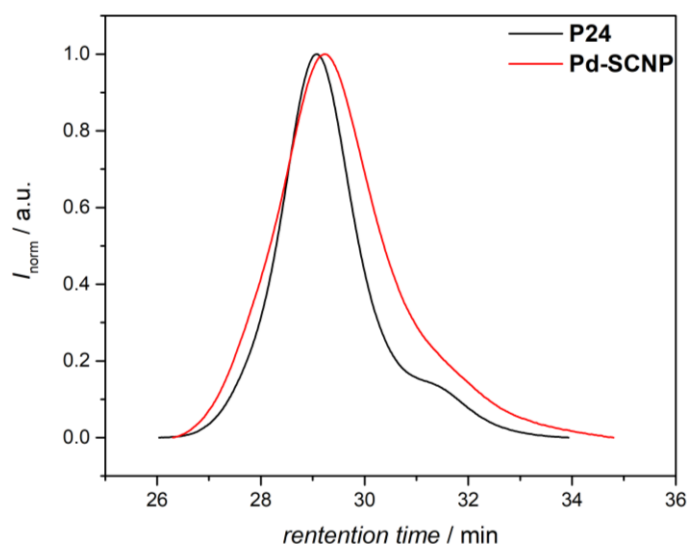


**Figure 26.** SEC traces of the unfolded precursor polymer **P24** and the SCNP upon metal complexation (Pd-SCNP) using  $[\text{Pd}(\text{COD})\text{Cl}_2]$  as metal complex, measured in THF ( $35 \text{ }^\circ\text{C}$ ,  $1 \text{ mL min}^{-1}$ , using PS standards for calibration).

\*DLS measurements were performed by Dr. Hatice Mutlu (KIT). The primary DLS data can be found in the Appendix, Section C).



### 3.1.3 Metal Complexation and Hydrogen Bond Driven Single-Chain Folding

---

After the addition of 10  $\mu\text{L}$  MeOH to the dual folded Pd-SCNP, the  $D_h$  increases to 7.9 nm, which is approximately the size of the mono-folded SCNP by hydrogen bonds, which displays a DLS derived  $D_h$  of 7.6 nm. These results are congruent with the expectation that the dual-folded Pd-SCNP is smaller than the mono-folded analogue. Disrupting the hydrogen bonds in the Pd-SCNP leads to an increase in hydrodynamic size, with a resulting diameter of 7.9 nm, which is close to the size of the only H-bonded SCNP, while still being smaller than the parent polymer **P24** with a hydrodynamic diameter of 8.6 nm obtained by DLS. The light scattering results for the SCNP featuring the H-bonds as well as the dual compacted Pd-SCNP that is collapsed by H-bonds and metal complexation, are in agreement with DOSY measurements. Both analytical methods reveal an increase of the diameter after the addition of MeOH to disrupt the hydrogen bonds (refer to Table 6). For the system that is collapsed by only the hydrogen bonds, an increase from 6.6 to 10.2 nm is observed, when the hydrogen bonds are disrupted. The DOSY<sup>§</sup> derived  $D_h$  for the Pd-SCNP that contains the metal complex as well as the H-bonds the diameter decreases to 3.5 nm (compared to 6.6 nm for the mono-folded analogue). After addition of MeOH to cleave the H-bonds in the Pd-SCNP, the diameter increases from 3.5 to 11.6 nm. Thus, DLS and DOSY measurements are congruent and display the expected smaller hydrodynamic volume of the dual compacted SCNP relative to the mono-folded SCNP that only features the hydrogen bonds. Generally, DOSY measurements indicate a more pronounced shift towards higher diameters (6.6 nm to 10.2 nm for the mono-folded SCNP and 3.5 nm to 11.2 nm for the dual-folded SCNP) and the diameter of the open chain is slightly larger compared to the DLS obtained diameter, *i.e.* 8.6 nm obtained by DLS compared to 10.2 nm from DOSY measurements for the mono-collapsed SCNP and 7.9 nm (DLS) compared to 11.2 nm (DOSY) for the dual-folded SCNP.

---

<sup>§</sup> DOSY measurements were performed by S. Spann (AK Luy, KIT). The primary DOSY data can be found in the Appendix, Section C.

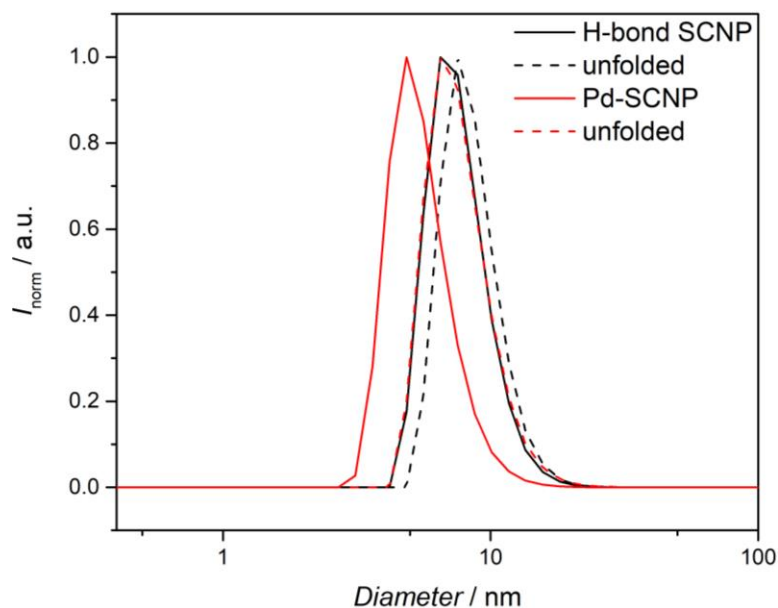


**Figure 27.** Dynamic light scattering (DLS) measurements of the folded precursor polymer **P24** by hydrogen bond formation (black line), the unfolded H-bond SCNP upon MeOH addition (10  $\mu$ L) yielding the parent polymer **P24** (black dotted line) as well as the dual folded Pd-SCNP folded by Pd complexation and hydrogen bonds (red line) and the disruption of the H-bonds in the dual folded Pd-SCNP (red dotted line) by addition of MeOH (10  $\mu$ L).

**Table 6.** Characterization data of the linear precursor polymer **P24**, the folded SCNP displaying only hydrogen bonding and the dual compacted Pd-SCNP, which additionally features the H-bonds.

| ID                                    | $M_n^a / \text{g mol}^{-1}$ | $\bar{D}^a$ | $D_{h,DLS}^b / \text{nm}$ | $D_{h,DOSY}^c / \text{nm}$ |
|---------------------------------------|-----------------------------|-------------|---------------------------|----------------------------|
| <b>P24</b>                            | 19600                       | 1.30        | -                         | -                          |
| <b>H-bond SCNP</b>                    | -                           | -           | 7.6                       | 6.6                        |
| <b>H-bond SCNP<sub>unfolded</sub></b> | -                           | -           | 8.6                       | 10.2                       |
| <b>Pd-SCNP</b>                        | 16400                       | 1.49        | 5.6                       | 3.5                        |
| <b>Pd-SCNP<sub>unfolded</sub></b>     | -                           | -           | 7.9                       | 11.6                       |

<sup>a</sup> Determined by SEC (35  $^{\circ}$ C, 1 mL  $\text{min}^{-1}$ ) using PS standards for calibration. <sup>b</sup> Determined by DLS. <sup>c</sup> Calculated hydrodynamic diameters from DOSY measurements using the Stokes-Einstein equation.

### 3.1.3 Metal Complexation and Hydrogen Bond Driven Single-Chain Folding

Moreover,  $^1\text{H}$  and  $^{31}\text{P}$  NMR underpin the Pd complexation. In the  $^1\text{H}$  NMR spectrum (refer to Figure 28), the aromatic region between approximately 7.5 and 8.5 ppm displays a broadening of the aromatic resonances adjacent to the phosphorous atom, which is attributed to the metal complexation. In addition, the HW/CA NH resonances split, which may be attributed to the formation of cis/trans metal complexes. The  $^{31}\text{P}$  spectrum shows a shift of the phosphorous resonance from -5.2 ppm to close to 29.1 ppm (refer to Figure 29). The resonance at 32.5 ppm is attributed to the oxidized  $\text{Ph}_3\text{P}=\text{O}$  species. The low resolution of the  $^{31}\text{P}$  NMR spectrum for the Pd-SCNP is attributed to (i) the low concentration of the solution, to ensure the single-chain folding regime for the hydrogen bonding system and (ii) the overall low number of P atoms per chain. Since the polymer was designed *via* the selective point folding avenue only two phosphorous atoms are tethered to one polymeric backbone. In the  $^1\text{H}$  NMR spectrum, the aromatic region between 8.5-7.5 ppm displays a splitting and broadening of the phosphine resonances **c**, indicating the formation of the metal complex, which is in agreement with previous studies using Pd (II) salts for complexation.<sup>[54,143]</sup> Furthermore, the NH protons of the HW moiety between 9-10 ppm are split up in multiple resonances, which is attributed to cis/trans isomers of the metal complex of the SCNP after the metal complexation.

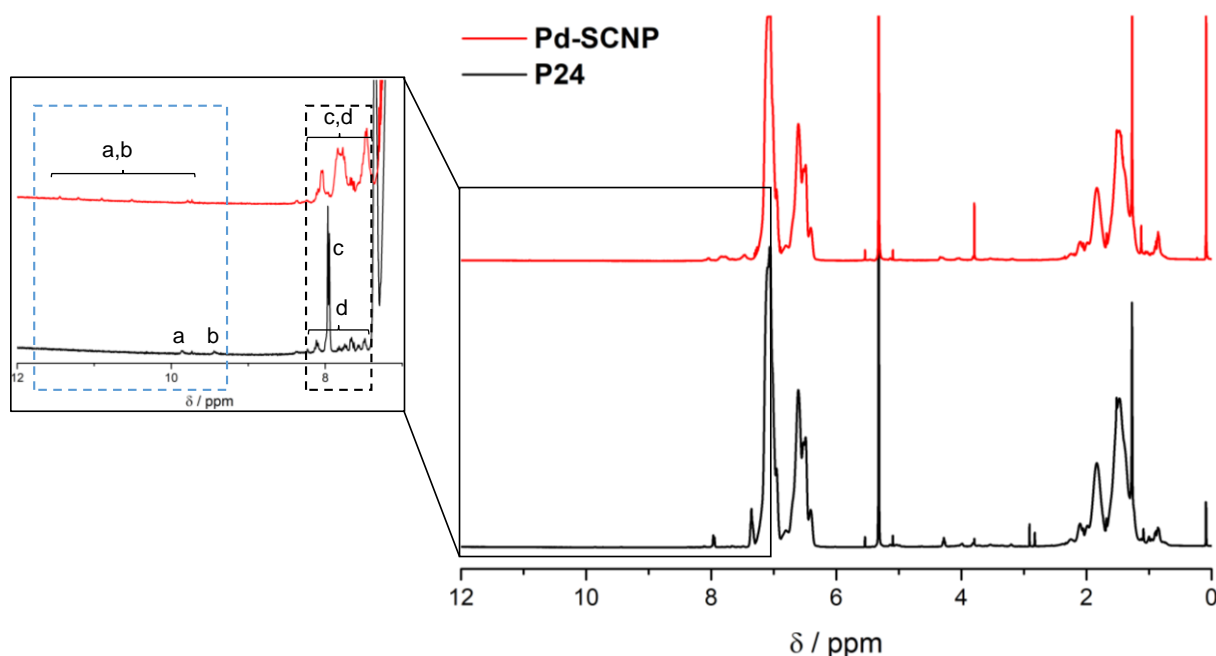


**Figure 28.**  $^1\text{H}$  NMR spectrum of the precursor polymer **P24** and the dual folded Pd-SCNP, measured in  $\text{DCM}-d_2$  (298 K). The full assignments of the resonances is provided in Figure 25 and the structural assignments Scheme 23.

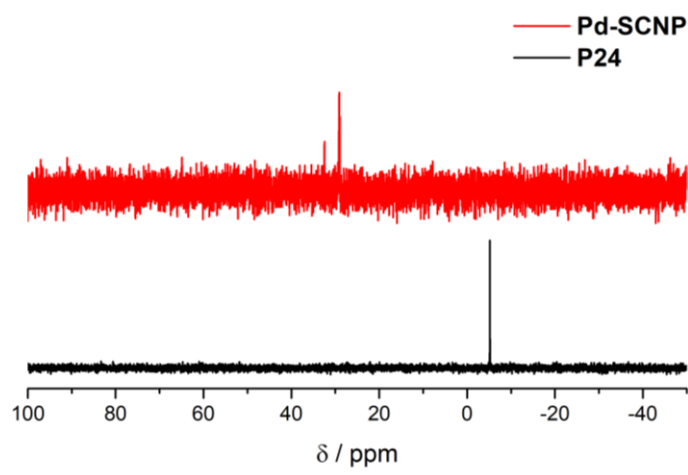


**Figure 29.**  $^{31}\text{P}\{^1\text{H}\}$  NMR spectrum of the dual folded Pd-SCNP and the precursor polymer **P25**, measured in  $\text{DCM-}d_2$  (298 K).

In summary, the present section described the synthesis of a multifunctional polymer based on a polystyrene backbone. The HW/CA recognition motif was tethered to the chain termini, while the triphenylphosphine units for metal complexation were attached at preselected points along the polymeric backbone in post-polymerization modifications. Single-chain nanoparticles featuring six hydrogen bonds of the HW/CA interaction were obtained in high dilution ( $1 \text{ mg mL}^{-1}$ ). The dual-folded SCNP was obtained by first inducing the collapse upon addition of a Pd (II) salt and subsequently establishing the hydrogen bonds in high dilution ( $1 \text{ mg mL}^{-1}$ ). The orthogonal interaction was followed by DLS and DOSY measurements. Both analytical methods display a lower hydrodynamic diameter for the dual-folded SCNP compared to the SCNP that only contains the hydrogen bonds for folding. In addition,  $^{31}\text{P}$  NMR spectroscopy as well as SEC measurements suggest the formation of a dual-folded SCNP, which results in the characteristic shift in the  $^{31}\text{P}$  NMR spectrum and the SEC chromatogram, respectively. Hence, the next step in the synthesis of enhanced SCNP systems was taken to prepare higher ordered nanoparticles combining different folding methodologies such as hydrogen bonding and metal complexation that also occur in nature to stabilize its naturally occurring proteins and enzymes.

### 3.2 The Repeat Unit Approach

As stated in Section 2.3 and 2.4, nature uses a plethora of ways and motifs to stabilize its formed architectures that fold dynamically. There also exists a wide variety of studies presenting different groups and functionalities that induce single-chain nanoparticles (SCNPs), whereas only a few examples are reported for the synthesis of SCNPs that fuse several functionalities to prepare dual- and dynamically folded architectures.<sup>[108,110,141,250]</sup> Within the current section, the non-covalent interaction of hydrogen bonds of the Hamilton Wedge (HW)/cyanuric acid (CA) moiety is fused with a host-guest system consisting of benzo-21-crown-7 (host) and a secondary ammonium salt (guest). The methodologies are combined to prepare a dual-folded system that is unfolded dynamically through the addition of different chemical trigger signals. The orthogonal interaction during the folding and unfolding represents a step towards finely controlling the folding state. Further, the relatively new area of light induced collapse in the field SCNPs is addressed by the preparation of a self-reporting refoldable system. The current status (folded vs unfolded) of the system can be read out by fluorescence. The SCNPs show fluorescence, while the open linear chain does not fluoresce. Compared to the dynamic SCNPs structures presented in Section 3.1, the single-chain polymeric nanoparticles synthesized employing the repeat unit approach are less well-defined due to the statistical interaction of the folding motifs. However, one of the advantage of the repeat unit approach is that it is synthetically less demanding and hence dominant in literature. The current chapter discusses the methodologies pioneered within this thesis for the generation of non-covalent and dynamic covalent crosslinks into dynamically switchable SCNP systems.

The first section presents a dynamic dual folding single-chain nanoparticle, where the hydrogen bonding system, (*i.e.* HW/CA presented in Section 3.1) is combined with the host-guest system consisting of the benzo-21-crown-7 (host) and secondary ammonium salt (guest) moieties. The orthogonal folding and unfolding was followed by nuclear magnetic resonance (NMR), dynamic light scattering (DLS) and diffusion ordered (DOSY) NMR spectroscopy. Folding is induced by UV-light triggered crosslinking of nitroxide (4-carboxy TEMPO) units, attached to a polymeric backbone

with a bifunctional linker featuring the 2-hydroxy-1-(4-(2-hydroxyethoxy)phenyl)-2-methylpropan-1-one (Irgacure 2959). Critically, the collapsed SCNPs display inherent fluorescence and thus the intramolecularly folded single-chain nanoparticles are self-reporting, whereas the fluorescence in the unfolded linear chain is spin-silenced by the presence of the nitroxide radical. The present system thus introduces a SCNP system where the folding state is self-reporting by fluorescence read out. All the folded and unfolded states were characterized by NMR, DLS and DOSY as well as fluorescence and electron paramagnetic resonance (EPR) spectroscopy. Both employed dynamic folding strategies are schematically illustrated in Figure 30.

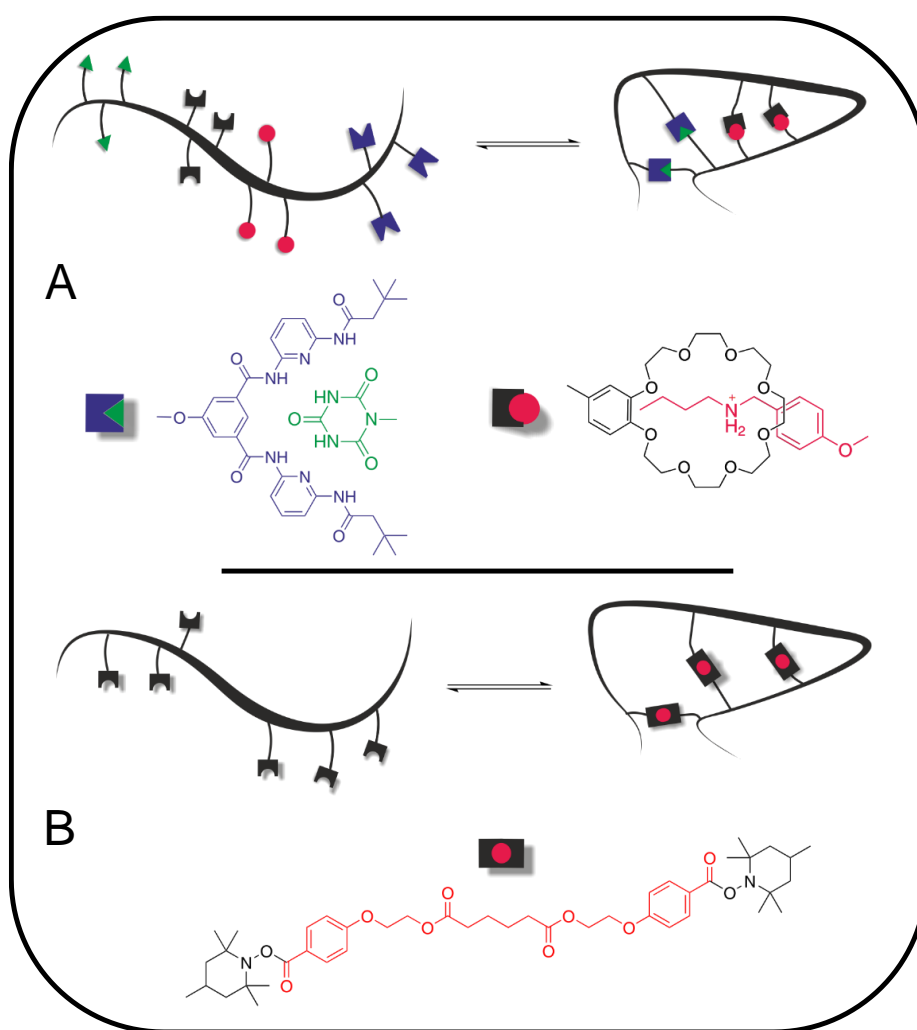


**Figure 30.** Schematic illustration of the repeat unit folding protocols for the preparation of dynamically folded/unfolded SCNPs presented in the current section. A) The single polymer chains are folded *via* a hydrogen bonding (Hamilton Wedge/Cyanuric Acid) and host-guest system (benzo-21-crown-7 (host and secondary ammonium salt (guest)) system. B) The UV-light triggered crosslinking reaction between a nitroxide and the photochemically generated radicals derived from the Irgacure 2959 moiety.

### 3.2.1 Reversible Dual Folding Driven by Hydrogen Bonds and Host-Guest Chemistry

Natural biomolecules reversibly fold by means of hydrogen bonds, aromatic stacking, host-guest chemistry, metal complexation or hydrophobic interactions. Inspired by nature, the current section describes the fusion of the hydrogen bonding motifs Hamilton Wedge (HW) and cyanuric acid (CA) and a host-guest system consisting of a benzo-21-crown-7 (B21C7, host) and a secondary ammonium salt (AS, guest). In order to mimic the dynamic folding/unfolding features of natural macromolecules such as proteins, the orthogonal unfolding is accomplished by the addition of different chemical stimuli. Accordingly, AB-type diblock and ABCD-type tetrablock copolymers were prepared by reversible addition fragmentation chain transfer (RAFT) polymerization and functionalized in post-polymerization modifications with the respective recognition units.\* In a proof of principle study, the host-guest system B21C7 (host) and AS (guest), was adopted from supramacromolecular chemistry and successfully transferred into the field of single-chain folding by proving the single-chain collapse of the B21C7 and AS functionalized diblock copolymer. Next, the host-guest chemistry was combined with hydrogen bonding interactions to orthogonally interact and stabilize the dual folded single-chain nanoparticles (SCNPs) enhancing the system complexity in order to mimic natural proteins and close the gap between synthetic protocols and nature step-by-step. Therefore, the HW and CA moieties were attached to the outer blocks A and D of the tetrablock copolymer and the B21C7 and AS moieties were grafted to the blocks B and C, respectively. Subsequently, dual compaction was conducted in highly diluted regimes.

---

\*Parts of the current section are reproduced or adapted from T. S. Fischer, D. Schulze-Sünninghausen, B. Luy, O. Altintas and C. Barner-Kowollik, *Angew. Chem. Int. Ed.* **2016**, *55*, 11276-11280. with permission from Wiley-VCH. D. Schulze-Sünninghausen performed the DOSY measurements, O. Altintas provided the RAFT-agent and the TMS-protected alkyne functional MMA based monomer and the TMS protected hydroxyl functional monomer. B. Luy contributed to scientific discussion. O. Altintas and C. Barner-Kowollik motivated and supervised the project as well as contributed to scientific discussions.

Importantly, the unfolding of the SCNPs is induced by external trigger signals to disrupt the respective stabilizing interactions and hence unfold the nanoparticles orthogonally and pathway independent. Both the folding and unfolding of the SCNPS was investigated by  $^1\text{H}$  NMR and diffusion ordered spectroscopy as well as dynamic light scattering.

### Small Molecule Synthesis

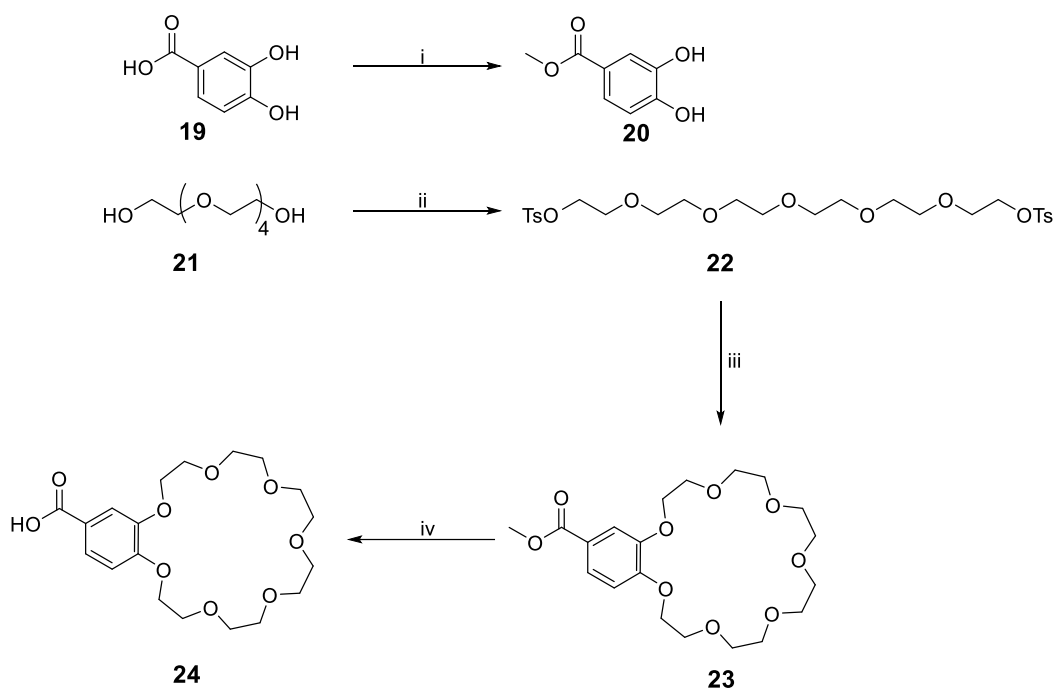
The collapse of the dual folding system is induced by the hydrogen bonding pair Hamilton Wedge and cyanuric acid as well as the B21C7 and AS host-guest complex. Those functionalities were prepared as small molecules and subsequently attached to the polymeric backbone in post-polymerization modifications. The HW moiety was grafted to the polymer in an etherification reaction, the CA functionality was attached by esterification and the B21C7 and AS moieties were clicked orthogonally to the polymer by CuAAC. The preparation of the HW moiety (**6**) featuring a hydroxyl functionality that can be linked to the polymer by etherification has been described in Section 3.1 and will not be discussed in the current chapter again.

The small molecule functionalities such as the CA moiety, azide functional B21C7, the azide functional ammonium salt moiety, the bromine functional monomer **M1**, the TIPS protected alkyne functional monomer **M2** and the functionalized ABCD-type tetrablock copolymer (**P31**) were previously synthesized (refer to the candidate's master thesis).<sup>[251]</sup> The AB-type diblock copolymer as well as the acid functional B21C7 and the azide functional ammonium salt will be discussed in the following section.

For the host-guest system, the benzo-21-crown-7 compound has been prepared featuring an acid functionality, able to undergo a nucleophilic substitution reaction in order to graft the B21C7 host to the polymeric backbone of the AB-type diblock copolymer. The crown ether moiety was synthesized in four steps (refer to Scheme 25). Initially, the acid functionality of dihydroxybenzoic acid (**19**) was protected *via* esterification with MeOH. The methyl protected compound **20** was subsequently reacted with the tosylated hexaethylene glycole **22** to form the protected benzo-21-crown-7 species **23**.



### 3.2.1 Reversible Dual Folding Driven by Hydrogen Bonds and Host-Guest Chemistry



**Scheme 25.** Synthetic route towards the B21C7 moiety **24**. (i) MeOH, H<sub>2</sub>SO<sub>4</sub>, reflux, 16 h. (ii) tosyl chloride, 16M KOH/H<sub>2</sub>O, THF, ambient temperature, 16 h. (iii) **20**, acetonitrile, reflux, 18 h. (iv) 1.2 M NaOH, THF/MeOH (2:1 v/v), ambient temperature, 5 h. Adapted from ref [252] with permission from Wiley-VCH. © 2016 WILEY-VCH Verlag GmbH & Co. KGaA, Weinheim.

The crown ether formation was confirmed by <sup>1</sup>H NMR spectroscopy by the characteristic shift from 4.16 to 4.19 ppm of the first and the last CH<sub>2</sub> resonances of **22** upon ring formation. Moreover, the aromatic protons of the tosyl groups at 7.33 and 7.79 ppm vanish and thus indicate the formation of the crown ether **23**. After deprotection of **23** using 1.2 M NaOH in a mixture of THF/MeOH (2:1 v/v), the targeted acid functional crown ether **24** was obtained. The identity of compound **24** was confirmed by <sup>1</sup>H and <sup>13</sup>C NMR spectroscopy (refer to Figure 31). The preparation protocols of all compounds and confirmation of all intermediate structures by <sup>1</sup>H NMR as well as the assignment can be found in the Experimental Section 5.3.1.

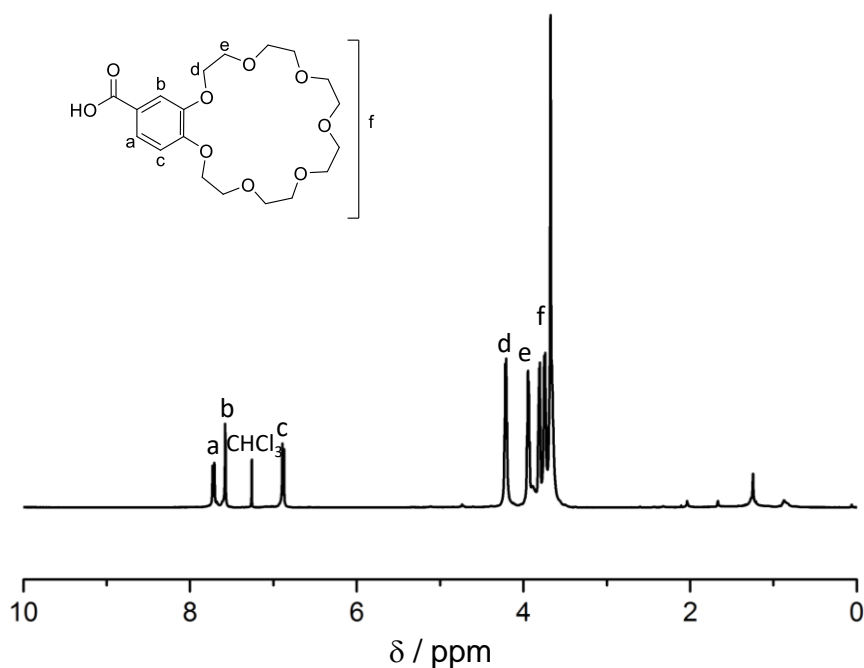
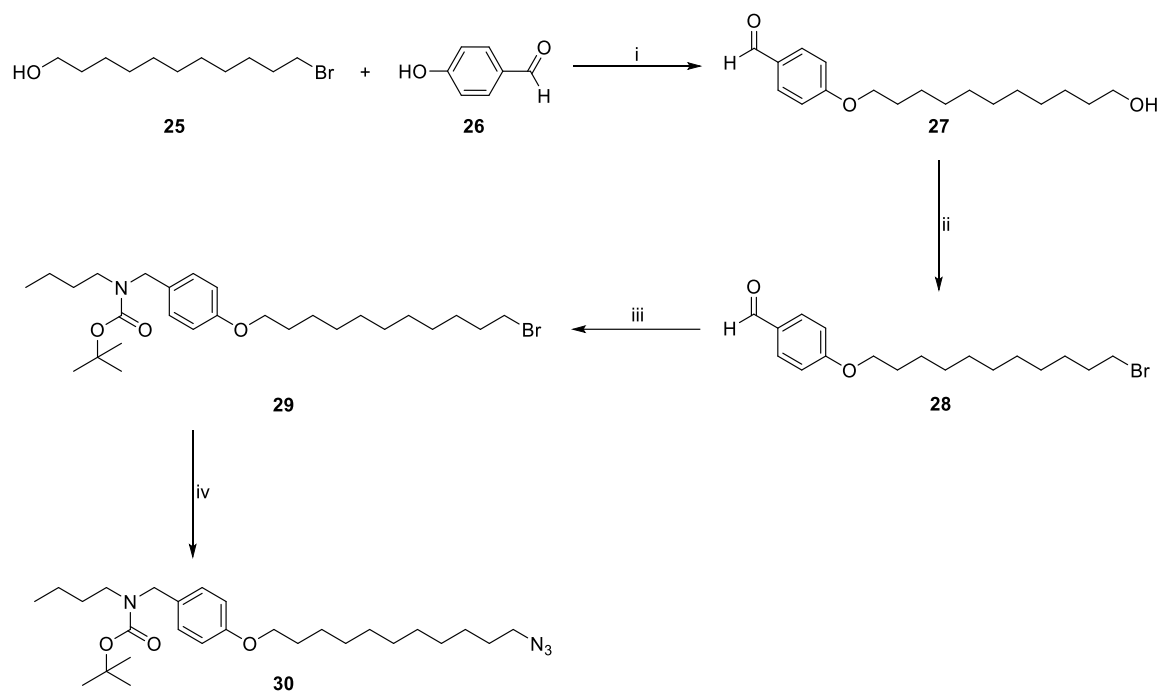


**Figure 31.**  $^1\text{H}$  NMR spectrum of the azide functional B21C7 moiety **24**, measured in  $\text{CDCl}_3$  (298 K). Reproduced from ref [252] with permission from Wiley-VCH. © 2016 WILEY-VCH Verlag GmbH & Co. KGaA, Weinheim.

Next, the corresponding functionality to the crown ether host – the secondary ammonium salt (guest) – was prepared in a four step synthesis (refer to Scheme 26). Initially, compound **27** was prepared by etherification of 11-bromoundecanol (**25**) and 4-hydroxybenzaldehyde (**26**). The hydroxyl functionality of **27** was exchanged by a bromine functionality in an Appel reaction to afford compound **28**. Subsequently, the aldehyde was simultaneously aminated and protected to the *tert*-butyloxycarbonyl (boc) ammonium salt analogue **29**. Further, the bromine functionality was converted to an azide in a nucleophilic substitution reaction to obtain the final secondary ammonium salt (AS) moiety **30**. The formation of the AS moiety was evidenced by both  $^1\text{H}$  NMR spectroscopy and high resolution mass spectrometry (refer to Figure 32 and Figure 33).

### 3.2.1 Reversible Dual Folding Driven by Hydrogen Bonds and Host-Guest Chemistry



**Scheme 26.** Overview over the synthetic steps for the preparation of the azide functional secondary ammonium salt **30**. (i)  $\text{K}_2\text{CO}_3$ , NaI, DMF, 100 °C, 16 h. (ii)  $\text{CBr}_4$ ,  $\text{PPh}_3$ , ambient temperature, 16 h. (iii) 1. *n*-butylamine, MeOH, ambient temperature, 16 h. 2.  $\text{NaBH}_4$ , MeOH. 3.  $\text{Boc}_2\text{O}$ , TEA, MeOH, ambient temperature, 16 h. (iv)  $\text{NaN}_3$ , DMF, ambient temperature, 16 h. Adapted from ref [252] with permission from Wiley-VCH. © 2016 WILEY-VCH Verlag GmbH & Co. KGaA, Weinheim.

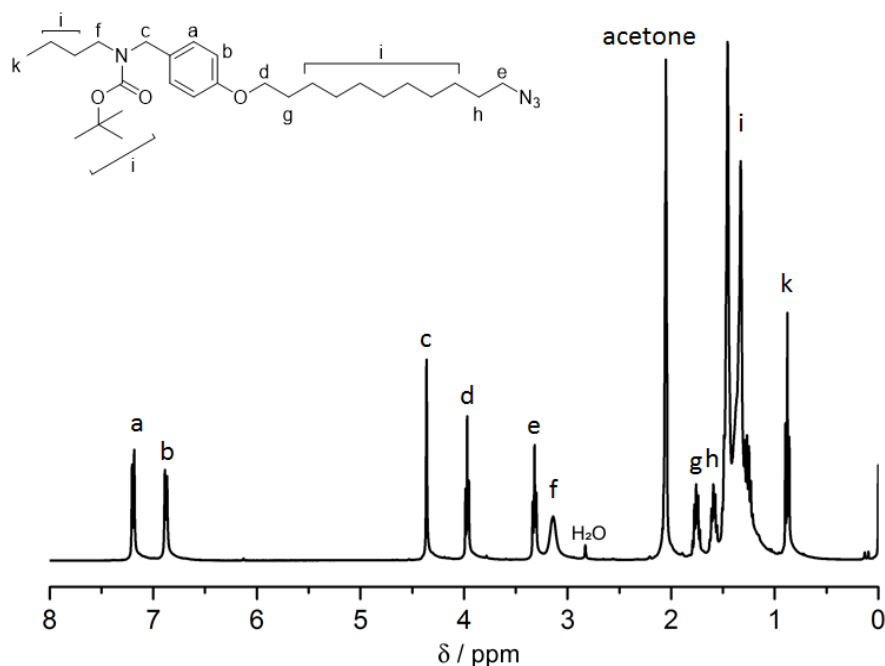


**Figure 32.**  $^1\text{H}$  NMR spectrum of the azide functional secondary AS moiety **30** recorded in acetone- $d_6$  (298 K). Reproduced from ref [252] with permission from Wiley-VCH. © 2016 WILEY-VCH Verlag GmbH & Co. KGaA, Weinheim.

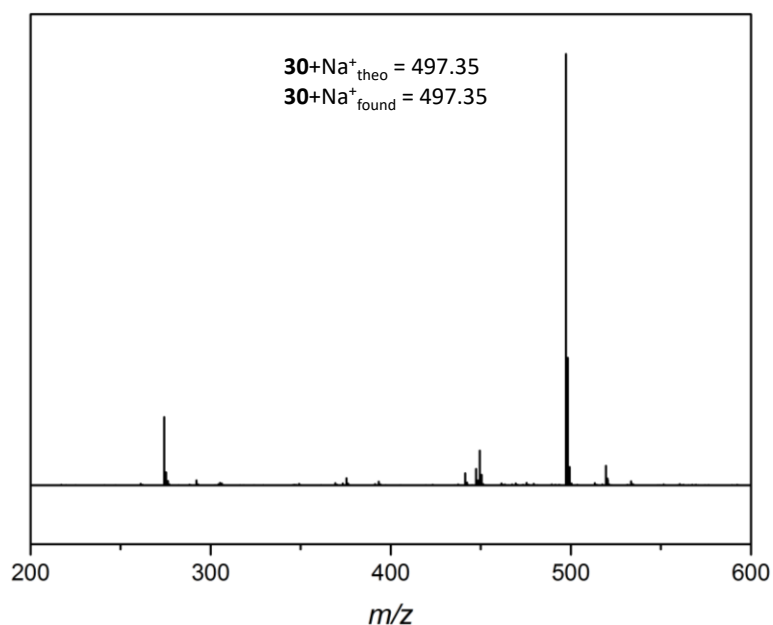


**Figure 33.** Mass spectrum of the azide functional secondary AS moiety **30**. Adapted from ref [252] with permission from Wiley-VCH. © 2016 WILEY-VCH Verlag GmbH & Co. KGaA, Weinheim.

### Synthesis of the Linear Precursor Polymers

The AB- and ABCD-type block copolymers were synthesized by reversible addition-fragmentation chain transfer (RAFT) polymerization in order to obtain well-defined block copolymers featuring narrow polydispersities. The synthetic strategy was designed to use block copolymers, in order to finely control the position of the functional groups along the polymeric backbone. Accordingly, the blocks in the copolymer feature different functionalities or protecting groups for the orthogonal attachment of the respective recognition motifs. Importantly, the final block copolymers are designed to have similar numbers of the folding motifs attached along the polymeric chain.

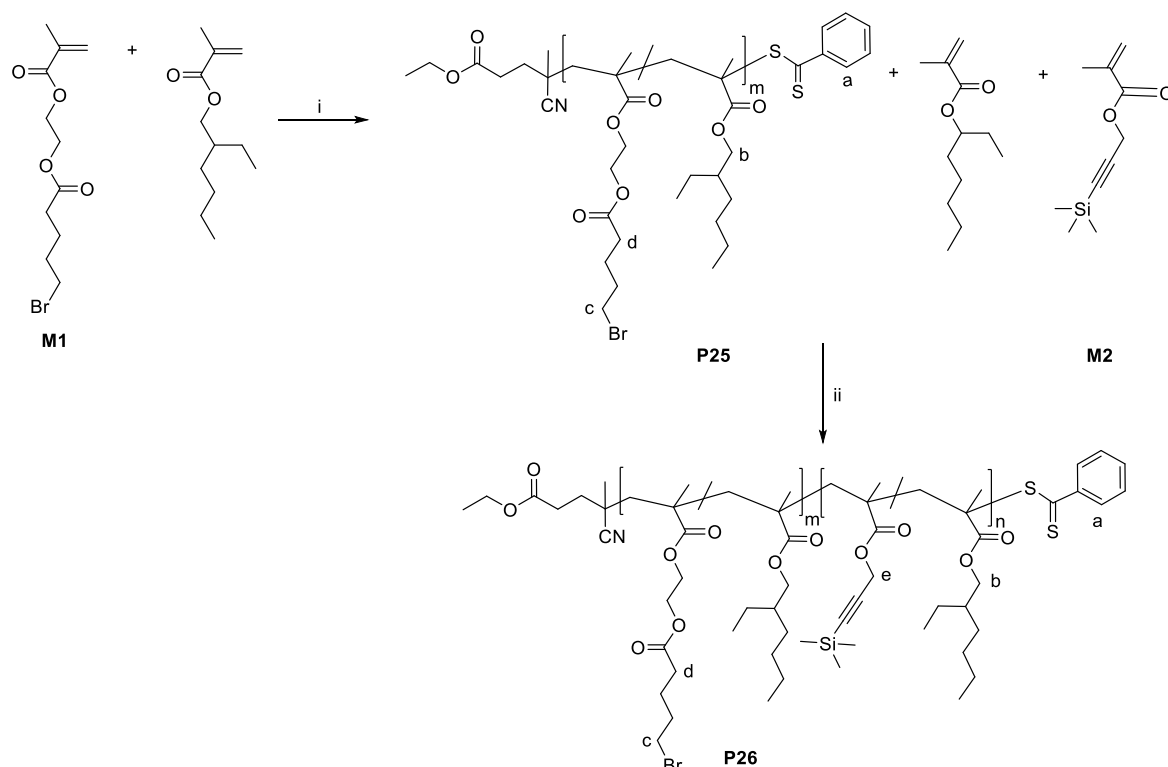
Initially, the AB type diblock copolymer was synthesized in a proof of principle study, adapting the B21C7-AS host-guest system to the field of single-chain folding. In a first step, 2-ethylhexyl methacrylate (EHMA) was copolymerized with the bromine functional monomer **M1** using the CTA and AIBN as radical source in dioxane (refer to Scheme 27). The conditions for the polymerization entailed a monomer to CTA ratio of 100:1 and a CTA to initiator ratio of 5. EHMA was used as a spacer within the blocks due to solubility reasons of the polymer after functionalization as well as for preventing

### 3.2.1 Reversible Dual Folding Driven by Hydrogen Bonds and Host-Guest Chemistry

interactions of close-by functional groups within one block and neighbouring blocks. In the first block, a functional group density of 5 mol% was targeted by adjusting the EHMA/**M1** ratio to 95:5. The  $^1\text{H}$  NMR spectrum of the obtained homopolymer **P25** (refer to Figure 35) reveals an incorporation of 5.2% of the bromine functionality, which is in good agreement with the employed feedstock ratio. The repeating units within the homoblock were calculated according to equation 28. For the calculation, the characteristic EHMA resonance at 3.83 ppm (**b**) that is associated with the  $\text{CH}_2$  resonances next to the carbonyl functionality was compared with the resonance 3.45 ppm (**c**) of the  $\text{CH}_2$  resonance next to the of bromine functionality of **M1**.

$$\% \text{Br} = \frac{c}{b+c} * 100 \quad (28)$$

The SEC chromatogram displays a monomodal distribution with a molecular weight ( $M_n$ ) of 16.1 kDa and a polydispersity index ( $\mathcal{D}$ ) of 1.05 (refer to Table 7 and Figure 34).



**Scheme 27.** Synthetic pathway for the preparation of the AB type diblock copolymer **P26**. (i) CTA, AIBN, dioxane, 60 °C, 16 h. (ii) AIBN, dioxane, 60 °C, 16 h. Adapted from ref [252] with permission from Wiley-VCH. © 2016 WILEY-VCH Verlag GmbH & Co. KGaA, Weinheim.

Second, the homoblock copolymer **P25** was employed as a macro-RAFT agent for chain-extension with the trimethyl silyl (TMS) protected alkyne functional monomer **M2**. Similar to the first copolymerization, the monomer/macro-CTA feedstock ratio was 100, whereas the macro-CTA to initiator ratio was increased to 7.5 in parallel to an increase of the monomer feedstock ratio from 95:5 to 90:10, which represents the ratio of EHMA to **M2**. In the obtained AB-type diblock copolymer, the molar ratio of the protected alkyne to the EHMA monomer was estimated to be close to 7.0 mol%. In order to calculate the amount of TMS protected alkyne, the resonances at 3.83 ppm (**b**), which are adjacent to the EHMA protons and the resonance at 4.56 ppm (**e**, adjacent to the protected alkyne) were compared. The EHMA protons of the homoblock copolymer were subtracted from the diblock copolymer and equation 28 was employed for the calculation for the incorporated percentage of the TMS protected alkyne functionality. Further, SEC measurements underpin the formation of the chain-extended polymer **P26**. In particular, the SEC traces depict the characteristic shift towards lower retention times after chain extension of **P26** compared to **P25** (refer to Figure 34, Table 7).

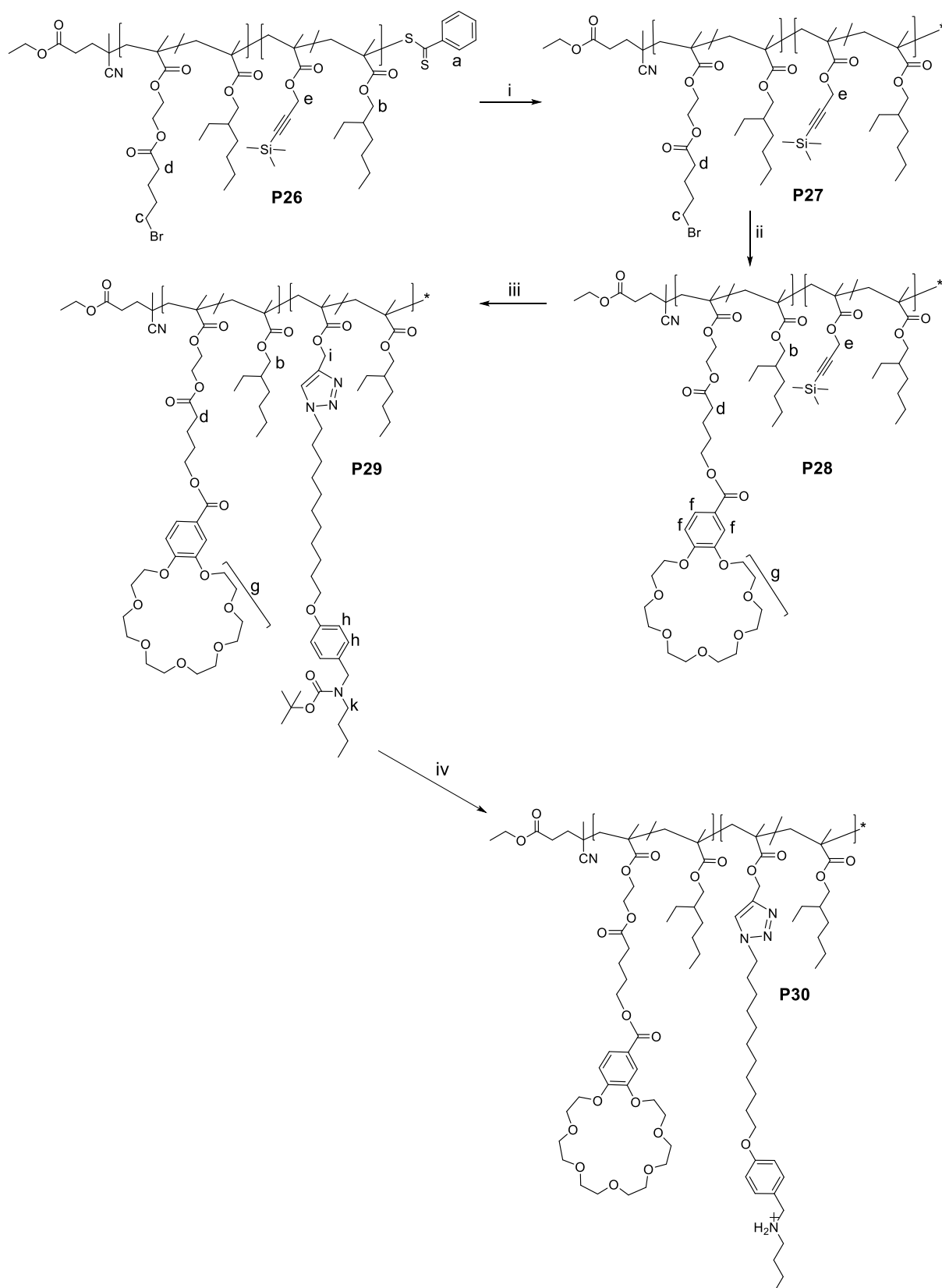
Prior to the functionalization of the diblock copolymer with the pendant functional groups – the B21C7 host and the AS guest – the RAFT dithiobenzoate end group was removed to avoid possible side reactions caused by the employed CuAAC reaction conditions.<sup>[108]</sup> The dithiobenzoate end group was removed in a radical-induced process using 20 equivalents of AIBN and 2 equivalents of lauroyl peroxide (LPO) in toluene yielding **P27** (refer to Scheme 28).<sup>[253]</sup> The progress of the reaction was visible by a decolouration of the solution starting from a pink and going to colourless. In addition to the optical changes within the solution, the <sup>1</sup>H NMR spectrum of **P27** (refer to Figure 35, blue curve) underpins the elimination of the dithiobenzoate, since the characteristic resonances of the benzoate moiety in the range of 7.84 – 7.32 ppm vanish. In the <sup>1</sup>H NMR spectrum, no end group could be identified, although AIBN or LPO are possible end groups due to the applied excess of AIBN (20 equivalents) and LPO (2 equivalents) during the reaction. The radical-induced reaction also leads to some extent of chain-chain coupling, which can be seen in the SEC traces of **P27**, where a small high molecular should at approximately double the  $M_n$  is detected (refer to Figure 34).

### 3.2.1 Reversible Dual Folding Driven by Hydrogen Bonds and Host-Guest Chemistry

**Table 7.** Molecular characteristics over the polymer **P25-P29**, giving the molecular weights and the polydispersities.

| ID         | $M_n / \text{g mol}^{-1}$ | $\bar{D}$ |
|------------|---------------------------|-----------|
| <b>P25</b> | 16100                     | 1.05      |
| <b>P26</b> | 26900                     | 1.07      |
| <b>P27</b> | 26300                     | 1.12      |
| <b>P28</b> | 36000                     | 1.10      |
| <b>P29</b> | 30600                     | 1.11      |

Thereafter, the acide functional B21C7 moiety **24** was linked to **P27** by a nucleophilic substitution reaction in order to decorate the polymer with the host moiety. The quantitative B21C7 grafting reaction was monitored by  $^1\text{H}$  NMR as well as SEC. Here, a significant increase of the molecular weight after the grafting reaction is detected by SEC (refer to Figure 34), which indicated the linking of the B21C7 moiety to the polymeric backbone. In addition, the characteristic resonances  $\text{CH}_2$  of the crown ether in the range of 4.3 – 4.2 ppm further evidence the successful reaction. Accordingly, the disappearance of the  $\text{CH}_2\text{-Br}$  resonance at 3.45 ppm as well as the newly occurring aromatic resonances of the B21C7 moiety at 7.64, 7.54 and 6.86 ppm (refer to Figure 35, pink curve) suggest the formation of **P28**. During the grafting reaction the potassium carbonate removes the TMS protecting group of the alkyne, resulting in a reduction of the resonances at 0.18 ppm.



**Scheme 28.** Synthetic pathway for the functionalization of the AB-type diblock copolymer. (i) LPO, AIBN, toluene, 30 °C, 3 h. (ii) **24**, K<sub>2</sub>CO<sub>3</sub>, THF/DMF (1:1 v/v), 50 °C, 48 h. (iii) **30**, CuSO<sub>4</sub>×5 H<sub>2</sub>O, sodium ascorbate, DMF, ambient temperature, 16 h. (iv) 1.) HCl, EA, ambient temperature, 16 h; 2.) NH<sub>4</sub>PF<sub>6</sub>, THF, H<sub>2</sub>O, ambient temperature, 16 h. Adapted from ref [252] with permission from Wiley-VCH. © 2016 WILEY-VCH Verlag GmbH & Co. KGaA, Weinheim.



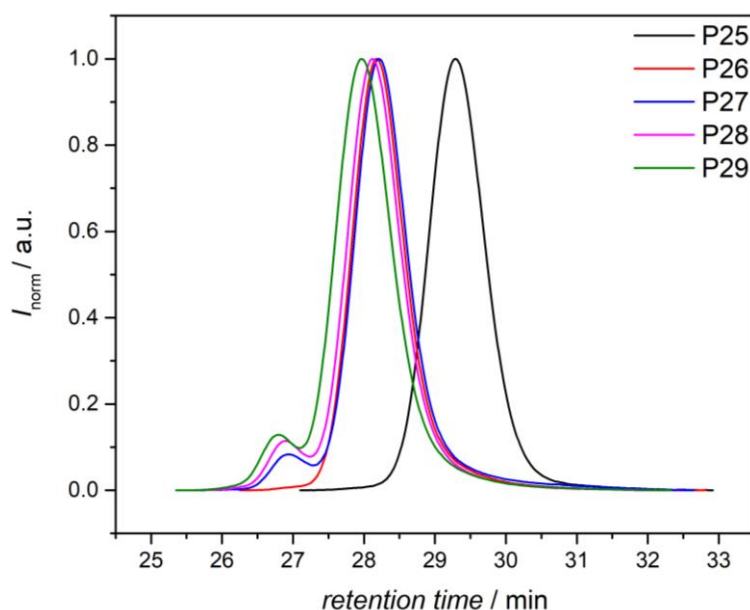


**Figure 34.** SEC traces of the homoblock copolymer **P25** ( $M_n = 16.1$  kDa,  $D = 1.05$ ), AB-type diblock copolymer **P26** ( $M_n = 26.9$  kDa,  $D = 1.07$ ), after removing the RAFT dithiobenzoate **P27** ( $M_n = 26.3$  kDa,  $D = 1.12$ ), the B21C7 functional **P28** ( $M_n = 36.0$  kDa,  $D = 1.10$ ) and the B21C7 and AS functional **P29** ( $M_n = 30.6$  kDa,  $D = 1.11$ ). For the final polymer **P30**, with the deprotected ammonium salt, SEC could not be conducted due to the ionic nature of the sample. All samples were measured in THF, 35 °C, 1 mL min<sup>-1</sup> using PMMA standards for calibration. Adapted from ref [252] with permission from Wiley-VCH. © 2016 WILEY-VCH Verlag GmbH & Co. KGaA, Weinheim.

In a last post-polymerization modification the secondary ammonium salt was linked to the polymer. For the attachment of the boc-protected AS moiety, CuAAC was applied using CuSO<sub>4</sub>·5 H<sub>2</sub>O/sodium ascorbate as catalytic system. DIPEA was additionally added in order to fully remove the TMS protecting group. The formation of **P29** was monitored by <sup>1</sup>H NMR spectroscopy (refer to Figure 35). Here, the formation of the triazole ring verifies the grafting of the AS moiety to the polymer. The formation is supported by the appearance of the aromatic protons of the AS moiety at 7.13 and 6.83 ppm. After the modification, the SEC chromatogram indicates a decrease of  $M_n$ , congruent with the expected shift towards lower retention times.

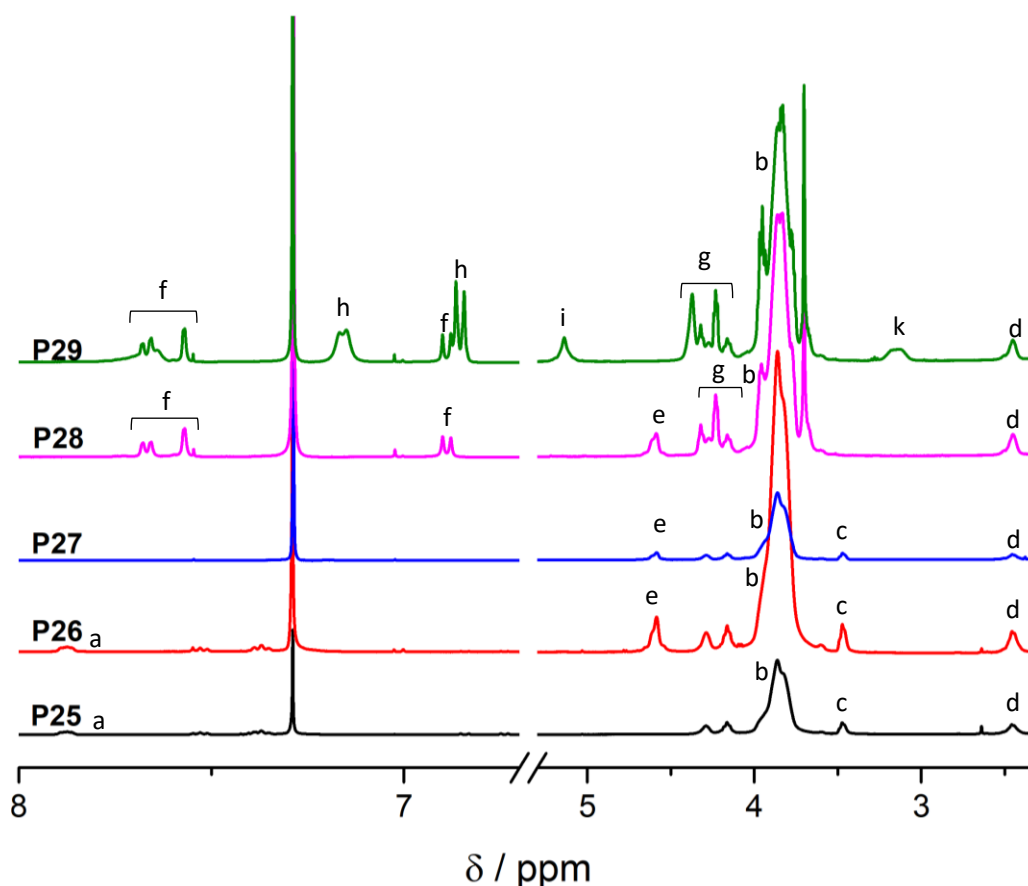


**Figure 35.** Relevant areas of the  $^1\text{H}$  NMR spectra of **P25-P29** in  $\text{CDCl}_3$  at ambient temperature. The aliphatic area from 2-0 ppm is omitted. The resonance assignments can be found in Scheme 28. Adapted from ref [252] with permission from Wiley-VCH. © 2016 WILEY-VCH Verlag GmbH & Co. KGaA, Weinheim.

The shift to lower retention times might be due to interactions between the functional groups within the polymer, leading to a reduced hydrodynamic volume. Further, the functionalities could interact with the columns in the SEC system or a higher deviation for the functionalized polymer **P29** from the Mark-Houwink-Sakurada (MHKS) parameters for pure PMMA could result in the shift towards lower retention times. To generate the secondary ammonium salt and the final polymer **P30**, the Boc protecting group was removed as a last step to prevent possible side reactions during the click ligation. After generating the polar AS, no SEC measurements are possible as due to interactions of the ionic polymer with the macroporous gel of the SEC columns, the polymer would probably not be eluted from the column. The structure of **P30** thus was confirmed by  $^1\text{H}$  NMR spectroscopy (refer to Figure 36). The aromatic region of the NMR displays changes of the shapes of the resonances of the aromatic resonances **f** and **g** of the B21C7 moiety (for the assignments refer to Scheme 28). The changes of

### 3.2.1 Reversible Dual Folding Driven by Hydrogen Bonds and Host-Guest Chemistry

the shape are attributed to the changed chemical environment upon the host-guest interaction of the B21C7-AS functionalities. Accordingly, the deprotection of the AS moiety is confirmed as well as the subsequent host-guest interaction.

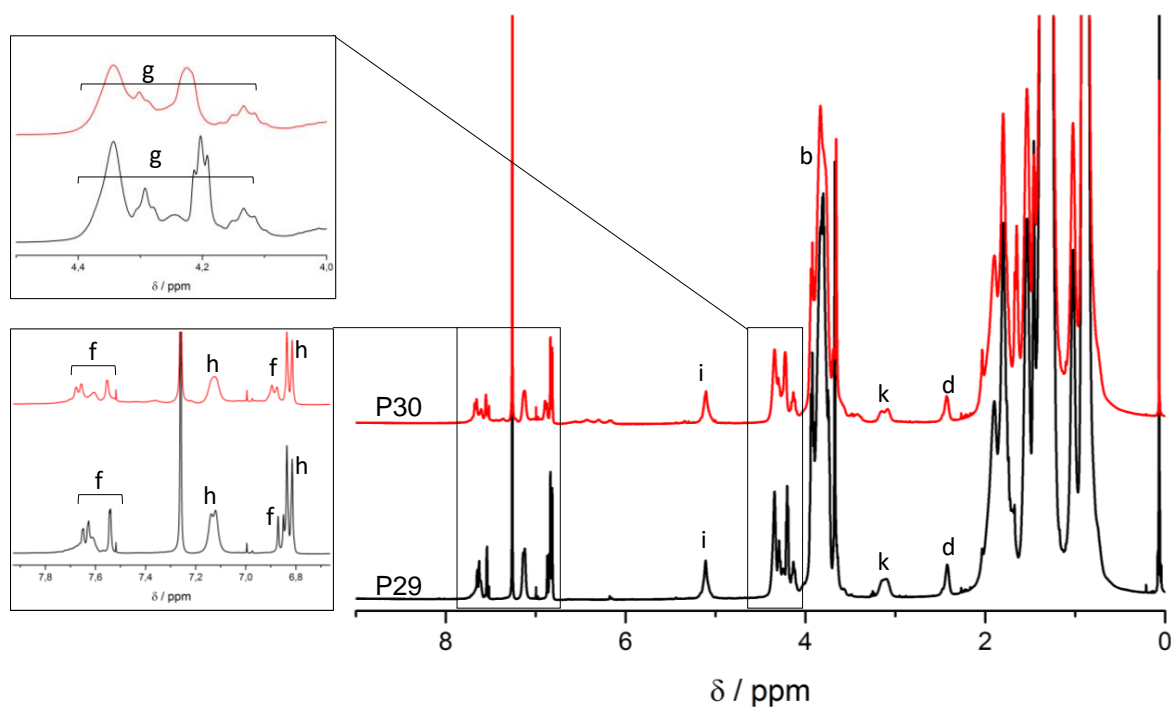


**Figure 36.**  $^1\text{H}$  NMR spectra of the Boc protected AS in polymers **P29** and the deprotected AS moiety in polymer **P30**. The NMRs were recorded in  $\text{CDCl}_3$  (298 K) the assignments of the resonances to the polymeric structures is depicted in Scheme 28.

The final AB-type diblock copolymer **P30** and the ABCD-type tetrablock copolymer **P31** are depicted in Figure 37.

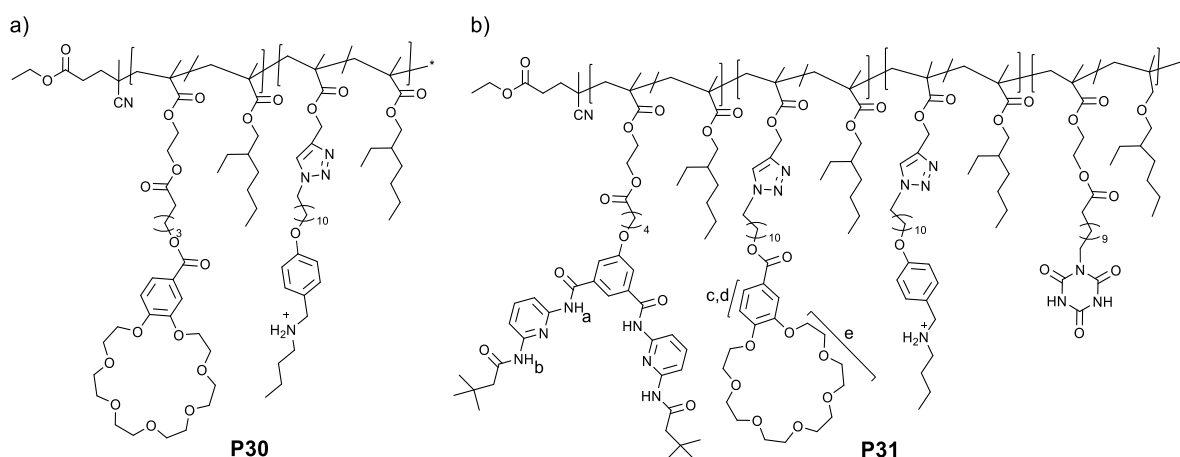
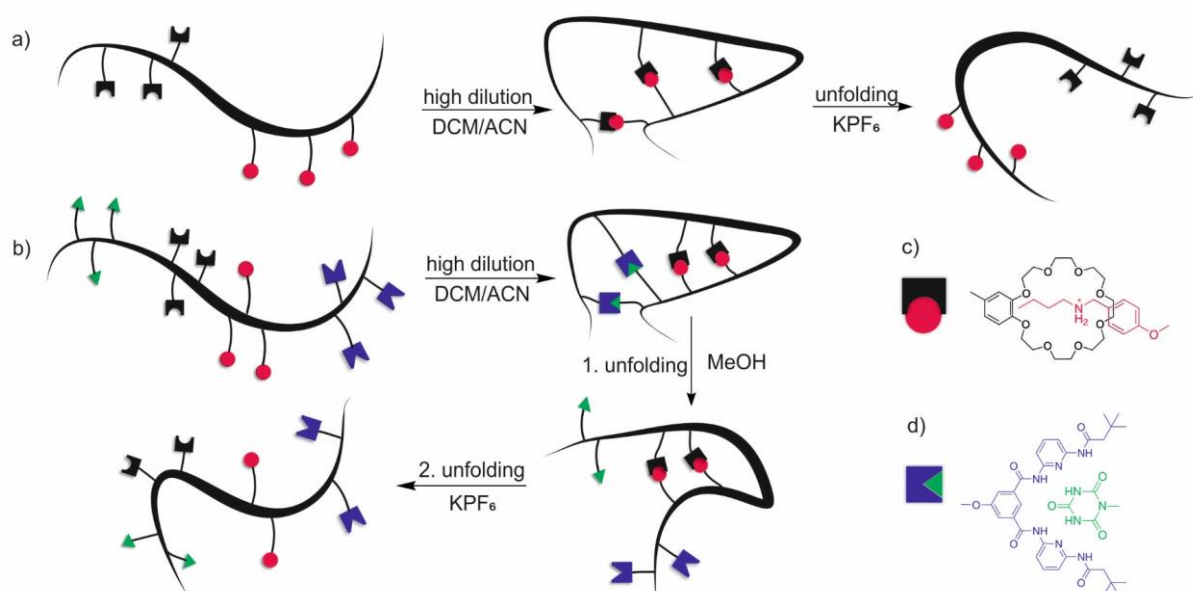


**Figure 37.** Chemical structures of a) the functional AB-type diblock copolymer **P30** and b) the functional ABCD-type tetrablock copolymer **P31**. Adapted from ref [252] with permission from Wiley-VCH. © 2016 WILEY-VCH Verlag GmbH & Co. KGaA, Weinheim.

## Single-Chain Folding and Unfolding

One of the most appealing features of supramolecular chemistry is its reversibility. Thus, for both polymers the intramolecular collapse based on non-covalent interactions such as host-guest interaction and hydrogen bonding was targeted (refer to Scheme 29). In order to demonstrate that the host-guest system consisting of the B21C7 host and the AS guest can be transferred from supramacromolecular chemistry into the field of single-chain technology, the AB-type diblock copolymer was initially tested with respect to its folding and unfolding behaviour.



**Scheme 29.** Schematic illustration of the designed folding/unfolding systems. a) the AB-type diblock copolymer featuring the B21C7 (host) and the AS (guest) folding units. b) the ABCD-type tetrablock copolymer featuring the orthogonal complementary motifs HW/CA and B21C7/AS. c) illustration of the multiple hydrogen bonds formed by the HW/CA pair. d) illustration of the host-guest interaction of the B21C7/AS system. Reproduced from ref [252] with permission from Wiley-VCH. © 2016 WILEY-VCH Verlag GmbH & Co. KGaA, Weinheim.

Thus, the diblock copolymer **P30** was investigated with regard to the concentrations that can be applied to ensure only intramolecular interactions of the complementary folding units are occurring. Therefore, samples of **P30** at different concentrations were subjected to DLS and DOSY. With increasing concentration, a slow transition from intramolecularly folded aggregates to intermolecular linked species is observed (refer to Figure 38). The formation of single-chain polymeric nanoparticles is assumed in the range up to approximately 7–8 mg mL<sup>-1</sup> from the DLS derived increase. DOSY

### 3.2.1 Reversible Dual Folding Driven by Hydrogen Bonds and Host-Guest Chemistry

measurements (refer to Table 8) underpin the transition from intra- to intermolecular interaction upon increasing the concentration. The hydrodynamic diameter calculated from DOSY measurements using the Stokes-Einstein equation 12, is close to 2.5 nm at concentrations of 2.5 mg mL<sup>-1</sup>, whereas at the concentrations of 20 mg mL<sup>-1</sup> the DOSY derived  $D_h$  increases to close to 5 nm (refer to Figure 38), indicating the formation of intermolecularly linked aggregates. In order to ensure the intramolecular folding, further investigations of the folding and unfolding behaviour of the host-guest system were carried out at the concentration of 2.5 mg mL<sup>-1</sup>. The concentration of 2.5 mg mL<sup>-1</sup> was selected due to the fact that both – DLS and DOSY measurements – suggest the formation of intramolecularly linked SCNPs.

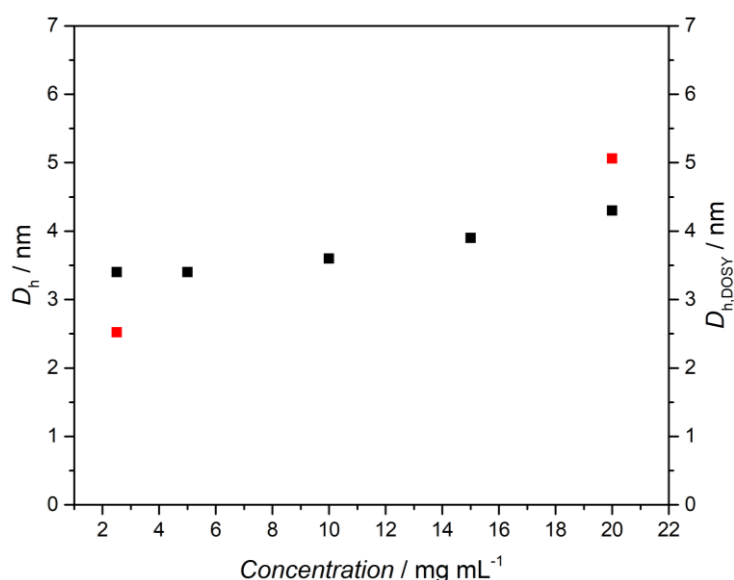


**Figure 38.** Concentration study of the diblock copolymer **P30** depicting the concentration dependent increase of the hydrodynamic diameter with increasing concentration obtained by DLS measurements (black symbols) and DOSY (red symbols). Adapted from ref [252] with permission from Wiley-VCH. © 2016 WILEY-VCH Verlag GmbH & Co. KGaA, Weinheim.

For the folded **P30**, a DLS derived hydrodynamic diameter ( $D_h$ ) of 3.4 nm is obtained (refer to Table 8). At this stage, it is assumed that the polymer is already folded by host-guest complexation, since highly diluted conditions of 2.5 mg mL<sup>-1</sup> are employed and intramolecular interactions of the host-guest system should dominate. To investigate the unfolding of the collapsed **P30**, a competitive guest molecule – in particular the potassium cation – was added, which is known to form a stronger complex with the B21C7 host than the AS moiety.<sup>[254]</sup> Upon the addition of an excess of potassium hexafluorophosphate (KPF<sub>6</sub>, 4 mg), DLS analysis reveals a shift of 1.4 nm from 3.4 nm for the folded **P30** to 4.8 nm for the unfolded analogue (refer to Figure 39),

indicating the successful unfolding of the B21C7/AS host-guest interaction in **P30**. The DLS measurements were conducted in a mixture of DCM/acetonitrile (9:1 v/v), due to the insolubility of KPF<sub>6</sub> in pure DCM. The DLS results were further underpinned by DOSY measurements that show a similar trend to higher  $D_h$  upon the addition of the competitive guest molecule K<sup>+</sup> (refer to Table 8). In particular, the DOSY derived  $D_h$  increases from 2.5 nm for the folded SCNP to 3.3 nm for the decomplexed host-guest motif in the open chain. Consequently, the host-guest system can be adapted in the field of single-chain folding as it has been demonstrated that intramolecular interactions are operational and can be addressed by an external stimulus.

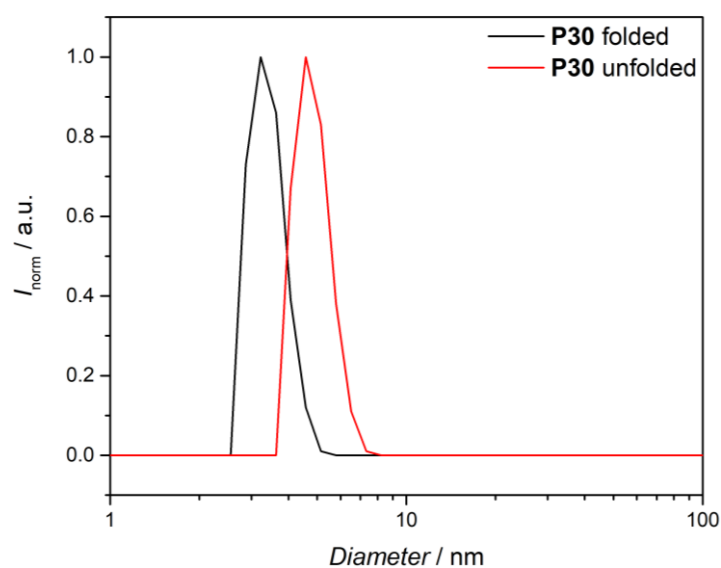


**Figure 39.** DLS plot for the folded and unfolded **P30** (number distributions), measured in a mixture of DCM/acetonitrile (9:1 v/v). Adapted from ref [252] with permission from Wiley-VCH. © 2016 WILEY-VCH Verlag GmbH & Co. KGaA, Weinheim.

### 3.2.1 Reversible Dual Folding Driven by Hydrogen Bonds and Host-Guest Chemistry

**Table 8.** DLS and DOSY derived data for the folded and unfolded polymers **P30** and **P31**. Adapted from ref [252] with permission from Wiley-VCH. © 2016 WILEY-VCH Verlag GmbH & Co. KGaA, Weinheim.

| ID                              | $D_{h,DLS}^a$ / nm | $D_{h,DOSY}^b$ / nm |
|---------------------------------|--------------------|---------------------|
| <b>P30 folded</b>               | 3.4                | 2.5                 |
| <b>P30 unfolded</b>             | 4.8                | 3.3                 |
| <b>P31 folded</b>               | 6.0                | 7.1                 |
| <b>P31+MeOH</b>                 | 7.9                | 8.7                 |
| <b>P31+MeOH+KPF<sub>6</sub></b> | 10.5               | 10.6                |
| <b>P31+KPF<sub>6</sub></b>      | 8.6                | 9.6                 |
| <b>P31+KPF<sub>6</sub>+MeOH</b> | 10.0               | 10.1                |

<sup>a</sup>Determined by DLS in a mixture of DCM/acetonitrile (9:1, v/v) at 25 °C,  $C_{\text{polymer}} = 2.5 \text{ mg mL}^{-1}$ . <sup>b</sup>Determined by DOSY, in a mixture of DCM/acetonitrile (9:1, v/v) at 25 °C,  $C_{\text{polymer}} = 2.5 \text{ mg mL}^{-1}$ , using the Stokes–Einstein Equation 12 for calculation.

Initially, for the dual folding system based on the ABCD tetrablock copolymer **P31**, the concentration dependency was investigated in analogy to the AB diblock copolymer system. The concentration dependent profile of the  $D_h$  obtained by DLS displays a smooth transition from intra- to intermolecularly interacting complementary motifs (refer to Figure 40). As a consequence of the slow transition between the intra- and intermolecular interactions, the intramolecularly folding regime is operational in the concentration range up to approximately  $8 \text{ mg mL}^{-1}$ . Beyond concentrations of  $8 \text{ mg mL}^{-1}$ , a clear increase in the  $D_h$  is obtained by DLS measurements (refer to Figure 40). In addition, DOSY measurements at different concentrations display an increase of the hydrodynamic diameter (calculated using the Stokes-Einstein equation 12). At low concentrations, *i.e.*  $2.5 \text{ mg mL}^{-1}$ , the  $D_h$  is close to 7 nm. In case the concentration is increased to  $18 \text{ mg mL}^{-1}$ , the hydrodynamic diameter increases to close to 11 nm, suggesting the formation of intermolecular aggregates. As for polymer **P30**, a concentration of  $2.5 \text{ mg mL}^{-1}$  was employed for the further analysis of the SCNPs to

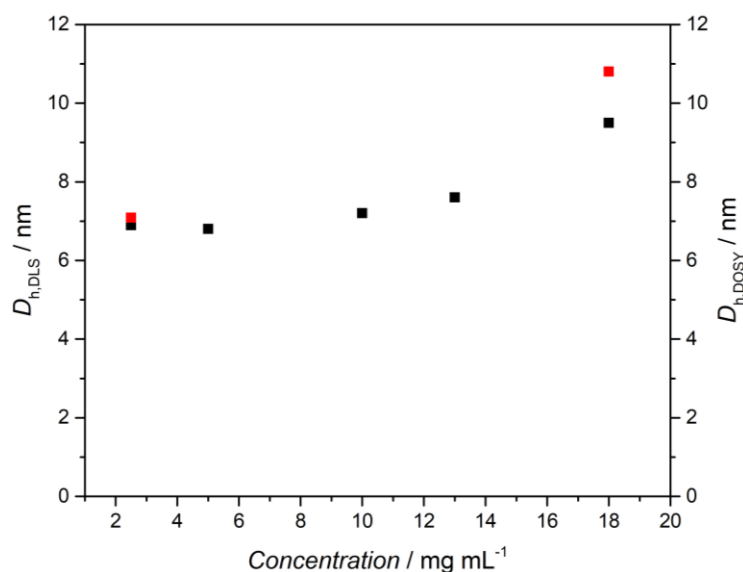


**Figure 40.** DLS data for the folded and unfolded **P31** (number distributions), measured in a mixture of DCM/acetonitrile (9:1 v/v). Adapted from ref [252] with permission from Wiley-VCH. © 2016 WILEY-VCH Verlag GmbH & Co. KGaA, Weinheim.

ensure the intramolecular interactions and exclude the formation of intermolecularly linked species.

The dual folding system **P31** features two recognition motifs that can be addressed independently by different chemical triggers. Theoretically, different pathways for the selective and orthogonal unfolding can be pursued by (i) disrupting the hydrogen bonds, while the host-guest interactions stay intact and (ii) initially unfold the host-guest system, followed by the rupture of the hydrogen bonds. To demonstrate the pathway independency for unfolding, both noted routes were addressed. Initially, the unfolding of the HW/CA hydrogen bonding system was triggered by the addition of methanol. DLS measurements were conducted in a mixture of DCM/acetonitrile (9:1 v/v) to provide solubility of the KPF<sub>6</sub> salt that is added in a second step. After the addition of 20  $\mu$ L MeOH, DLS measurements indicate an increase for the  $D_h$  of about 2 nm from 6.0 nm of the dual folded SCNP to 7.9 nm for the SCNP that only features the intact host-guest system (refer to Table 8 entry 3 and 4, and Figure 41). Subsequently, the competitive guest cation K<sup>+</sup> has been added in form of KPF<sub>6</sub>, to completely unfold the SCNP and disrupt the host-guest interactions. The addition of the potassium salt leads to a further increase of  $D_h$  by about 2 nm from 7.9 nm of the MeOH unfolded hydrogen bonds in **P31** to 10.5 nm for the completely unfolded **P31** (refer to Figure 41). Moreover, the addition of the external trigger signals for unfolding was inverted to



### 3.2.1 Reversible Dual Folding Driven by Hydrogen Bonds and Host-Guest Chemistry

confirm the pathway independent orthogonal triggered unfolding of the HW/CA hydrogen bonding system and the B21C7/AS host-guest complex. The inversion leads to similar results: after the addition of  $\text{KPF}_6$  the hydrodynamic diameter increases by close to 2.5 nm from 6.0 nm for the dual folded SCNP to 8.6 nm for the SCNP featuring only the hydrogen bonds. Upon the addition of MeOH (20  $\mu\text{L}$ ), the increase is less pronounced with 1.4 nm, resulting in an increase from 8.6 nm for the SCNP with intact HW/CA interactions to 10.0 nm for the dual unfolded single-chain nanoparticle (refer to Figure 41). The overall trend towards higher  $D_h$  after the addition of the trigger signals, MeOH for the hydrogen bonding motif and  $\text{KPF}_6$  for the host-guest system, was demonstrated to be in agreement in both avenues. Further evidence for the pathway independency as well as orthogonal unfolding were obtained by DOSY measurements (refer to Table 8), yielding similar trends. The DOSY derived  $D_h$  for pathway (i) displays an increase from 7.1 nm for the dual folded SCNP to 8.7 nm after the addition of MeOH to cleave the hydrogen bonds and a further increase to 10.6 nm after the addition of the competitive guest ( $\text{K}^+$ ) to yield the completely unfolded SCNP. When the potassium salt is added first, the  $D_{h,\text{DOSY}}$  increases from 7.1 nm for the folded SCNP to 9.6 nm for the decomplexed host-guest system and to 10.1 nm for the unfolded SCNP after the addition of MeOH to trigger the unfolding of the hydrogen bonds. As mono-exponential fits to the correlation functions were not always satisfying, and thus one sample (**P31** +  $\text{KPF}_6$  and MeOH) was selected to study the diffusion coefficient in detail. At longer run times (4h 30 minutes and 32 seconds, performing 96 gradient increment steps and extended relaxation delays of 20 s between scans) and thus a higher S/N ratio due to the employed cryoprobe that further enhances the S/N ratio, two components became visible. The smaller component may be attributed to low molecular weight oligomers formed by the continuous initiation during the RAFT process (that are not visible in a weight distribution and DLS) and which overlap with the corresponding high molecular weight polymer NMR resonances. Corresponding diffusion coefficients of a bi-exponential fit (refer to Appendix, Section D) displays a slight decrease to the mono-exponential fit. However, as only relative effective hydrodynamic radii are needed for following the folding behavior of the polymers, the best matching mono-exponential fits were used for comparison. Here, an estimated increased systematic error towards smaller radii of close to 15% is accepted.

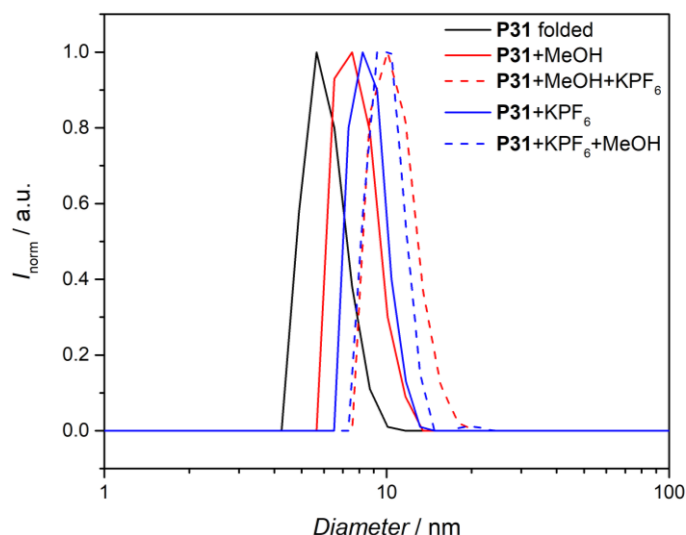


**Figure 41.** DLS data for the folded and unfolded **P31** (number distributions), measured in a mixture of DCM/acetonitrile (9:1 v/v). Adapted from ref [252] with permission from Wiley-VCH. © 2016 WILEY-VCH Verlag GmbH & Co. KGaA, Weinheim.

Subsequently,  $^1\text{H}$  NMR spectroscopy was employed to gain more information about the folding/unfolding of the system (refer to Figure 42). The resonances **a** and **b** at 9.65 and 9.31 ppm are assigned to the amide protons of the HW moiety and indicate the interaction with the CA moiety.<sup>[48]</sup> The imide protons of the CA moiety are probably in a coalescence regime, with a broad NH proton resonance, attributed to a strong exchange broadening.<sup>[50,52]</sup> The resonances **c**, **d** and **e** are associated with the B21C7 moiety.<sup>[254,255]</sup> The changes of the shape of the aromatic resonances arising from the B21C7 moiety in the range of 7.7–6.9 ppm (resonances **c** and **d**) and the resonance **e**, which is assigned to the ethyleneoxy bridged of the B21C7 adjacent to the phenol ring at 4.21 ppm, suggest the intact host-guest interaction of the B21C7 moiety with the AS functionality. After the addition of MeOH that disrupt the hydrogen bonds, the resonances at 9.31 and 9.65 ppm vanish, indicating the cleavage of the hydrogen bond system. The changes of the resonances **c**, **d** and **e** after the addition of the  $\text{KPF}_6$  salt, suggest a change of the environment of the B21C7 moiety, due to the decomplexation of the AS motif and the new interaction of the B21C7 host with the potassium cation as a guest molecule.

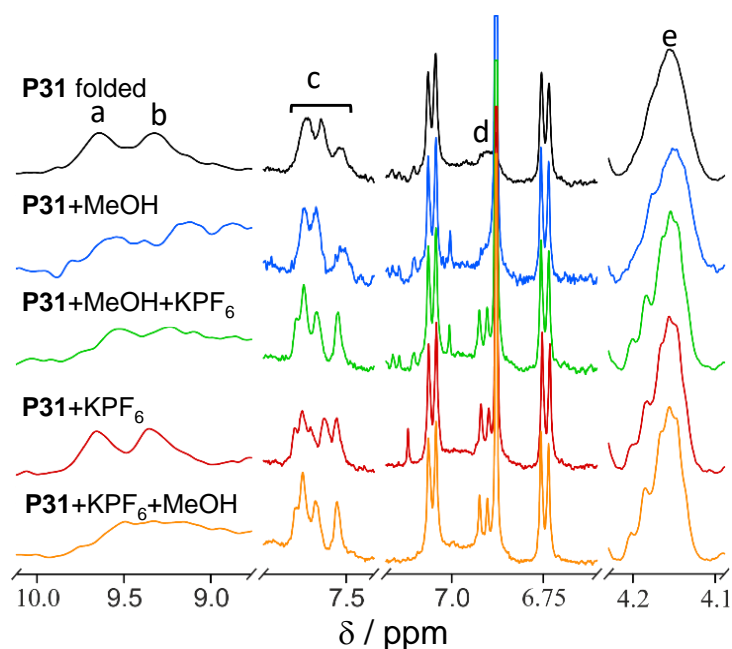


**Figure 42.** Relevant sections of the  $^1\text{H}$  NMR spectra for the unfolding of the tetrablock copolymer **P31**. Resonances labelled **a** and **b** indicate the interaction of the complementary motifs HW–CA, the resonances labelled **c–e** indicate the host–guest interaction of B21C7–AS. The assignments of the resonances can be found in Figure 37b. Reproduced from ref [252] with permission from Wiley-VCH. © 2016 WILEY-VCH Verlag GmbH & Co. KGaA, Weinheim.

In summary, the synthesis of an AB-type diblock copolymer and an ABCD type tetrablock copolymer was reported. The copolymers were functionalized in post-polymerization modifications. The diblock copolymer was decorated with the B21C7 (host) and secondary AS (guest). The tetrablock copolymer features the HW/CA hydrogen bonding motif on the outer blocks A and D and the host-guest units (B21C7/AS) on the middle blocks B and C. Subsequently, the SCNP of the functionalized diblock copolymer was formed in high dilution ( $2.5 \text{ mg mL}^{-1}$ ) and readily unfolded by the addition of a competitive guest cation ( $\text{K}^+$ ). Further, the orthogonal folding of the tetrablock copolymer was achieved in high dilution ( $2.5 \text{ mg mL}^{-1}$ ). Importantly, the reversibility of the dual folded system was triggered by the addition of external stimuli. In particular, methanol was added to disrupt the hydrogen bonds of the HW/CA unit and a competitive guest cation ( $\text{K}^+$ ) to decomplex the host-guest interaction. The orthogonality and pathway independent unfolding was followed by  $^1\text{H}$  and DOSY NMR spectroscopy as well as DLS measurements. The orthogonal interaction of the employed recognition motifs as well as the orthogonally and independently triggered unfolding of the system presents a critical step in the synthesis of artificial enzymes to finely control the shape of the single-chain nanoparticle.

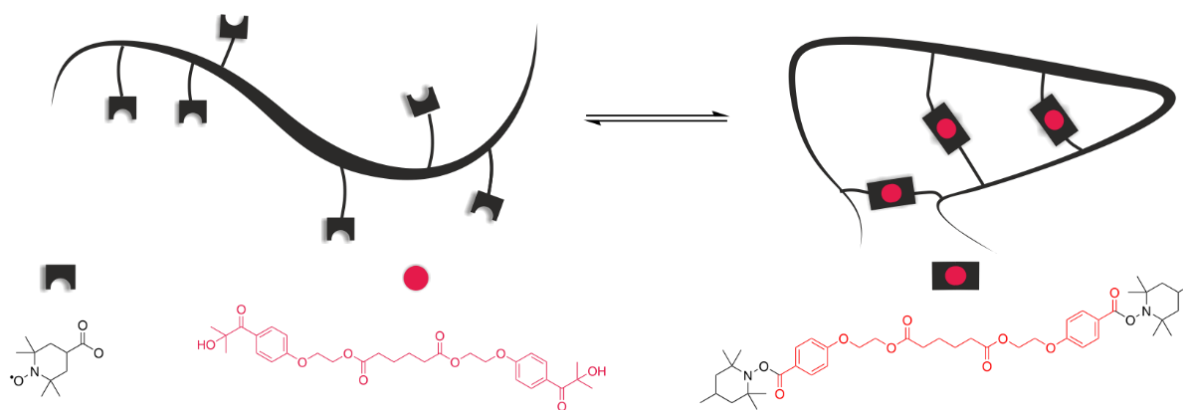


### 3.2.2 Self-Reporting Refoldable Dynamic-Covalent Fluorescent Single-Chain Nanoparticles

In addition to the presented non-covalent interactions in the previous Section, during the current thesis a further project based on dynamic-covalent crosslinking was designed. Instead of the often permanent nature of crosslinks described in Section 2.3, the current project targets reversible crosslinking. By taking inspiration from nature, the designed methodology features a system that – theoretically – can be reused in several folding cycles. In nature, proteins can dynamically switch between the folded and unfolded state. An appropriate candidate to realize the reversibility in a covalently crosslinked system are nitroxides. As known from nitroxide mediated polymerization, for instance, nitroxides are reversibly capped and reactivated due to the labile C-O bond (refer to Section 2.1). The labile C-O bond is exploited to switch between the open chain having the stable free nitroxide radical and the capped species in the crosslinked single-chain nanoparticle. Within the current section, a polystyrene (PS) based copolymer that contains different amounts of free stable nitroxide radicals within the polymeric backbone was folded by UV-light, using a novel bifunctional crosslinker displaying the 2-hydroxy-4'-(2-hydroxyethoxy)-2-methylpropiophenone (Irgacure 2959) functionality on both chain termini. A schematic overview of the designed methodology is demonstrated in Scheme 30.\*

---

\*Parts of the current Section were taken from T. S. Fischer, S. Spann, Q. An, B. Luy, M. Tsotsalas, J. P. Blinco, H. Mutlu and C. Barner-Kowollik, *Chem. Sci.*, **2018**, 9, 4696-4702. with permission of the Royal Society of Chemistry. T. S. Fischer and H. Mutlu designed the experiments. T. S. Fischer conducted all experiments unless otherwise stated and wrote the manuscript. S. Spann performed the DOSY measurements, Q. An performed EPR measurements. B. Luy and M. Tsotsalas contributed to scientific discussions. J. P. Blinco, H. Mutlu and C. Barner Kowollik supervised the project and contributed to scientific discussions.

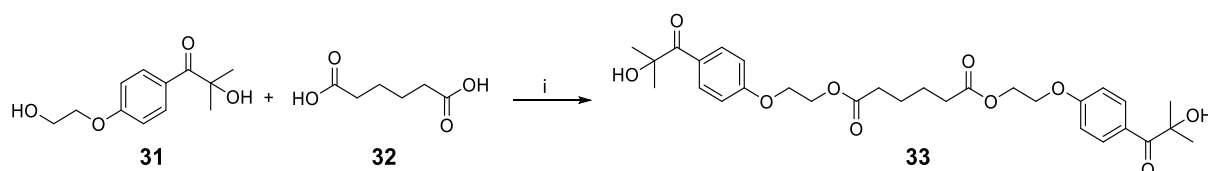


**Scheme 30.** Schematic illustration of the single-chain collapse induced by the UV-light triggered crosslinking reaction of the Irgacure 2959 moiety and the TEMPO functionality.

### Small Molecule Synthesis

The synthesis of the NMP initiator **16** can be found in Section 3.1.2 and will not be described here.

The bifunctional crosslinker **33** was prepared in a one-step synthetic procedure (refer to Scheme 31).



**Scheme 31.** Synthesis of the bifunctional crosslinker **33**, featuring the Irgacure 2959 functionalities on both chain termini. (i) DMAP, EDC·HCl, DCM, ambient temperature, 48 h.

In a Steglich esterification<sup>[234]</sup>, the diacid adipic acid (**32**) was endowed with the Irgacure 2959 moiety (**31**) on both acid functionalities, by using an excess of **31** (3 equivalents). The compound **33** was obtained in good yields (81%) and characterized by <sup>1</sup>H (refer to Figure 43) and <sup>13</sup>C NMR spectroscopy. The <sup>1</sup>H NMR spectrum suggests the formation of **33**.

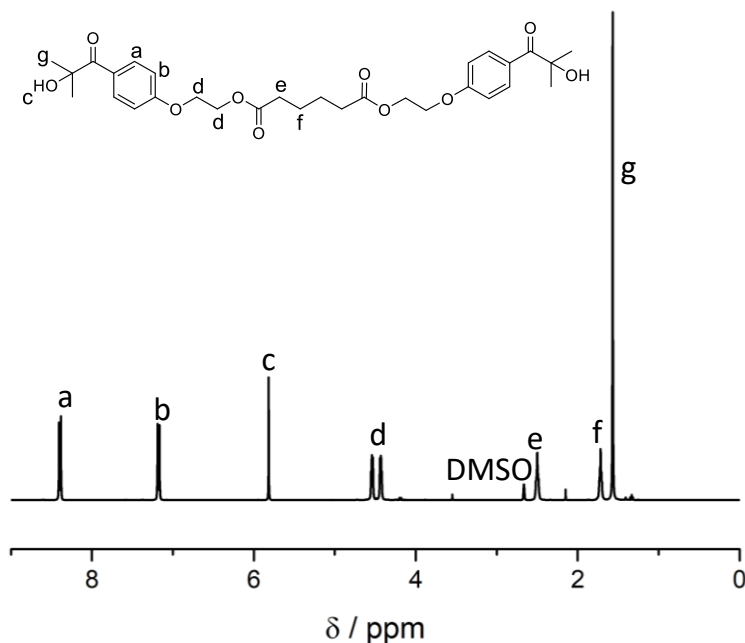


**Figure 43.**  $^1\text{H}$  NMR spectrum of the bifunctional crosslinker **33**, recorded in  $\text{DMSO-}d_6$  (298K). Adapted from ref [256] with permission of the Royal Society of Chemistry.

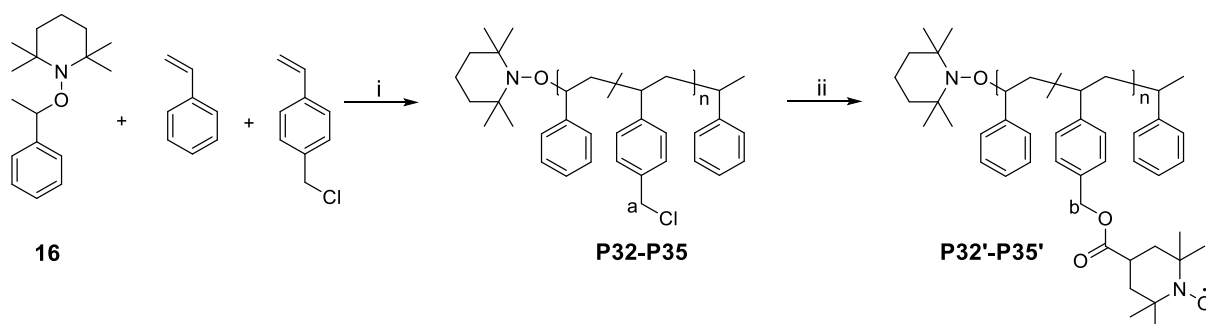
### Synthesis of the Linear Precursor Polymers

In order to progress towards the controlled synthesis displayed in nature, within the current project well-defined polymers were prepared using nitroxide-mediated polymerization (NMP). Accordingly, well-defined polymeric scaffolds with narrow polydispersities are obtained. The designed copolymers are synthesized by the copolymerization of styrene and 4-(chloromethyl)styrene (CMS) yielding the poly(styrene-*stat*-4-(chloromethyl)styrene) **P32-P35** (refer to Scheme 32). By employing different feedstock ratios of styrene and the CMS monomer, copolymers that hold different amounts of the CMS unit within the polymeric backbone were obtained. Table 9 summarizes the employed feedstock ratios as well as the afforded molecular characteristics of the isolated polymers. In addition, the chain-length was increased to close to three times from 10.1 kDa of **P32** to 31.6 kDa of **P35**.

**Table 9.** Overview over the employed feedstock ratios of the monomers, the monomer/initiator ratio and molecular characteristics of the synthesized polymer **P32-P35** as well as the determined amount of CMS within the polymers.

| ID         | Styrene/4-(chloromethyl)styrene | Monomer/Initiator | $M_n^a / \text{g mol}^{-1}$ | $\bar{D}^a$ | %CMS <sup>b</sup> |
|------------|---------------------------------|-------------------|-----------------------------|-------------|-------------------|
| <b>P32</b> | 190:10                          | 200:1             | 10100                       | 1.2         | 7.8               |
| <b>P33</b> | 175:35                          | 210:1             | 10900                       | 1.3         | 19.6              |
| <b>P34</b> | 150:50                          | 200:1             | 8600                        | 1.4         | 30.5              |
| <b>P35</b> | 750:30                          | 780:1             | 31600                       | 1.4         | 5.0               |

<sup>a</sup> Determined *via* SEC (35 °C, 1 ml min<sup>-1</sup> using PS standards for calibration). <sup>b</sup> Calculated *via* NMR using the reported equation from literature.<sup>[85]</sup>



**Scheme 32.** Synthetic procedure towards the nitroxide functional polymers **P32'-P35'**. (i) **P32**: 18 h at 125 °C in toluene. **P33-P35**: 20 h at 125 °C in toluene. (ii) K<sub>2</sub>CO<sub>3</sub>, 4-carboxy TEMPO in DMF for 72 h at 50 °C.

In a post-polymerization modification, the polymers were decorated with 4-carboxy-2,2,6,6-tetramethylpiperidine 1-oxyl (4-carboxy TEMPO) in a nucleophilic substitution reaction (refer to Scheme 32) to afford the polymers **P32'-P35'**. The reaction was followed by <sup>1</sup>H NMR (refer to Figure 105-Figure 108 in the Appendix). Although no quantitative information can be obtained from the <sup>1</sup>H NMR spectra, due to the persistent nitroxide radicals, which causes line broadening effect as been already described in Section 3.1.2. Qualitatively, the CH<sub>2</sub> resonance of the CMS group (**a**) shifted downfield from 4.52 to 5.15 ppm for **b** and suggests the quantitative conversion of the chlorine to yield the TEMPO polymer **P32'-P35'**.



### 3.2.2 Self-Reporting Refoldable Dynamic Covalent Fluorescent SCNPs

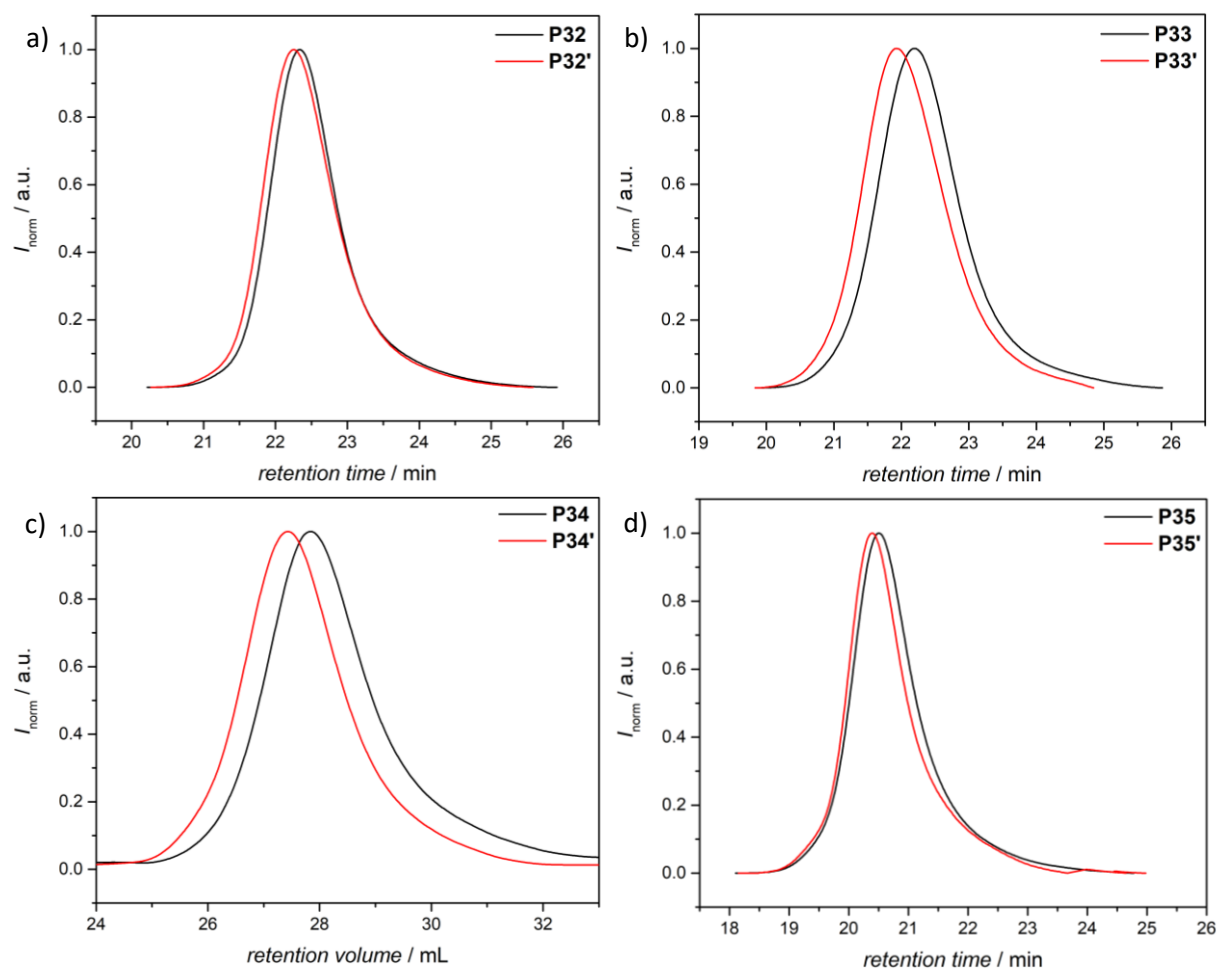


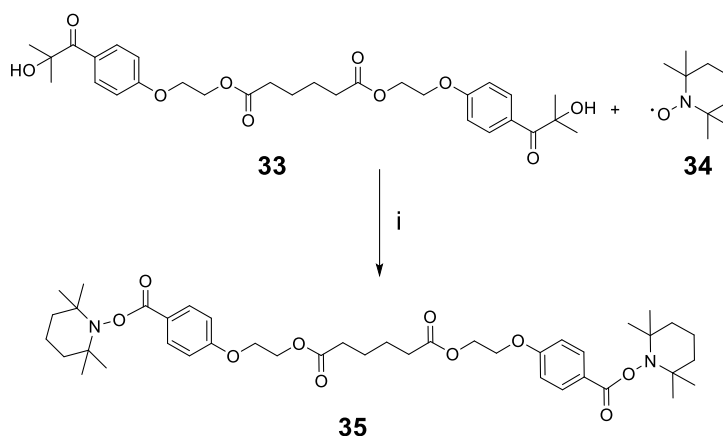
**Figure 44.** SEC traces of the parent polymers **P32-P35** (black curves) and after post-polymerization modification **P32'-P35'** (red curves) featuring the persistent nitroxide radicals. All samples were measured in THF, 35 °C, 1 ml min<sup>-1</sup> using PS standards for calibration. Adapted from ref [256] with permission of the Royal Society of Chemistry.

Furthermore, the post-polymerization modification was characterized by SEC. Here, the SEC chromatograms for all polymeric samples display the expected shift towards lower retention times (refer to Figure 44) and thus higher molecular weights (refer to Table 10), underpinning the successful modification of the parent polymers **P32-P35**.

## UV-light Triggered Single-Chain Collapse

The Irgacure 2959 functionality is commonly used as a photo-initiator or photo responsive group.<sup>[257–261]</sup> Inspired by the photochemistry and especially the UV-light triggered ligation of the Irgacure2969 moiety with the TEMPO radical,<sup>[261]</sup> the crosslinking strategy presented in Scheme 30 to produce SCNPs was designed.

Further, the group of *Bottle* showed and deprotection of protected nitroxide moieties by using *meta*-chlorperbenzoic acid (*m*CPBA).<sup>[262]</sup> To evaluate and investigate the protection/deprotection reactions prior to the polymeric study, exemplary small molecule studies for the system were employed. Here, the bifunctional crosslinker **33** was reacted with 2,2,6,6-tetramethylpiperidinyloxy (TEMPO, **34**, refer to Scheme 33) under the same conditions as for the following folding reaction of the polymers **P32'**-**P35'**, using an Arimed B6 lamp ( $\lambda_{\max} = 320$  nm), anisole as solvent and stirring over night. The formation of species **35** was confirmed by high resolution electrospray ionization (ESI) mass spectrometry. Here, the experimentally found mass ( $m/z_{\text{exp}} = 775.4153$  for **35** charged with a  $\text{Na}^+$  ion) deviated by the acceptable value of  $m/z = 0.0013$  from the theoretical  $m/z$  ratio of **35** (charged with  $\text{Na}^+$ ), with  $m/z_{\text{theo}} = 775.4140$ .

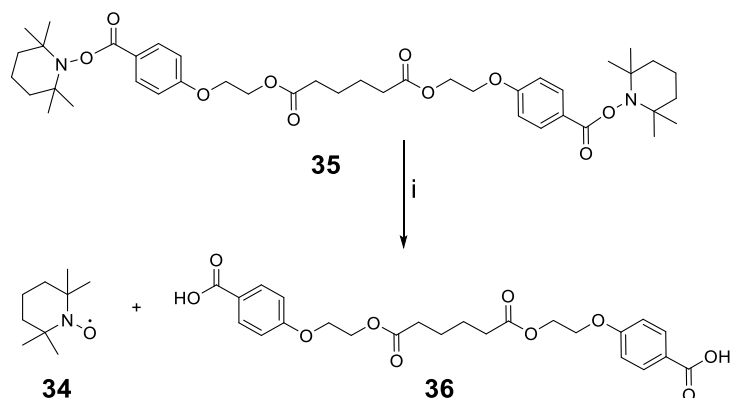


**Scheme 33.** Small molecule test reaction to prove the UV-light ( $\lambda_{\max} = 320$  nm) induced crosslinking reaction. (i) anisole,  $h\nu$  (Arimed B6,  $\lambda_{\max} = 320$  nm), ambient temperature, 20 h. Adapted from ref [256] with permission of the Royal Society of Chemistry.

Next, the test molecule **35** was subjected to an exemplary reaction for the unfolding of the SCNPs under oxidative conditions by employing *m*CPBA (refer to Scheme 34). After the reaction, the reformation of the free nitroxide radical TEMPO (**34**) and **36**,

### 3.2.2 Self-Reporting Refoldable Dynamic Covalent Fluorescent SCNPs

which is attributed to parts of the reacted crosslinker, were obtained and confirmed by mass spectrometry. Here, the TEMPO fragment (**34**) was found ( $m/z_{\text{exp}} = 158.1543$ ;  $m/z_{\text{theo}} = 158.1545$ ) and  $m/z_{\text{exp}} = 497.1428$  was assigned to species **36**, with a theoretical  $m/z$  ratio of 497.1418. Accordingly, the employed conditions are suitable for the deprotection of the TEMPO moiety. In addition, both exemplary small molecule reactions for the folding/unfolding were followed by gas chromatography-mass spectrometry (GC-MS). The GC-MS chromatogram shows the reformation of the TEMPO radical under the employed oxidative reaction conditions (refer to Figure 45). Furthermore, the 2,2,6,6 tetramethylpiperidine derivative is detected, which occurs as a side product during the oxidative cleavage. The piperidine species can be reoxidized, by employing a bigger excess of *m*CPBA, since *m*CPBA is also used for the oxidation of piperidine derivatives to the nitroxide radicals.<sup>[263]</sup>



**Scheme 34.** Exemplary small molecule test reaction for the unfolding reaction for the SCNP structures. (i) *m*CPBA, DCM, 35 °C, 2 h. Adapted from ref [256] with permission of the Royal Society of Chemistry.

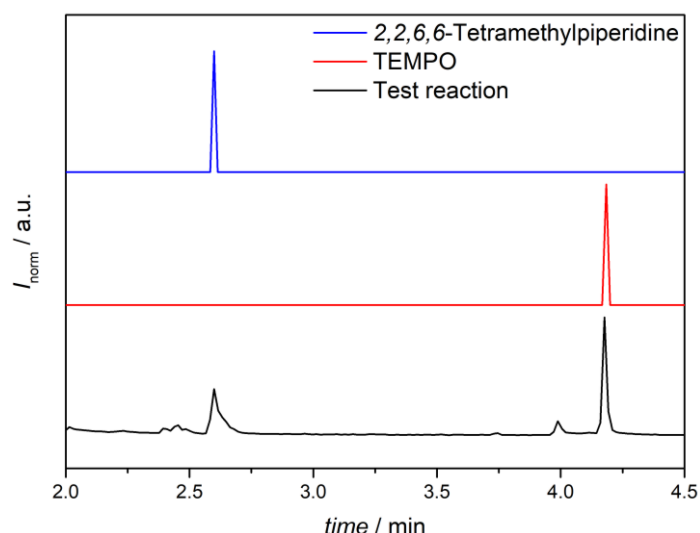


**Figure 45.** GC-MS traces of 2,2,6,6 tetramethylpiperidine, 2,2,6,6-tetramethylpiperidinyloxy (TEMPO) and the reaction mixture of **34-36** for the unfolding/deprotection reaction. Adapted from ref [256] with permission of the Royal Society of Chemistry.

After establishing the concept for the folding/unfolding for the polymers on a small molecule basis, the crosslinking reaction was transferred to the polymers **P32'-P35'**. Initially, the crosslinking reaction was conducted by employing a stoichiometric amount of the bifunctional crosslinker **33**, yielding the SCNPs **NP1-NP4** (refer to Figure 46a-f). The intramolecular crosslinking was obtained under highly diluted conditions by employing concentrations in the range of  $6 \times 10^{-5} \text{ mg mL}^{-1}$  to  $4 \times 10^{-5} \text{ mg mL}^{-1}$ , using anisole as solvent. After the collapse, the SEC traces for the unfolded precursor polymers (**P32'-P35'**) are shifted towards higher retention times (refer to Figure 46a-d), indicating the formation of intramolecular crosslinks. At higher concentrations ( $1 \times 10^{-4} \text{ mg mL}^{-1}$ ), intermolecular crosslinking is observed (refer to Figure 46e). Furthermore, the solvent was changed to investigate the influence of the solvent on the folding reaction. Anisole was identified as the most appropriate solvent for the folding reaction, since (i) the compound dissolved in anisole completely and (ii) the crosslinking reaction with a stoichiometric amount of **33** displayed the expected shift towards higher retention times obtained by SEC. Further examined solvents were toluene and acetonitrile (ACN). In pure toluene the crosslinker remains insoluble, thus a small quantity of acetonitrile was added (10 mL) in order to dissolve the crosslinker. The crosslinking in toluene displays a shift towards higher retention times obtained by SEC measurements (refer to Figure 46f), suggesting the formation of intramolecular aggregates, yet being less pronounced as for anisole. Pure acetonitrile shows a poor

### 3.2.2 Self-Reporting Refoldable Dynamic Covalent Fluorescent SCNPs

solubility for the TEMPO polymer and furthermore a shift to lower retention times, indicating intermolecular crosslinking is detected in SEC measurements. Hence, for further investigations, anisole was employed as solvent. In addition, a flame-dried flask was used for all crosslinking reaction as well as was degassing of the mixture prior to the UV-light induced SCNP collapse to exclude any side reaction due to moisture and oxygen.

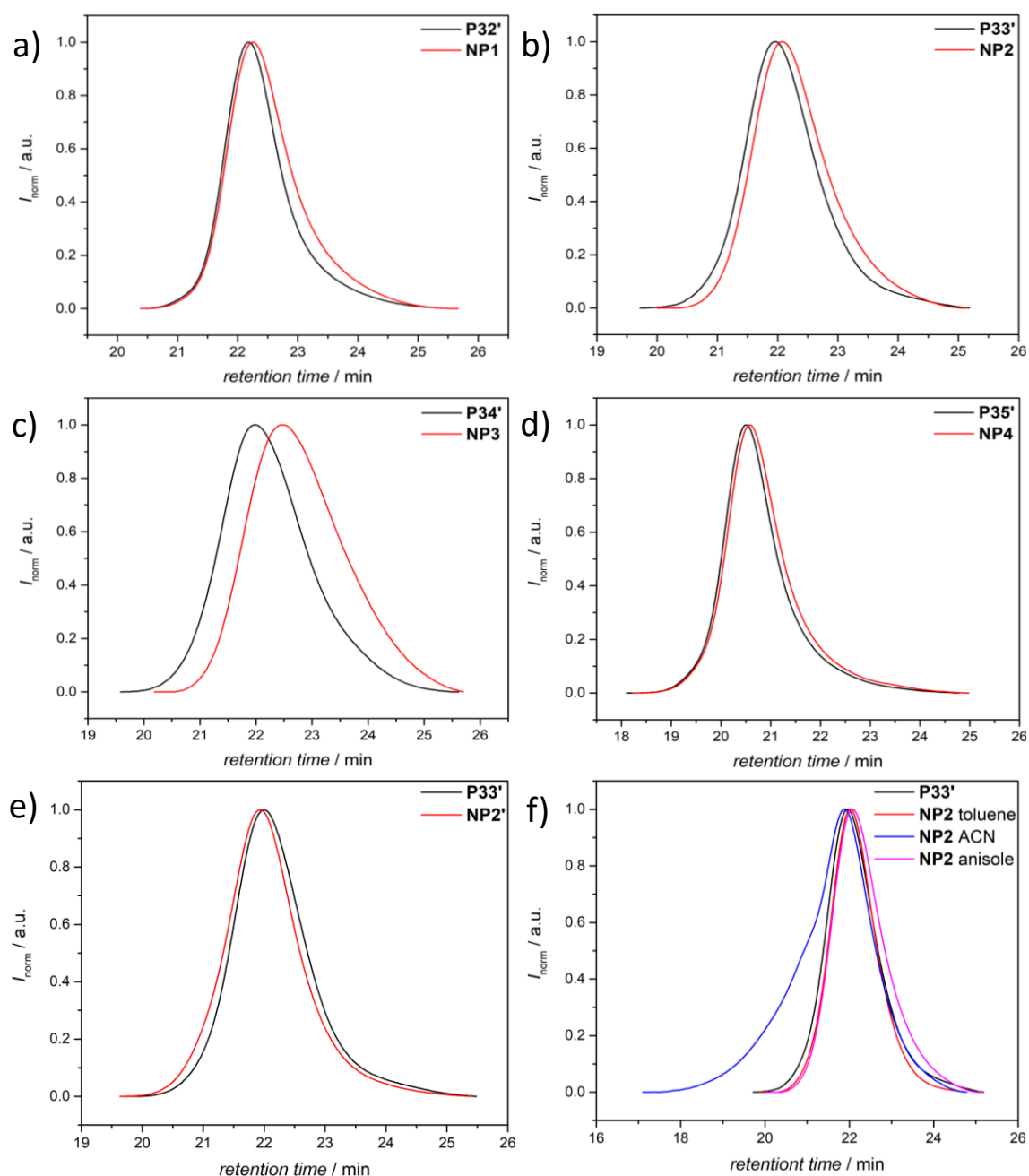


**Figure 46.** a)-d) SEC traces of the unfolded precursor polymers **P32'-P35'** and the single-chain polymeric nanoparticles **NP1-NP4**. e) SEC traces for the UV-light induced crosslinking reaction at higher concentrations leading to intermolecular crosslinking. f) Solvent screening of the crosslinking reaction. All SEC traces were measured in THF, 35 °C, 1 ml min<sup>-1</sup>, using PS standards for calibration. Adapted from ref [256] with permission of the Royal Society of Chemistry.

**Table 10.** Molecular characteristics of the polymers **P32'-P35'** and the SCNPs **NP1-NP5**. The molecular weights, dispersities, the DLS and DOSY derived  $D_h$ , the density of TEMPO and the employed amount of crosslinker **33** for the single-chain collapse are collated. Adapted from ref [256] with permission of the Royal Society of Chemistry.

| ID                            | $M_n^a / \text{g mol}^{-1}$ | $\mathcal{D}^a$ | $D_{h,\text{DLS}}^b / \text{nm}$ | $D_{h,\text{DOSY}}^c / \text{nm}$ | density of TEMPO  | <b>33</b> (eq.) <sup>f</sup> |
|-------------------------------|-----------------------------|-----------------|----------------------------------|-----------------------------------|-------------------|------------------------------|
| <b>P32'</b>                   | 11100                       | 1.2             | 1.7                              | -                                 | 7.8 <sup>d</sup>  | -                            |
| <b>P33'</b>                   | 13200                       | 1.3             | 1.9                              | -                                 | 19.6 <sup>d</sup> | -                            |
| <b>P34'</b>                   | 11500                       | 1.4             | 1.9                              | -                                 | 30.8 <sup>d</sup> | -                            |
| <b>P35'</b>                   | 33300                       | 1.2             | 3.0                              | 3.4                               | 3.89 <sup>e</sup> | -                            |
| <b>NP1</b>                    | 10100                       | 1.3             | 1.4                              | -                                 | -                 | 1                            |
| <b>NP2</b>                    | 11700                       | 1.4             | 1.4                              | -                                 | -                 | 1                            |
| <b>NP3</b>                    | 7800                        | 1.4             | 1.1                              | -                                 | -                 | 1                            |
| <b>NP4</b>                    | 27400                       | 1.3             | 2.4                              | -                                 | -                 | 1                            |
| <b>NP5</b>                    | 18500                       | 1.5             | 2.8                              | 2.6                               | 0.43 <sup>e</sup> | 2                            |
| <b>NP5<sub>unfolded</sub></b> | 33400                       | 1.4             | 3.2                              | 3.5                               | 2.16 <sup>e</sup> | -                            |
| <b>NP5<sub>refolded</sub></b> | 16200                       | 1.6             | 2.3                              | 2.9                               | 0.03 <sup>e</sup> | 2                            |

<sup>a</sup> Determined *via* SEC in THF (35 °C, 1 mL min<sup>-1</sup>) as eluent, calibrated with PS standards. <sup>b</sup> Determined *via* DLS in DMAc + LiBr (0.3%) as solvent. <sup>c</sup> Determined *via* DOSY. <sup>d</sup> Assumption based on complete shift of CH<sub>2</sub>-Cl resonance from the CMS group after modification. Determined *via* <sup>1</sup>H NMR. <sup>e</sup> Determined by EPR. <sup>f</sup> Equivalents were calculated to the corresponding amount of TEMPO.

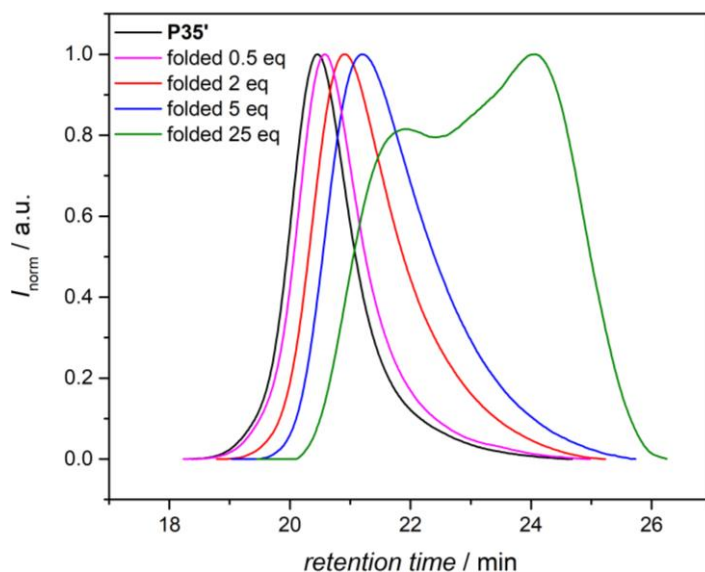
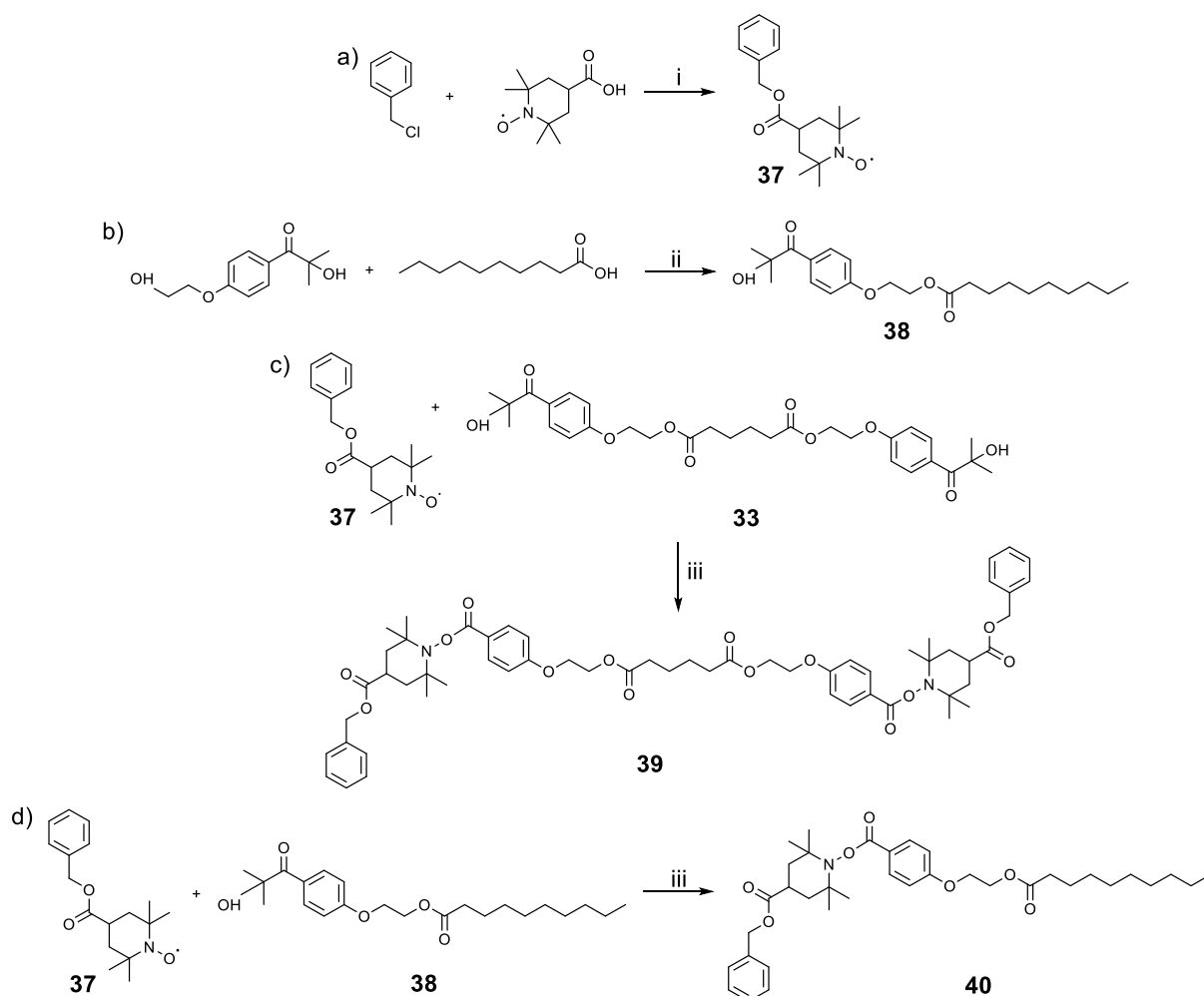


**Figure 47.** SEC traces of **P35'** before (black curve) and after (pink, red, blue and green curves) the crosslinking reaction, investigating the influence of different amounts of crosslinker **33** on the single-chain collapse. Adapted from ref [256] with permission of the Royal Society of Chemistry.

Inspired by the work of the *Berda* group,<sup>[264]</sup> the influence of crosslinker equivalents (with respect to the amount of incorporated nitroxide within the polymer) was explored. Similar to the observations of the *Berda* team, with an increasing quantity of **33** an increased shift towards higher retention times was obtained. When the photoactive crosslinker **33** is employed in large excess (25 equivalents), interchain coupling of the crosslinker is observed as side reaction (refer to Figure 47, green curve). Hence, for further crosslinking reactions of the precursor polymer **P35'** 2 equivalents of **33** were employed to yield a pronounced shift detected by SEC and thus to exclude side reactions of the crosslinker. Folding **P35'** with 2 equivalents of **33** leads to a collapse of close to 44% from 33.3 kDa for the open linear polymer chain to 18.5 kDa to the SCNP **NP5** (refer to Table 10, entry 4 and entry 9, Figure 48). Interestingly, the SCNPs **NP1-NP5** display inherent fluorescence and thus the folded state reports itself in terms of fluorescence.

Further the fluorescence was investigated on a small molecular basis to examine if the fluorescence is only detected when polymers are applied or even in small molecules. In particular, the small molecule benzyl-TEMPO (**37**) was prepared, in order to simulate the monomeric repeating unit of the polymer featuring the nitroxide moiety. In addition, a monofunctional “crosslinker” (**38**) was synthesized (refer to Scheme 35).



**Scheme 35.** a) Synthesis of the benzyl-TEMPO moiety **37** and b) the monofunctional photo active compound **38**. (i)  $K_2CO_3$ , DMF, 50 °C, 72 h. (ii) DMAP, EDC $\times$ HCl, DCM, ambient temperature, 24 h. (iii) anisole, Arimed B6 ( $\lambda_{max}$  = 320 nm), ambient temperature, 24 h.

Subsequently, **37** was reacted with the bifunctional crosslinker **33** as well as the monofunctional analogue **38**. The latter reaction represents the formation of only one crosslink instead of two that **33** is forming. The reaction mixture of the monofunctional photo active compound **38** with the benzyl-TEMPO **37** shows some fluorescence in the range of between 300-400 nm and the reaction mixture of **39** from the reaction of **37** with **33**, some minor fluorescence signal in the same range. Whereas the bifunctional crosslinker **33** itself depicts no overall fluorescence. As a result, the detected fluorescence in the small molecules significantly differs from the fluorescence that is detected for the polymers, especially to the fluorescence of the SCNPs. Note that the signal at close to 480 nm is a systematic artefact signal, which is attributed to the double wavelength that has been used for excitation and is visible in all other small



molecular and polymeric samples as well as pure DCM. As a conclusion of the small molecular fluorescence study, the inherent fluorescence of the single-chain nanoparticles **NP5** is attributed to the crosslink formation, leading to a self-reporting polymeric system. Compared to other fluorescent SCNPs, no fluorophore has to be attached prior or after the SCNP formation due to the generation of the fluorophore by the reaction itself.<sup>[265]</sup>

Strikingly, polystyrene (PS) readily displays fluorescence in solution and in fine particles. The fluorescence of PS is attributed to monomer fluorescence and  $\pi$ -stacking, although being less intensive compared to pyrene, for instance.<sup>[266,267]</sup> Accordingly, the synthesized parent polymer **P35** displays fluorescence in the range from about 270 to 375 nm (excitation wavelength  $\lambda_{\text{exc}} = 240$  nm; refer to Figure 49). TEMPO is known for quenching of fluorescence, thus **P35'**, where the TEMPO is attached, the fluorescence is spin silenced and overall no fluorescence is recorded. Consequently, the system of the established polymers become profluorescent.<sup>[236,268]</sup> After the crosslinking reaction, the SCNP **NP5** reveals fluorescence in the range of 380-550 nm and thus is shifted to higher wavelength compared to the fluorescence of the initial PS polymer. In order to verify the fluorescence is generated by the reaction of the TEMPO moiety with the UV active crosslinker, the monofunctional photo active moiety **38** was reacted with the precursor polymer **P35'** to yield species **NP5'**. The fluorescence spectrum of **NP5'** (refer to Figure 49) shows fluorescence in the same range as the SCNPs **NP5** and the same contour line of the recorded fluorescence is detected. The lower fluorescence intensity of **NP5'** compared to **NP5** is attributed to the fact that the employed crosslinker **38** in **NP5'** is monofunctional and thus only a single link with the polymeric backbone is generated, while the crosslinker **33** in the SCNPs **NP5** features two reactive groups for crosslinking.

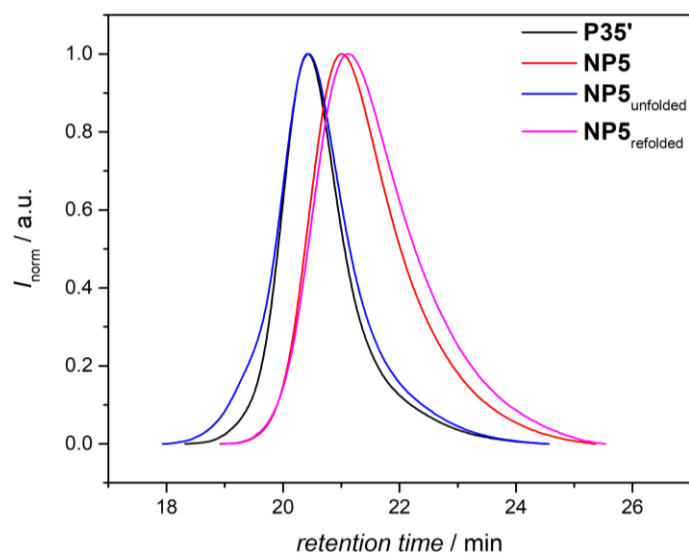


**Figure 48.** SEC traces of the precursor polymer **P35'** (black curve), the folded single-chain nanoparticle **NP5** (red curve), the unfolded polymer **NP5<sub>unfolded</sub>** (blue curve) and the refolded SCNP **NP5<sub>refolded</sub>** (pink curve). All samples were measured in THF, 35 °C, 1 ml min<sup>-1</sup>, using PS standards for calibration. Adapted from ref [256] with permission of the Royal Society of Chemistry.

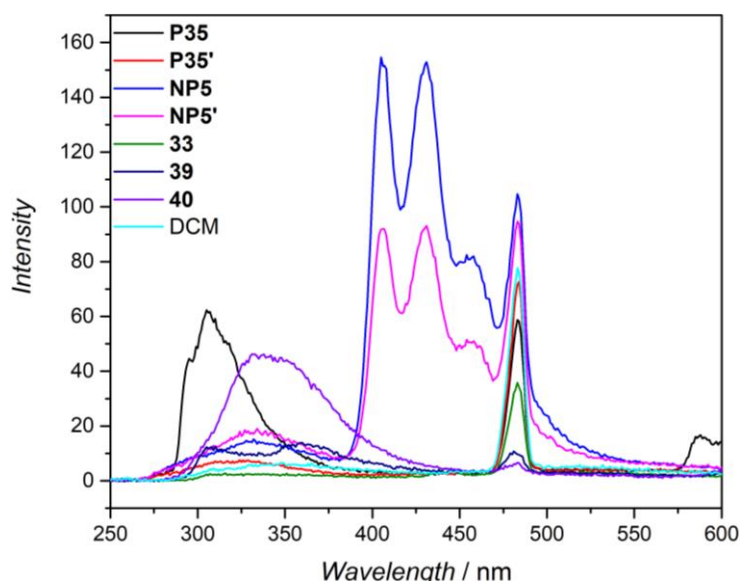


**Figure 49.** Fluorescence spectra of the parent polymer **P35**, the precursor polymer for folding **P35'**, the SCNP **NP5**, the **NP5'**, the bifunctional crosslinker **33**, the reaction mixture of **39** and **40** as well as pure DCM (measured in DCM,  $c = 0.2 \text{ mg mL}^{-1}$ , excitation wavelength  $\lambda_{\text{exc}} = 240 \text{ nm}$ ). Adapted from ref [256] with permission of the Royal Society of Chemistry.

In addition to SEC and fluorescence analysis, the single-chain polymeric nanoparticles were characterized by DLS, <sup>1</sup>H NMR and electron paramagnetic resonance (EPR) spectroscopy as well as DOSY. The DLS and DOSY results are collated in Table 10. Both, the DLS and DOSY derived hydrodynamic diameter ( $D_h$ ) are in good agreement.

### 3.2.2 Self-Reporting Refoldable Dynamic Covalent Fluorescent SCNPs

The precursor polymer **P35'** has a DLS derived  $D_h$  of 3.0 nm, which shrinks upon the SCNP collapse to 2.8 nm for **NP5** (refer to Figure 50). In DOSY measurements, the calculated  $D_h$  decreases from 3.4 nm for the open chain (**P35'**) to 2.6 nm for the nanoparticle **NP5**, indicating the successful collapse towards single-chain architectures. Furthermore, EPR measurements reveal a significant decrease of the TEMPO density. In the linear precursor polymer **P35'**, a TEMPO density of close to 3.89 has been calculated, while in **NP5** the calculated TEMPO density is close to 0.43. Hence, EPR measurements underpin the SEC data and depict an almost quantitative crosslinking of **P35'**. In addition, the  $g$ -factor and the hyperfine coupling constants ( $a_N$ ) of **P35'** are in agreement with the classical TEMPO-based nitroxide structure.<sup>[269]</sup> The  $g$ -value and  $a_N$  for **NP5** are 2.0071 and 15.5 (refer to Table A10). The respective values in literature slightly differ with a reported  $g$ -value of 2.0060 and  $a_N = 14.6$ . The deviation can be explained by the fact that the polymeric sample was measured in toluene, while the TEMPO moiety has been reported in ethyl ether.<sup>[269]</sup>

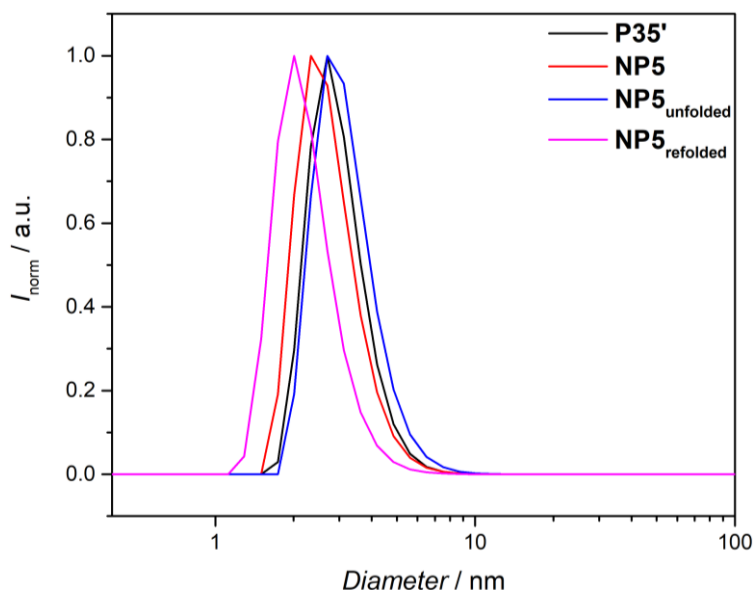


**Figure 50.** DLS analysis of **P35'**, the folded nanoparticle **NP5**, the unfolded **NP5<sub>unfolded</sub>** and the refolded particle **NP5<sub>refolded</sub>**. The samples were measured in DMAc + 0.3% LiBr, the average (minimum of 3 measurements per sample) number size distributions are shown. Adapted from ref [256] with permission of the Royal Society of Chemistry.

Further information about the crosslinking reaction is obtained by  $^1\text{H}$  NMR analysis. The  $^1\text{H}$  NMR spectrum of the crosslinked **NP5** displays the characteristic  $\text{CH}_2$  resonances **b** and **c** of the crosslinker at 4.21 and 4.44 ppm (refer to Figure 51), respectively. Further the resonances indicate the formation of crosslinks. Resonance

**d** is assigned to the  $CH_2$  next to the carbonyl group. The aromatic protons of the aryl rings of the crosslinker (label **f**) in the aromatic region of the  $^1H$  NMR spectrum at 8.03 ppm further demonstrates the incorporation of crosslinker into the nanoparticles. The resonances marked with a star are attributed to solvent impurities. The high resonance intensity of the solvent impurities is due to the high quantity of solvent (500 mL) relative to the low amount of polymer (close to 30 mg) employed for the crosslinking reaction to ensure the formation of SCNPs.

After the precursor polymer **P35** has been successfully folded, in a next step the SCNPs **NP5** were unfolded to re-establish the open chain, featuring the intact nitroxide radicals. For the unfolding, the above discussed conditions established in the small molecule study were employed for the polymeric system to unfold **NP5** (refer to Scheme 36). After the unfolding/deprotection reaction, the SEC trace of the unfolded **NP5<sub>unfolded</sub>** is shifted back to lower retention times and displays an almost identical distribution as the linear precursor polymer **P35'** (refer to Figure 48 blue curve).

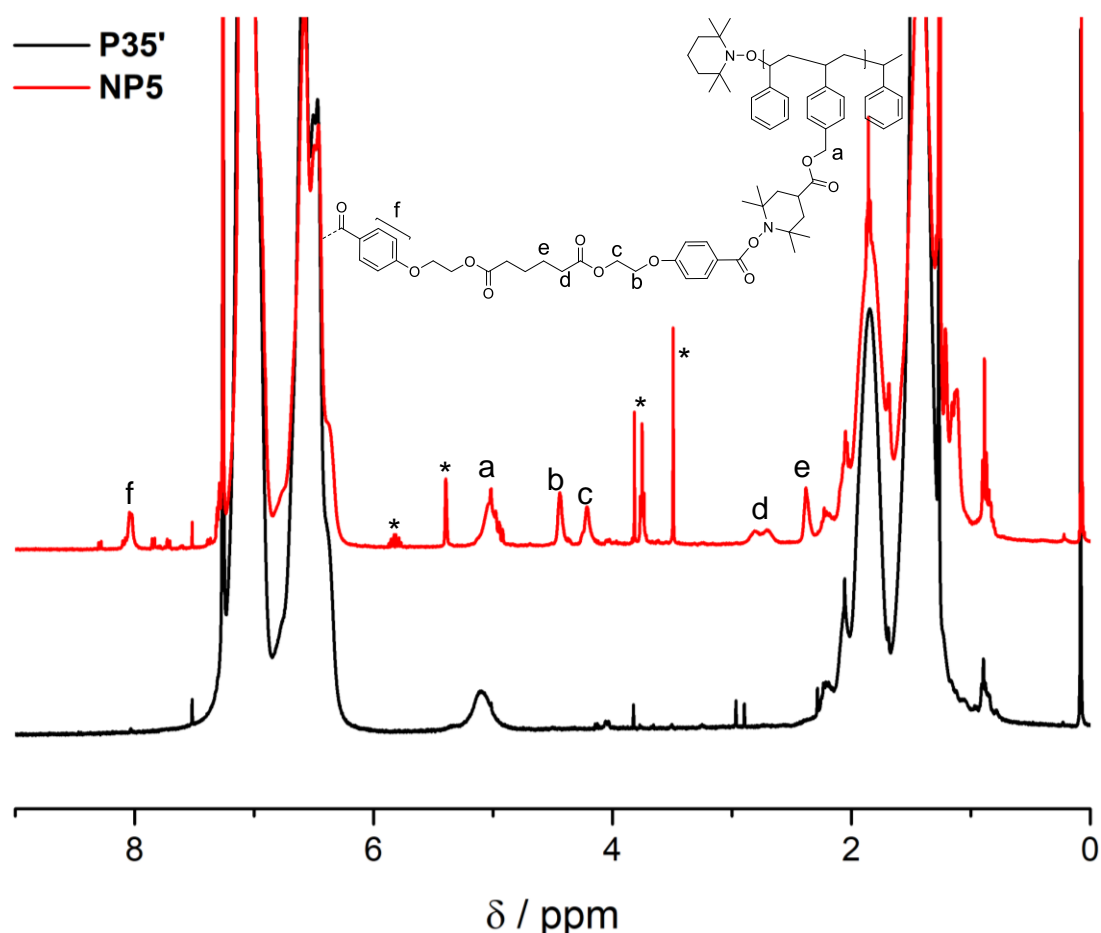
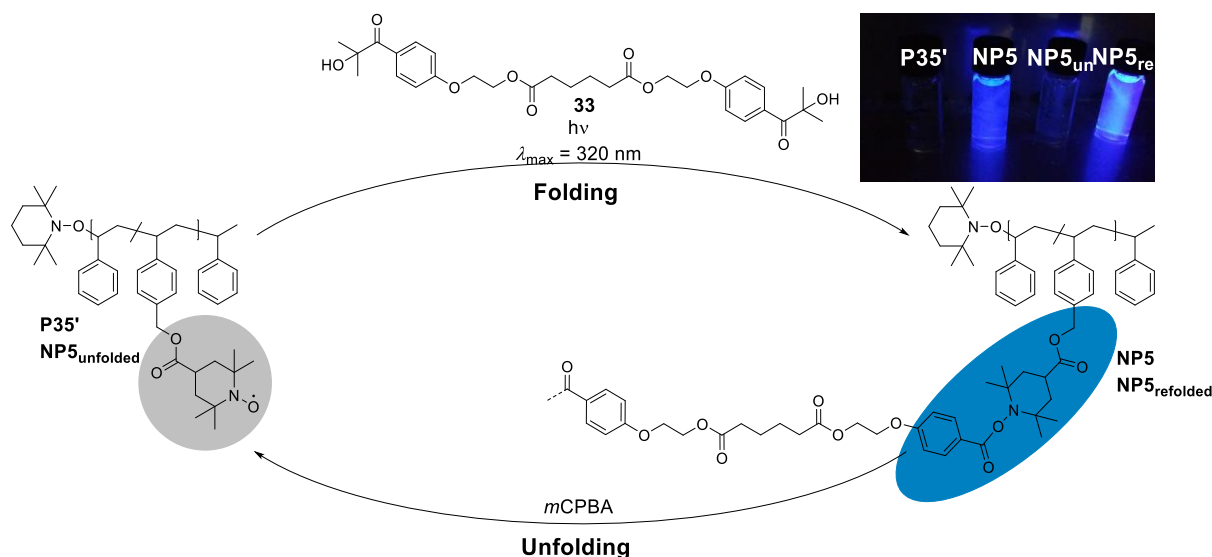


**Figure 51.**  $^1H$  NMR spectra of the precursor polymer **P35'** and the folded **NP5**, measured in  $CDCl_3$  (298 K).

### 3.2.2 Self-Reporting Refoldable Dynamic Covalent Fluorescent SCNPs



**Scheme 36.** Folding cycle of the precursor polymer **P35'** with the bifunctional crosslinker **33**. The folding is induced by UV-light ( $\lambda_{\max} = 320$  nm) resulting in the intramolecular folded SCNPs **NP5** and **NP5<sub>refolded</sub>**. The unfolding of SCNP **NP5** was induced by *m*CPBA restoring the initial state (**NP5<sub>unfolded</sub>**). Adapted from ref [256] with permission of the Royal Society of Chemistry.

The molecular weight of the unfolded polymer (33.4 kDa) is almost identical to the initially measured one for **P35'** (33.3 kDa). The small deviation can be attributed to systematic errors and the calibration variations of the SEC system.

In addition, the DLS and DOSY derived hydrodynamic diameters show an increase after the unfolding reaction. The  $D_h$  obtained by DLS increases from 2.8 nm for the collapsed **NP5** to 3.2 nm for **NP5<sub>unfolded</sub>**, which is slightly higher compared to the initial precursor, which has a  $D_h$  of 3.4 nm (refer to Figure 50 and Table 10). The calculated  $D_h$  from DOSY measurements indicate the same trend to slightly higher diameters of the unfolded species **NP5<sub>unfolded</sub>**. In particular, the  $D_h$  increases from 2.6 nm for **NP5** to 3.5 nm of **NP5<sub>unfolded</sub>** in the linear open chain. This phenomenon can be explained by the hypothesis that for some crosslinks only one crosslinking site is opened after the unfolding reaction, while the second functionality – of the bifunctional crosslinker – stays attached to the TEMPO moiety. The partial opening of one crosslink leads to slightly higher molecular weights as well as hydrodynamic diameter. The hypothesis is further verified by  $^1\text{H}$  NMR and EPR spectroscopy. The  $^1\text{H}$  NMR (refer to Figure 110 in the Appendix) spectrum reveals a decrease of the before mentioned resonances at 4.21 and 4.44 ppm of about 82%, which is congruent with the reported yields for the deprotection of nitroxide species reported by *Chalmers et al.*<sup>[262]</sup> Moreover, EPR

measurements display a lower TEMPO density in the unfolded SCNP, being close to 2.16 as for the precursor polymer **P35'** (3.89, refer to Table 10, entries 4 and 10) and thus confirming the assumption of the cleavage of only one crosslink in some parts of the polymer. The characteristic shape of the EPR spectrum of the unfolded **NP5<sub>unfolded</sub>** is the same as for the precursor polymer **P35'** (refer to Figure 52). Importantly, to successfully develop a self-reporting system, the unfolded polymer must be spin-silenced due to the presence of the re-established nitroxide radicals. Indeed, for the unfolded **NP5<sub>unfolded</sub>** no fluorescence is recorded (refer to Figure 53, blue curve).

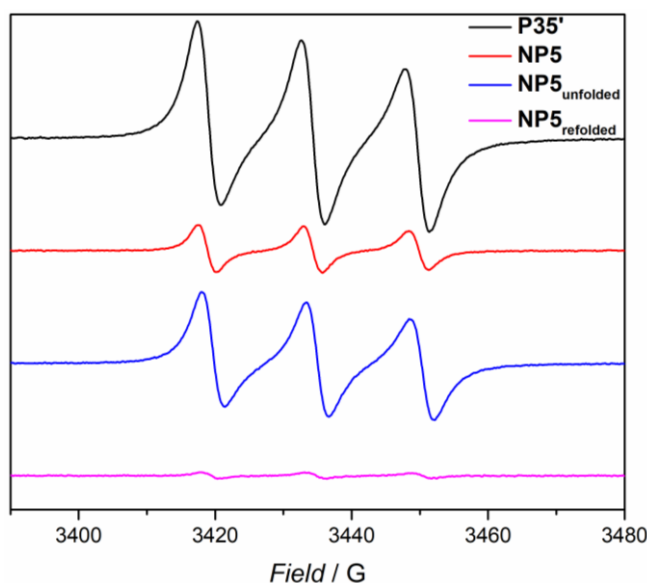


**Figure 52.** EPR signals for the parent polymer **P35'**, the folded SCNP **NP5**, the unfolded **NP5<sub>unfolded</sub>** and refolded SCNP **NP5<sub>refolded</sub>**. All samples were measured in toluene at ambient temperature. Adapted from ref [256] with permission of the Royal Society of Chemistry.

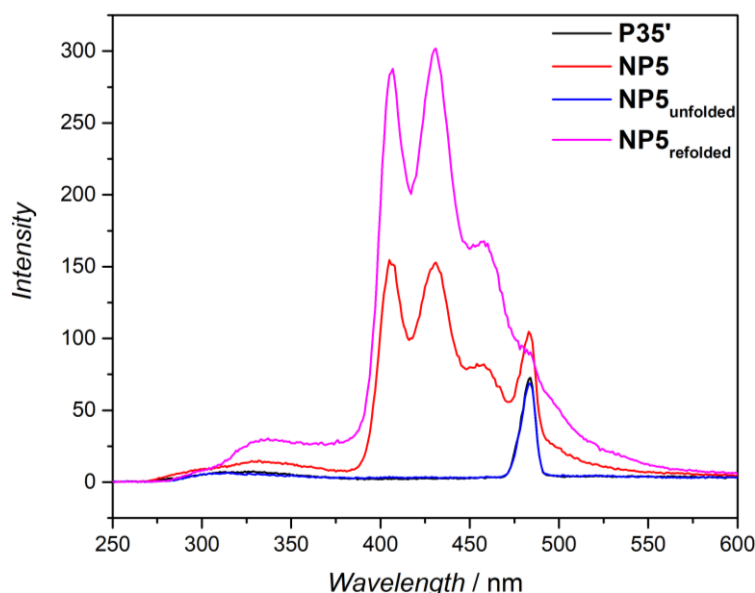


**Figure 53.** Fluorescence spectra for the linear precursor polymer **P35'**, the initially folded **NP5**, the unfolded **NP5<sub>unfolded</sub>** and the refolded SCNP **NP5<sub>refolded</sub>**. All samples were measured in DCM at a concentration of  $c = 0.2 \text{ mg ml}^{-1}$ . Adapted from ref [256] with permission of the Royal Society of Chemistry.

In a crucial step to unambiguously demonstrate that the nitroxide radicals have been re-established and hence the reversibility of the system verified, the unfolded **NP5<sub>unfolded</sub>** was re-subjected to the UV-light induced folding reaction. As for the initial folding reaction, 2 equivalents of the crosslinker **33** were employed in favour of a pronounced shift obtained the SEC. After the crosslinking reaction, the SEC chromatogram (refer to Figure 47, pink curve) displays a shift to higher retention times, attributed to the lower hydrodynamic volume of the refolded **NP5<sub>refolded</sub>** compared to the **NP5<sub>unfolded</sub>**. The shift of **NP5<sub>refolded</sub>** is even larger as for the initially folded **NP5**, indicating a higher crosslinking density. The larger decrease of the  $M_n$  (a decrease from 33.4 kDa to 16.2 kDa for the refolding, compared to a shift from 33.3 kDa to 18.5 kDa for the initial folding reaction; refer to Table 10), is attributed to the use of *m*CPBA: As mentioned before, *m*CPBA is often used as oxidizing agent for piperidine derivatives to the nitroxide radical. In this particular case, the *m*CPBA may restore some nitroxide radicals that were not accessible for the first folding reaction and thus the crosslinking density of the refolded SCNP is higher and consequently an increased shift towards higher retention times is obtained.

The formation of more compact SCNPs in the refolded system is corroborated by DLS, EPR and fluorescence measurements. DLS displays a shift to smaller  $D_h$ , indicated by

a decrease from 3.2 nm for the **NP5**<sub>unfolded</sub> to 2.3 nm to **NP5**<sub>refolded</sub>. In addition to DLS measurements, the DOSY measurements also show a decrease of the polymer after crosslinking, although the refolded nanoparticles are slightly larger (2.6 nm) as the initially folded one (2.9 nm). Nevertheless, the successful refolding of the system is demonstrated. Moreover, EPR measurements (refer to Table 10 and Figure 52) depict a decreased TEMPO density with 0.03 for the refolded SCNP compared to 0.43 for the initially folded **NP5**. Hence, EPR measurements suggest almost quantitative conversion of the TEMPO moiety after refolding. In addition, after the collapse the system does fluoresce again, while in the unfolded state the fluorescence is quenched by the presence of nitroxide radicals. Thus, the self-reporting nature of the developed system is demonstrated.

In summary, the formation of SCNP based on the UV-light triggered reaction of a nitroxide radical with the 2-hydroxy-4'-(2-hydroxyethoxy)-2-methylpropiophenone (Irgacure 2959) moiety has been reported. Further, the reversibility between the open linear polymer chain and the collapsed SCNP was demonstrated by unfolding the SCNPs under oxidative conditions using *meta*-chloroperbenzoic acid (*m*CPBA) to restore the nitroxide radicals. By employing the same reaction conditions for the refolding reaction, the reversibility of the system was unambiguously demonstrated. Moreover, the dynamic covalent crosslinking was followed by <sup>1</sup>H NMR, EPR, DOSY and fluorescence spectroscopy as well as DLS. The current state of the polymer (folded or unfolded) can be followed by fluorescence readout. The folded SCNP displays fluorescence, while the presence of the stable nitroxide radical quenches the fluorescence. The demonstrated reversibility is a further step towards the overall aim of preparing artificial complex biomolecules. The polymer was demonstrated to be switchable between the open form and the collapsed SCNP, mimicking the dynamic folding/unfolding of enzymes. Further, the presented system could potentially be applied as a sensor, due to the self-reporting features *via* fluorescence. For this application, further investigations will have to be carried out. In particular, preparing a water soluble analogue to the presented methodology and examine the folding/unfolding behaviour in biological environments.



## CONCLUSIONS AND OUTLOOK

The field of single-chain folding explores new strategies for preparing so-called single-chain nanoparticles (SCNPs), which are promising materials for applications such as sensing, catalysis or drug delivery. Nevertheless, the ultimate goal of the single-chain realm is to mimic nature by preparing artificial enzyme analogues. In the current thesis, new concepts are introduced to move closer to this aim.

Natural macromolecules such as proteins and enzymes display a dynamical transition between the folded and unfolded states. Thus, the current thesis focuses on the mimicry of this phenomenon and new methodologies towards dynamical single-chain nanoparticles were established in the field of single-chain folding. The methodologies herein developed towards dynamic SCNPs were divided into two classes of single-chain polymeric nanoparticles: (i) the selective point folding route, and (ii) the repeat unit approach. In the selective point folding avenue, the existing concept of the hydrogen bonding system of the complementary motif consisting of Hamilton Wedge (HW)/cyanuric acid (CA) was enhanced by attaching a nitroxide spin-label, which is used to gain further information about the folding mechanism of the system. In addition, nitroxide containing polymers were introduced to high resolution mass spectrometry as a powerful analytical methodology to verify the composition and chemical structure of such polymers. The developed analytical methodology lies the basis as an analytical concept to image folding systems containing nitroxide radicals. Inspired by nature where enzymes often are stabilized by hydrogen bonds and further contain complexed metals, the HW/CA folding unit was merged with the concept of metal complexation of phosphine containing polymers through a palladium (II) salt to increase the system complexity, to synthesize an orthogonal dual folding motif.

In the realm of the repeat unit approach, the recognition units of the HW/CA moieties were combined with the host-guest system consisting of benzo-21-crown-7 and a secondary ammonium salt. Ultimately, a self-reporting refoldable fluorescent dynamical folding system was designed based on the photochemically induced reaction of nitroxides with a photo-active bifunctional crosslinker.

The research illustrated in Section 3.1 is based on the selective point folding avenue. The initially presented system for folding, which consists of the CA/HW folding motif at the  $\alpha$ - and  $\omega$ -positions, respectively, forms six hydrogen bonds and thus induces a cyclization of the polymeric backbone. Since the system has already been investigated, the aim of the current thesis was to obtain detailed information regarding the folding mechanism. Hence, a spin-label – namely 4-Carboxy-2,2,6,6-tetramethylpiperidine 1-oxyl (4-carboxy-TEMPO) – has been inserted in close proximity (penultimate position) to the HW moiety. Thus, the spin-label can be exploited in nuclear magnetic resonance (NMR) experiments to gain information about the distance of the folded polymers. The nitroxide spin-label influences the relaxation time of the system and thus can be exploited to overall determine the length of the hydrogen bonds of the HW/CA pair. The folding and unfolding of the prepared systems in high dilution has been demonstrated by diffusion ordered spectroscopy (DOSY) by the characteristic increase of the hydrodynamic diameter ( $D_h$ ) upon the addition of MeOH, which disrupts the hydrogen bonds and re-established the linear open chain. Further, the molecular weight of the polymer was varied in the range from 5500 g mol<sup>-1</sup> to 30200 g mol<sup>-1</sup> along with dispersities between 1.05 and 1.09, in order to investigate the influence of the chain-length on the single-chain collapse. NMR experiments for the structural information as well as the determination of the folding distance between the complementary motifs are still under investigation by S. Spann (AK Luy, KIT).

In order to establish an analytical basis to determine structural information of nitroxide containing SCNPs that is prohibited by other methods such as NMR, due to the presence of the paramagnetic centre, nitroxide containing polymers featuring different amounts of free stable nitroxide radicals (11.3 to 29.1 mol%) attached to the styrene based polymeric backbone were prepared. Further, the chain-length ( $4800 \geq M_n/g \text{ mol}^{-1} \geq 11100$ ) was altered. The prepared nitroxide containing polymers have been investigated by high resolution electrospray ionization (ESI) mass spectrometry. Here, for the first time structural and chemical information about

nitroxide radical containing polymers become accessible, due to the fact that paramagnetic centres prohibit proper NMR analysis. The recorded ESI mass spectra display an increasing amount of higher molecular weight aggregates associated with an increasing amount of nitroxides within the polymers. In addition, a drift of the baseline for polymers that contain about 30 mol% of TEMPO radicals within the polymeric backbone is detected. The experimental mass spectroscopic patterns were unambiguously assigned and further fit the simulation of the isotopic pattern with different species contributing to the respective peaks. Thus, mass spectrometry was introduced as analytical tool for the characterization to the field of nitroxide containing polymers. The established methodology allows for the structural determination of such species, which are not easily obtained by other methods that usually are employed in the characterization of polymers such as NMR. In addition, the developed analytical method serves as a basis for the structural characterization of SCNPs containing nitroxide radicals.

Furthermore, the hydrogen bonding system (HW/CA) has been combined with the methodology of metal complexation to prepare more sophisticated folding systems. The merge of the hydrogen bonding and metal complexation brings the field of single-chain folding one step closer to the ultimate aim of preparing artificial enzymes, since natural occurring macromolecules, *i.e.* proteins and enzymes, are often stabilized by multiple concepts such as hydrogen bonds, metal complexation and aromatic stacking. Here, a styrene based polymer was prepared, featuring the hydrogen bonding system in  $\alpha$ - and  $\omega$ -position, whereas the phosphine groups were placed at preselected points along the polymeric backbone. The orthogonal and controlled collapse under highly diluted conditions ( $1 \text{ mg mL}^{-1}$ ) was examined by dynamic light scattering investigations. DLS measurements depict a significant increase after a competitive solvent (*i.e.* methanol) is added in small amounts. Compared to the dual compacted SCNPs that features the hydrogen bonds and the metal complexation, the SCNP only containing the hydrogen bonds has an increased  $D_h$ . Thus, the successful dual compaction is demonstrated. Furthermore, DOSY results underpin the DLS results by displaying the same trends towards lower hydrodynamic diameter of the dual folded system and an increased  $D_h$  after the addition of MeOH.

In the repeat unit approach, a system that fuses the hydrogen bonding motif HW/CA presented in Section 3.1 with the host-guest system consisting of the benzo-21-crown-

7 (B21C7; host) and a secondary ammonium salt (AS; guest) adopted from supramacromolecular chemistry, is established. In a proof of principle study, the B21C7/AS host-guest system was orthogonally linked to a well-defined methacrylate based AB-type diblock copolymer that has been synthesized *via* the reversible addition-fragmentation chain transfer polymerization (RAFT) technique. Here, the B21C7 host was attached to the A block, while the AS guest motif was grafted to the B block in post-polymerization modifications. Each block features close to 5 mol% of the respective functionality. The single-chain collapse was subsequently induced in high dilution conditions and characterized by DLS and DOSY. Both characterization methods show the same trend towards higher  $D_h$  after addition of a competitive host such as a potassium salt (KPF<sub>6</sub>).

Furthermore, a well-defined ABCD type tetrablock copolymer was prepared by RAFT polymerization and modified in post-polymerization modifications with the hydrogen bonding motif (HW/CA) on the blocks A and D as well as the host-guest system (B21C7/AS) on the middle blocks B and C. Each block entails up to 5 mol% of the respective functional group. The orthogonal interaction of the motifs at concentrations of 2.5 mg mL<sup>-1</sup> was investigated by means of <sup>1</sup>H NMR spectroscopy, DLS and DOSY. To mimic the dynamic folding/unfolding of enzymes, the dynamic nature of the non-covalent folding points was demonstrated by unfolding the dual folded system pathway independent as well as orthogonally by adding different chemical trigger signals. The orthogonal unfolding was examined by (i) cleavage of the hydrogen bonds by adding MeOH to destroy the hydrogen bonds and (ii) the addition of a competitive guest (K<sup>+</sup>) leading to the decomplexation of the host-guest interaction. The orthogonal unfolding was demonstrated by means of DLS and DOSY. Here, for each unfolding event a significant increase in the hydrodynamic diameter of about 2 nm is detected. In order to demonstrate the pathway independence of the unfolding, the addition of trigger signals was inverted. Importantly, DLS and DOSY measurements display similar results for the increase of the hydrodynamic diameter obtained by DLS and DOSY. In addition, the concentration dependency of the intra- vs. intermolecular interactions was examined by DLS and DOSY measurements by increasing the concentrations. Thus, the intramolecular single-chain collapse is verified up to concentrations of about 8 mg mL<sup>-1</sup>, while at higher concentrations intermolecular interactions dominate. The established concept marks a further step in the overall aim of the field of single-chain technology to mimic natural occurring enzymes. In particular, the selectively

addressable interacting recognition motifs marks an important step towards controlling the folding process as well as the current state of the (folded) system.

Finally, the photo-induced collapse of nitroxide containing polymers with a bifunctional photoactive crosslinker was examined. Here, statistical copolymers consisting of styrene and 4-(chloromethyl) styrene were prepared by nitroxide-mediated polymerization (NMP) and decorated in post-polymerization modifications with 4-carboxy TEMPO. The polymers vary in molecular weights ( $11100 \geq M_n/g \text{ mol}^{-1} \geq 33300$ ) and TEMPO density (3.9 – 30.5 mol%) linked to the polymeric backbone. Thereafter, the folding reaction was induced by UV-light ( $\lambda_{\text{max}} = 320 \text{ nm}$ ) by employing a bifunctional crosslinker featuring the photoactive 2-hydroxy-4'-(2-hydroxyethoxy)-2-methylpropiophenone (Irgacure 2959) moiety on both chain termini. The intramolecular collapse was achieved under highly diluted conditions ( $0.04 \text{ mg mL}^{-1}$ ) to avoid intermolecular crosslinking. Initially, the amount of crosslinker was evaluated. Stoichiometric amounts of the crosslinker led to a very slight shift obtained by SEC, whereas with increasing excess of the crosslinker the shift becomes more and more pronounced. By employing a huge excess (25 equivalents) of the bifunctional crosslinker, the interchain coupling of the crosslinker is observed. After the single-chain collapse, the SCNPs were unfolded under oxidative conditions using *meta*-chloroperbenzoic acid (*m*CPBA) to regenerate the nitroxide radicals and the initial linear polymer chain. Inspired by the dynamic folding/unfolding of enzymes, the unfolded polymer was subjected to a refolding reaction employing the same conditions as for the initial folding reaction to unambiguously demonstrate the dynamic nature of the system. The initial folding, unfolding and refolding reaction were investigated by means of SEC measurements, which display the characteristic shift towards higher retention times for the SCNPs. Further, similar molecular weights and dispersities for the unfolded linear precursor and unfolded analogue were obtained. The refoldable system was further examined by DLS and DOSY, which confirm the SCNPs formation and re-establishment of the initial state for the unfolded SCNPs. The decrease/increase upon folding/unfolding of the nitroxide radical content for the open chain and the folded SCNPs was further followed by EPR spectroscopy. Moreover, the folded and refolded SCNPs further display inherent fluorescence, while in the open chain the fluorescence is spin-silenced through the presence of the nitroxide radical. Consequently, the established system is self-reporting *via* fluorescence.

In summary, the present thesis reports significant steps towards the overall aim of mimicking nature and the ultimate goal for the preparation of artificial enzymes, by establishing synthetic protocols for dynamic single-chain nanoparticles. The last section for the preparation of self-reporting refoldable fluorescent SCNPs may be of broad interest, as the reversibility of the system was demonstrated and a smooth transition between the folded state and the open chain is ensured. Further, the current state of the system can be easily assessed by a simple fluorescence readout, which might be interesting for potential applications such as sensing.

Nonetheless, the precise and exclusive control observed in nature is still beyond the reach of synthetic chemists, independent of the selected route – selective point folding or the repeat unit approach. Continuous efforts in the field of single-chain folding are required, *e.g.* establishing monodisperse single-chain nanoparticles. Monodisperse SCNPs would mark another significant step in mimicking nature, due to the fact that natural enzymes and proteins show monodispersity. In addition, monodispersity guarantees a uniform configuration of the system and thus all catalytic active sites are equally defined. Further, existing methodologies must be transferred into aqueous media in order to emulate natural enzymes. Accordingly, the collapse needs to be controlled in terms of the secondary and higher ordered structures – similar to the secondary, tertiary or even quaternary structures of enzymes – to implement a certain structure such as helical arrangement to the collapsed nanoparticles. Moreover, computational simulation could spur efforts to identify systems capable of combining features such as monodisperse folding systems leading to a helical structure to mimic the structure of DNA, for example. Another important point that needs to be addressed are the appropriate analytical methods to unambiguously characterize and demonstrate the formation of those structures. For the in-depth characterization of the established SCNPs systems, a combination of multiple analytical methods must be carried out to fully characterize the single-chain nanoparticles. In addition, the combination of recognition units to produce even higher folded architectures, such as triple folding systems are envisioned to be realized to close the gap between the existing single-chain technology toolbox of synthetic chemists and nature. In order to achieve a specific function of single-chain nanoparticles with a certain application, investigations in biological environments must be carried out to close the gap between natural and artificial macromolecules step-by-step.

## EXPERIMENTAL SECTION

### 5.1 Materials

1-Ethyl-3-(3-dimethylaminopropyl)carbodiimid (EDC×HCl) (≥99%, Roth), 1,8-diazabicycloundec-7-ene (DBU, ≥97%, Fluka), 2-Hydroxy-4'-(2-hydroxyethoxy)-2-methylpropiophenone (>98%, TCI), 2,2-dimethoxypropane (98%, Sigma-Aldrich), 2,2-bis(hydroxymethyl)propionic acid (98%, Sigma-Aldrich), 2,6-diaminopyridine (98%, Acros), 3,4-dihydroxybenzoic acid (≥97%, Sigma-Aldrich), 4-Carboxy-2,2,6,6-tetramethylpiperidine 1-oxyl (4-carboxy-TEMPO, >97%, TCI), 4-cyano(phenylcarbonothioylthio)pentanoic acid (97%, Sigma-Aldrich), 4-(diphenylphosphino)benzoic acid (97%, Sigma-Aldrich), 4-hydroxybenzaldehyde (98%, Acros), 5-bromovaleryl chloride (97%, Sigma-Aldrich), 5-hydroxyisophthalic acid (99%, Acros), 6-bromo-1-hexanol (97%, Sigma-Aldrich), 11-bromoundecanoic acid (99%, Sigma-Aldrich), 11-bromoundecanol (>97%, TCI), acetone (p.a., VWR), acetone-*d*<sub>6</sub> (99.8%, D Eurlisotop), anhydrous acetonitrile (99.8%, Acros), ammonium hexafluorophosphate (NH<sub>4</sub>PF<sub>6</sub>, 99%, Acros), anisole (99%, Acros), azobisisobutyronitrile (AIBN, ≥97%, Sigma-Aldrich), benzoylchloride (99%, ABCR), bromoacetyl chloride (97%, ABCR), butan-1-amine (99.5%, Sigma-Aldrich), chloroform-*d*<sub>6</sub> (99.8 atom% D, Sigma-Aldrich), copper sulphate pentahydrate (98%, Acros), cyanuric acid (99%, ABCR), cyclohexane (p.a., VWR), anhydrous dichloromethane (Acros, 99.8%), dichloromethane-*d*<sub>2</sub> (99.8 atom% D, Sigma-Aldrich), decanoic acid (98%, Sigma-Aldrich), dichloromethane (p.a., VWR), *N,N*-dicyclohexylcarbodiimide (DCC, 99%, Acros), diethylether (p.a., VWR), *N,N*-

diisopropylethylamine (DIPEA,  $\geq 99,5\%$ , Sigma-Aldrich), anhydrous dimethyl formamide (DMF, 99.8%, Acros), dichloro(1,5-cyclooctadiene)palladium (II) (99%, Sigma-Aldrich), dimethylaminopyridine ( $\geq 99\%$ , Sigma-Aldrich), dimethylpropylamine ( $\geq 98\%$ , Sigma-Aldrich), dimethyl sulfoxide- $d_6$  (DMSO- $d_6$ , 99.8% D, Eurlisotop), anhydrous dioxane ( $\geq 99,5\%$ , Acros), di-*tert*-butyl dicarbonate (97+%, Alfa Aesar), Dowex<sup>®</sup> MB Mixed Ion Exchange Resin (Sigma-Aldrich), ethyl acetate (p.a., VWR), ethylenediaminetetraacetic acid (EDTA,  $\geq 99\%$ , Roth), ethylmagnesium bromide (0.9 M in THF, Acros), hexaethylene glycol (97%, Sigma-Aldrich), hexane (p.a., VWR), hydrochloric acid (HCl) (37%, Roth), hydroxyethylmethacrylate (97%, Acros), lauroyl peroxide (LPO, 97%, Alfa Aesar), methacryloyl chloride ( $\geq 97\%$ , Sigma-Aldrich), methanol (p.a., VWR), neutral Aluminum oxide (Acros), oxalylchloride (98%, Acros), potassium carbonate ( $\geq 99\%$ , Alfa Aesar), potassium hexafluorophosphate ( $\geq 98\%$ , Alfa Aesar), propargylalcohol ( $> 98\%$ , TCI), *p*-toluenesulfonyl chloride (98%, ABCR), sodium ascorbate (98%, VWR), sodium azide (99%, Acros), sodium borohydride (98+%, Acros), sodium chloride ( $\geq 99,8\%$ , Roth), sodium hydrogencarbonate ( $\geq 99\%$ , Roth), sodium hydroxid ( $\geq 99\%$ , Roth), sodium sulphate ( $\geq 99\%$ , Roth), sulphuric acid (H<sub>2</sub>SO<sub>4</sub>, 96%, Roth), *tert*-butylacetyl chloride ( $\geq 98.5\%$ , Sigma-Aldrich), *tert*-butylchloride (99%, Sigma-Aldrich), tetrabrom methane (98%, Acros), anhydrous tetrahydrofuran (THF, 99.5%, Acros), tetrahydrofurane (THF, p.a., VWR), tetra-*n*-butylammonium fluoride (TBAF, 1M in THF, Alfa Aesar), tin (II) ethylhexanoate (92.5-100%, Sigma-Aldrich), triethylamine (99 %, Fischer Scientific), triisopropylsilyl chloride (97%, Sigma-Aldrich), tris[2-(dimethylamino)ethyl]amine (Me<sub>6</sub>TREN,  $> 98\%$ , TCI), triphenylphosphane ( $\geq 99\%$ , Merck), anhydrous toluene (99.85%, Acros) were used as received. 2-Ethylhexyl methacrylate (EHMA) ( $\geq 99\%$ , TCI) was passed through a short column of neutral alumina (ACROS) and stored at -20 °C. Styrene ( $> 99.5\%$ , Sigma-Aldrich) was passed over a column of basic alumina (Acros) and 4-(chloromethyl)styrene ( $> 90\%$ , TCI) was distilled before usage and stored at -20 °C.



## 5.2 Instrumentation

### Nuclear Magnetic Resonance Spectroscopy (NMR)

The structures of the synthesized compounds were confirmed *via*  $^1\text{H}$ - and  $^{13}\text{C}$ -NMR spectroscopy using a Bruker AM 400 MHz spectrometer for hydrogen nuclei and 100 MHz for carbon nuclei. Samples were dissolved in  $\text{CDCl}_3$ ,  $\text{DMSO-}d_6$ , acetone- $d_6$ ,  $\text{CD}_2\text{Cl}_2$  or  $\text{CD}_2\text{Cl}_2/\text{acetonitrile-}d_3$  (for the self-assembly study). The chemical shifts are reported in ppm relative to the solvent's residual  $^1\text{H}$  or  $^{13}\text{C}$  signal of the employed solvent. The coupling constants ( $J$ ) are reported in Hertz [Hz]. Abbreviations used below in the description of the materials' syntheses include singlet (s), broad singlet (bs), doublet (d), triplet (t), quartet (q), and unresolved multiplet (m).

### Size Exclusion Chromatography (SEC)

SEC was performed to obtain the molecular weight distribution of the synthesized polymers. The employed system was a PL-SEC 50 Plus (Polymer Laboratories) running on tetrahydrofuran (THF) (HPLC-grade) featuring an autosampler, a Plgel Mixed C guard column (50  $\times$  7.5 mm), followed by three Plgel Mixed C linear columns (300  $\times$  7.5 mm, 5  $\mu\text{m}$  bead-size) and a differential refractive index (RI) detector. The device was operated at 35  $^\circ\text{C}$  column temperature with a flow rate of 1  $\text{mL}\cdot\text{min}^{-1}$ . The calibration was carried out with linear poly(methyl methacrylate) standards ranging from 160 to  $6\cdot 10^6$   $\text{g}\cdot\text{mol}^{-1}$ . The injected samples were dissolved in THF (2  $\text{mg}\cdot\text{mL}^{-1}$ ) and filtered through a 0.2  $\mu\text{m}$  filter.

Alternative measurements were performed on an Agilent Series 1200 running on tetrahydrofuran (THF, HPLC grade) featuring an autosampler, a Plgel Mixed C guard column (50  $\times$  7.5 mm), followed by three Plgel Mixed C linear columns (300  $\times$  7.5 mm, 5 $\mu\text{m}$  bead-size), and a differential refractive index (RI) detector. The device was operated at 35  $^\circ\text{C}$  with a flow rate of 1  $\text{mL}\cdot\text{min}^{-1}$ . The calibration was carried out with linear poly(styrene) standards ranging from 476 to  $2.5\cdot 10^6$   $\text{g}\cdot\text{mol}^{-1}$ . The injected samples were dissolved in THF (2  $\text{mg}\cdot\text{mL}^{-1}$ ).

### **Dynamic Light Scattering (DLS)**

The DLS measurements were performed on a Nicomp 380 DLS instrument from Particle Sizing Systems, Santa Barbara, USA (laser diode: 90 mW, 658 nm). The polymer solutions were prepared by dissolving the polymer samples in DCM at different concentrations (2.5, 5 and 10 mg mL<sup>-1</sup>, which were filtered over a 0.2 µL filter before being analysed. The measurements were performed in automatic mode and evaluated by a standard Gaussian and an advanced evaluation method, the latter using an inverse Laplace algorithm to analyze for multimodal distributions. Numbers given in the text are the number weighted average values as calculated by the NICOMP evaluation. All measurements were performed at 90° to the incident beam.

Alternative measurements were performed on a Zetasizer Nano ZS light scattering apparatus (Malvern Instruments, UK) equipped with He-Ne laser (at a wavelength of 633 nm, 4 mW) to determine the apparent hydrodynamic diameters ( $D_{h,app}$ ) at 25 °C. The Nano ZS instrument incorporates a non-invasive backscattering (NIBS) optic with a detection angle of 173°. The polymer samples were dissolved at a concentration of 2 mg mL<sup>-1</sup> in DMAc (+0.3% LiBr) and filtered into quartz cuvettes over a 0.2 µL filter prior to the measurement. The prepared samples were stabilized for 30 min prior to DLS analysis at ambient temperature. All values of the apparent hydrodynamic diameter for each polymer mixture were averaged over three measurements (60 runs/measurement), and were automatically provided by the instrument using a cumulative analysis.

The autocorrelation functions are shown in the Appendix (Section 7).

### **Electrospray Ionization Mass Spectrometry (ESI MS)**

Mass spectra were recorded on a Q Exactive (Orbitrap) mass spectrometer (Thermo Fisher Scientific, San Jose, CA, USA) equipped with a HESI II probe. All spectra were recorded in negative ion mode, using DCM/MeOH (doped with 0.1% NaCl) (3:1, v/v) in a concentration of 0.5 mg·mL<sup>-1</sup> as solvent. The Fourier-Transform resolution was set to 140 000, employing three microscans during an acquisition time between 3 and 6 min, measuring with a capillary temperature of 320 °C. The aux gas flow was set to (dimensionless) 0.00, the sheath gas to 10.00, and the spare gas to 0.00. The flow rate

was set to 5  $\mu\text{L}\cdot\text{min}^{-1}$ . The spray voltage was set to 3.6 keV for the PS-co-CMS (9.3%), 3.9 keV for PS-co-TEMPO (11.3%), 3.3 keV for PS-co-CMS (15.3%), 3.3 keV for PS-co-TEMPO (16.3%), 2.8 keV for PS-co-CMS (35.7%), 3.0 keV PS-co-TEMPO (27.8%), 4.3 keV for PS-co-CMS (34.9%), 3.7 keV for PS-co-TEMPO (29.1%) and 3.2 keV for the CA-PS-HW/TEMPO polymer.

### Electron Paramagnetic Resonance Spectroscopy (EPR)

Electron paramagnetic resonance (EPR) spectroscopy was performed on a Magnettech MiniScope MS400 spectrometer. All samples were recorded in chloroform at 23 °C. A TEMPO calibration curve was employed for quantitative EPR measurements.

Alternative measurements were performed on a Bruker EMXNano spectrometer. All samples were recorded in toluene at 23 °C. The following parameters were used for the measurement: Centre field: 3434 G; sweep width: 100 G; sweep time: 180 s; sample  $g$ -factor: 2.00; receiver gain: 40 dB; modulation amplitude: 0.452 G; number of scans: 1; microwave attenuation: 60 dB; number of points: 2212; modulation frequency: 100 kHz, modulation phase: 0; conversion time: 81.38 ms; time constant: 1.28 ms; points/modulation amplitude: 10.

The  $g$ -factors were calculated according to:

$$g = \frac{71,4484 \cdot \nu}{B}$$

### Fluorescence Spectroscopy

Fluorescence emission spectra were recorded on a Varian Cary Eclipse fluorescence spectrometer, using quartz cuvettes loaded with 400  $\mu\text{L}$  of sample. An excitation wavelength of 240 nm (slit 2.5 nm) was used and the emission was recorded from 250 to 800 nm (slit 10nm).

### Ultraviolet/Visible light (UV/Vis) Spectroscopy

The UV/Vis spectra were recorded on a Cary 100 UV-Visible Spectrophotometer (Agilent Technologies, USA) equipped with a tungsten halogen light source (190 to 900 nm, accuracy +/-2 nm) and a R928 PMT detector. The analysis was performed at ambient temperature.

### Diffusion Ordered Spectroscopy (DOSY) NMR

DOSY experiments were performed on a 400 MHz Bruker Avance III HD spectrometer equipped with a broadband  $^1\text{H}$  decoupling probe (PABBO) and a 600 MHz Bruker Avance III spectrometer equipped with a cryogenically cooled probe head using an Eddy current compensated bipolar gradient pulse sequence (BPLED) at the temperature of 300.5 K. Proton pulse lengths were determined to be 9.68  $\mu\text{s}$  on the 400 MHz spectrometer and 8.12  $\mu\text{s}$  on the 600 MHz spectrometer. Bipolar gradients of  $\delta = 2.4\text{-}4.4$  ms (depending on the diffusion behaviour of the measured sample) length were incremented from  $G = 0.96$  G/cm to 47.19 G/cm in 32 steps. 8 scans with 4k complex data points were recorded for each increment with 8 dummy scans per experiment, leading to an overall experiment time of 16 minutes and 2 seconds per sample. The d1 time was set to 3 sec with an acquisition time of 512ms. The diffusion delay  $\Delta$  was set to 100 ms. Processing was achieved using the Topspin 3.1 software with the Dynamics Center 2.0.4. After apodization using an exponential window function with an additional linewidth of 0.3 Hz, 1D increment spectra were Fourier transformed and the signal decay due to gradients was fitted using

$$f(G) = I_0 \cdot e^{\left(-\gamma_H^2 \cdot G^2 \cdot \delta^2 \cdot \left(\Delta - \frac{\delta}{3}\right)\right) \cdot D}$$

with the proton gyromagnetic ratio  $\gamma_H$  and the full signal intensity  $I_0$ . The resulting diffusion coefficients ( $D$ ) of the polymer signals and the solvent are the result of the fitting procedure.

Alternative measurements were performed on a 400 MHz Bruker Avance III HD spectrometer equipped with a broadband  $^1\text{H}$  decoupling probe (PABBO) and a 600 MHz Bruker Avance III spectrometer equipped with a cryogenically cooled probe head

using an Eddy current compensated bipolar gradient pulse sequence (BPLED) at the temperature of 300.5 K. Proton pulse lengths were determined to be 9.68  $\mu\text{s}$  on the 400 MHz spectrometer and 8.12  $\mu\text{s}$  on the 600 MHz spectrometer. Bipolar gradients of  $\delta = 2.4\text{-}4.4$  ms (depending on the diffusion behaviour of the measured sample) length were incremented from  $G = 0.96$  G/cm to 47.19 G/cm in 32 steps. 8 scans with 4k complex data points were recorded for each increment with 8 dummy scans per experiment, leading to an overall experiment time of 16 minutes and 2 seconds per sample. The d1 time was set to 3 sec with an acquisition time of 512ms. The diffusion delay  $\Delta$  was set to 100 ms. Processing was achieved using the Topspin 3.1 software with the Dynamics Center 2.0.4. After apodization using an exponential window function with an additional linewidth of 0.3 Hz, 1D increment spectra were Fourier transformed and the signal decay due to gradients was fitted using

$$f(G) = I_0 \cdot e^{\left(-\gamma_H^2 \cdot G^2 \cdot \delta^2 \cdot \left(\Delta - \frac{\delta}{3}\right)\right) \cdot D}$$

with the proton gyromagnetic ratio  $\gamma_H$  and the full signal intensity  $I_0$ . The resulting diffusion coefficients ( $D$ ) of the polymer signals and the solvent are the result of the fitting procedure. As mono-exponential fits were not always satisfying, one sample (**P31** +  $\text{KPF}_6$  and MeOH) was selected to study the diffusion coefficient in detail. At longer run times (4h 30 minutes and 32 seconds, performing 96 gradient increment steps and extended relaxation delays of 20 s between scans) and thus higher S/N ratio due to the employed cryoprobe, two components become visible (for a detailed discussion of the components refer to the discussion in Section 3.2.1; the primary DOSY data are collated in the Appendix, Section 7).

**Conversion of the Diffusion Coefficient  $D$  to the Hydrodynamic Diameter  $D_h$** 

The hydrodynamic diameter were calculated with the Stokes-Einstein equation:<sup>[52]</sup>

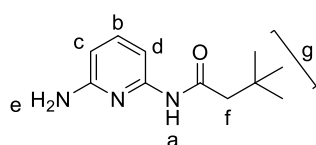
$$R_h = \frac{kT}{6\pi\eta D}$$

where  $R_h$  is the hydrodynamic radius of the polymer coil in meters,  $k$  is the Boltzmann constant ( $1.380 \times 10^{-23} \text{ J K}^{-1}$ ),  $T$  is the temperature in Kelvin (298 K),  $\eta$  is the viscosity of the solvent in Pascal seconds (0.413 mPa s) and  $D$  is the diffusion coefficient.<sup>[52]</sup>

## 5.3 Experimental Procedures

### 5.3.1 Small Molecule Syntheses

#### Synthesis of *N*-(6-aminopyridin-2-yl)-3,3-dimethylbutanamide (**3**)



Following a modified literature procedure,<sup>[270]</sup> to a solution 2,6-diaminopyridine (25.0 g, 0.23 mol, 1.0 equiv.) in dioxane (250 mL), *tert*-butylacetylchloride (15.42 g, 0.115 mol, 0.5 equiv.) dissolved in dioxane was added over the course of 1 h. The mixture was stirred for 2 h at ambient temperature and the precipitate was filtered off. The organic phase was evaporated under reduced pressure. After column chromatography (ethyl acetate/DCM 1:4) the product was obtained as an off-white solid (18.8 g, 91 mmol, 79%).

<sup>1</sup>H NMR (400 MHz, DMSO)  $\delta$  / ppm = 9.66 (s, 1H, NH<sup>a</sup>), 7.31 (t, <sup>3</sup>J = 7.8 Hz, 1H, CH<sup>b</sup>), 7.24 (d, <sup>3</sup>J = 7.8 Hz, 1H, CH<sup>c</sup>), 6.15 (d, <sup>3</sup>J = 7.9 Hz, 1H, CH<sup>d</sup>), 5.68 (s, 2H, NH<sub>2</sub><sup>e</sup>), 2.21 (s, 2H, CH<sub>2</sub><sup>f</sup>), 0.98 (s, 9H, CH<sub>3</sub><sup>g</sup>).

<sup>13</sup>C NMR (101 MHz, DMSO)  $\delta$  / ppm = 170.4, 158.4, 150.4, 138.8, 103.2, 100.9, 49.1, 30.8, 29.6.

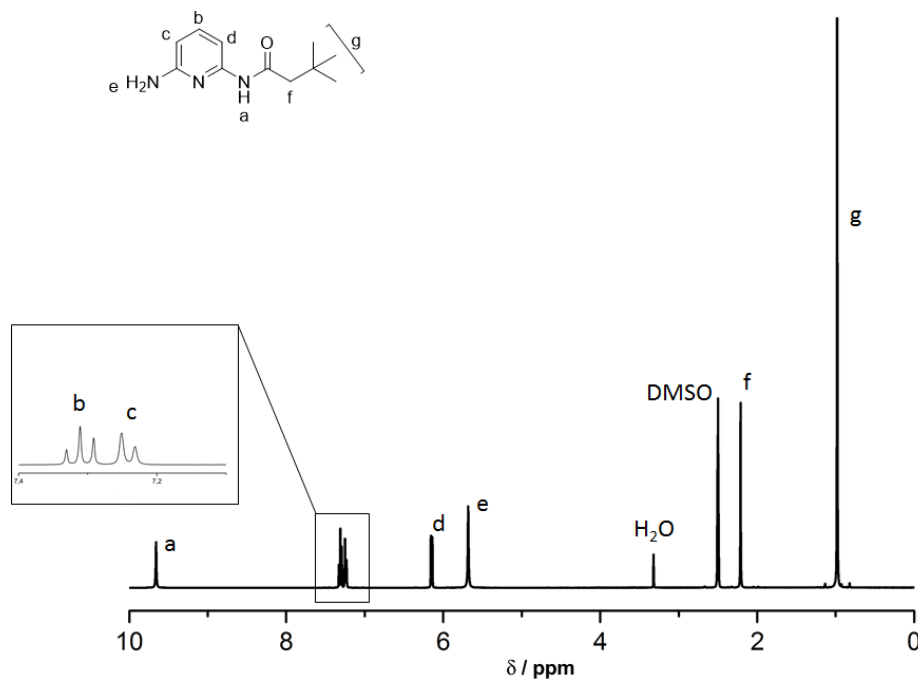
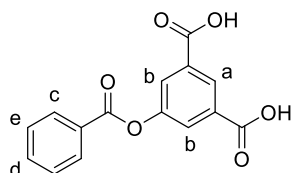


**Figure 54.**  $^1\text{H}$  NMR spectrum of **3** ( $\text{DMSO-}d_6$ , 298 K).

### Synthesis of 5-(benzoyloxy)isophthalic acid (**4**)



According to a literature procedure,<sup>[271]</sup> 5-hydroxyisophthalic acid (13.85 g, 75 mmol, 1.0 equiv.) was dissolved in 100 mL water and (9.20 g, 230 mmol, 3.0 equiv.) sodium hydroxide were added. Subsequently, the suspension was cooled with ice and within four hours a solution of 8.55 mL (75 mmol, 1.0 equiv.) benzoyl chloride in 50 mL diethyl ether was added. The mixture was stirred for four additional hours at ambient temperature. The organic phase was separated and the crude product was precipitated from the aqueous phase after adding dilute hydrochloric acid. After filtration and washing with water, the product was purified by crystallisation from acetone/water (1/1). The product was obtained as a white solid (19.8 g, 69.0 mmol, 92%).

$^1\text{H}$  NMR (400 MHz,  $\text{DMSO}$ )  $\delta$  / ppm = 8.41 (d,  $^4J = 2.2$  Hz, 1H,  $\text{CH}^a$ ), 8.24 – 8.09 (m, 2H,  $\text{CH}^b$ ), 8.05 – 7.85 (m, 2H,  $\text{CH}^c$ ), 7.76 (t,  $^3J = 7.4$  Hz, 1H,  $\text{CH}^d$ ), 7.62 (t,  $^3J = 7.7$  Hz, 2H,  $\text{CH}^e$ ).

$^{13}\text{C}$  NMR (101 MHz,  $\text{DMSO}$ )  $\delta$  / ppm = 164.5, 134.1, 129.9, 129.0, 128.8, 127.4.



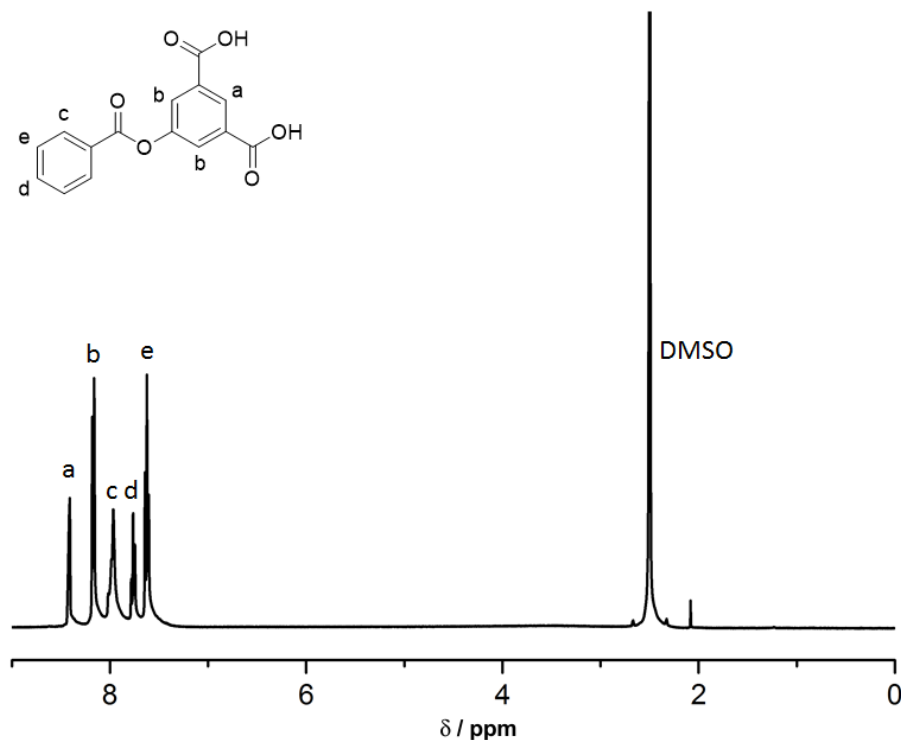
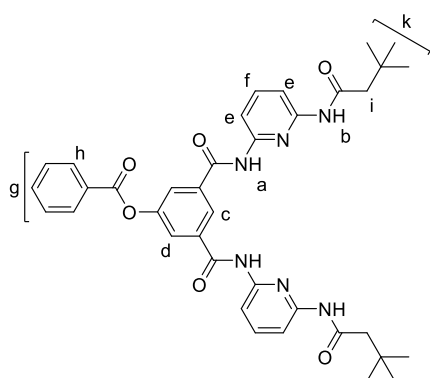


**Figure 55.**  $^1\text{H}$  NMR spectrum of **4** ( $\text{DMSO-}d_6$ , 298 K).

**Synthesis of 3-((3-(3,3-dimethylbutanamido)phenyl)carbonyl)-5-((6-(3,3-dimethylbutanamido)-pyridin-2-yl)carbonyl)phenyl benzoate (**5**)**



According to a literature procedure,<sup>[272]</sup> 5-(benzyloxy)isophthalic acid (2.0 g, 7.0 mmol, 1.0 equiv.) was dissolved in dry THF (50 mL) and dry DMF (2 mL). Oxalylchloride was added dropwise and the solution was stirred for 6 h. The solvent was removed under vacuum.

**3** (3.62 g, 17.5 mmol, 2.5 equiv) and triethylamine (2.84 g, 28.0 mmol, 4.0 equiv.) were dissolved in dry THF (40 mL), subsequently the diacid chloride dissolved in dry THF (40 mL) was added dropwise at 0 °C. The solution was stirred for 16 h at ambient temperature. The precipitate was filtered off and the solvent removed under vacuum. The crude product was purified by column chromatography (dichloromethane/ethyl acetate 4:1). The product was obtained as a white solid (3.70 g, 5.6 mmol, 80%).

$^1\text{H}$  NMR (400 MHz,  $\text{CDCl}_3$ )  $\delta$  / ppm = 8.50 (s, 2H,  $\text{NH}^{\text{a}}$ ), 8.33 (s, 2H,  $\text{NH}^{\text{b}}$ ), 8.15 (s, 1H,  $\text{CH}^{\text{f}}$ ), 8.04 (d,  $^4J = 7.4$  Hz, 2H,  $\text{CH}^{\text{d}}$ ), 7.94 – 7.89 (m, 4H,  $\text{CH}^{\text{e}}$ ), 7.82 (d,  $^3J = 8.0$  Hz, 2H,  $\text{CH}^{\text{g}}$ ), 7.59 (dt,  $^3J = 16.2$  Hz,  $^3J = 7.8$  Hz, 3H,  $\text{CH}^{\text{h}}$ ), 7.44 (t,  $^3J = 7.8$  Hz, 2H,  $\text{CH}^{\text{h}}$ ), 2.25 (s, 4H,  $\text{CH}_2^{\text{j}}$ ), 1.07 (s, 18H,  $\text{CH}_3^{\text{k}}$ ).

$^{13}\text{C}$  NMR (101 MHz, DMSO)  $\delta$  / ppm = 171.0, 167.3, 165.3, 157.8, 150.5, 150.1, 140.0, 135.5, 132.8, 130.8, 129.3, 128.6, 118.2, 117.7, 110.5, 110.0, 59.8, 49.0, 30.9, 29.6, 20.8, 14.1.

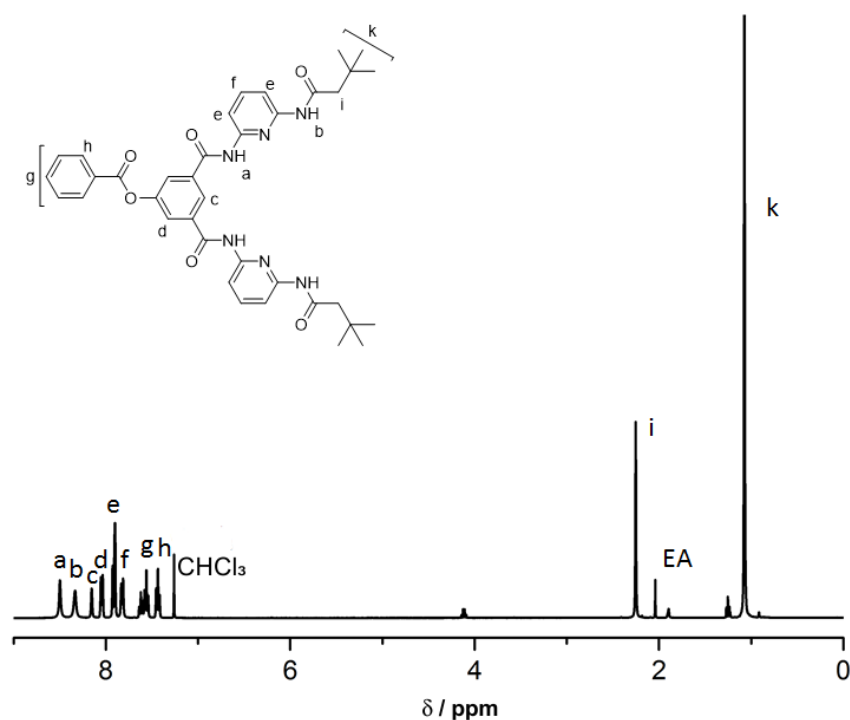
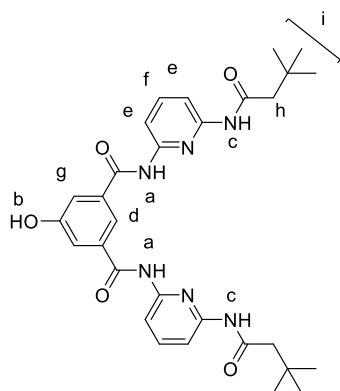


**Figure 56.**  $^1\text{H}$  NMR spectrum of **5** ( $\text{CDCl}_3$ , 298 K).

### Synthesis of *N*1-(3-(3,3-dimethylbutanamido)phenyl)-*N*3-(6-(3,3-dimethylbutanamido)pyridi-2-yl)-5-hydroxyisophthalamide (**6**)



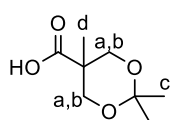
According to a literature procedure,<sup>[272]</sup> 1.5 M NaOH solution (32.3 mL) was added to a solution of **5** (3.71 g, 5.6 mmol, 1.0 equiv.) in THF and MeOH (2:1, 72 mL). The reaction mixture was stirred at ambient temperature for 5 h. Subsequently, the organic solvent was removed under vacuum. The solution was poured in water (240 mL) and concentrated HCl was added dropwise to generate a white

precipitate, which was filtered, washed and dried under vacuum. The product was obtained as a white solid (2.0 g, 3.5 mmol, 63%).

$^1\text{H}$  NMR (400 MHz, DMSO)  $\delta$  / ppm = 10.44 (s, 2H,  $\text{NH}^{\text{p}}$ ), 10.25 (s, 1H,  $\text{OH}^{\text{b}}$ ), 10.14 (s, 2H,  $\text{NH}^{\text{c}}$ ), 8.02 (s, 1H,  $\text{CH}^{\text{d}}$ ), 7.89 – 7.81 (m, 4H,  $\text{CH}^{\text{e}}$ ), 7.80 – 7.74 (m, 2H,  $\text{CH}^{\text{f}}$ ), 7.55 (d,  $^4J = 1.4$  Hz, 2H,  $\text{CH}^{\text{g}}$ ), 2.32 (s, 4H,  $\text{CH}_2^{\text{h}}$ ), 1.03 (s, 18H,  $\text{CH}_3^{\text{i}}$ ).

$^{13}\text{C}$  NMR (101 MHz, DMSO)  $\delta$  / ppm = 171.6, 165.8, 158.2, 150.8, 150.3, 140.8, 135.9, 118.7, 118.3, 110.9, 110.4, 49.5, 31.4, 30.

### Synthesis of 2,2,5-trimethyl-1,3-dioxane-5-carboxylic acid (7)



According to a literature procedure,<sup>[273]</sup> in a flame dried Schlenk-flask 2,2-bis-(hydroxymethyl)propionic acid (10 g, 74.55 mmol, 1.0 equiv.), 2,2-dimethoxypropane (13.8 mL, 111.83 mmol, 1.5 equiv.) and *p*-TsOH monohydrate (0.71 g, 3.7 mmol, 0.05 equiv.) were mixed in dry acetone (50 mL). The mixture was stirred at ambient temperature for 2 h. After the addition of  $\text{NH}_3/\text{EtOH}$  (1:1, v/v) solution (1 mL) most of the solvent was removed under vacuum. The residue was dissolved in DCM (250 mL) and subsequently extracted twice with water (40 mL). The organic phase was dried with  $\text{Na}_2\text{SO}_4$  and evaporated under vacuum to give the product as white crystals (9.65 g, 55.0 mmol, 74%).

$^1\text{H}$  NMR (400 MHz,  $\text{CDCl}_3$ )  $\delta$  / ppm = 11.13 (s, 1H, OH), 4.19 (d,  $J = 12.0$  Hz, 2H,  $\text{CH}_2^{\text{a}}$ ), 3.67 (d,  $J = 12.0$  Hz, 2H,  $\text{CH}_2^{\text{b}}$ ), 1.42 (d,  $J = 12.5$  Hz, 6H,  $\text{CH}_3^{\text{c}}$ ), 1.21 (s, 3H,  $\text{CH}_3^{\text{d}}$ ).

$^{13}\text{C}$  NMR (101 MHz,  $\text{CDCl}_3$ )  $\delta$  / ppm = 180.4, 98.5, 66.0, 41.9, 25.3, 22.1, 18.6.

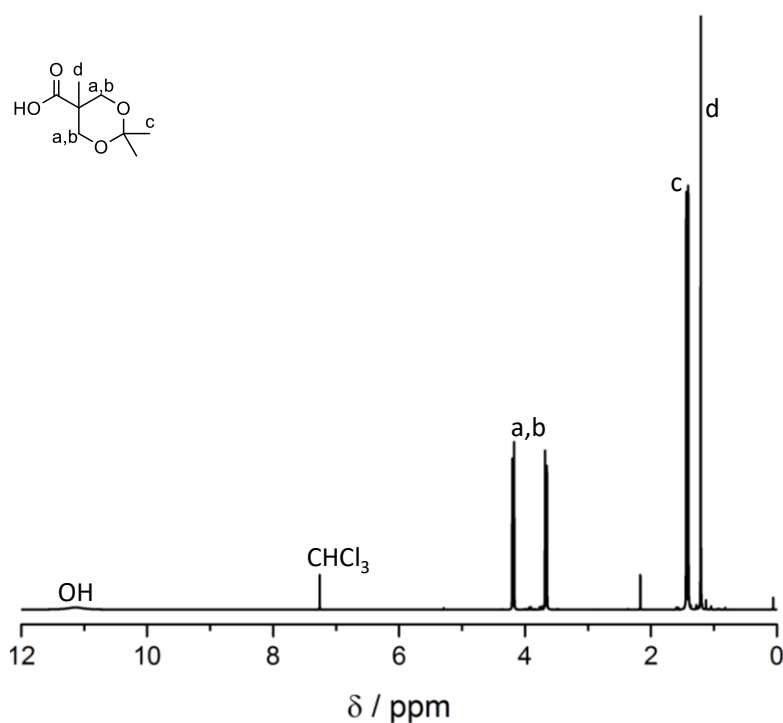
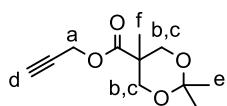


**Figure 57.**  $^1\text{H}$  NMR spectrum of **7** ( $\text{CDCl}_3$ , 298 K).

### Synthesis of Prop-2-yn-1-yl 2,2,5-trimethyl-1,3-dioxane-5-carboxylate (**8**)



Following a modified literature procedure,<sup>[274]</sup> propargyl alcohol (4.9 mL, 85 mmol, 1.5 equiv.), **7** (6.6 g, 57 mmol, 1.0 equiv.) and DMAP (2.3 g, 28.0 mmol, 0.5 equiv.) were mixed in dry DCM (70 mL). After 5 min of stirring, DCC (9.4 g, 68.0 mmol, 1.2 equiv.) dissolved in dry DCM (50 mL) was rapidly added. The mixture was subsequently stirred for 24 h at ambient temperature. The white precipitate was filtered off and the resulting solution extracted two times with  $\text{H}_2\text{O}/\text{DCM}$  (1:4) mixture (250 mL). The organic phase was dried with  $\text{Na}_2\text{SO}_4$  and the solvent evaporated under vacuum. The remaining crude product was purified by column chromatography with *n*-hexane/ethyl acetate (9:1) as the eluent. The product was obtained as a yellowish oil (6.06 g, 29 mmol, 75 %).

$^1\text{H}$  NMR (400 MHz,  $\text{CDCl}_3$ )  $\delta$  / ppm = 4.74 (d,  $^4J = 2.5$  Hz, 2H,  $\text{CH}_2^a$ ), 4.21 (d,  $^4J = 11.9$  Hz, 2H,  $\text{CH}_2^b$ ), 3.66 (d,  $^4J = 11.9$  Hz, 2H,  $\text{CH}_2^c$ ), 2.46 (t,  $^4J = 2.5$  Hz, 1H,  $\text{CH}^d$ ), 1.45 – 1.37 (m, 6H,  $\text{CH}_3^e$ ), 1.22 (s, 3H,  $\text{CH}_3^f$ ).

$^{13}\text{C}$  NMR (101 MHz,  $\text{CDCl}_3$ )  $\delta$  / ppm = 98.3, 77.6, 75.1, 66.0, 52.5, 42.1, 24.7, 22.8, 18.6.

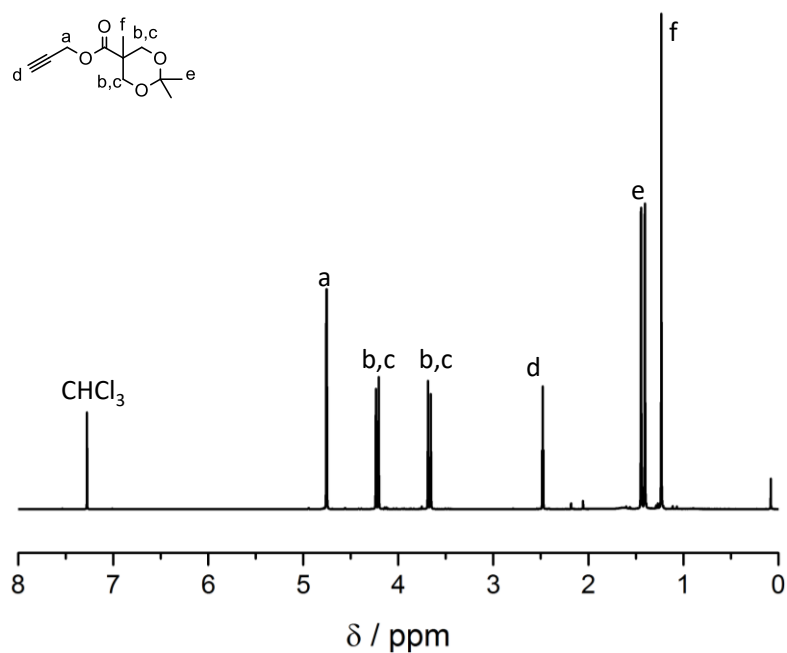
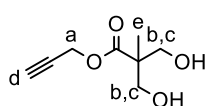


**Figure 58.**  $^1\text{H}$  NMR spectrum of **8** ( $\text{CDCl}_3$ , 298 K).

### Synthesis of Prop-2-yn-1-yl 3-hydroxy-2-(hydroxymethyl)-2-methylpropanoate (**9**)



Following a literature procedure,<sup>[273]</sup> **8** (6.8 g, 32.0 mmol, 1.0 equiv.) was dissolved in methanol (50 mL). Dowex  $\text{H}^+$  resin (6.8 g) was added and the mixture was stirred 12 h at ambient temperature. Finally the

Dowex  $\text{H}^+$  resin was filtered off and the solvent was removed under vacuum. The product was obtained as a white solid (4.94 g, 29.0 mmol, 82%).

$^1\text{H}$  NMR (400 MHz,  $\text{CDCl}_3$ )  $\delta$  / ppm = 4.75 (d,  $^4J = 2.5$  Hz, 2H,  $\text{CH}_2^a$ ), 3.90 (d,  $^2J = 11.3$  Hz, 2H,  $\text{CH}_2^b$ ), 3.72 (d,  $^2J = 11.3$  Hz, 2H,  $\text{CH}_2^c$ ), 2.87 (s, 2H, OH), 2.49 (t,  $^4J = 2.5$  Hz, 1H,  $\text{CH}^d$ ), 1.09 (s, 3H,  $\text{CH}_3^e$ ).

$^{13}\text{C}$  NMR (101 MHz,  $\text{CDCl}_3$ )  $\delta$  / ppm = 175.2, 77.4, 75.4, 67.9, 52.6, 49.5, 17.1.

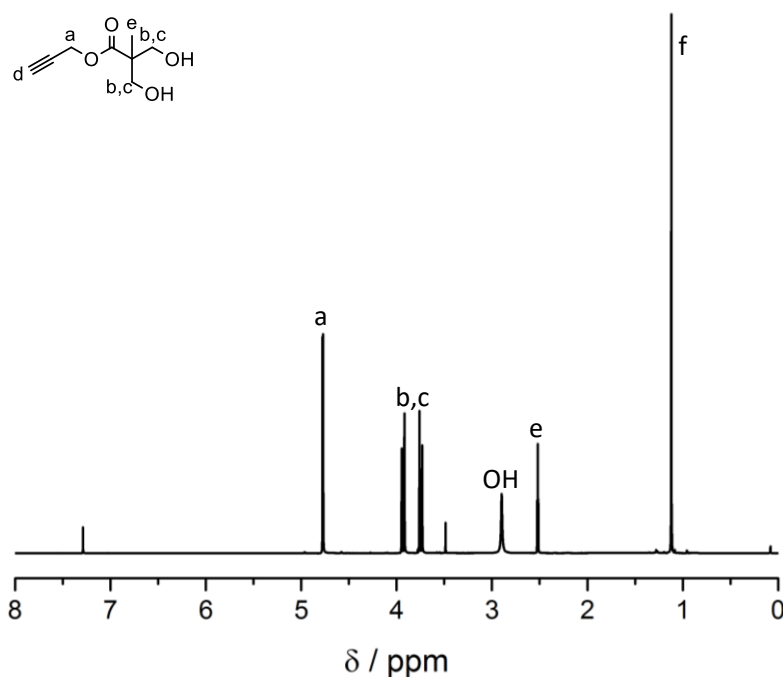
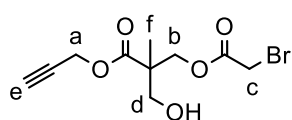


**Figure 59.**  $^1\text{H}$  NMR spectrum of **9** ( $\text{CDCl}_3$ , 298 K).

### Synthesis of Prop-2-yn-1-yl 3-(2-bromoacetoxy)-2-(hydroxymethyl)-2-methylpropanoate (**10**)



Following a modified literature procedure,<sup>[275]</sup> **9** (2.0 g, 11.62 mmol, 1.0 equiv.) and triethylamine (1.61 mL, 11.62 mmol, 1.0 equiv.) were dissolved in dry THF (40 mL) in a

flame dried Schlenk-flask and cooled with an ice bath. To this mixture a solution of bromoacetyl chloride (1.17 mL, 11.62 mmol, 1.0 equiv.) in dry THF (10 mL) was slowly added. After the addition, the mixture was stirred for 12 h at ambient temperature. The white precipitate was filtered off and the solvent evaporated under vacuum. The remainder was dissolved in DCM (200 mL) and subsequently extracted with  $\text{NaHCO}_3$  (50 mL) and water (50 mL). The organic phase was separated, dried with  $\text{Na}_2\text{SO}_4$  and evaporated under reduced pressure. The crude product was purified by column chromatography using ethyl acetate/*n*-hexane as eluent (gradient, 1:9-1:4-1:1). The product was obtained as a yellow oil (1.58 g, 5.4 mmol, 46%).

$^1\text{H}$  NMR (400 MHz,  $\text{CDCl}_3$ )  $\delta$  / ppm = 4.74 (d,  $^3J = 2.5$  Hz, 2H,  $\text{CH}_2^a$ ), 4.39 (dd,  $^1J = 36.0$  Hz,  $^2J = 11.1$  Hz, 2H,  $\text{CH}_2^b$ ), 3.84 (s, 2H,  $\text{CH}_2^c$ ), 3.74 (s, 2H,  $\text{CH}_2^d$ ), 2.49 (t,  $^4J = 2.5$  Hz, 1H,  $\text{CH}^e$ ), 2.27 (s, 1H, OH), 1.26 (s, 3H,  $\text{CH}_3^f$ ).

$^{13}\text{C}$  NMR (101 MHz,  $\text{CDCl}_3$ )  $\delta$  / ppm = 167.3, 77.3, 75.5, 67.3, 65.1, 52.3, 48.5, 25.5, 17.4.

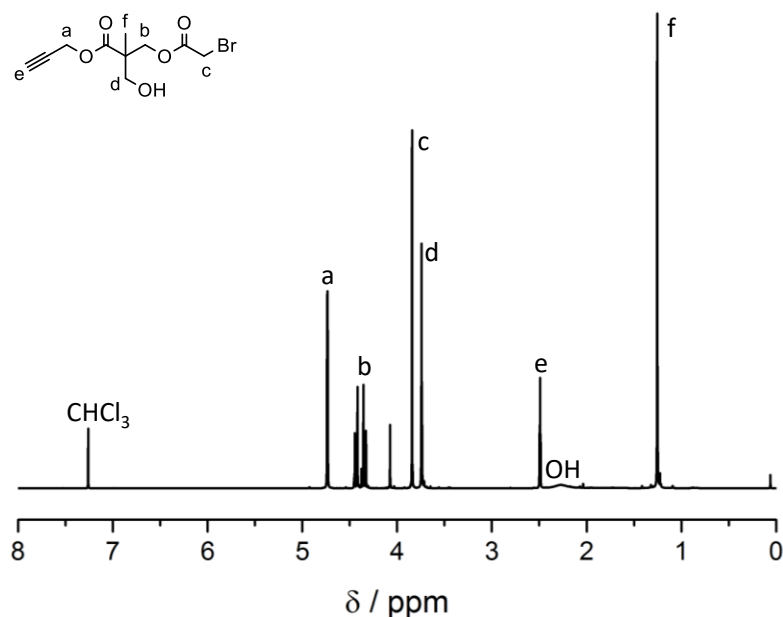
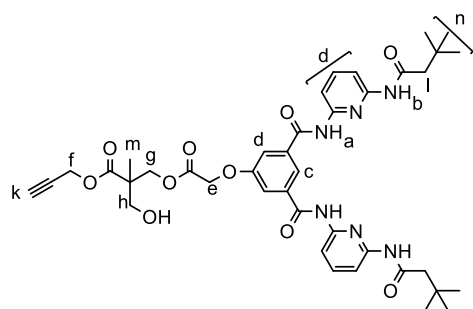


**Figure 60.**  $^1\text{H}$  NMR spectrum of **10** ( $\text{CDCl}_3$ , 298 K).

### Synthesis of Prop-2-yn-1-yl 3-(2-(3,5-bis((6-(3,3-dimethylbutanamido)pyridin-2-yl)carbamoyl)phenoxy)acetoxy)-2-(hydroxymethyl)-2-methylpropanoate (**11**)



**10** (0.524 g, 1.79 mmol, 1.0 equiv.) and **6** (1.00 g, 1.79 mmol, 1.0 equiv.) were each dissolved in dry DMF (5 mL). The solutions were combined and subsequently  $\text{K}_2\text{CO}_3$  (0.562 g, 3.57 mmol, 2.0 equiv.) was added. The reaction mixture was stirred at ambient temperature for 72 h. DCM

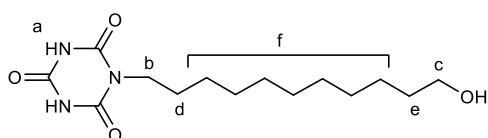
(200 mL) was added and the solution was washed with water (50 mL). The organic phase was separated, dried with  $\text{Na}_2\text{SO}_4$  and subsequently the solvent removed under reduced pressure. The crude product was purified *via* column chromatography using EA/DCM as eluent (gradient from 1:10 to 1:1). The product was obtained as a white solid (815 mg, 1.05 mmol, 59%).

$^1\text{H}$  NMR (400 MHz, DMSO)  $\delta$  / ppm = 10.49 (s, 2H,  $\text{NH}^a$ ), 10.01 (s, 2H,  $\text{NH}^b$ ), 8.18 (s, 1H,  $\text{CH}^c$ ), 7.93 – 7.69 (m, 8H,  $\text{CH}^d$ ), 5.01 (s, 2H,  $\text{CH}_2^e$ ), 4.69 (d,  $^4J = 2.4$  Hz, 2H,  $\text{CH}_2^f$ ),

4.28 (dd,  $^1J = 41.4$  Hz,  $^2J = 10.8$  Hz, 2H,  $CH_2^g$ ), 3.53 (m, 3H,  $CH_2^{h,k}$ ), 2.31 (s, 4H,  $CH_2^l$ ), 1.10 (s, 3H,  $CH_3^m$ ), 1.02 (s, 18H,  $CH_3^n$ ).

$^{13}C$  NMR (101 MHz,  $CDCl_3$ )  $\delta$  / ppm = 174.8, 171.0, 168.5, 164.1, 158.4, 149.9, 149.5, 141.2, 136.2, 120.0, 117.0, 110.2, 109.8, 77.4, 76.0, 66.9, 65.2, 64.9, 60.5, 53.3, 51.4, 49.2, 31.5, 30.0, 21.2, 18.4, 14.3.

### Synthesis of 1-(11-hydroxyundecyl)-1,3,5-triazinane-2,4,6-trione (14)



Following a modified literature procedure,<sup>[48]</sup> cyanuric acid (10 g, 77.47 mmol, 5.0 equiv.) and 11-bromo-1-undecanol (3.89 g, 15.49 mmol, 1.0 equiv.) were dissolved in dry DMF (70 mL) in a flame dried Schlenk-flask 1,8-diazabicyclo[5.4.0]undec-7-ene (DBU, 2.36 mL, 15.49 mmol, 1.0 equiv.) was subsequently added dropwise to the solution. The mixture was heated to 70 °C and stirred for 24 h. The solvent was removed under vacuum, the residual was dissolved in methanol and filtered. The solvent was evaporated again and the remaining crude product was purified *via* column chromatography. A mixture of MeOH and DCM (gradient, 1:25-1:15) was used as the eluent. The product was obtained as a white solid (464 mg, 1.57 mmol, 20%).

$^1H$  NMR (400 MHz, DMSO)  $\delta$  / ppm = 11.26 (m, 2H,  $NH^a$ ), 4.30 (s, 1H,  $OH$ ), 4.08 – 3.52 (m, 2H,  $CH_2^b$ ), 3.36 (q,  $^2J = 11.0$  Hz,  $^3J = 6.3$  Hz, 2H,  $CH_2^c$ ), 1.50 (m, 2H,  $CH_2^d$ ), 1.45 – 1.32 (m, 2H,  $CH_2^e$ ), 1.24 (s, 14H,  $CH_2^f$ ).

$^{13}C$  NMR (101 MHz, DMSO)  $\delta$  / ppm = 149.9, 148.7, 60.7, 32.6, 29.1, 29.0, 28.9, 28.7, 27.2, 26.1, 25.5.



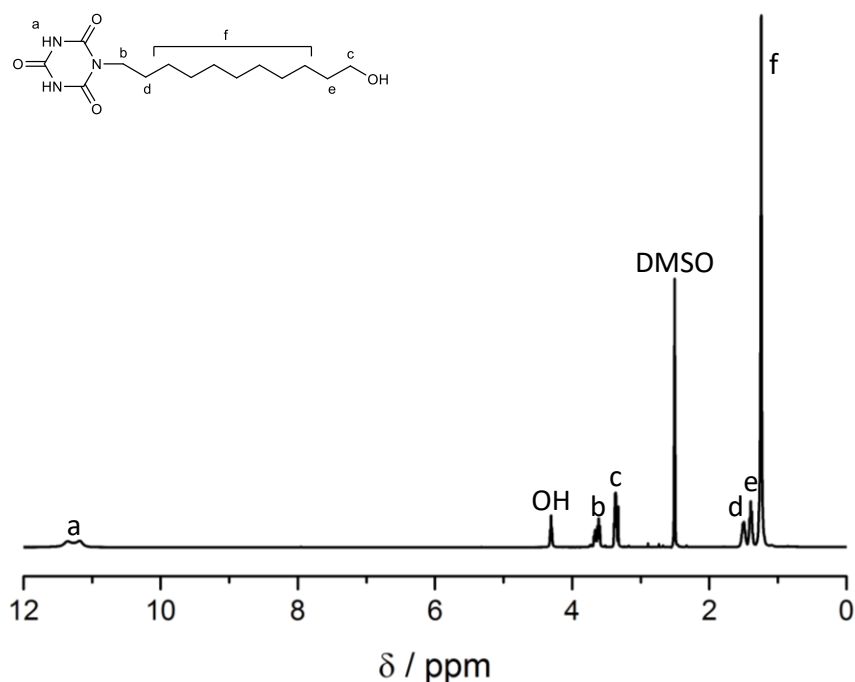
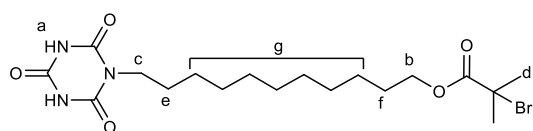


**Figure 61.**  $^1\text{H}$  NMR spectrum of **14** (DMSO- $d_6$ , 298 K).

### Synthesis of 11-(2,4,6-trioxo-1,3,5-triazinan-1-yl)undecyl 2-bromo-2-methylpropanoate (**15**)



Following a modified literature procedure,<sup>[48]</sup> **14** (0.6 g, 2.0 mmol, 1.0 equiv.), TEA (0.35 mL, 2.51 mmol, 1.25 equiv.) and DMAP (24.5 mg

0.2 mmol, 0.04 equiv.) were dissolved in dry THF (15 mL) in a flame dried Schlenk-flask. The solution was cooled with an ice bath and  $\alpha$ -bromoisobutyryl bromide (0.31 mL, 2.51 mmol, 1.25 equiv.) dissolved in THF (10 mL) was added dropwise. The mixture was stirred for 24 h at ambient temperature. Subsequently, the precipitate was filtered off and the solvent was evaporated under reduced pressure. The remainder was dissolved in DCM (200 mL), washed with  $\text{NaHCO}_3$  (50 mL) and water (50 mL). The organic phase was separated and dried with  $\text{Na}_2\text{SO}_4$  and removed under vacuum. The crude product was purified *via* column chromatography (methanol/DCM 1:25). The product was obtained as a white solid (250 mg, 0.56 mmol, 36%).

$^1\text{H}$  NMR (400 MHz, DMSO)  $\delta$  / ppm = 11.37 (s, 2H,  $\text{NH}^a$ ), 4.12 (t,  $^3J = 6.4$  Hz, 2H,  $\text{CH}_2^b$ ), 3.70 – 3.53 (m, 2H,  $\text{CH}_2^c$ ), 1.88 (s, 6H,  $\text{CH}_3^d$ ), 1.65 – 1.55 (m, 2H,  $\text{CH}_2^e$ ), 1.55 – 1.41 (m, 2H,  $\text{CH}_2^f$ ), 1.40 – 1.18 (m, 14H,  $\text{CH}_2^g$ ).

$^{13}\text{C}$  NMR (101 MHz, DMSO)  $\delta$  / ppm = 170.8, 149.8, 148.6, 65.6, 57.4, 30.2, 28.8, 28.5, 27.8, 27.3, 26.1, 25.2.

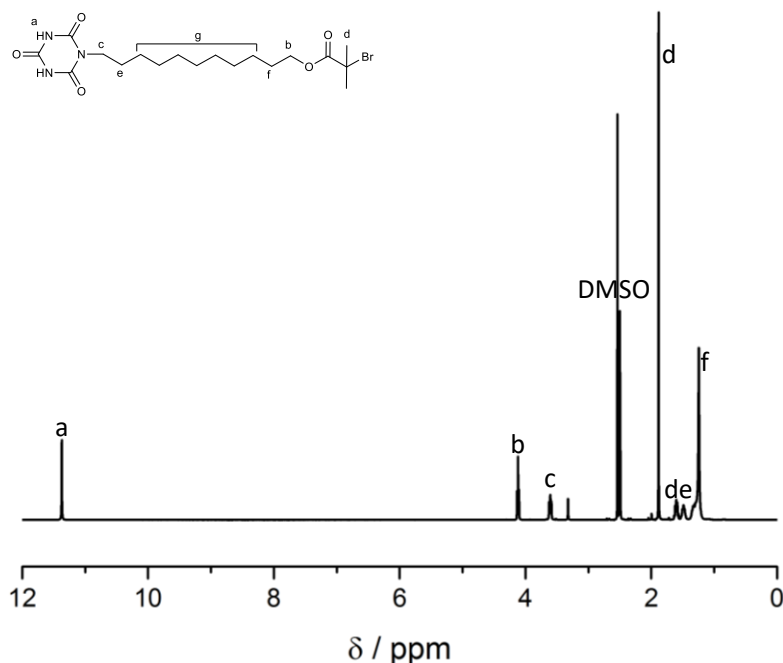
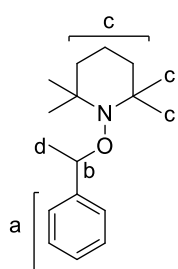


**Figure 62.**  $^1\text{H}$  NMR spectrum of **15** (DMSO- $d_6$ , 298 K).

### Synthesis of 2,2,6,6-tetramethyl-1-(1-phenylethoxy)piperidine (**16**)



Following a literature procedure,<sup>[227]</sup> a solution of copper(I) bromide (0.930 g, 6.48 mmol, 1.2 equiv.) and PMDETA (1.1 g, 6.48 mmol, 1.2 equiv.) in dry toluene (18 mL) was added to a solution of (1-bromoethyl)benzene (1.0 g, 5.4 mmol, 1.0 equiv.) and TEMPO (0.928 g, 5.94 mmol, 1.1 equiv.) in dry toluene (18 mL) under dry and oxygen free conditions. The reaction mixture was stirred at 50°C for 1 h and subsequently filtered. The solvent was removed under reduced pressure and the residue was purified by column chromatography using toluene as eluent. The product was crystallized in the cold (5 °C). The product was obtained as white solid (1.31 g, 5.00 mmol, 93%).

$^1\text{H}$  NMR (400 MHz,  $\text{CDCl}_3$ )  $\delta$  / ppm = 7.35 – 7.20 (m, 5H,  $\text{CH}^a$ ), 4.84 – 4.73 (m, 1H,  $\text{CH}^b$ ), 1.61 – 0.92 (m, 18H,  $\text{CH}_2^c$ ,  $\text{CH}_3^c$ ), 0.66 (s, 3H,  $\text{CH}_3^d$ ).

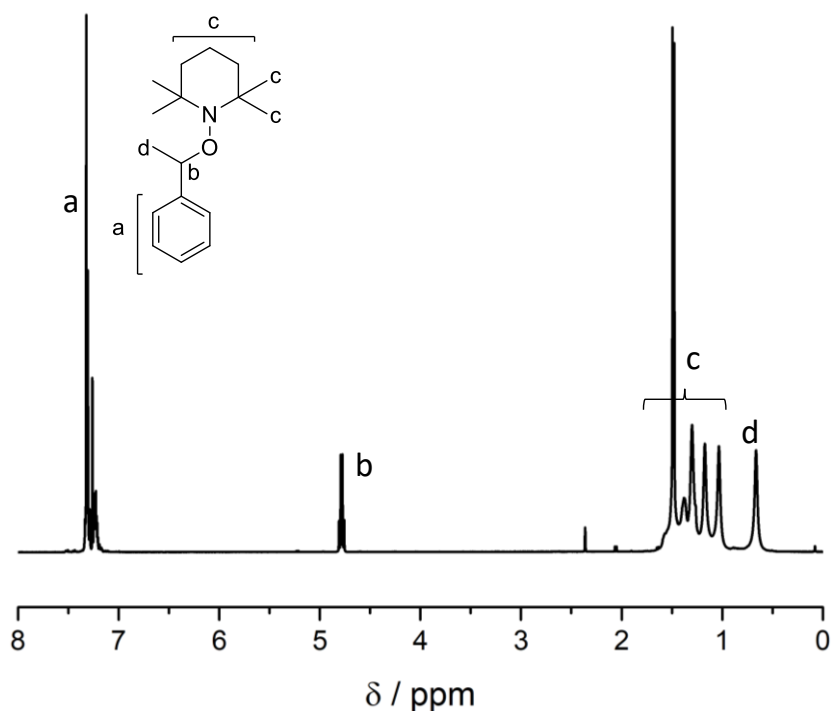
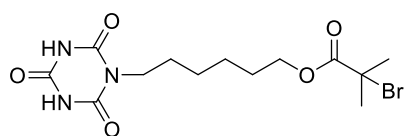


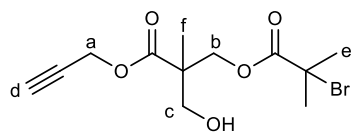
**Figure 63.**  $^1\text{H}$  NMR spectrum of **16** ( $\text{CDCl}_3$ , 298 K).

### Synthesis of 6-(2,4,6-trioxo-1,3,5-triazinan-1-yl)hexyl 2-bromo-2-methylpropanoate (**17**)



Based on a literature procedure,<sup>[48]</sup> 1-(6-hydroxyhexyl)-1,3,5-triazinane-2,4,6-trione (0.56 g, 2.44 mmol, 1.0 equiv.), TEA (0.42 mL, 3.05 mmol, 1.25 equiv.) and DMAP (29.8 mg, 0.24 mmol, 0.1 equiv.) were dissolved in dry THF (15 mL) in a flame dried Schlenk-flask. The solution was cooled with an ice bath and  $\alpha$ -bromoisobutyryl bromide (0.38 mL, 3.05 mmol, 1.25 equiv.) dissolved in THF (10 mL) was added dropwise. The mixture was stirred for 24 h at ambient temperature. Subsequently, the precipitate was filtered off and the solvent was evaporated under reduced pressure. The remainder was dissolved in DCM (200 mL), washed with  $\text{NaHCO}_3$  (50 mL) and water (50 mL). The organic phase was separated and dried with  $\text{Na}_2\text{SO}_4$  and removed under vacuum. The crude product was purified *via* column chromatography (methanol/DCM 1:25). The product was obtained as a white solid (440 mg, 1.16 mmol, 47%).

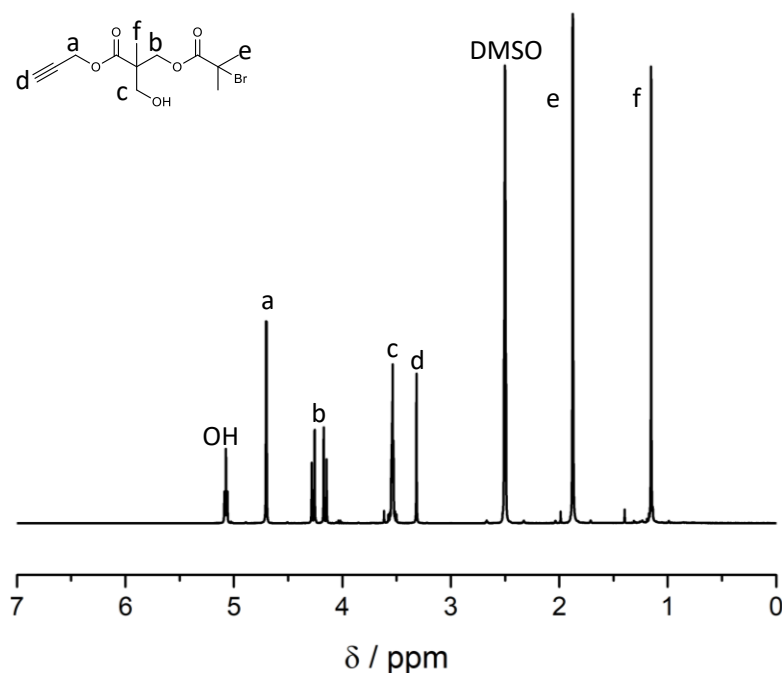
### Synthesis of Prop-2-yn-1-yl 3-((2-bromo-2-methylpropanoyl)oxy)-2-(hydroxymethyl)-2-methylpropanoate (18)



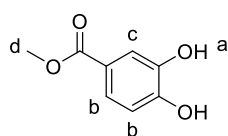
Based on a modified literature procedure,<sup>[276]</sup> **9** (1.0 g, 5.8 mmol, 1.0 equiv.) and trimethylamine (8.9 mL, 6.4 mmol, 1.1 equiv.) were dissolved in DCM (40 mL). The solution was cooled to 0 °C and bromoisobutyryl bromide (0.72 mL, 5.8 mmol, 1.0 equiv.) dissolved in DCM (10 mL) was added dropwise. The solution was allowed to warm to ambient temperature and subsequently stirred overnight. The solution was filtered and extracted with sat. NaHCO<sub>3</sub> solution and brine. The organic phase was dried over Na<sub>2</sub>SO<sub>4</sub>, filtered and the solvent removed under reduced pressure. The product was obtained after column chromatography (CH/EE 4:1) as a yellowish oil (1.5 g, 4.8 mmol, 83%).

<sup>1</sup>H NMR (400 MHz, DMSO)  $\delta$  / ppm = 5.07 (t, <sup>3</sup>J = 5.5 Hz, 1H, OH), 4.70 (d, <sup>4</sup>J = 2.5 Hz, 2H, CH<sub>2</sub><sup>a</sup>), 4.21 (dd, <sup>1</sup>J = 44.2 Hz, <sup>2</sup>J = 10.7 Hz, 2H, CH<sub>2</sub><sup>b</sup>), 3.59 – 3.46 (m, 2H, CH<sub>2</sub><sup>c</sup>), 3.32 (s, 1H, CH<sup>d</sup>), 1.88 (s, 6H, CH<sub>3</sub><sup>e</sup>), 1.15 (s, 3H, CH<sub>3</sub><sup>f</sup>).

<sup>13</sup>C NMR (101 MHz, DMSO)  $\delta$  / ppm = 172.6, 170.4, 78.3, 77.7, 66.9, 63.7, 57.0, 52.1, 48.4, 30.2, 16.8.



**Figure 64.** <sup>1</sup>H NMR spectrum of the alkyne and hydroxyl functional ATRP initiator **16** (DMSO-*d*<sub>6</sub>, 298 K).

**Synthesis of Methyl 3,4-dihydroxybenzoate (20)**

Following a modified literature procedure,<sup>[277]</sup> dihydroxybenzoic acid (5 g, 37.8 mmol, 1.0 equiv.) was dissolved in MeOH (50 mL) and H<sub>2</sub>SO<sub>4</sub> (5 mL) was added dropwise. The solution was refluxed for 16 h. The reaction mixture was cooled to ambient temperature and diluted with water (30 mL). The methanol was evaporated and the pH-value was adjusted to ~6 with NaHCO<sub>3</sub>. The mixture was extracted with ethyl acetate and the organic phase was washed with brine, dried over Na<sub>2</sub>SO<sub>4</sub> and the solvent removed under reduced pressure. The product was obtained as white solid (5.2 g, 31 mmol, 87%).

<sup>1</sup>H NMR (400 MHz, Acetone)  $\delta$  / ppm = 8.45 (s, 2H, -OH<sup>a</sup>), 7.54 – 7.35 (m, 2H, CH<sup>b</sup>), 6.89 (d, <sup>4</sup>J = 8.3 Hz, 1H, CH<sup>c</sup>), 3.80 (s, 3H, CH<sub>3</sub><sup>d</sup>).

<sup>13</sup>C NMR (101 MHz, Acetone)  $\delta$  / ppm = 167.3, 150.9, 145.8, 123.5, 123.1, 117.3, 116.0, 52.1.

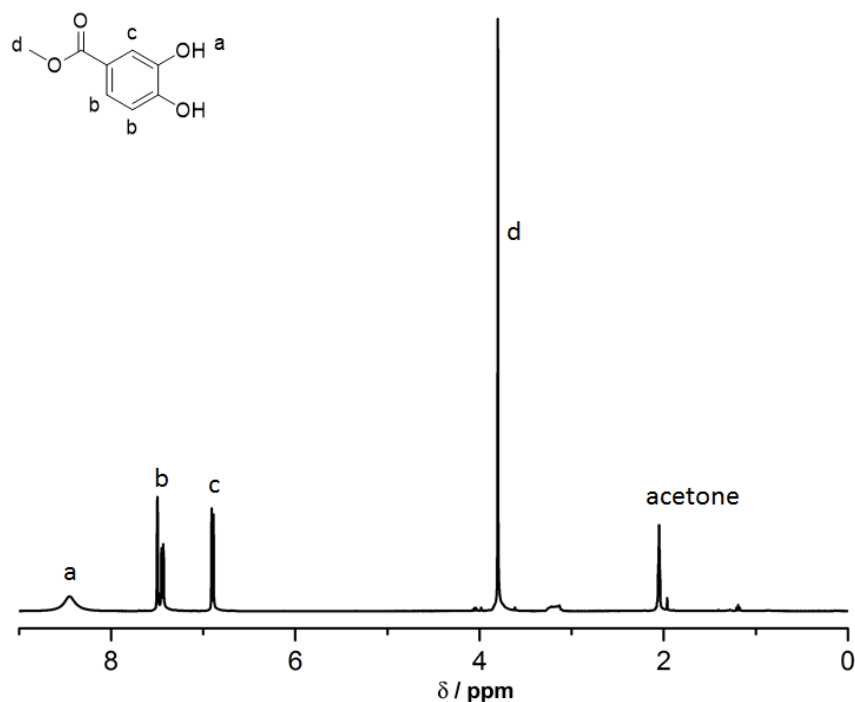
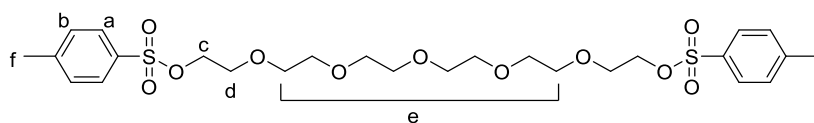


**Figure 65.** <sup>1</sup>H NMR spectrum of **20** (acetone-*d*<sub>6</sub>, 298 K).

### Synthesis of 3,6,9,12,15-pentaoxaheptadecane-1,17-diyl bis(4-methylbenzenesulfonate) (**22**)



According to a literature procedure,<sup>[278]</sup> hexaethylene glycol (5.0 g,

17.7 mmol, 1.0 equiv.) and tosyl chloride (10.13 g, 53.1 mmol, 3.0 equiv.) were dissolved in THF (60 mL) and cooled to 0 °C. Then a 16 M KOH/water solution (19.23 mL) was added dropwise. The ice bath was removed and the solution stirred for 16 h at ambient temperature. The mixture was poured into ice water and the phases were separated. The water phase was extracted with diethyl ether. The organic phase was washed with brine, dried over Na<sub>2</sub>SO<sub>4</sub> and the solvent removed under reduced pressure. The product was obtained as a colourless oil (9 g, 15 mmol, 86%).

<sup>1</sup>H NMR (400 MHz, CDCl<sub>3</sub>)  $\delta$  / ppm = 7.79 (d, <sup>3</sup>J = 8.3 Hz, 4H, CH<sup>a</sup>), 7.33 (d, <sup>3</sup>J = 8.0 Hz, 4H, CH<sup>b</sup>), 4.17 – 4.11 (m, 4H, CH<sub>2</sub><sup>c</sup>), 3.71 – 3.65 (m, 4H, CH<sub>2</sub><sup>d</sup>), 3.59 (d, <sup>3</sup>J = 15.0 Hz, 16H, CH<sub>2</sub><sup>e</sup>), 2.44 (s, 6H, CH<sub>3</sub><sup>f</sup>).

<sup>13</sup>C NMR (101 MHz, CDCl<sub>3</sub>)  $\delta$  / ppm = 144.9, 133.2, 130.0, 128.1, 70.9, 70.7, 70.7, 70.6, 69.4, 68.8, 21.8.

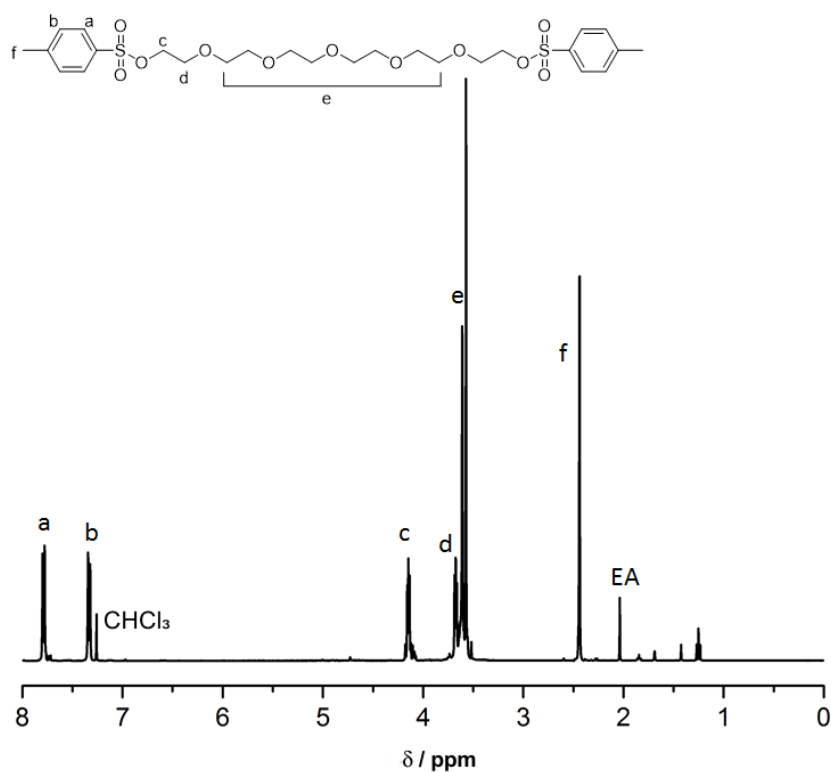
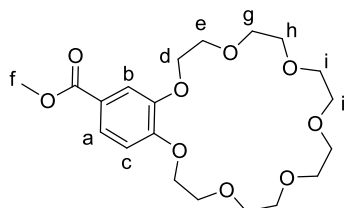


**Figure 66.** <sup>1</sup>H NMR spectrum of **22** (CDCl<sub>3</sub>, 298 K).

### Synthesis of Methyl 2,3,5,6,8,9,11,12,14,15,17,18-dodecahydrobenzo[b][1,4,7,10,13,16,19]heptaoxa-cyclohenicosine-21-carboxylate (**23**)



Following a modified literature procedure,<sup>[279]</sup> **20** (2.56 g, 15.2 mmol, 1.0 equiv.) and  $K_2CO_3$  (12.6 g, 45.7 mmol, 3.0 equiv.) were dissolved in acetonitrile (75 mL). A solution of **22** (8.99g, 15.2 mmol, 1.0 equiv.) dissolved in acetonitrile

(25 mL) was added dropwise and subsequently stirred for 18 h under reflux. The solvent was removed, and the result was extracted with DCM/ $H_2O$  and dried over  $Na_2SO_4$ . The solvent was removed under reduced pressure. After column chromatography (DCM/methanol 96:4), the product was obtained as a brown oil (4.14 g, 10.0 mmol, 66%).

$^1H$  NMR (400 MHz,  $CDCl_3$ )  $\delta$  / ppm = 7.64 (dd,  $^3J = 8.4$  Hz,  $^4J = 2.0$  Hz, 1H,  $CH^a$ ), 7.54 (t,  $^3J = 4.1$  Hz, 1H,  $CH^b$ ), 6.86 (d,  $^3J = 8.5$  Hz, 1H,  $CH^c$ ), 4.27 – 4.10 (m, 4H,  $CH_2^d$ ), 3.92 (m, 3H,  $CH_2^e$ ), 3.86 (m, 4H,  $CH_3^f$ ,  $CH_2^e$ ), 3.82 – 3.77 (m, 3H,  $CH_2^g$ ), 3.76 – 3.69 (m, 4H,  $CH_2^h$ ), 3.65 (m, 9H,  $CH_2^{g,i}$ ).

$^{13}C$  NMR (101 MHz,  $CDCl_3$ )  $\delta$  / ppm = 166.9, 153.0, 148.4, 124.0, 123.0, 114.6, 112.4, 71.5, 71.4, 71.3, 71.3, 71.1, 70.8, 70.8, 69.7, 69.6, 69.4, 69.2, 52.1.

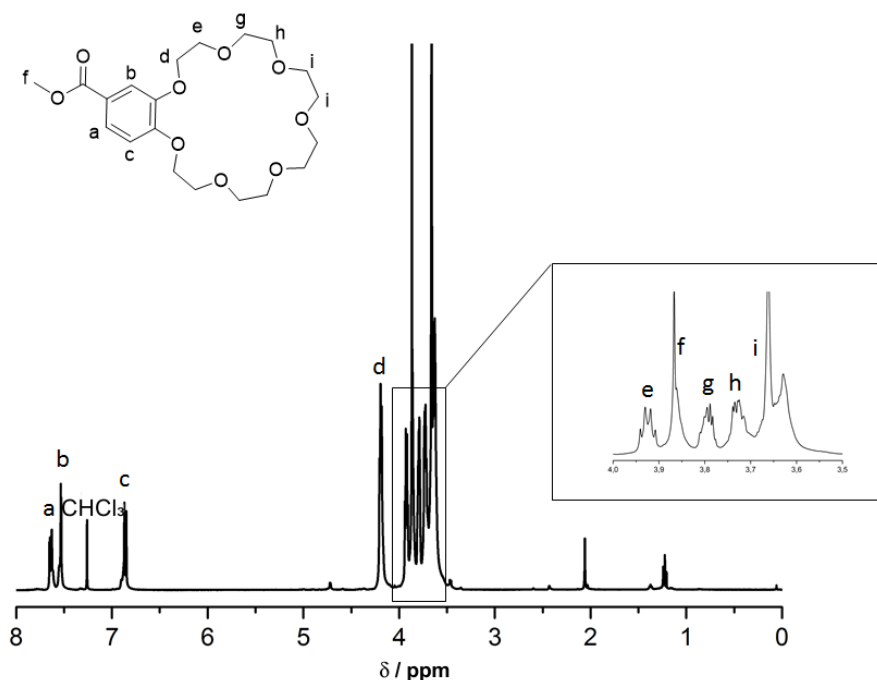
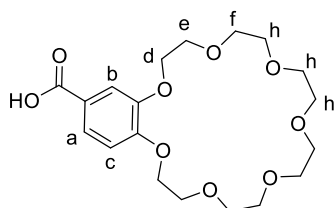


**Figure 67.**  $^1H$  NMR spectrum of **23** ( $CDCl_3$ , 298 K). Adapted from ref [252] with permission from Wiley-VCH. © 2016 WILEY-VCH Verlag GmbH & Co. KGaA, Weinheim.

### Synthesis of 2,3,5,6,8,9,11,12,14,15,17,18-dodecahydrobenzo[b][1,4,7,10,13,16,-19]-heptaoxa-cyclohenicosine-21-carboxylic acid (24)



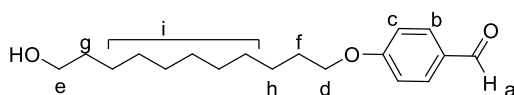
Following a modified literature procedure,<sup>[272]</sup> 1.2 M NaOH solution (4.2 mL) was added to a solution of **23** (0.5 g, 1.21 mmol, 1.0 equiv.) in THF and methanol (2:1, 6.3 mL).

The mixture was stirred for 5 h at ambient temperature and subsequently concentrated. The solution was poured into 4 mL distilled water and concentrated HCl was added dropwise. The water phase was extracted with ethyl acetate (4×), dried over Na<sub>2</sub>SO<sub>4</sub> and the solvent removed under reduced pressure. The product was obtained as a white solid (2.3 g, 5.8 mmol, 83%).

<sup>1</sup>H NMR (400 MHz, CDCl<sub>3</sub>) δ / ppm = 7.72 (dd, <sup>3</sup>J = 8.4 Hz, <sup>4</sup>J = 1.9 Hz, 1H, CH<sup>a</sup>), 7.58 (d, <sup>4</sup>J = 1.9 Hz, 1H, CH<sup>b</sup>), 6.88 (d, <sup>3</sup>J = 8.5 Hz, 1H, CH<sup>c</sup>), 4.21 (dd, <sup>3</sup>J = 8.7 Hz, <sup>4</sup>J = 4.3 Hz, 4H, CH<sub>2</sub><sup>d</sup>), 3.94 (dd, <sup>3</sup>J = 8.9 Hz, <sup>4</sup>J = 4.6 Hz, 4H, CH<sub>2</sub><sup>e</sup>), 3.85 – 3.79 (m, 4H, CH<sub>2</sub><sup>f</sup>), 3.78 – 3.72 (m, 4H, CH<sub>2</sub><sup>g</sup>), 3.70 – 3.64 (m, 8H, CH<sub>2</sub><sup>h</sup>).

<sup>13</sup>C NMR (101 MHz, CDCl<sub>3</sub>) δ / ppm = 171.3, 153.7, 148.4, 124.9, 122.1, 114.9, 112.3, 71.5, 71.4, 71.3, 71.2, 71.2, 71.1, 70.7, 69.8, 69.6, 69.4, 69.2.

### Synthesis of 4-((10-hydroxydecyl)oxy)benzaldehyde (27)



According to an existing literature procedure,<sup>[280]</sup> a solution of 4-hydroxybenzaldehyde (2.44 g, 20 mmol, 1.0 equiv.), 11-bromoundecanol (5 g, 20 mmol, 1.0 equiv.), K<sub>2</sub>CO<sub>3</sub> (39.8 g, 288 mmol, 14 equiv.) and NaI (0.42 g, 2.8 mmol, 0.14 equiv.) was suspended in DMF (150 mL) and heated to 100 °C for 16 h. The solution was filtered and the solvent was removed under vacuum. The solid was dissolved in ethyl acetate, washed with brine and dried over Na<sub>2</sub>SO<sub>4</sub>. The solvent was removed under reduced pressure. The product was obtained as a white solid (5.4 g, 18 mmol, 97%).

<sup>1</sup>H NMR (400 MHz, CDCl<sub>3</sub>) δ / ppm = 9.86 (s, 1H, CHO<sup>a</sup>), 7.81 (d, <sup>3</sup>J = 8.7 Hz, 2H, CH<sup>b</sup>), 6.98 (d, <sup>3</sup>J = 8.7 Hz, 2H, CH<sup>c</sup>), 4.03 (t, <sup>3</sup>J = 6.5 Hz, 2H, CH<sub>2</sub><sup>d</sup>), 3.63 (t, <sup>3</sup>J = 6.6 Hz, 2H, CH<sub>2</sub><sup>e</sup>), 1.79 (m, 2H, CH<sub>2</sub><sup>f</sup>), 1.55 (m, 2H, CH<sub>2</sub><sup>g</sup>), 1.50 – 1.41 (m, 2H, CH<sub>2</sub><sup>h</sup>), 1.29 (s, 14H, CH<sub>2</sub><sup>i</sup>).



$^{13}\text{C}$  NMR (101 MHz,  $\text{CDCl}_3$ )  $\delta$  / ppm = 191.0, 164.4, 132.1, 129.9, 114.9, 68.6, 63.2, 32.9, 29.7, 29.6, 29.6, 29.5, 29.4, 29.2, 26.1, 25.9.

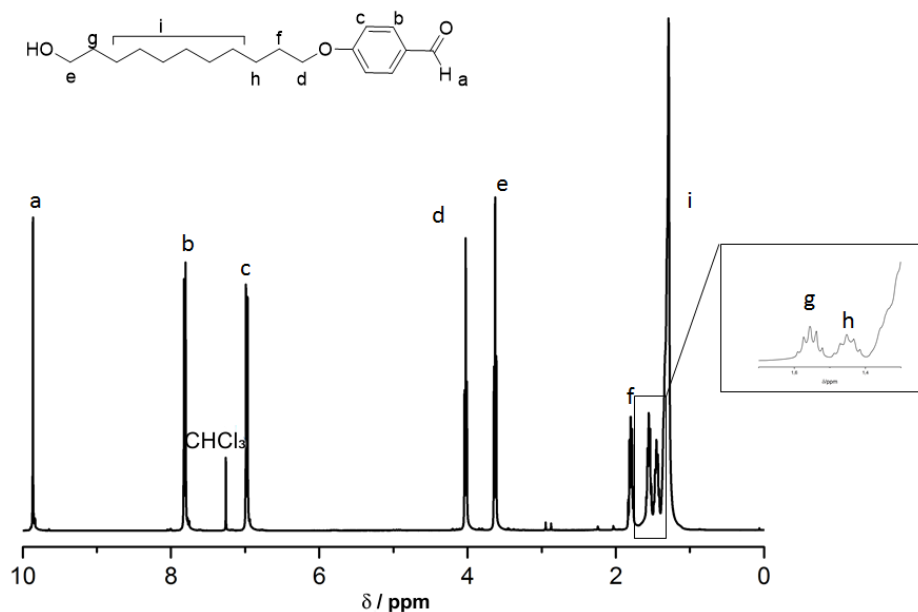
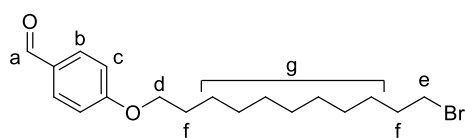


**Figure 68.**  $^1\text{H}$  NMR spectrum of **27** ( $\text{CDCl}_3$ , 298 K).

### Synthesis of 4-((10-bromodecyl)oxy)benzaldehyde (**28**)



According to an existing literature procedure,<sup>[280]</sup> **27** (1.5 g, 5.4 mmol, 1.0 equiv.),  $\text{CBr}_4$  (1.79 g, 5.4 mmol, 1.0 equiv.) and  $\text{PPh}_3$  (1.42 g, 5.4 mmol, 1.0 equiv.)

were dissolved in DCM (100 mL) at 0 °C. The solution was allowed to warm up to ambient temperature and stirred for 16 h. The solvent was removed under reduced pressure. After column chromatography (petrol ether/DCM 3:1) the product was obtained as a white solid (2.4 g, 6.7 mmol, 64%).

$^1\text{H}$  NMR (400 MHz,  $\text{CDCl}_3$ )  $\delta$  / ppm = 9.87 (s, 1H,  $\text{CHO}^a$ ), 7.82 (d,  $^3J = 8.4$  Hz, 2H,  $\text{CH}^b$ ), 6.98 (d,  $^3J = 8.6$  Hz, 2H,  $\text{CH}^c$ ), 4.03 (t,  $^3J = 6.5$  Hz, 2H,  $\text{CH}_2^d$ ), 3.40 (t,  $^3J = 6.8$  Hz, 2H,  $\text{CH}_2^e$ ), 1.91 – 1.76 (m, 4H,  $\text{CH}_2^f$ ), 1.51 – 1.21 (m, 14H,  $\text{CH}_2^g$ ).

$^{13}\text{C}$  NMR (101 MHz,  $\text{CDCl}_3$ )  $\delta$  / ppm = 190.9, 164.4, 132.1, 129.9, 114.9, 68.6, 34.2, 33.0, 29.6, 29.6, 29.5, 29.4, 29.2, 28.9, 28.3, 26.1.

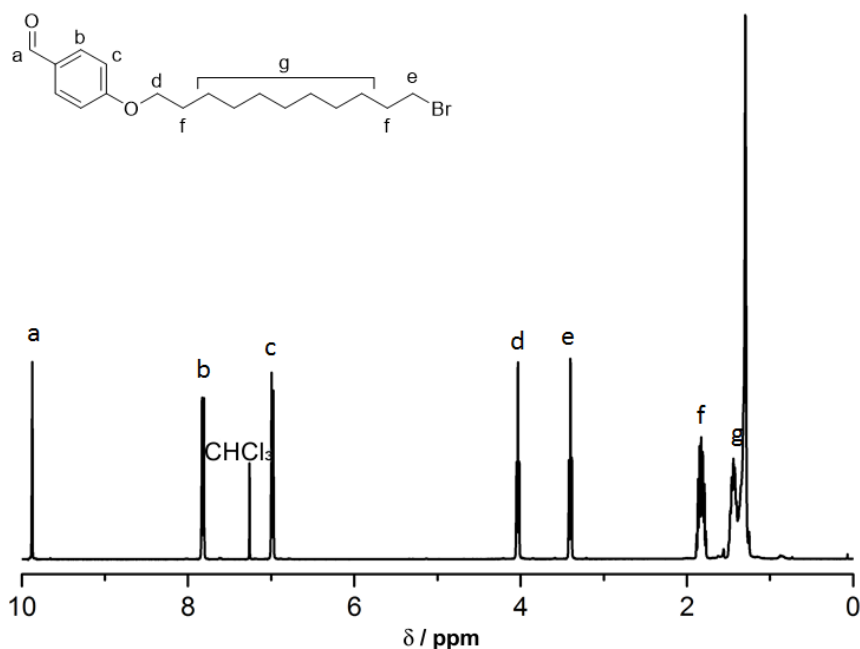
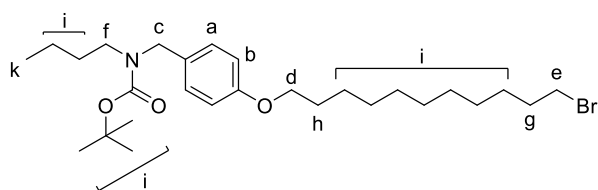


**Figure 69.**  $^1\text{H}$  NMR spectrum of **28** ( $\text{CDCl}_3$ , 298 K).

### Synthesis of *tert*-butyl (4-((11-bromoundecyl)oxy)benzyl)(butyl)carbamate (**29**)



Following a modified literature procedure,<sup>[281]</sup> a solution of **28** (2.4 g, 6.7 mmol, 1.0 equiv.) and butan-1-amine (0.5 g, 6.7 mmol, 1.0 equiv.) in MeOH

(16.5 mL) was stirred at ambient temperature for 16 h. Subsequently,  $\text{NaBH}_4$  (0.4 mg) was added. The reaction was quenched by addition of water. The solution was extracted with DCM, the organic phase was dried over  $\text{Na}_2\text{SO}_4$  and the solvent removed under reduced pressure. The crude product,  $\text{Boc}_2\text{O}$  (1.46 g, 6.7 mmol, 1.0 equiv.) and triethylamine (0.68 g, 6.7 mmol, 1.0 equiv.) in MeOH (33 mL) were stirred at ambient temperature for 16 h. The solvent was removed. After column chromatography (EA/cyclohexane = 1:30) the product was obtained as a yellow liquid (2.6 g, 5.1 mmol, 76%).

$^1\text{H}$  NMR (400 MHz, Acetone)  $\delta$  / ppm = 7.19 (d,  $^3J = 8.6$  Hz, 2H,  $\text{CH}^a$ ), 6.88 (d,  $^3J = 8.4$  Hz, 2H,  $\text{CH}^b$ ), 4.36 (s, 2H,  $\text{CH}_2^c$ ), 3.97 (t,  $^3J = 6.5$  Hz, 2H,  $\text{CH}_2^d$ ), 3.49 (t,  $^3J = 6.8$  Hz, 2H,  $\text{CH}_2^e$ ), 3.14 (s, 2H,  $\text{CH}_2^f$ ), 1.86 (dd,  $^3J = 14.3$  Hz,  $^3J = 7.3$  Hz, 2H,  $\text{CH}_2^g$ ), 1.80 – 1.71 (m, 2H,  $\text{CH}_2^h$ ), 1.54 – 1.29 (m, 26H,  $\text{CH}_2^i$ ), 0.88 (t,  $^3J = 7.3$  Hz, 3H,  $\text{CH}_3^k$ ).

$^{13}\text{C}$  NMR (101 MHz, Acetone)  $\delta$  / ppm = 159.4, 131.8, 115.2, 79.4, 68.5, 46.6, 34.8, 33.6, 30.3, 30.2, 30.2, 30.1, 28.8, 28.6, 26.8, 20.6, 14.1.

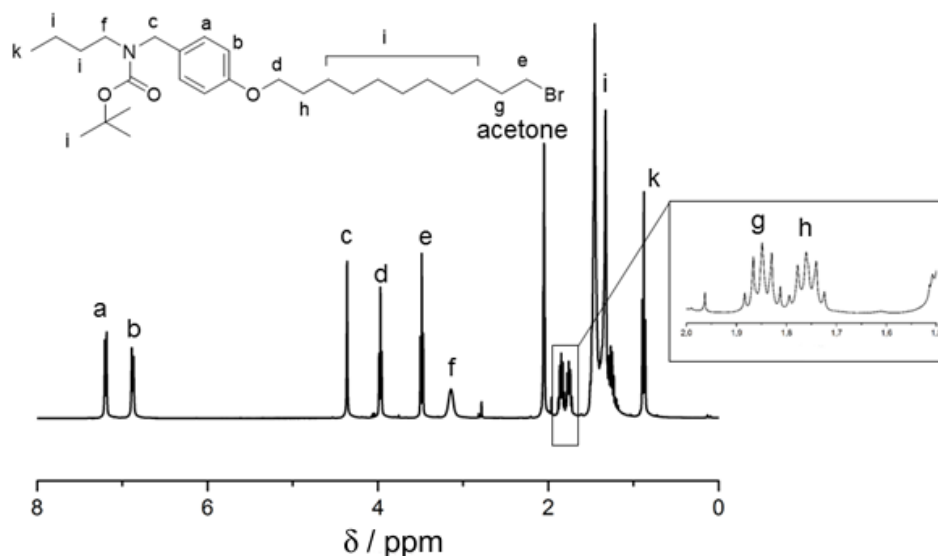
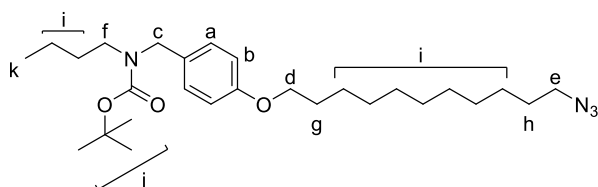


**Figure 70.**  $^1\text{H}$  NMR spectrum of **29** (acetone- $d_6$ , 298 K). Adapted from ref [252] with permission from Wiley-VCH. © 2016 WILEY-VCH Verlag GmbH & Co. KGaA, Weinheim.

### Synthesis of *tert*-butyl (4-((11-azidoundecyl)oxy)benzyl)(butyl)carbamate (**30**)



**29** (0.96 g, 1.87 mmol, 1.0 equiv.) was dissolved in DMF (10 mL), subsequently  $\text{NaN}_3$  (0.61 g, 9.35 mmol, 5.0 equiv.) was added. The mixture was stirred at ambient

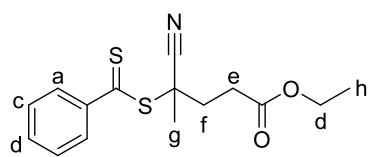
temperature for 16 h. The mixture diluted with ethyl acetate and extracted with water, the organic phase dried over  $\text{Na}_2\text{SO}_4$  and the solvent removed under reduced pressure. The product was obtained as a pale yellow oil (0.83 g, 1.8 mmol, 94%).

$^1\text{H}$  NMR (400 MHz,  $\text{CDCl}_3$ )  $\delta$  / ppm = 7.14 (s, 2H,  $\text{CH}^{\text{a}}$ ), 6.83 (d,  $^3J = 8.6$  Hz, 2H,  $\text{CH}^{\text{b}}$ ), 4.36 (s, 2H,  $\text{CH}_2^{\text{c}}$ ), 3.93 (t,  $^3J = 6.5$  Hz, 2H,  $\text{CH}_2^{\text{d}}$ ), 3.25 (t,  $^3J = 7.0$  Hz, 2H,  $\text{CH}_2^{\text{e}}$ ), 3.12 (m, 2H,  $\text{CH}_2^{\text{f}}$ ), 1.82 – 1.71 (m, 2H,  $\text{CH}_2^{\text{g}}$ ), 1.65 – 1.54 (m, 2H,  $\text{CH}_2^{\text{h}}$ ), 1.51 – 1.25 (m, 27H,  $\text{CH}_2^{\text{i}}$ ,  $\text{CH}_3^{\text{j}}$ ), 0.88 (t,  $^3J = 7.3$  Hz, 3H,  $\text{CH}_3^{\text{k}}$ ).

$^{13}\text{C}$  NMR (101 MHz, Acetone)  $\delta$  / ppm = 159.3, 131.7, 115.2, 79.4, 68.5, 52.0, 46.6, 30.3, 30.1, 29.5, 28.6, 27.4, 26.8, 20.6, 14.1.

ESI MS  $m/z$ : [**30**+ $\text{Na}^+$ ], calculated = 497.35, found: 497.35.

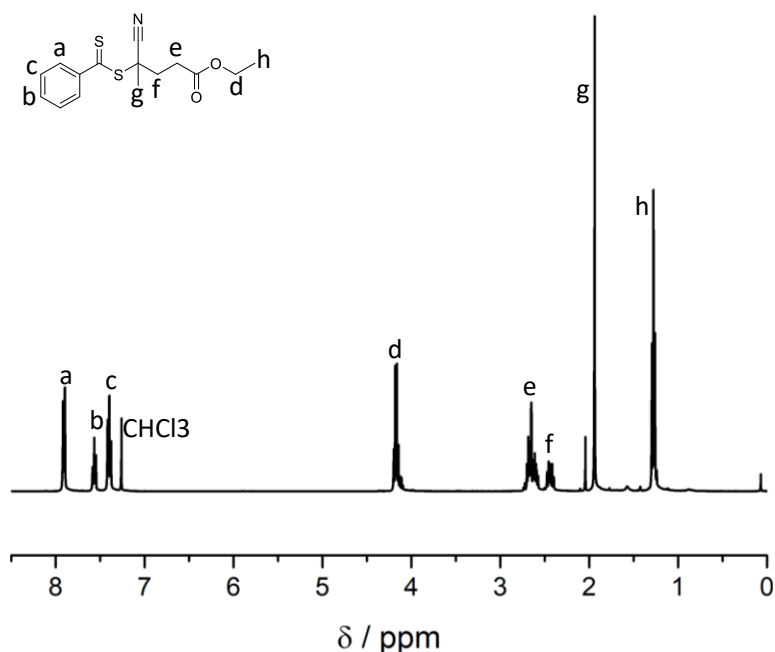
### Synthesis of Ethyl 4-cyano-4-((phenylcarbonothioyl)thio)pentanoate (CTA)



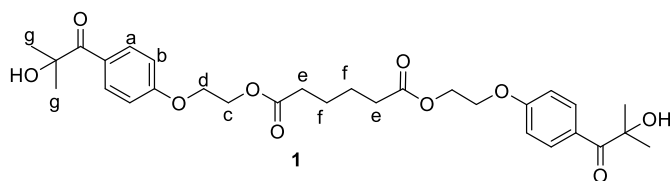
Following a literature procedure,<sup>[108]</sup> 4-cyano-4-((phenylcarbonothioyl)thio)pentanoic acid (0.5 g, 1.78 mmol, 1.0 equiv.) was dissolved in 5 mL of dry dichloromethane (DCM). Ethanol (1.03 mL, 17.8 mmol, 10.0 equiv.) and DMAP (0.044 g, 0.35 mmol, 0.2 equiv.) were dissolved in 5 mL of dry DCM and subsequently added to the mixture. DCC (0.55 g, 2.67 mmol, 1.5 equiv.) dissolved in 5 mL of dry DCM was added to the solution. The reaction was carried out at ambient temperature for 24 h. Solids were filtered off, the filtrate concentrated and the crude product was purified by column chromatography on silica gel eluting with ethyl acetate/*n*-hexane (1/9) to yield the product as a pale yellow liquid (0.45 g, 1.45 mmol, 80%).

<sup>1</sup>H NMR (400 MHz, CDCl<sub>3</sub>)  $\delta$  / ppm = 7.90 (d, <sup>3</sup>J = 8.5 Hz, 2H, CH<sup>a</sup>), 7.56 (d, <sup>3</sup>J = 7.4 Hz, 1H, CH<sup>b</sup>), 7.39 (t, <sup>3</sup>J = 7.8 Hz, 2H, CH<sup>c</sup>), 4.17 (q, <sup>3</sup>J = 7.1 Hz, 2H, CH<sub>2</sub><sup>d</sup>), 2.70–2.60 (m, 2H, CH<sub>2</sub><sup>e</sup>), 2.51–2.37 (m, 2H, CH<sub>2</sub><sup>f</sup>), 1.94 (s, 3H, CH<sub>3</sub><sup>g</sup>), 1.28 (t, <sup>3</sup>J = 7.1 Hz, 3H, CH<sub>2</sub><sup>h</sup>).

<sup>13</sup>C NMR (100 MHz, CDCl<sub>3</sub>)  $\delta$  / ppm = 222.3, 171.6, 144.4, 133.0, 128.6, 126.7, 118.5, 61.1, 45.8, 33.5, 29.9, 24.1, 14.2.



**Figure 71.** <sup>1</sup>H NMR spectrum of the CTA (CDCl<sub>3</sub>, 298 K).

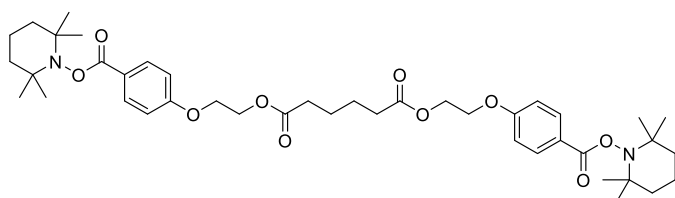
**Synthesis of bis(2-(4-(2-hydroxy-2-methylpropanoyl)phenoxy)ethyl) adipate (**33**)**

Adipic acid (1.0 g, 6.8 mmol, 1.0 equiv.), DMAP (125 mg, 1.03 mmol, 0.15 equiv.) and 2-hydroxy-1-(4-(2-hydroxyethoxy)-

phenyl)-2-methyl-propan-1-one (Irgacure 2959, 4.60 g, 20.5 mmol, 3.0 equiv.) were dissolved in dry DCM (100 mL) and the mixture was cooled to 0 °C. Subsequently, EDCxHCl (5.25 g, 27.3 mmol, 4.0 equiv.) was dissolved in 20 mL dry DCM and added in a dropwise manner. The solution was allowed to warm to ambient temperature and stirred for another 48 h. The solution was washed with distilled water (3x). The organic phase was dried over Na<sub>2</sub>SO<sub>4</sub> and the solvent was removed under reduced pressure. The product was isolated after column chromatography on silica gel (cyclohexane/ethyl acetate 1:1) as a white solid (3.07g, 5.5 mmol, 81%).

<sup>1</sup>H NMR (400 MHz, DMSO) δ / ppm = 8.23 (d, <sup>3</sup>J = 9.0 Hz, 4H, CH<sup>a</sup>), 7.01 (d, <sup>3</sup>J = 9.0 Hz, 4H, CH<sup>b</sup>), 5.65 (s, 2H, C-OH), 4.38 (m, 4H, CH<sub>2</sub><sup>c</sup>), 4.31 – 4.22 (m, 2H, CH<sub>2</sub><sup>d</sup>), 2.34 (s, 4H, CH<sub>2</sub><sup>e</sup>), 1.55 (s, 4H, CH<sub>2</sub><sup>f</sup>), 1.40 (s, 12H, CH<sub>3</sub><sup>g</sup>).

<sup>13</sup>C NMR (101 MHz, DMSO) δ / ppm = 202.0, 172.7, 161.4, 132.5, 127.8, 113.8, 76.7, 66.0, 62.2, 33.0, 28.2, 23.8.

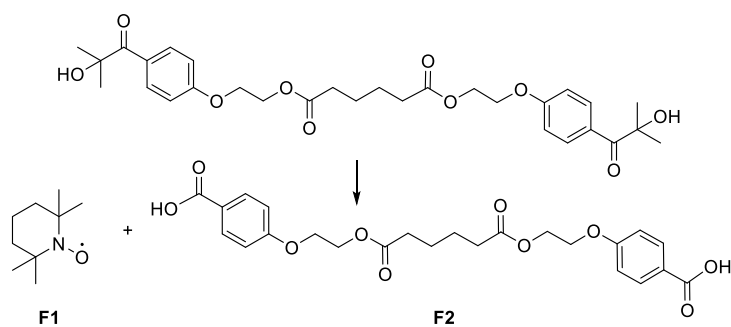
**Model Reaction for the UV-light Induced Crosslinking Reaction****Bis(2-(4-(((2,2,6,6-tetramethylpiperidin-1-yl)oxy)carbonyl)phenoxy)-ethyl) adipate (**35**)**

TEMPO (50 mg, 0.32 mmol, 2.1 equiv.) and **33** (71.7 mg, 0.152 mmol, 1.0 equiv.) were dissolved in 20 mL anisole. The

solution was purged for 10 min with argon and the flask was put in a photo reactor equipped with an Arimed B6 lamp ( $\lambda_{\text{max}} = 320$  nm). The mixture was irradiated overnight under stirring. Subsequently, the solvent was removed.

ESI MS *m/z*: [**35**+Na<sup>+</sup>], calculated = 775.4140; found = 775.4153.

### Model Reaction for Deprotection/Unfolding



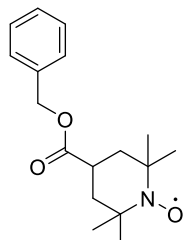
**35** (50 mg, 0.066 mmol, 1.0 equiv.) was dissolved in 4 mL DCM and heated to 35 °C. *m*CPBA (57 mg 0.33 mmol, 5.0 equiv.) dissolved in 1 mL DCM was added dropwise and

the solution was stirred at 35 °C for 0.5 h. NaHCO<sub>3</sub> was added to quench the reaction. Subsequently, the solution was diluted with DCM and extracted with sat. NaHCO<sub>3</sub> solution. The solvent was removed under reduced pressure.

ESI MS *m/z*: [**F1**+H<sub>2</sub><sup>+</sup>], calculated = 158.1545; found = 158.1543.

[**F2**+Na<sup>+</sup>] calculated = 497.1418; found = 497.1428.

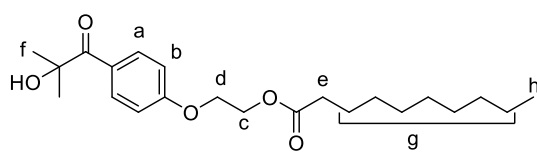
### Synthesis of Benzyl Carboxy-TEMPO (37)



Benzylchloride (50 mg, 0.395 mmol, 1.0 equiv.), K<sub>2</sub>CO<sub>3</sub> (273 mg, 1.97 mmol, 5.0 equiv.) and 4-carboxy-TEMPO (158 mg, 0.79 mmol, 2.0 equiv.) were dissolved in DMF (10 mL). The mixture was stirred at 50 °C for 48 h. Subsequently, the mixture was diluted with ethyl acetate and extracted three times with brine. The organic phase was dried over

Na<sub>2</sub>SO<sub>4</sub>, filtered and the solvent removed under reduced pressure. The crude product was diluted with THF (10 mL) and precipitated twice into cold methanol (200 mL).

ESI MS *m/z*: [**37**+Na<sup>+</sup>], calculated = 313.1648; found = 313.1647.

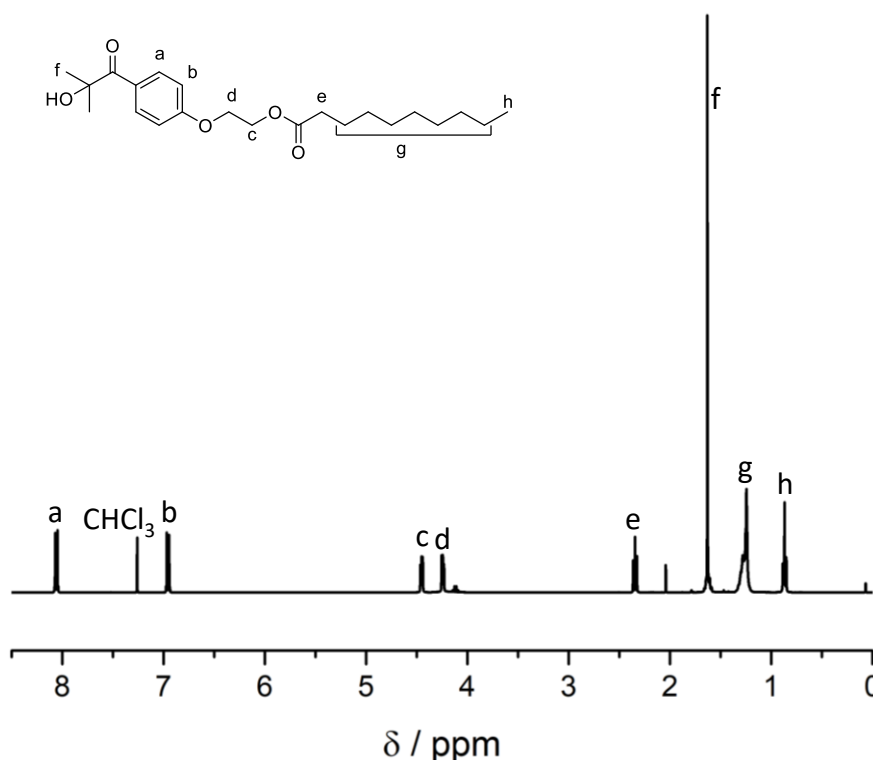
**Synthesis of Bis(2-(4-(2-hydroxy-2-methylpropanoyl)phenoxy)ethyl) adipate (38)**

Decanoic acid (384 mg, 2.23 mmol, 1.0 equiv.), DMAP (40.8 mg, 0.33 mmol, 0.15 equiv.) and 2-hydroxy-1-(4-(2-hydroxy-

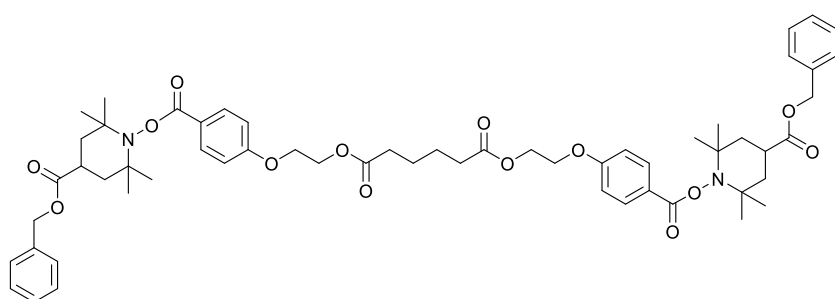
ethoxy)phenyl)-2-methylpropan-1-one (Irgacure2959 (500 mg, 2.23 mmol, 1.0 equiv.) were dissolved in dry DCM (50 mL) and cooled to 0 °C. Subsequently, EDC×HCl (1.71 g, 8.9 mmol, 4.0 equiv.) was dissolved in 10 mL dry DCM and added dropwise. The solution was allowed to warm to ambient temperature and was stirred for another 24 h. The solution was washed with water (3×). The organic phase was dried over Na<sub>2</sub>SO<sub>4</sub> and the solvent was removed under reduced pressure. The product was obtained as a colourless oil (0.27 g, 0.7 mmol, 32%) after column chromatography (cyclohexane/ethyl acetate 7:3).

<sup>1</sup>H NMR (400 MHz, CDCl<sub>3</sub>) δ / ppm = 8.06 (d, <sup>3</sup>J = 9.1 Hz, 4H, CH<sup>a</sup>), 6.96 (d, <sup>3</sup>J = 9.1 Hz, 4H, CH<sup>b</sup>), 4.45 (m, 4H, CH<sub>2</sub><sup>c</sup>), 4.24 (m, 4H, CH<sub>2</sub><sup>d</sup>), 2.34 (t, J = 7.5 Hz, 4H, CH<sub>2</sub><sup>e</sup>), 1.63 (s, 6H, CH<sub>3</sub><sup>f</sup>), 1.35 – 1.18 (m, 14H, CH<sub>2</sub><sup>g</sup>), 0.87 (t, <sup>3</sup>J = 6.9 Hz, 6H, CH<sub>3</sub><sup>h</sup>).

<sup>13</sup>C NMR (101 MHz, CDCl<sub>3</sub>) δ / ppm = 202.7, 173.9, 162.5, 132.5, 126.4, 114.3, 75.9, 66.3, 62.3, 34.3, 32.0, 29.4, 28.8, 25.0, 22.8, 14.2.

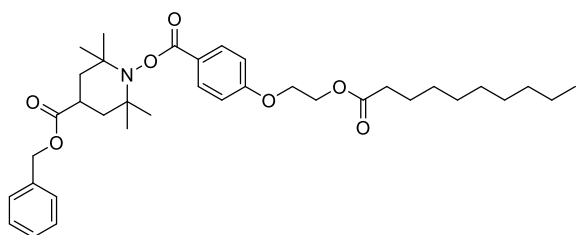


**Figure 72.** <sup>1</sup>H NMR spectrum of **38** (CDCl<sub>3</sub>, 298 K).

**Synthesis of Bis(2-(4-(((4-((benzyloxy)carbonyl)-2,2,6,6-tetramethylpiperidin-1-yl)oxy)carbonyl)phenoxy)ethyl) adipate (39)**

**37** (25 mg, 0.086 mmol, 1.0 equiv.) and **33** (96 mg, 0.17 mmol, 2.0 equiv.) were dissolved in anisole (20 mL). The solution

was purged for 30 min with argon and the flask was put in a photo reactor equipped with an Arimed B6 lamp ( $\lambda_{\max} = 320$  nm). The mixture was irradiated overnight under stirring. Subsequently, the solvent was removed prior to fluorescence analysis.

**Synthesis of Benzyl 1-((4-(2-(decanoyloxy)ethoxy)benzoyl)oxy)-2,2,6,6-tetramethylpiperidine-4-carboxylate (40)**

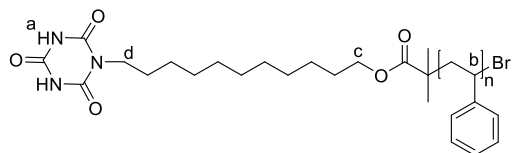
**37** (25 mg, 0.086 mmol, 1.0 equiv) and **38** (32.5 mg, 0.086 mmol, 1.0 equiv.) were dissolved in anisole (20 mL). The solution

was purged for 30 min with argon and the flask was put in a photo reactor equipped with an Arimed B6 lamp ( $\lambda_{\max} = 320$  nm). The mixture was irradiated overnight under stirring. Subsequently, the solvent was removed prior to fluorescence analysis.



### 5.3.2 Polymer Syntheses

#### General Procedure for the Synthesis of CA-PS-Br (P1-P3)



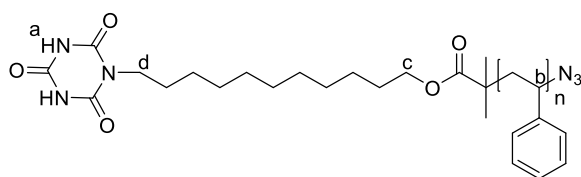
Styrene,  $\text{CuBr}_2$  (0.1 equiv.), and  $\text{Me}_6\text{TREN}$  (0.1 equiv.) were dissolved in anisole (5 mL) in a flame-dried Schlenk flask and subsequently purged with argon for 30 min. **15** (1.0 equiv.) and  $\text{Sn}(\text{EH})_2$  (0.5 equiv.) were each dissolved in anisole (1.5 mL) in separate round-bottom flasks and purged with argon for 10 min. After removing oxygen, the initiator and reducing agent were transferred to the reaction flask *via* a cannula. The reaction mixture was subsequently placed into an oil bath tempered at 90 °C for various hours and the flask was next cooled to ambient temperature in a water bath and opened to the atmosphere. The copper catalyst was removed by passing the solution over a short column of neutral alumina oxide. The solvent was evaporated and the crude polymer dissolved in THF and precipitated twice into cold methanol (200 mL). The polymer was dried overnight under high vacuum and isolated as a white solid.

$^1\text{H}$  NMR (400 MHz,  $\text{CDCl}_3$ )  $\delta$  / ppm = 7.69 (2H,  $\text{NH}^a$ ), 7.41 – 6.09 (5H, ArH of PS), 4.43 – 4.38 (1H,  $\text{CH}^b$ ), 3.76 (2H,  $\text{CH}_2^c$ ), 3.57 (2H,  $\text{CH}_2^d$ ), 1.88– 1.27 (aliphatic protons of PS).

**Table 11.** Overview over the polymerization conditions.

| ID        | Monomer | Initiator | $\text{CuBr}_2$ | Ligand | Reducing agent | Time |
|-----------|---------|-----------|-----------------|--------|----------------|------|
| <b>P1</b> | 100     | 1         | 0.1             | 0.1    | 0.5            | 3 h  |
| <b>P2</b> | 400     | 1         | 0.1             | 0.1    | 0.5            | 3 h  |
| <b>P3</b> | 200     | 1         | 0.1             | 0.1    | 0.5            | 24 h |

### General Procedure for the Synthesis of CA-PS-N<sub>3</sub> (P4-P6)

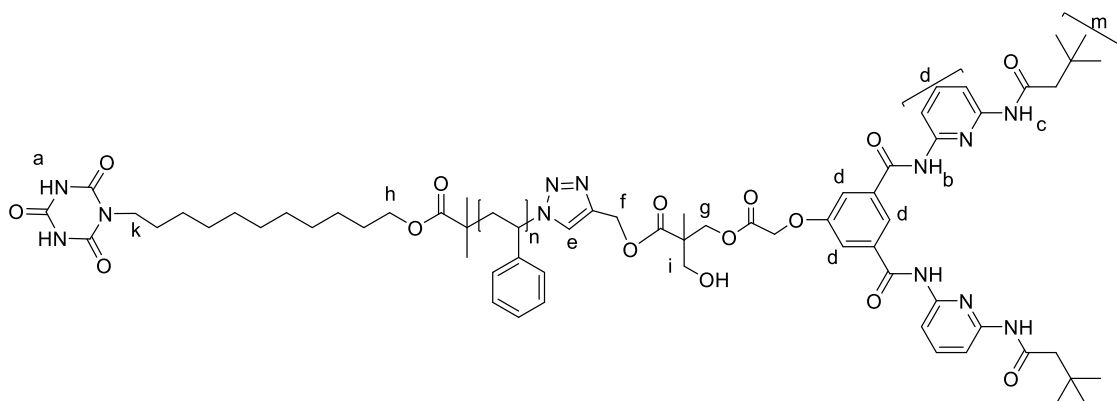


**P1-P3** (1.0 equiv.) was dissolved in DMF (10 mL) and NaN<sub>3</sub> (10.0 equiv.) was added. The mixture was stirred for 72 h at ambient temperature. The reaction mixture was

subsequently diluted with ethyl acetate and washed with distilled water. The organic phase was dried with Na<sub>2</sub>SO<sub>4</sub>, filtered and the solvent removed under reduced pressure. The residue was diluted with THF and precipitated into cold MeOH (200 mL). The polymer was dried overnight under high vacuum and isolated as a white solid.

<sup>1</sup>H NMR (400 MHz, CDCl<sub>3</sub>) δ / ppm = 7.87 (2H of cyanuric acid), 7.10 – 6.38 (5H, ArH of PS), 3.94 (1H, CH-N<sub>3</sub>), 3.82 (2H, CH<sub>2</sub>CH<sub>2</sub>-N), 3.56 (2H, CH<sub>2</sub>CH<sub>2</sub>-OCO), 1.88– 1.27 (aliphatic protons of PS).

### General Procedure for the Synthesis of CA-PS-HW/OH (P7-P9)

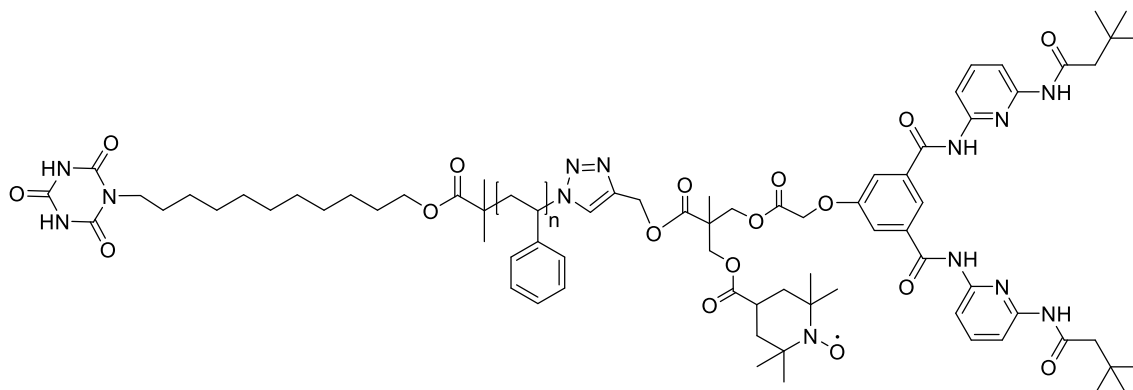


**P4-P6** (1.0 equiv.), **11** (1.5 equiv.), CuSO<sub>4</sub>·5H<sub>2</sub>O (2.0 equiv.), sodium ascorbate (2.0 equiv.) were dissolved in dry DMF (10 mL) and stirred for 24 h at ambient temperature. Subsequently, azide functional Merrifield resin (500 mg) was added and the solution was stirred for 24 h at ambient temperature. The solids were filtered off, the solution diluted with DCM and subsequently extracted with 5% EDTA solution. The organic phase was separated and dried with Na<sub>2</sub>SO<sub>4</sub>, concentrated and precipitated into cold MeOH. The polymer was dried under high vacuum. The product was obtained as a white solid.

<sup>1</sup>H NMR (400 MHz, CD<sub>2</sub>Cl<sub>2</sub>) δ / ppm = 12.71 (2H, NH<sup>a</sup>), 9.92 – 9.49 (4H, NH<sup>b,c</sup>), 8.24 – 7.67 (9H, CH<sup>n</sup>), 7.41 – 6.09 (5H, ArH of PS), 5.18 – 5.07 (3H, CH<sup>e</sup>, CH<sub>2</sub><sup>i</sup>), 4.69

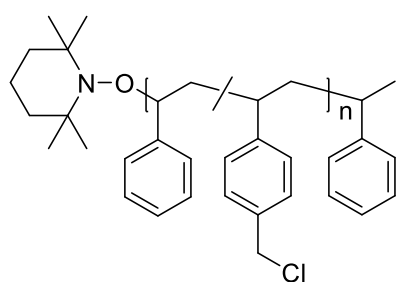
(2H,  $CH_2^g$ ), 4.36 (2H,  $CH_2^h$ ), 3.94 (2H,  $CH_2^i$ ), 3.61 (2H,  $CH_2^k$ ), 1.84-1.22 (aliphatic protons of PS), 1.11 (18H,  $CH_3^m$ ).

### General Procedure for the Synthesis of CA-PS-HW/TEMPO



Dry DCM (20 mL) was purged with argon in a flame dried Schlenk-flask for 15 minutes. **P7-P9** (1.0 equiv.), 4-carboxy-TEMPO (8.5 equiv.) and DMAP (5 equiv.) were dissolved in dry DCM (6 mL) in a flame dried Schlenk-flask. DCC (10.0 equiv.) dissolved in dry DCM (2 mL) was added rapidly through a septum. The mixture was stirred at ambient temperature and protected from light for 48 h. The solids were filtered off and the solvent removed under vacuum. The residue was diluted with DCM and precipitated into cold MeOH (80 mL). The polymer was dried under high vacuum.

### General Procedure for the Synthesis of PS-co-CMS (P13-P16)

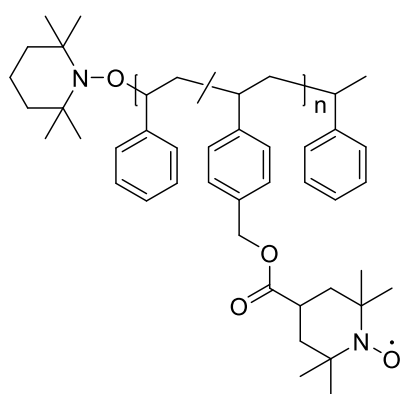


Styrene (2.25 mL, 19.6 mmol, 95.0 equiv.), 4-(chloromethyl)styrene (0.31 mL, 2.18 mmol, 5.0 equiv.) and 2,2,6,6-tetramethyl-1-(1-phenyl-ethoxy)piperidine (57.0 mg, 0.218 mmol, 1.0 equiv.) were placed into a flame-dried Schlenk flask and deoxygenated by four consecutive freeze-pump-thaw cycles. Subsequently, the reaction mixture was placed into an oil bath tempered at 125 °C. After 2 h the polymerization was stopped by cooling the flask with liquid nitrogen and opening it to the atmosphere. The crude product was diluted with THF (20 mL) and precipitated twice into cold methanol (200 mL). The polymer was afforded as a white powder by filtration and dried under high vacuum.

For **P2**, the styrene (4-chloromethyl) styrene ratio was adjusted to 90:10. For the polymer **P3** the styrene (4-chloromethyl) styrene ratio was adjusted to 70:30 and the reaction time reduced to 0.5 h in bulk. For the polymer **P4** the styrene (4-chloromethyl) styrene ratio was adjusted to 70:30 and the reaction time reduced to 1 h.

$^1\text{H NMR}$  (400 MHz,  $\text{CDCl}_3$ )  $\delta$  / ppm = 7.09 – 6.50 (aromatic protons of PS and initiator), 4.52 (bs, 2H,  $\text{CH}_2\text{Cl}$ ), 2.33 – 0.93 (m, aliphatic protons of PS and initiator).

### General Procedure for the Nitroxide Grafting Yielding **P13'**-**P16'**

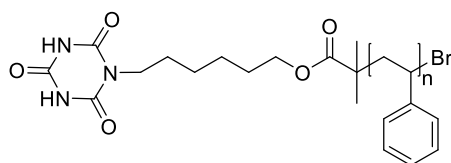


The PS-*co*-CMS polymer (**P13-P16**, 200 mg, 0.41 mmol CMS, 1.0 eq.),  $\text{K}_2\text{CO}_3$  (286 mg, 2.07 mmol, 5.0 eq.) and 4-carboxy-TEMPO (165 mg, 0.83 mmol, 2.0 eq.) were dissolved in DMF (10 mL). The mixture was stirred at 50 °C for 72 h. Subsequently, the mixture was diluted with ethyl acetate and washed three times with brine. The organic phase was dried over  $\text{Na}_2\text{SO}_4$  and filtered. The solvent was removed under reduced pressure. The

crude product was diluted with THF (10 mL) and precipitated twice into cold methanol (200 mL). After drying overnight under high vacuum, the product was obtained as an orange solid.

$^1\text{H NMR}$  (400 MHz,  $\text{CDCl}_3$ , 298 K)  $\delta$  / ppm = 7.12 – 6.63 (aromatic protons of PS and initiator), 5.15 (bs, 2H,  $\text{CH}_2\text{-OCO}$ ), 2.33 – 0.96 (m, aliphatic protons of PS, initiator and carboxy TEMPO).

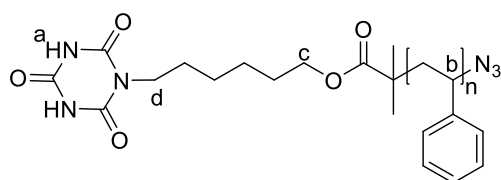
### Synthesis of CA-PS-Br (**P17**)



Styrene,  $\text{CuBr}_2$  (0.1 equiv.), and  $\text{Me}_6\text{TREN}$  (0.1 equiv.) were dissolved in anisole (5 mL) in a flame-dried Schlenk flask and subsequently purged with argon for 30 min. **15** (1.0 equiv.) and  $\text{Sn}(\text{EH})_2$  (0.5 equiv.) were each dissolved in anisole (1.5 mL) in separate round-bottom flasks and purged with argon for 10 min. After removing oxygen, the initiator and reducing

agent were transferred to the reaction flask *via* a cannula. The reaction mixture was subsequently placed into an oil bath tempered at 90 °C for three hours and the flask was next cooled to ambient temperature in a water bath and opened to the atmosphere. The copper catalyst was removed by passing the solution over a short column of neutral alumina oxide. The solvent was evaporated and the crude polymer dissolved in THF and precipitated twice into cold methanol (200 mL). The polymer was dried overnight under high vacuum and isolated as a white solid.

### Synthesis of CA-PS-N<sub>3</sub> (P18)



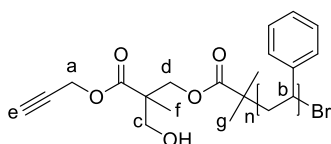
The previously obtained **P17** was directly subjected to bromine-azide exchange. Therefore, **P17** (1.0 equiv.) was dissolved in DMF (10 mL) and NaN<sub>3</sub> (10.0 equiv.) was added.

The mixture was stirred for 72 h at ambient temperature. The reaction mixture was diluted with ethyl acetate and washed with distilled water. The organic phase was dried with Na<sub>2</sub>SO<sub>4</sub>, filtered and the solvent removed under reduced pressure. The residue was diluted with THF and precipitated into cold MeOH (200 mL). The polymer was dried overnight under high vacuum and isolated as a white solid.

<sup>1</sup>H NMR (400 MHz, CDCl<sub>3</sub>) δ / ppm = 7.87 (2H, NH<sup>a</sup>), 7.10 – 6.38 (5H, ArH of PS), 3.94 (1H, CH<sup>b</sup>), 3.82 (2H, CH<sub>2</sub><sup>c</sup>), 3.56 (2H, CH<sup>d</sup>), 1.88– 1.27 (aliphatic protons of PS).

$M_n = 14800$  Da.  $\bar{D} = 1.12$ .

### Synthesis of Alkyne-Hydroxy Functional PS-Br (P19)



Styrene (7.13 mL, 62.3 mmol, 100 equiv.), CuBr<sub>2</sub> (8.9 mg, 0.0623 mmol, 0.1 equiv.), and Me<sub>6</sub>TREN (16.6 μL, 0.0623 mmol, 0.1 equiv.) were put in a Schlenk flask and

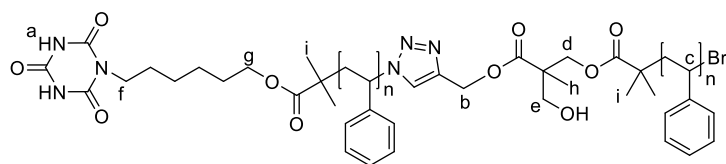
subsequently purged with argon for 30 min. **17** (200 mg, 0.623 mmol, 1.0 equiv.) and Sn(EH)<sub>2</sub> (126.1 mg, 0.0311 mmol, 0.05 equiv.) were each dissolved in anisole (3 mL) in separate round-bottom flasks and purged with argon for 10 min. After removing oxygen, the initiator and reducing agent were transferred to the reaction flask *via* a

cannula. The reaction mixture was subsequently placed into an oil bath tempered at 90 °C for 3 h and the flask was next cooled to ambient temperature in a water bath and opened to the atmosphere. The copper catalyst was removed by passing the solution over a short column of neutral alumina oxide. The solvent was evaporated and the crude polymer dissolved in THF and precipitated twice into cold methanol (100 mL). The polymer was dried overnight under high vacuum and isolated as a white solid.

$^1\text{H}$  NMR (400 MHz,  $\text{CDCl}_3$ )  $\delta$  / ppm = 7.10 – 6.39 (5H, ArH of PS), 4.67 (s, 2H,  $\text{CH}_2^{\text{a}}$ ), 4.60 – 4.34 (m, 1H,  $\text{CH}^{\text{b}}$ ), 3.76 (m, 2H,  $\text{CH}_2^{\text{c}}$ ), 3.48 (m, 3H,  $\text{CH}_2^{\text{d}}$ ,  $\text{CH}^{\text{e}}$ ). 1.88 – 1.27 (aliphatic protons of PS), 1.10 – 1.09 (m, 3H,  $\text{CH}_3^{\text{f}}$ ), 0.97 – 0.88 (m, 6H,  $\text{CH}_3^{\text{g}}$ ).

$M_n$  = 6200 Da.  $D$  = 1.12.

### Synthesis of P20

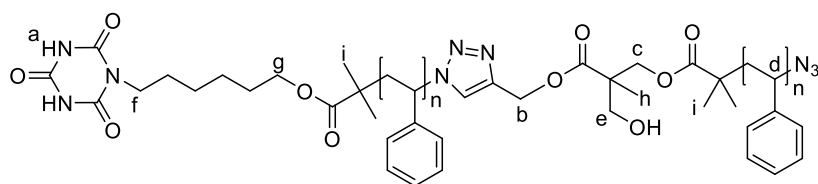


**P18** (400 mg, 0.025 mmol, 1.0 equiv.), **P19** (190 mg, 0.038 mmol, 1.5 equiv.), CuI (24 mg, 0.13 mmol, 5.0 equiv.),

and DIPEA (21  $\mu\text{l}$ , 0.13 mmol, 5.0 equiv.) were dissolved in DMF (10 mL) and stirred for 24 h at ambient temperature under inert atmosphere. Subsequently, azide functional Merrifield resin (100 mg) was added and the mixture was stirred for another 24 h at ambient temperature. The solution was diluted with EA, filtered and extracted with 5% EDTA solution to remove the copper catalyst. The organic phase was dried over  $\text{Na}_2\text{SO}_4$ , filtered and the solvent removed under reduced pressure. The residue was diluted with THF and precipitated into cold MeOH (100 mL). The product was dried overnight under high vacuum. The product was obtained as a white solid.

$^1\text{H}$  NMR (400 MHz,  $\text{CDCl}_3$ )  $\delta$  / ppm = 7.87 (2H,  $\text{NH}^{\text{a}}$ ), 7.10 – 6.38 (5H, ArH of PS), 5.09 – 5.04 (m, 2H,  $\text{CH}_2^{\text{b}}$ ), 4.55 – 4.41 (m, 1H,  $\text{CH}^{\text{c}}$ ), 4.05 – 4.03 (m, 2H,  $\text{CH}_2^{\text{d}}$ ), 3.82 – 3.79 (m, 2H,  $\text{CH}_2^{\text{e}}$ ), 3.54 – 3.32 (4H,  $\text{CH}_2^{\text{f,g}}$ ), 2.20 – 1.26 (aliphatic protons of PS and CA), 1.09 (m, 3H,  $\text{CH}_3^{\text{h}}$ ), 0.98 – 0.87 (12H,  $\text{CH}_3^{\text{h}}$ ).

### Synthesis of P21



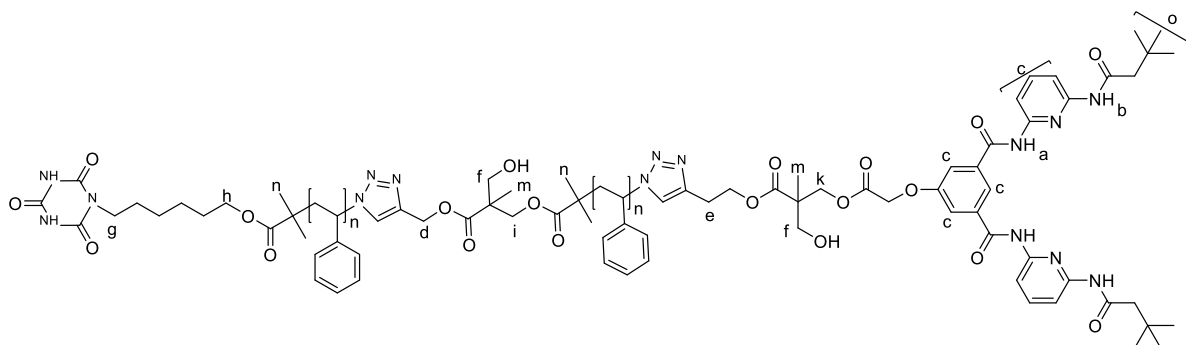
**P20** was subjected to bromine-azide exchange as previously described.

**P20** (410 mg, 25  $\mu\text{mol}$ , 1.0 equiv.),  $\text{NaN}_3$  (65 mg, 1.0 mmol, 40 equiv.) were dissolved in dry DMF (10 mL) and stirred for 24 h at ambient temperature. Subsequently, the solution diluted with ethyl acetate and extracted with water. The organic phase was dried with  $\text{Na}_2\text{SO}_4$ , filtered and the solvent removed. The remainder was diluted with DCM and precipitated into cold MeOH (80 mL). The product was obtained as a white solid.

$^1\text{H}$  NMR (400 MHz,  $\text{CDCl}_3$ )  $\delta$  / ppm = 7.87 (2H,  $\text{NH}^a$ ), 7.10 – 6.38 (5H, ArH of PS), 5.09 – 5.04 (m, 2H,  $\text{CH}_2^b$ ), 4.05 – 4.03 (m, 2H,  $\text{CH}_2^d$ ), 3.96 – 3.88 (m, 1H,  $\text{CH}^e$ ), 3.82 – 3.79 (m, 2H,  $\text{CH}_2^e$ ), 3.54 – 3.32 (4H,  $\text{CH}_2^{f,g}$ ), 2.20 – 1.26 (aliphatic protons of PS and CA), 1.09 (m, 3H,  $\text{CH}_3^h$ ), 0.98 – 0.87 (12H,  $\text{CH}_3^h$ ).

$M_n = 18100$  Da.  $D = 1.33$ .

### Synthesis of P22

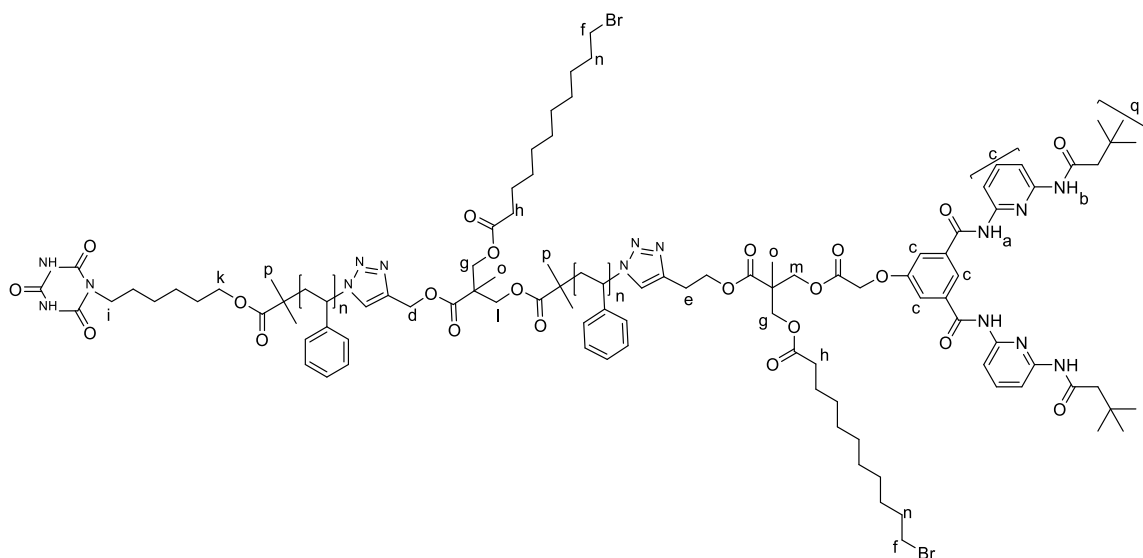


**P21** (360 mg, 21  $\mu\text{mol}$ , 1.0 equiv.) and **11** (32 mg, 42  $\mu\text{mol}$ , 2.0 equiv.) were dissolved in dry DMF (10 mL),  $\text{CuSO}_4 \cdot 5\text{H}_2\text{O}$  (26.4 mg, 0.11 mmol, 5.0 equiv.) and sodium ascorbate (21 mg, 0.11 mmol, 45.0 equiv.) were added and the solution was stirred for 24 h at ambient temperature. Subsequently, the solution was diluted with ethyl acetate and extracted with 5% EDTA solution. The organic phase was dried with  $\text{Na}_2\text{SO}_4$ , filtered and the solvent removed. The remainder was diluted with THF and precipitated into cold MeOH (80 mL). The product was obtained as a white solid.

$^1\text{H}$  NMR (400 MHz,  $\text{CD}_2\text{Cl}_2$ )  $\delta$  / ppm = 9.85 (s, 2H,  $\text{NH}^{\text{a}}$ ), 9.33 (s, 2H,  $\text{NH}^{\text{b}}$ ), 8.23 – 7.70 (m, 9H,  $\text{CH}^{\text{c}}$ ), 7.10 – 6.41 (m, 5H, ArH of PS), 5.14 – 5.04 (m, 4H,  $\text{CH}_2^{\text{d,e}}$ ), 3.83 – 3.78 (m, 4H,  $\text{CH}_2^{\text{f}}$ ), 3.53 – 3.25 (m, 8H,  $\text{CH}_2^{\text{g-k}}$ ), 2.24 – 1.21 (m, aliphatic protons of PS, CA and HW), 1.10 – 0.77 (m, 30H,  $\text{CH}_3^{\text{m-o}}$ ).

$M_n = 18400$  Da.  $D = 1.30$ .

### Synthesis of P23



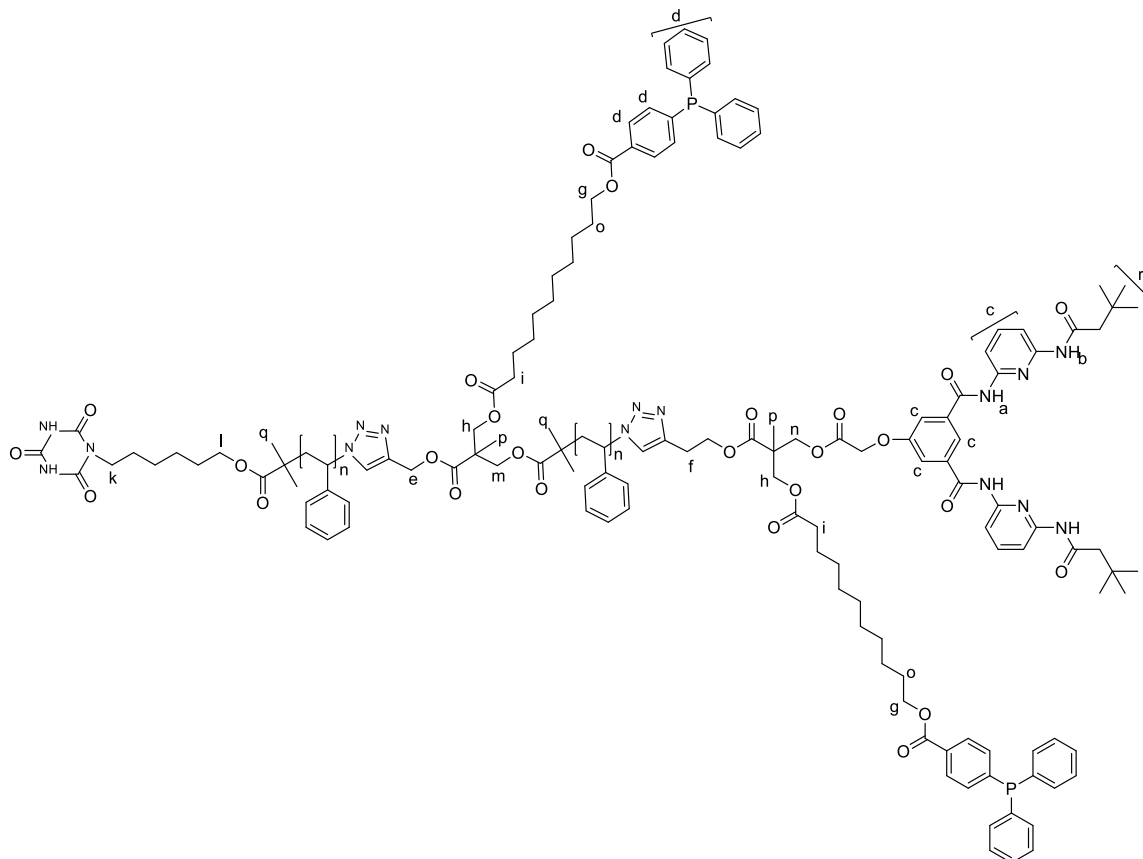
**P22** (335 mg, 0.018 mmol, 1.0 equiv.) was dissolved in DCM (7 mL). 11-bromoundecanoic acid (48.3 mg, 0.18 mmol, 10 equiv.) and DMAP (11.1 mg, 0.091 mmol, 5.0 equiv.) were added. To this solution DCC (56.3 mg, 0.273 mmol, 15.0 equiv.) dissolved in 2 mL DCM and 1 mL DMF was added rapidly and the solution was stirred for 72 h at ambient temperature. Subsequently, the solution was filtered and the solvent removed. The residue was diluted with ethyl acetate and extracted with water and brine. The organic phase was separated, dried over  $\text{Na}_2\text{SO}_4$ , filtered and the solvent removed under reduced pressure. The remainder was dissolved in THF and precipitated into cold MeOH (50 mL). The product was obtained as a white solid.

$^1\text{H}$  NMR (400 MHz,  $\text{CD}_2\text{Cl}_2$ )  $\delta$  / ppm = 9.87 (s, 2H,  $\text{NH}^{\text{a}}$ ), 9.45 (s, 2H,  $\text{NH}^{\text{b}}$ ), 8.23 – 7.66 (m, 9H,  $\text{CH}^{\text{c}}$ ), 7.10 – 6.41 (m, 5H, ArH of PS), 5.14 – 5.04 (m, 4H,  $\text{CH}_2^{\text{d,e}}$ ), 4.03 – 3.99 (m, 4H,  $\text{CH}_2^{\text{f}}$ ), 3.81 – 3.72 (m, 4H,  $\text{CH}_2^{\text{g}}$ ), 3.54 – 3.51 (m, 4H,  $\text{CH}_2^{\text{h}}$ ), 3.44 – 3.38 (m, 8H,  $\text{CH}_2^{\text{j-m}}$ ), 3.22 – 3.18 (m, 4H,  $\text{CH}_2^{\text{n}}$ ), 2.24 – 1.21 (m, aliphatic protons of PS, CA and HW), 1.09 – 0.85 (m, 30H,  $\text{CH}_3^{\text{o-q}}$ ).



$M_n = 17200$  Da.  $\bar{D} = 1.34$ .

### Synthesis of P24



**P23** (27.5 mg, 0.0116 mmol, 1.0 equiv.), 4-(diphenylphosphino)benzoic acid (35.6 mg, 0.116 mmol, 10 equiv.) and  $K_2CO_3$  (16.1 mg, 0.116 mmol, 10 equiv.) were dissolved in dry and degassed DMF (10 mL) and stirred at 50 °C for 24 h. Subsequently, the solution was filtered and diluted with ethyl acetate. The mixture was extracted with water and brine. The organic phase was separated and dried over  $Na_2SO_4$ , filtered and the solvent removed under reduced pressure. The remainder was dissolved in THF and precipitated into cold MeOH (50 mL). The product was obtained as a white solid.

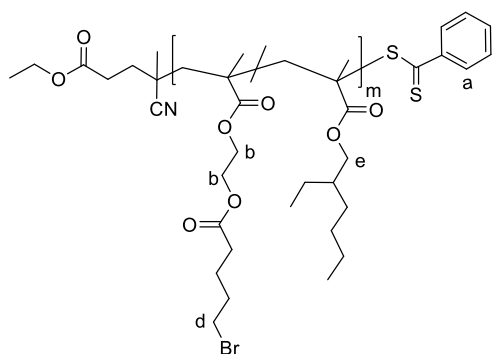
$^1H$  NMR (400 MHz,  $CD_2Cl_2$ )  $\delta$  / ppm = 9.87 (s, 2H,  $NH^a$ ), 9.45 (s, 2H,  $NH^b$ ), 8.23 – 7.48 (m, 9H,  $CH^{c,d}$ ), 7.10 – 6.41 (m, 5H, ArH of PS), 5.14 – 5.04 (m, 4H,  $CH_2^{e,f}$ ), 4.03 – 3.99 (m, 4H,  $CH_2^g$ ), 3.81 – 3.72 (m, 4H,  $CH_2^h$ ), 3.54 – 3.51 (m, 4H,  $CH_2^i$ ), 3.44 – 3.38 (m, 8H,  $CH_2^{k-n}$ ), 3.22 – 3.18 (m, 4H,  $CH_2^o$ ), 2.24 – 1.21 (m, aliphatic protons of PS, CA and HW), 1.09 – 0.85 (m, 30H,  $CH_3^{p-r}$ ).

$M_n = 16900$  Da.  $\bar{D} = 1.30$ .

### Synthesis of the Single-Chain Nanoparticles Induced by Pd(II) Complexation

**P24** (50 mg, 2.8  $\mu\text{mol}$ , 1.0 equiv.) was dissolved in a flame-dried Schlenk flask in 10 mL dry and degassed DCM. The palladium (II) complex ( $[\text{Pd}[\text{COD}]\text{Cl}_2$ ; 0.8 mg, 2.8  $\mu\text{mol}$ , 1.0 equiv.) was dissolved in 50 mL dry and degassed DCM and stirred for 10 min to dissolve the metal complex. Subsequently, the polymer solution was added *via* syringe pump (1 ml  $\text{h}^{-1}$ ) to the metal complex solution. After complete addition the mixture was stirred for another hour. The mixture was concentrated and precipitated into cold MeOH. The product was obtained as a yellow solid.

### Synthesis of Homopolymer Featuring Alkyl Bromide on Side Chains (P25)



2-Ethylhexyl methacrylate (EHMA, 4.04 g, 20.4 mmol, 95.0 equiv.), ethyl 4-cyano-4-((phenylcarbo-thioyl)thio)pentanoate (CTA, 66 mg, 0.214 mmol, 1.0 equiv.), **M1** (0.314 g, 1.08 mmol, 5.0 equiv.) and AIBN (7 mg, 0.04 mmol, 0.2 equiv.), dioxane (5 mL) and a stir bar were added into a Schlenk-tube. After three

freeze-pump-thaw cycles, the tube was backfilled with argon, sealed, placed in an oil bath at 60 °C and removed after 16 h. The tube was cooled with liquid nitrogen to stop the reaction. The mixture was diluted with THF and precipitated three times into 250 mL cold methanol. The polymer was dried overnight under vacuum. The product was obtained as a pink solid.

$^1\text{H}$  NMR (400 MHz,  $\text{CDCl}_3$ )  $\delta$  / ppm = 7.85 – 7.32 (2H,  $\text{CH}^a$ ), 4.26 – 4.13 (2H,  $\text{CH}_2^b$ ), 3.83 (2H,  $\text{CH}_2^c$ ), 3.45 (2H,  $\text{CH}_2^d$ ).

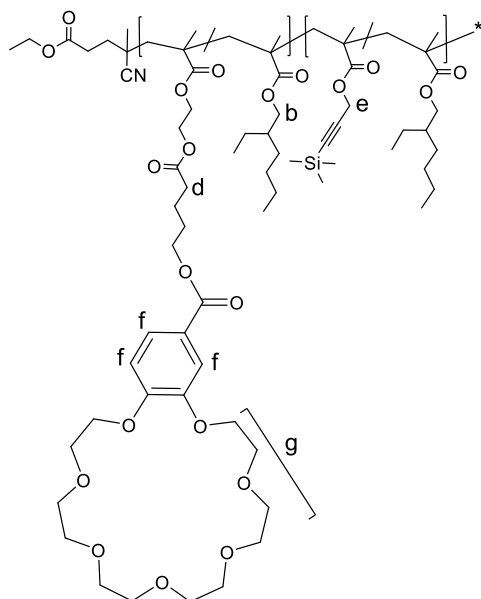
$M_n, \text{SEC} = 16100 \text{ Da}$ ,  $D = 1.05$ .



$^1\text{H NMR}$  (400 MHz,  $\text{CDCl}_3$ )  $\delta$  / ppm = 4.56 (2H,  $\text{CH}_2^{\text{a}}$ ),, 3.84 (4H,  $\text{CH}_2^{\text{b}}$ ), 3.45 (2H,  $\text{CH}_2^{\text{c}}$ ), 0.17 (9H,  $\text{CH}_3^{\text{d}}$ ) ppm.

$M_{\text{n, SEC}} = 26300$  Da,  $\bar{D} = 1.12$ .

### Synthesis of the Copolymer Featuring CE Functionality (P28)



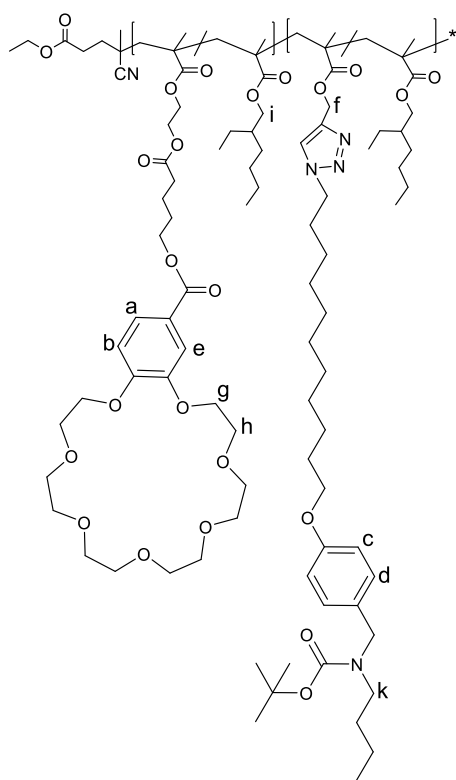
**P27** (0.65 g, 24.7  $\mu\text{mol}$ , 1.0 equiv.) was dissolved in THF (4 mL), **24** (0.30 g, 0.74 mmol, 30.0 equiv.) and DMF (4 mL) were added. Subsequently, potassium carbonate (1.02 g, 7.41 mmol, 300 equiv.) was added and stirred at 60  $^\circ\text{C}$  for 72 h. The solution was diluted with ethyl acetate and washed twice with water. The organic phase was dried over  $\text{Na}_2\text{SO}_4$ , filtered and evaporated under vacuum. The mixture was diluted with THF and precipitated twice into cold methanol (80 mL). The polymer was dried overnight under high

vacuum and obtained as a white solid.

$^1\text{H NMR}$  (400 MHz,  $\text{CDCl}_3$ )  $\delta$  / ppm = 7.64 (1H,  $\text{CH}^{\text{a}}$ ), 7.54 (1H,  $\text{CH}^{\text{b}}$ ), 6.86 (1H,  $\text{CH}^{\text{c}}$ ), 4.56 (2H,  $\text{CH}_2^{\text{d}}$ ), 4.29 (2H,  $\text{CH}_2^{\text{e}}$ ), 4.20 (2H,  $\text{CH}_2^{\text{f}}$ ), 3.81 (4H,  $\text{CH}_2^{\text{g}}$ ), 0.18 (9H,  $\text{CH}_3^{\text{h}}$ ).

$M_{\text{n, SEC}} = 36000$  Da,  $\bar{D} = 1.10$ .

### Synthesis of the Copolymer Featuring CE and AS Functionality (P29)

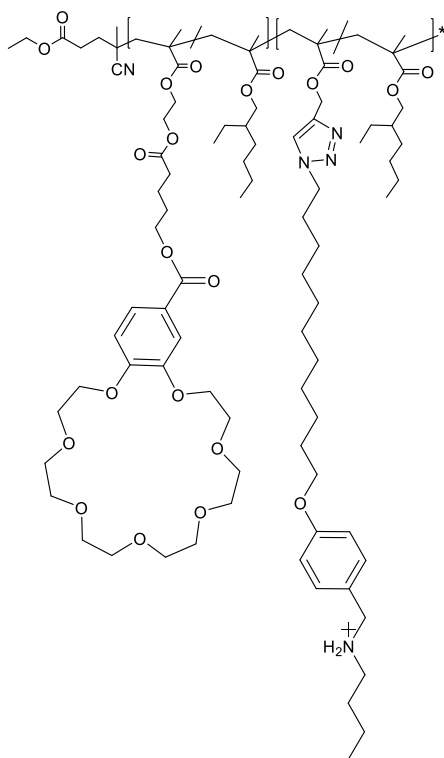


**P28** (450 mg, 11.1  $\mu\text{mol}$ , 1.0 equiv.) was dissolved in THF (4 mL), **30** (60 mg, 0.11 mmol, 10.0 equiv.) and DMF (4 mL) were added. Subsequently,  $\text{CuSO}_4 \times 5\text{H}_2\text{O}$  (90 mg), sodium ascorbate (90 mg) and DIPEA (0.5 mL) were added. The solution was stirred overnight at ambient temperature. THF was removed from the solution under vacuum and subsequently ethyl acetate was added, washed with 5% EDTA solution, dried over  $\text{Na}_2\text{SO}_4$  and the solvent was removed under vacuum. The residue was precipitated once into cold methanol (80 mL). The polymer was obtained as a yellow solid.

$^1\text{H}$  NMR (400 MHz,  $\text{CDCl}_3$ )  $\delta$  /ppm = 7.64 (1H,  $\text{CH}^a$ ), 7.54, (1H,  $\text{CH}^b$ ), 7.13 (2H,  $\text{CH}^c$ ), 6.86 (1H,  $\text{CH}^d$ ), 6.83 (2H,  $\text{CH}^e$ ), 5.11 (2H,  $\text{CH}_2^f$ ), 4.34 (2H,  $\text{CH}_2^g$ ), 4.29 (4H,  $\text{CH}_2^h$ ), 4.20 (4H,  $\text{CH}_2^h$ ), 3.81 (4 H,  $\text{CH}_2^i$ ), 3.10 (2H,  $\text{CH}_2^k$ ).

$M_n, \text{SEC} = 30600 \text{ Da}$ ,  $\bar{D} = 1.11$ .

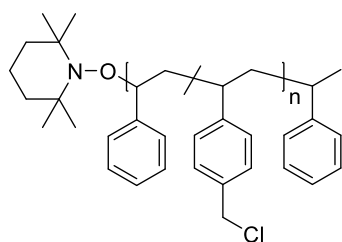
### Procedure for the Deprotection of the AS Moiety (P30)



**P29** (200 mg, 6.54  $\mu\text{mol}$ , 1.0 equiv.) was dissolved in ethyl acetate (5 mL) and cooled with an ice bath. Subsequently, 10% HCl solution (5 mL) was added dropwise and the solution was allowed to reach ambient temperature. The mixture was stirred overnight, diluted with ethyl acetate, washed with brine, dried over  $\text{Na}_2\text{SO}_4$  and the solvent removed under vacuum. The resulting solid was dissolved in THF (5 mL) and saturated ammonium hexafluorophosphate solution was added dropwise until a precipitate developed. The solution was stirred overnight. Subsequently, THF was removed under reduced pressure and the water phase extracted with ethyl acetate. The organic phase was washed three

times with water, dried over  $\text{Na}_2\text{SO}_4$  and the solvent was removed under reduced pressure. The polymer was precipitated into cold methanol (80 mL) and dried under vacuum. The polymer was obtained as a white solid.

### Synthesis of PS-*stat*-CMS P32



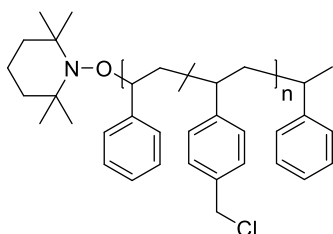
Styrene (2.5 mL, 21.8 mmol, 190 equiv.), 4-(chloromethyl)styrene (0.16 mL, 1.15 mmol, 10.0 equiv.) and 2,2,6,6-tetramethyl-1-(1-phenylethoxy)piperidine (30 mg, 0.218 mmol, 1.0 equiv.) and 2.66 mL of dry toluene were

placed into a flame-dried Schlenk flask and deoxygenated by four consecutive freeze-pump-thaw cycles. Subsequently, the reaction mixture was placed into an oil bath tempered at 125  $^{\circ}\text{C}$ . After 18 h, the polymerization was stopped by cooling the flask with liquid nitrogen and exposing the reaction mixture to the ambient atmosphere. The crude product was diluted with THF (10 mL) and precipitated twice into ice cold methanol (200 mL). The polymer was yielded as a white powder by filtration and dried under high vacuum.

$M_n = 10100 \text{ g mol}^{-1}$ ,  $D = 1.22$ .

$^1\text{H NMR}$  (400 MHz,  $\text{CDCl}_3$ )  $\delta$  / ppm = 7.09 – 6.50 (aromatic protons of PS and initiator), 4.52 (bs, 2H,  $\text{CH}_2\text{Cl}$ ), 2.33 – 0.93 (m, aliphatic protons of PS and initiator).

### Synthesis of PS-*stat*-CMS P33



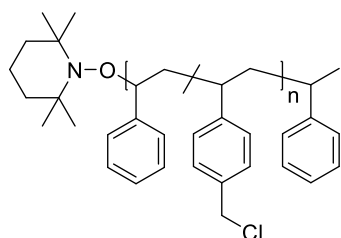
Styrene (2.3 mL, 20.1 mmol, 175 equiv.), 4-(chloromethyl)styrene (0.57 mL, 4.02 mmol, 35.0 equiv.) and 2,2,6,6-tetramethyl-1-(1-phenylethoxy)piperidine (30 mg, 0.218 mmol, 1.0 equiv.) and 2.8 mL dry toluene were placed

into a flame-dried Schlenk flask and deoxygenated by four consecutive freeze-pump-thaw cycles. Subsequently, the reaction mixture was placed into an oil bath tempered at 125 °C. After 20 h, the polymerization was stopped by cooling the flask with liquid nitrogen and exposing the reaction mixture to the ambient atmosphere. The crude product was diluted with THF (10 mL) and precipitated twice into ice cold methanol (200 mL). The polymer was afforded as a white powder by filtration and dried under high vacuum.

$M_n = 10900 \text{ g mol}^{-1}$ ,  $D = 1.31$ .

$^1\text{H NMR}$  (400 MHz,  $\text{CDCl}_3$ )  $\delta$  / ppm = 7.09 – 6.50 (aromatic protons of PS and initiator), 4.52 (bs, 2H,  $\text{CH}_2\text{Cl}$ ), 2.33 – 0.93 (m, aliphatic protons of PS and initiator).

### Synthesis of PS-*stat*-CMS P34



Styrene (2.0 mL, 17.2 mmol, 150 equiv.), 4-(chloromethyl)styrene (0.81 mL, 5.74 mmol, 50.0 equiv.) and 2,2,6,6-tetramethyl-1-(1-phenylethoxy)piperidine (30 mg, 0.218 mmol, 1.0 equiv.) and 2.7 mL dry toluene were placed

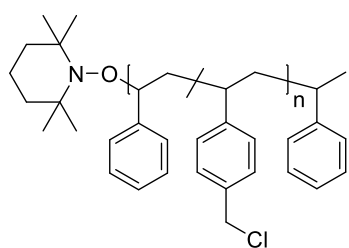
into a flame-dried Schlenk flask and deoxygenated by four consecutive freeze-pump-thaw cycles. Subsequently, the reaction mixture was placed into an oil bath tempered at 125 °C. After 20 h, the polymerization was stopped by cooling the flask with liquid nitrogen and opening it to the atmosphere. The crude product mixture was diluted with THF (10 mL) and precipitated twice into cold methanol

(200 mL). The polymer was afforded as a white powder by filtration and dried under high vacuum.

$M_n = 8600 \text{ g mol}^{-1}$ ,  $D = 1.42$ .

$^1\text{H NMR}$  (400 MHz,  $\text{CDCl}_3$ )  $\delta$  / ppm = 7.09 – 6.50 (aromatic protons of PS and initiator), 4.52 (bs, 2H,  $\text{CH}_2\text{Cl}$ ), 2.33 – 0.93 (m, aliphatic protons of PS and initiator).

### Synthesis of PS-*stat*-CMS P35



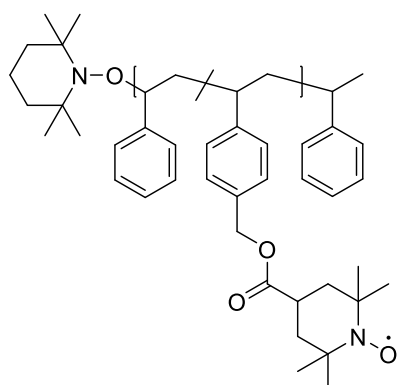
Styrene (11.8 mL, 104 mmol, 750 equiv.), 4-(chloromethyl)styrene (0.58 mL, 4.13 mmol, 30 equiv.) and initiator (36 mg, 0.14 mmol, 1.0 equiv.) was dissolved in 8 mL dry toluene in a flame-dried Schlenk flask and deoxygenated by four consecutive freeze-pump-thaw

cycles. Subsequently, the reaction mixture was placed into an oil bath tempered at 125 °C. After 20 h, the polymerization was stopped by cooling the flask with liquid nitrogen and opening it to the atmosphere. The crude product was diluted with THF (20 mL) and precipitated twice into cold methanol (200 mL). The polymer was afforded as a white powder by filtration and dried under high vacuum.

$M_n = 31600 \text{ g mol}^{-1}$ ,  $D = 1.35$ .

$^1\text{H NMR}$  (400 MHz,  $\text{CDCl}_3$ )  $\delta$  / ppm = 7.09 – 6.50 (aromatic protons of PS and initiator), 4.52 (bs, 2H,  $\text{CH}_2\text{Cl}$ ), 2.33 – 0.93 (m, aliphatic protons of PS and initiator).

### General Procedure for the Synthesis of PS-*stat*-TEMPO P32'-P35'



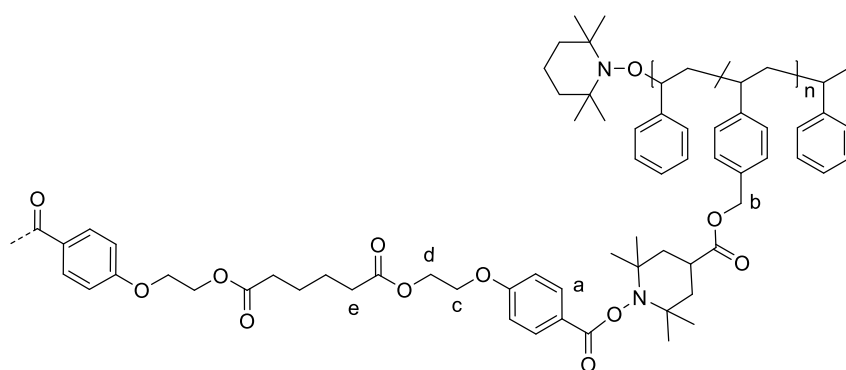
The PS-*stat*-CMS polymer (**P32-P35**, 300 mg),  $\text{K}_2\text{CO}_3$  (5.0 equiv. per CMS) and 4-carboxy-TEMPO (2.0 equiv. per CMS) were dissolved in DMF (10 mL). The mixture was stirred at 50 °C for 72 h. Subsequently, the mixture was diluted with ethyl acetate and extracted three times with brine. The organic phase was dried over  $\text{Na}_2\text{SO}_4$ , filtered and the solvent removed under reduced



pressure. The crude product was diluted with THF (10 mL) and precipitated twice into cold methanol (200 mL).

$^1\text{H}$  NMR (400 MHz,  $\text{CDCl}_3$ , 298 K)  $\delta$  / ppm = 7.12 – 6.63 (aromatic protons of PS and initiator), 5.15 (bs, 2H,  $\text{CH}_2\text{-OCO}$ ), 2.33 – 0.96 (m, aliphatic protons of PS, initiator and carboxy TEMPO).

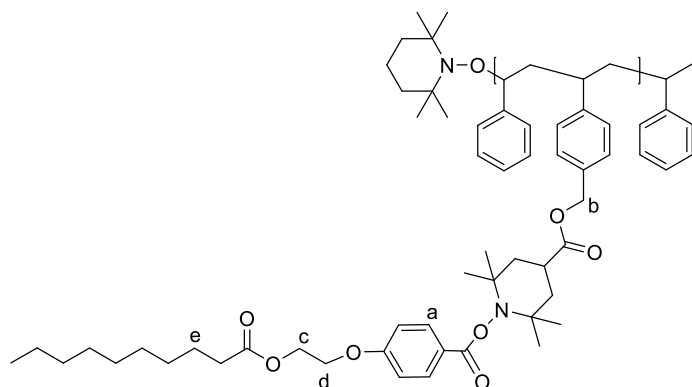
### General Procedure for the Folding of the Linear Precursors



The linear parent precursor polymer (20 mg, 1.0 equiv.) and **33** (0.5 equiv. per TEMPO) were dissolved in a flame dried Schlenk-flask in 500 mL anisole. The

solution was purged for 30 min with argon and subsequently put in a photo reactor equipped with an Arimed B6 lamp ( $\lambda_{\text{max}} = 320$  nm). The mixture was irradiated for 24 h under stirring. The solvent was removed under reduced pressure, the remainder dissolved in THF and precipitated into cold MeOH (20 mL). The polymer was dried under high vacuum and obtained as a yellow-brownish solid.

$^1\text{H}$  NMR (400 MHz, DMSO)  $\delta$  / ppm = 8.03 (m, 2H,  $\text{CH}^{\text{a}}$ ), 7.12 – 6.63 (aromatic protons of PS and initiator), 5.02 (bs, 2H,  $\text{CH}_2^{\text{b}}$ ), 4.44 (m, 2H,  $\text{CH}_2^{\text{c}}$ ), 4.21 (2H,  $\text{CH}_2^{\text{c}}$ ), 2.81 – 2.71 (m, 4H,  $\text{CH}_2^{\text{e}}$ ), 2.33 – 0.96 (m, aliphatic protons of PS, initiator and carboxy TEMPO).

**Photoreaction of P35' with 38 (NP5')**

**P4'** (20 mg, 0.0031 mmol TEMPO, 1.0 equiv. TEMPO) and **38** (2.4 mg 0.0063 mmol, 2.0 equiv.) were dissolved in 500 mL anisole. The solution was purged for 30 min with argon and the flask was put in a photo reactor equipped with an Arimed B6 lamp ( $\lambda_{\max} = 320$  nm).

The mixture was irradiated overnight under stirring. Subsequently, the solvent was removed, the remainder dissolved in THF and precipitated into cold MeOH (20 mL).

$^1\text{H}$  NMR (400 MHz, DMSO)  $\delta$  / ppm = 8.03 (m, 2H,  $\text{CH}^{\text{a}}$ ), 7.12 – 6.63 (aromatic protons of PS and initiator), 5.02 (bs, 2H,  $\text{CH}_2^{\text{b}}$ ), 4.45 (m, 2H,  $\text{CH}_2^{\text{c}}$ ), 4.24 (2H,  $\text{CH}_2^{\text{c}}$ ), 2.81 – 2.71 (m, 4H,  $\text{CH}_2^{\text{e}}$ ), 2.33 – 0.96 (m, aliphatic protons of PS and **2**, initiator and carboxy TEMPO).

**General Procedure for the Unfolding of the SCNPs**

The SCNPs were dissolved in 4 mL dry DCM and heated to 35 °C. *m*CPBA (10.0 equiv. per TEMPO) dissolved in 1 mL DCM was added dropwise. The mixture was stirred at 35 °C for 4 h. The reaction was quenched by adding  $\text{NaHCO}_3$ . Subsequently, the solution was diluted with DCM and extracted three times with sat.  $\text{NaHCO}_3$  solution, dried over  $\text{Na}_2\text{SO}_4$ , filtered and the solvent removed under reduced pressure. The polymer was precipitated in cold MeOH. The polymer was dried under high vacuum to afford a white solid.

$^1\text{H}$  NMR (400 MHz, DMSO)  $\delta$  / ppm = 8.05 (m, 2H,  $\text{CH}^{\text{a}}$ ), 7.12 – 6.63 (aromatic protons of PS and initiator), 5.02 (bs, 2H,  $\text{CH}_2^{\text{b}}$ ), 4.45 (m, 2H,  $\text{CH}_2^{\text{c}}$ ), 4.23 (2H,  $\text{CH}_2^{\text{c}}$ ), 2.33 – 0.96 (m, aliphatic protons of PS, initiator and carboxy TEMPO).

## 6

## BIBLIOGRAPHY

- [1] J. F. V. Vincent, O. A. Bogatyreva, N. R. Bogatyrev, A. Bowyer, A.-K. Pahl, *J. R. Soc. Interface* **2006**, *3*, 471–482.
- [2] M. W. G. de Bolster, *Pure Appl. Chem.* **1997**, *69*, 1251–1303.
- [3] B. Bhushan, *Philos. Trans. R. Soc. A Math. Phys. Eng. Sci.* **2009**, *367*, 1445–1486.
- [4] S. C. Solleder, R. V. Schneider, K. S. Wetzel, A. C. Boukis, M. A. R. Meier, *Macromol. Rapid Commun.* **2017**, *38*, 1600711.
- [5] G. Székely, M. Schaepertoens, P. R. J. Gaffney, A. G. Livingston, *Polym. Chem.* **2014**, *5*, 694–697.
- [6] K. Takizawa, C. Tang, C. J. Hawker, *J. Am. Chem. Soc.* **2008**, *130*, 1718–1726.
- [7] H. Zhang, X. Li, Q. Shi, Y. Li, G. Xia, L. Chen, Z. Yang, Z. X. Jiang, *Angew. Chem. Int. Ed.* **2015**, *54*, 3763–3767.
- [8] N. Zydziak, W. Konrad, F. Feist, S. Afonin, S. Weidner, C. Barner-Kowollik, *Nat. Commun.* **2016**, *7*, 13672.
- [9] C. B. Anfinsen, *Science* **1973**, *181*, 223–230.
- [10] C. M. Dobson, *Nature* **2003**, *426*, 884–890.
- [11] C. Branden, J. Tooze, *Introduction to Protein Structure*, Garland Science, New York, **1999**.
- [12] V. M. Kung, G. Cornilescu, S. H. Gellman, *Angew. Chem. Int. Ed.* **2015**, *54*,

- 14336–14339.
- [13] O. C. Ezezika, S. Haddad, T. J. Clark, E. L. Neidle, C. Momany, *J. Mol. Biol.* **2007**, *367*, 616–629.
- [14] W. A. Braunecker, K. Matyjaszewski, *Prog. Polym. Sci.* **2007**, *32*, 93–146.
- [15] O. Altintas, A. P. Vogt, C. Barner-Kowollik, U. Tunca, *Polym. Chem.* **2012**, *3*, 34–45.
- [16] D. Danilov, C. Barner-Kowollik, W. Wenzel, *Chem. Commun.* **2015**, *51*, 6002–6005.
- [17] M. Szwarc, *Nature* **1956**, *178*, 1168–1169.
- [18] J. Nicolas, Y. Guillaneuf, C. Lefay, D. Bertin, D. Gigmes, B. Charleux, *Prog. Polym. Sci.* **2013**, *38*, 63–235.
- [19] M. K. Georges, R. P. N. Veregin, P. M. Kazmaier, G. K. Hamer, *Macromolecules* **1993**, *26*, 2987–2988.
- [20] V. Sciannamea, R. Jerome, C. Detrembleur, *Chem. Rev.* **2008**, *108*, 1104–1126.
- [21] A. Studer, T. Schulte, *Chem. Rec.* **2005**, *5*, 27–35.
- [22] G. Moad, E. Rizzardo, *Macromolecules* **1995**, *28*, 8722–8728.
- [23] D. Benoit, V. Chaplinski, R. Braslau, C. J. Hawker, *J. Am. Chem. Soc.* **1999**, *121*, 3904–3920.
- [24] M. Kato, M. Kamigaito, M. Sawamoto, T. Higashimura, *Macromolecules* **1995**, *28*, 1721–1723.
- [25] J. S. Wang, K. Matyjaszewski, *J. Am. Chem. Soc.* **1995**, *117*, 5614–5615.
- [26] V. Coessens, T. Pintauer, K. Matyjaszewski, *Prog. Polym. Sci.* **2001**, *26*, 337–377.
- [27] Q. Lou, D. A. Shipp, *ChemPhysChem* **2012**, *13*, 3257–3261.
- [28] P. L. Golas, K. Matyjaszewski, *QSAR Comb. Sci.* **2007**, *26*, 1116–1134.
- [29] Y. A. Kabachii, S. Y. Kochev, L. M. Bronstein, I. B. Blagodatskikh, P. M. Valetsky,

- Polym. Bull.* **2003**, *50*, 271–278.
- [30] J. A. M. Brandts, P. Van De Geijn, E. E. Van Faassen, J. Boersma, G. Van Koten, *J. Organomet. Chem.* **1999**, *584*, 246–253.
- [31] Y. Kotani, M. Kamigaito, M. Sawamoto, *Macromolecules* **1999**, *32*, 2420–2424.
- [32] K. Matyjaszewski, M. Wei, J. Xia, N. E. McDermott, *Macromolecules* **1997**, *30*, 8161–8164.
- [33] W. A. Braunecker, Y. Itami, K. Matyjaszewski, *Macromolecules* **2005**, *38*, 9402–9404.
- [34] V. Percec, B. Barboiu, A. Neumann, J. C. Ronda, M. Zhao, *Macromolecules* **1996**, *29*, 3665–3668.
- [35] B. Wang, Y. Zhuang, X. Luo, S. Xu, X. Zhou, *Macromolecules* **2003**, *36*, 9684–9686.
- [36] C. Granel, P. Dubois, R. Jérôme, P. Teyssié, *Macromolecules* **1996**, *29*, 8576–8582.
- [37] P. Lecomte, I. Drapier, P. Dubois, P. Teyssié, R. Jérôme, *Macromolecules* **1997**, *30*, 7631–7633.
- [38] A. Kaur, T. G. Ribelli, K. Schroder, K. Matyjaszewski, T. Pintauer, *Inorg. Chem.* **2015**, *54*, 1474–1486.
- [39] W. Jakubowski, K. Matyjaszewski, *Angew. Chemie Int. Ed.* **2006**, *45*, 4482–4486.
- [40] W. Jakubowski, K. Min, K. Matyjaszewski, *Macromolecules* **2006**, *39*, 39–45.
- [41] N. Jasinski, A. Lauer, P. J. M. Stals, S. Behrens, S. Essig, A. Walther, A. S. Goldman, C. Barner-Kowollik, *ACS Macro Lett.* **2015**, *4*, 298–301.
- [42] J. Chiefari, Y. K. Chong, F. Ercole, J. Krstina, J. Jeffery, T. P. T. Le, R. T. A. Mayadunne, G. F. Meijs, C. L. Moad, G. Moad, E. Rizzardo, S. Thang, *Macromolecules* **1998**, *31*, 5559–5562.
- [43] S. Perrier, *Macromolecules* **2017**, *50*, 7433–7447.

- [44] G. Moad, E. Rizzardo, S. H. Thang, *Aust. J. Chem.* **2005**, *58*, 379–410.
- [45] C. Barner-Kowollik, *Handbook of RAFT Polymerization*, Wiley-VCH, Weinheim, **2008**.
- [46] G. Moad, E. Rizzardo, S. H. Thang, *Aust. J. Chem.* **2009**, *62*, 1402–1472.
- [47] G. Moad, E. Rizzardo, S. H. Thang, *Polym. Int.* **2008**, *49*, 1079–1131.
- [48] O. Altintas, P. Gerstel, N. Dingenouts, C. Barner-Kowollik, *Chem. Commun.* **2010**, *46*, 6291–6293.
- [49] O. Altintas, T. Rudolph, C. Barner-Kowollik, *J. Polym. Sci. Part A Polym. Chem.* **2011**, *49*, 2566–2576.
- [50] O. Altintas, E. Lejeune, P. Gerstel, C. Barner-Kowollik, *Polym. Chem.* **2012**, *3*, 640–651.
- [51] C. Burd, M. Weck, *Macromolecules* **2005**, *230*, 7225–7230.
- [52] O. Altintas, P. Krolla-Sidenstein, H. Gliemann, C. Barner-Kowollik, *Macromolecules* **2014**, *47*, 5877–5888.
- [53] B. V. K. J. Schmidt, N. Fechner, J. Falkenhagen, J.-F. Lutz, *Nat. Chem.* **2011**, *3*, 234–238.
- [54] J. Willenbacher, O. Altintas, P. W. Roesky, C. Barner-Kowollik, *Macromol. Rapid Commun.* **2014**, *35*, 45–51.
- [55] O. Altintas, C. Barner-Kowollik, *Macromol. Rapid Commun.* **2016**, *37*, 29–46.
- [56] A. Sanchez-Sanchez, A. Arbe, J. Kohlbrecher, J. Colmenero, J. A. Pomposo, *Macromol. Rapid Commun.* **2015**, *36*, 1592–1597.
- [57] E. J. Foster, E. B. Berda, E. W. Meijer, *J. Am. Chem. Soc.* **2009**, *131*, 6964–6966.
- [58] B. J. B. Folmer, R. P. Sijbesma, E. W. Meijer, *J. Am. Chem. Soc.* **2001**, *123*, 2093–2094.
- [59] J. H. K. K. Hirschberg, F. H. Beijer, H. A. van Aert, P. C. M. M. Magusin, R. P. Sijbesma, E. W. Meijer, *Macromolecules* **1999**, *32*, 2696–2705.

- 
- [60] S. H. M. Söntjens, R. P. Sijbesma, M. H. P. Van Genderen, E. W. Meijer, *Macromolecules* **2001**, *34*, 3815–3818.
- [61] H. Ohkawa, G. B. W. L. Ligthart, R. P. Sijbesma, E. W. Meijer, *Macromolecules* **2007**, *40*, 1453–1459.
- [62] J. Hentschel, A. M. Kushner, J. Ziller, Z. Guan, *Angew. Chem. Int. Ed.* **2012**, *51*, 10561–10565.
- [63] C. C. Neikirk, J. W. Chung, R. D. Priestley, *RSC Adv.* **2013**, *3*, 16686.
- [64] S. Mavila, O. Eivgi, I. Berkovich, N. G. Lemcoff, *Chem. Rev.* **2016**, *116*, 878–961.
- [65] E. Harth, B. Van Horn, V. Y. Lee, D. S. Germack, C. P. Gonzales, R. D. Miller, C. J. Hawker, *J. Am. Chem. Soc.* **2002**, *124*, 8653–8660.
- [66] J. Pyun, C. Tang, T. Kowalewski, J. M. J. Fréchet, C. J. Hawker, *Macromolecules* **2005**, *38*, 2674–2685.
- [67] Y. Huang, D. R. Paul, *J. Polym. Sci. Part B Polym. Phys.* **2007**, *45*, 1390–1398.
- [68] J. L. Segura, N. Martín, *Chem. Rev.* **1999**, *99*, 3199–3246.
- [69] M. Meldal, *Macromol. Rapid Commun.* **2008**, *29*, 1016–1051.
- [70] G. Delaittre, N. K. Guimard, C. Barner-Kowollik, *Acc. Chem. Res.* **2015**, *48*, 1296–1307.
- [71] C. J. Hawker, K. L. Wooley, *Science* **2005**, *309*, 1200–1205.
- [72] J. F. Lutz, *Angew. Chem. Int. Ed.* **2007**, *46*, 1018–1025.
- [73] W. H. Binder, R. Sachsenhofer, *Macromol. Rapid Commun.* **2007**, *28*, 15–54.
- [74] H. Nandivada, X. Jiang, J. Lahann, *Adv. Mater.* **2007**, *19*, 2197–2208.
- [75] D. Fournier, R. Hoogenboom, U. S. Schubert, *Chem. Soc. Rev.* **2007**, *36*, 1369–1380.
- [76] A. Ruiz De Luzuriaga, N. Ormategui, H. J. Grande, I. Odriozola, J. A. Pomposo, I. Loinaz, *Macromol. Rapid Commun.* **2008**, *29*, 1156–1160.

- [77] N. Ormategui, I. Garcia, D. Padro, G. Cabanero, H. J. Grande, I. Loinaz, *Soft Matter* **2012**, *8*, 734–740.
- [78] A. R. De Luzuriaga, I. Perez-Baena, S. Montes, I. Loinaz, I. Odriozola, I. García, J. A. Pomposo, *Macromol. Symp.* **2010**, *296*, 303–310.
- [79] A. Sanchez-Sanchez, I. Asenjo-Sanz, L. Buruaga, J. A. Pomposo, *Macromol. Rapid Commun.* **2012**, *33*, 1262–1267.
- [80] C. Glaser, *Chem. Ber.* **1869**, *2*, 422–424.
- [81] A. S. Hay, *J. Org. Chem.* **1962**, *27*, 3320–3321.
- [82] I. Perez-Baena, I. Asenjo-Sanz, A. Arbe, A. J. Moreno, F. Lo Verso, J. Colmenero, J. A. Pomposo, *Macromolecules* **2014**, *47*, 8270–8280.
- [83] N. Wedler-Jasinski, T. Lueckerath, H. Mutlu, A. S. Goldmann, A. Walther, M. H. Stenzel, C. Barner-Kowollik, *Chem. Commun.* **2017**, *53*, 157–160.
- [84] A. M. Hanlon, I. Martin, E. R. Bright, J. Chouinard, K. J. Rodriguez, G. E. Patenotte, E. B. Berda, *Polym. Chem.* **2017**, *8*, 5120–5128.
- [85] O. Altintas, J. Willenbacher, K. N. R. Wuest, K. K. Oehlenschlaeger, P. Krolla-Sidenstein, H. Gliemann, C. Barner-Kowollik, *Macromolecules* **2013**, *46*, 8092–8101.
- [86] C. Heiler, J. T. Offenloch, E. Blasco, C. Barner-Kowollik, *ACS Macro Lett.* **2016**, *6*, 56–61.
- [87] Y. Wang, C. I. Rivera Vera, Q. Lin, *Org. Lett.* **2007**, *9*, 4155–4158.
- [88] M. A. Tasdelen, Y. Yagci, *Angew. Chem. Int. Ed.* **2013**, *52*, 5930–5938.
- [89] E. S. Yim, B. Zhao, D. Myung, L. C. Kourtis, C. W. Frank, D. Carter, R. L. Smith, S. B. Goodman, *J. Biomed. Mater. Res. Part A* **2009**, *91*, 894–902.
- [90] Z. Li, L. Qian, L. Li, J. C. Bernhammer, H. V. Huynh, J. S. Lee, S. Q. Yao, *Angew. Chem. Int. Ed.* **2016**, *55*, 2002–2006.
- [91] J. He, L. Tremblay, S. Lacelle, Y. Zhao, *Soft Matter* **2011**, *7*, 2380.
- [92] W. Fan, X. Tong, Q. Yan, S. Fu, Y. Zhao, *Chem. Commun.* **2014**, *50*, 13492–



- 13494.
- [93] G. Njikang, G. Liu, S. A. Curda, *Macromolecules* **2008**, *41*, 5697–5702.
- [94] F. Zhou, M. Xie, D. Chen, *Macromolecules* **2014**, *47*, 365–372.
- [95] H. D. Becker, *Chem. Rev.* **1993**, *93*, 145–172.
- [96] P. G. Frank, B. T. Tuten, A. Prasher, D. Chao, E. B. Berda, *Macromol. Rapid Commun.* **2014**, *35*, 249–253.
- [97] B. Zhu, G. Qian, Y. Xiao, S. Deng, M. Wang, A. Hu, *J. Polym. Sci. Part A Polym. Chem.* **2011**, *49*, 5330–5338.
- [98] A. Sanchez-Sanchez, S. Akbari, A. Etxeberria, A. Arbe, U. Gasser, A. J. Moreno, J. Colmenero, J. A. Pomposo, *ACS Macro Lett.* **2013**, *2*, 491–495.
- [99] A. Sanchez-Sanchez, S. Akbari, A. J. Moreno, F. Lo Verso, A. Arbe, J. Colmenero, J. A. Pomposo, *Macromol. Rapid Commun.* **2013**, *34*, 1681–1686.
- [100] Y. Bai, H. Xing, G. A. Vincil, J. Lee, E. J. Henderson, Y. Lu, N. G. Lemcoff, S. C. Zimmerman, *Chem. Sci.* **2014**, *5*, 2862–2868.
- [101] K. Watanabe, R. Tanaka, K. Takada, M.-J. Kim, J.-S. Lee, K. Tajima, T. Isono, T. Satoh, *Polym. Chem.* **2016**, *7*, 4782–4792.
- [102] A. M. Hanlon, C. K. Lyon, E. B. Berda, *Macromolecules* **2016**, *49*, 2–14.
- [103] O. Altintas, C. Barner-Kowollik, *Macromol. Rapid Commun.* **2012**, *33*, 958–971.
- [104] J. A. Pomposo, Ed. , *Single-Chain Polymer Nanoparticles*, Wiley-VCH, **2017**.
- [105] T. Terashima, T. Mes, T. F. A. De Greef, M. A. J. Gillissen, P. Besenius, A. R. A. Palmans, E. W. Meijer, *J. Am. Chem. Soc.* **2011**, *133*, 4742–4745.
- [106] T. Mes, R. Van Der Weegen, A. R. A. Palmans, E. W. Meijer, *Angew. Chem. Int. Ed.* **2011**, *50*, 5085–5089.
- [107] E. B. Berda, E. J. Foster, E. W. Meijer, *Macromolecules* **2010**, *43*, 1430–1437.
- [108] O. Altintas, M. Artar, G. Ter Huurne, I. K. Voets, A. R. A. Palmans, C. Barner-Kowollik, E. W. Meijer, *Macromolecules* **2015**, *48*, 8921–8932.

- [109] T. Mes, M. M. J. Smulders, A. R. A. Palmans, E. W. Meijer, *Macromolecules* **2010**, *43*, 1981–1991.
- [110] N. Hosono, M. A. J. Gillissen, Y. Li, S. S. Sheiko, A. R. A. Palmans, E. W. Meijer, *J. Am. Chem. Soc.* **2013**, *135*, 501–510.
- [111] J. A. Berrocal, F. Di Meo, M. Garcia, R. Gosens, E. W. Meijer, M. Linares, A. R. A. Palmans, *Chem. Commun.* **2016**, *52*, 10870–10873.
- [112] M. A. J. Gillissen, T. Terashima, E. W. Meijer, A. R. A. Palmans, I. K. Voets, *Macromolecules* **2013**, *46*, 4120–4125.
- [113] E. Huerta, B. Van Genabeek, P. J. M. Stals, E. W. Meijer, A. R. A. Palmans, *Macromol. Rapid Commun.* **2014**, *35*, 1320–1325.
- [114] P. J. M. Stals, C.-Y. Cheng, L. van Beek, A. C. Wauters, A. R. A. Palmans, S. Han, E. W. Meijer, *Chem. Sci.* **2016**, *7*, 2011–2015.
- [115] M. Artar, T. Terashima, M. Sawamoto, E. W. Meijer, A. R. A. Palmans, *J. Polym. Sci. Part A Polym. Chem.* **2014**, *52*, 12–20.
- [116] E. Huerta, P. J. M. Stals, E. W. Meijer, A. R. A. Palmans, *Angew. Chem. Int. Ed.* **2013**, *52*, 2906–2910.
- [117] P. J. M. Stals, M. A. J. Gillissen, T. F. E. Paffen, T. F. A. De Greef, P. Lindner, E. W. Meijer, A. R. A. Palmans, I. K. Voets, *Macromolecules* **2014**, *47*, 2947–2954.
- [118] N. Hosono, A. M. Kushner, J. Chung, A. R. A. Palmans, Z. Guan, E. W. Meijer, *J. Am. Chem. Soc.* **2015**, *137*, 6880–6888.
- [119] M. Seo, B. J. Beck, J. M. J. Paulusse, C. J. Hawker, S. Y. Kim, *Macromolecules* **2008**, *41*, 6413–6418.
- [120] J. Romulus, M. Weck, *Macromol. Rapid Commun.* **2013**, *34*, 1518–1523.
- [121] F. Wang, H. Pu, X. Che, *Chem. Commun.* **2016**, *52*, 3516–3519.
- [122] E. A. Appel, J. Del Barrio, J. Dyson, L. Isaacs, O. A. Scherman, *Chem. Sci.* **2012**, *3*, 2278–2281.
- [123] J. Szejtli, *Chem. Rev.* **1998**, *98*, 1743–1754.

- 
- [124] J. Willenbacher, B. V. K. J. Schmidt, D. Schulze-Suenninghausen, O. Altintas, B. Luy, G. Delaittre, C. Barner-Kowollik, *Chem. Commun.* **2014**, *50*, 7056–7059.
- [125] J. Lagona, P. Mukhopadhyay, S. Chakrabarti, L. Isaacs, *Angew. Chem. Int. Ed.* **2005**, *44*, 4844–4870.
- [126] J. W. Lee, S. Samal, N. Selvapalam, H. J. Kim, K. Kim, *Acc. Chem. Res.* **2003**, *36*, 621–630.
- [127] D. Whang, Y. M. Jeon, J. Heo, K. Kim, *J. Am. Chem. Soc.* **1996**, *118*, 11333–11334.
- [128] D. Whang, K. Kim, *J. Am. Chem. Soc.* **1997**, *119*, 451–452.
- [129] E. Lee, J. Heo, K. Kim, *Angew. Chem. Int. Ed.* **2000**, *39*, 2699–2701.
- [130] Y. Liu, Z. Huang, X. Tan, Z. Wang, X. Zhang, *Chem. Commun.* **2013**, *49*, 5766.
- [131] L. Wang, Z. Sun, Y. Miaomiao, Y. Shao, L. Fang, X. Liu, *Polym. Chem.* **2016**, *7*, 3669–3673.
- [132] X. Lu, L. Isaacs, *Angew. Chem. Int. Ed.* **2016**, *55*, 8076–8080.
- [133] E. A. Appel, J. Dyson, J. Delbarrio, Z. Walsh, O. A. Scherman, *Angew. Chem. Int. Ed.* **2012**, *51*, 4185–4189.
- [134] D. J. Hill, M. J. Mio, R. B. Prince, T. S. Hughes, J. S. Moore, *Chem. Rev.* **2001**, *101*, 3893–4011.
- [135] S. Basasoro, M. Gonzalez-Burgos, A. J. Moreno, F. Lo Verso, A. Arbe, J. Colmenero, J. A. Pomposo, *Macromol. Rapid Commun.* **2016**, *37*, 1060–1065.
- [136] J. Jeong, Y.-J. Lee, B. Kim, B. Kim, K.-S. Jung, H. Paik, *Polym. Chem.* **2015**, *6*, 3392–3397.
- [137] H. Cao, Z. Cui, P. Gao, Y. Ding, X. Zhu, X. Lu, Y. Cai, *Macromol. Rapid Commun.* **2017**, 1700269.
- [138] A. Arbe, J. A. Pomposo, A. J. Moreno, F. LoVerso, M. González-Burgos, I. Asenjo-Sanz, A. Iturrospe, A. Radulescu, O. Ivanova, J. Colmenero, *Polymer* **2016**, *105*, 532–544.

- [139] Y. Bai, X. Feng, H. Xing, Y. Xu, B. K. Kim, N. Baig, T. Zhou, A. A. Gewirth, Y. Lu, E. Oldfield, S. C. Zimmerman, *J. Am. Chem. Soc.* **2016**, *138*, 11077–11080.
- [140] S. Mavila, C. E. Diesendruck, S. Linde, L. Amir, R. Shikler, N. G. Lemcoff, *Angew. Chem. Int. Ed.* **2013**, *52*, 5767–5770.
- [141] S. Mavila, I. Rozenberg, N. G. Lemcoff, *Chem. Sci.* **2014**, *5*, 4196–4203.
- [142] I. Berkovich, S. Mavila, O. Iliashevsky, S. Kozuch, G. Lemcoff, *Chem. Sci.* **2016**, *7*, 1773–1778.
- [143] J. Willenbacher, O. Altintas, V. Trouillet, N. Knöfel, M. J. Monteiro, P. W. Roesky, C. Barner-Kowollik, *Polym. Chem.* **2015**, *6*, 4358–4365.
- [144] F. Wang, H. Pu, M. Jin, D. Wan, *Macromol. Rapid Commun.* **2016**, *37*, 330–336.
- [145] Y. Azuma, T. Terashima, M. Sawamoto, *ACS Macro Lett.* **2017**, 830–835.
- [146] N. D. Knöfel, H. Rothfuss, J. Willenbacher, C. Barner-Kowollik, P. W. Roesky, *Angew. Chem. Int. Ed.* **2017**, *56*, 4950–4954.
- [147] B. P. Zietz, H. H. Dieter, M. Lakomek, H. Schneider, B. Keßler-Gaedtke, H. Dunkelberg, *Sci. Total Environ.* **2003**, *302*, 127–144.
- [148] Z. Chen, H. Meng, G. Xing, C. Chen, Y. Zhao, G. Jia, T. Wang, H. Yuan, C. Ye, F. Zhao, Z. Chai, C. Zhu, X. Fang, B. Ma. L. Wan, *Toxicol. Lett.* **2006**, *163*, 109–120.
- [149] J. Lu, N. Ten Brummelhuis, M. Weck, *Chem. Commun.* **2014**, *50*, 6225–6227.
- [150] M. A. J. Gillissen, I. K. Voets, E. W. Meijer, A. R. A. Palmans, *Polym. Chem.* **2012**, *3*, 3166–3174.
- [151] J. Wang, B. Djukic, J. Cao, A. Alberola, F. S. Razavi, M. Pilkington, *Inorg. Chem.* **2007**, *46*, 8560–8568.
- [152] C. Kaes, A. Katz, M. W. Hosseini, *Chem. Rev.* **2000**, *100*, 3553–3590.
- [153] H. Irving, D. H. Mellor, *J Chem Soc* **1962**, 5222–5237.
- [154] M. A. El-Sayed, *J. Chem. Phys.* **1963**, *38*, 2834–2838.
- [155] M. Hesse, H. Meier, B. Zeeh, *Spektroskopische Methoden in Der Organischen*

- 
- Chemie*, Georg Thieme Verlag KG, Stuttgart, **2005**.
- [156] B. Valeur, M. N. Berberan-Santos, *J. Chem. Educ.* **2011**, *88*, 731–738.
- [157] D. M. Jameson, J. C. Croney, P. D. J. Moens, *Methods Enzymol.* **2003**, *360*, 1–43.
- [158] C. T. Adkins, J. N. Dobish, S. Brown, E. Harth, *ACS Macro Lett.* **2013**, *2*, 710–714.
- [159] C. Song, L. Li, L. Dai, S. Thayumanavan, *Polym. Chem.* **2015**, *6*, 4828–4834.
- [160] Y. Liu, T. Pauloehrl, S. I. Presolski, L. Albertazzi, A. R. A. Palmans, E. W. Meijer, *J. Am. Chem. Soc.* **2015**, *137*, 13096–13106.
- [161] T. Terashima, T. Sugita, K. Fukae, M. Sawamoto, *Macromolecules* **2014**, *47*, 589–600.
- [162] Y. Koda, T. Terashima, M. Sawamoto, *Macromolecules* **2016**, *49*, 4534–4543.
- [163] T. Terashima, T. Sugita, M. Sawamoto, *Polym. J.* **2015**, *47*, 667–677.
- [164] K. Matsumoto, T. Terashima, T. Sugita, M. Takenaka, M. Sawamoto, *Macromolecules* **2016**, *49*, 7917–7927.
- [165] G. M. ter Huurne, L. N. J. de Windt, Y. Liu, E. W. Meijer, I. K. Voets, A. R. A. Palmans, *Macromolecules* **2017**, *50*, 8562–8569.
- [166] T. Sun, R. R. Chance, W. W. Graessley, D. J. Lohse, *Macromolecules* **2004**, *37*, 4304–4312.
- [167] J. C. Moore, *J. Polym. Sci. Part A Gen. Pap.* **1964**, *2*, 835–843.
- [168] J. M. G. Cowie, *Chemie Und Physik Der Synthetischen Polymeren*, Vieweg, **1997**.
- [169] M. D. Lechner, K. Gehrke, E. H. Nordmeier, *Makromolekulare Chemie*, Birkhäuser Verlag, Basel, **2010**.
- [170] S. Mori, G. B. Howard, *Size Exclusion Chromatography*, Springer, Berlin, Heidelberg, **1999**.
- [171] J. A. Pomposo, I. Perez-Baena, L. Buruaga, A. Alegría, A. J. Moreno, J.
-

- Colmenero, *Macromolecules* **2011**, *44*, 8644–8649.
- [172] L. J. Fetters, N. Hadjichristidis, J. S. Linder, J. W. Mays, *J. Phys. Chem. Ref. Data* **1994**, *23*, 619–640.
- [173] J. A. Pomposo, J. Rubio-Cervilla, A. J. Moreno, F. Lo Verso, P. Bacova, A. Arbe, J. Colmenero, *Macromolecules* **2017**, *50*, 1732–1739.
- [174] J. E. Tanner, *J. Chem. Phys.* **1970**, *52*, 2523–2526.
- [175] K. F. Morris, C. S. Johnson, *J. Am. Chem. Soc.* **1992**, *114*, 3139–3141.
- [176] P. Groves, *Polym. Chem.* **2017**, *8*, 6700–6708.
- [177] N. Ormategui, I. García, D. Padro, G. Cabañero, H. J. Grande, I. Loinaz, *Soft Matter* **2012**, *8*, 734–740.
- [178] L. Abbassi, Y. M. Chabre, N. Kottari, A. A. Arnold, S. André, J. Josserand, H.-J. Gabius, R. Roy, *Polym. Chem.* **2015**, *6*, 7666–7683.
- [179] E. Blasco, B. T. Tuten, H. Frisch, A. Lederer, C. Barner-Kowollik, *Polym. Chem.* **2017**, *8*, 5845–5851.
- [180] Y. Cohen, L. Avram, L. Frish, *Angew. Chem. Int. Ed.* **2005**, *44*, 520–554.
- [181] E. O. Stejskal, J. E. Tanner, *J. Chem. Phys.* **1965**, *42*, 288–292.
- [182] W. S. Price, *Concepts Magn. Reson.* **1998**, *9*, 299–336.
- [183] W. S. Price, *Concepts Magn. Reson.* **1998**, *10*, 197–237.
- [184] C. S. Johnson, *Prog. Nucl. Magn. Reson. Spectrosc.* **1999**, *34*, 203–256.
- [185] E. L. Hahn, *Phys. Rev.* **1950**, *80*, 580–594.
- [186] D. H. Wu, A. D. Chen, C. S. Johnson, *J. Magn. Reson. Ser. A* **1995**, *115*, 260–264.
- [187] G. Wider, V. Dötsch, K. Würthrich, *J. Magn. Reson. Ser. A* **1994**, *108*, 255–258.
- [188] M. Drescher, *Chemie Unserer Zeit* **2012**, *46*, 150–157.
- [189] P. W. Atkins, J. de Paula, *Physikalische Chemie*, Wiley-VCH, **2013**.

- 
- [190] C. H. Hamann, W. Vielstich, *Elektrochemie*, Wiley-VCH, **2005**.
- [191] M. M. Roessler, E. Salvadori, *Chem. Soc. Rev.* **2018**, *47*, 2534–2553.
- [192] P. Stepan, *Light Scattering, Size Exclusion Chromatography and Asymmetric Flow Field Flow Fractionation*, John Wiley & Sons, Inc., New Jersey, **2011**.
- [193] R. Borsali, R. Pecora, Eds. , *Soft-Matter Characterization*, Springer, **2008**.
- [194] W. Schärtl, *Light Scattering from Polymer Solutions and Nanoparticle Dispersions*, Springer Laboratory, Berlin, Heidelberg, **2007**.
- [195] B. J. Berne, R. Pecora, *Dynamic Light Scattering: With Applications to Chemistry, Biology and Physics*, Dover Publications, Mineola, NY, **2000**.
- [196] J. B. Fenn, M. Mann, C. K. A. I. Meng, S. F. Wong, C. M. Whitehouse, *Electrospray Ionization for Mass Spectrometry of Large Biomolecules*, **1989**.
- [197] K. Tanaka, H. Waki, Y. Ido, S. Akita, Y. Yoshida, T. Yoshida, T. Matsuo, *Protein and Polymer Analyses up to  $m/z$  100 000 by Laser Ionization Time-of-Flight Mass Spectrometry*, **1988**.
- [198] N. Bradshaw, E. F. H. Hall, N. E. Sanderson, *J. Anal. At. Spectrom.* **1989**, *4*, 801–803.
- [199] S. Weyer, J. B. Schwieters, *Int. J. Mass Spectrom.* **2003**, *226*, 355–368.
- [200] S. D. Hanton, *Chem. Rev.* **2001**, *101*, 527–569.
- [201] P. M. Peacock, C. N. Mcewen, *Anal. Chem.* **2008**, *80*, 4349–4361.
- [202] R. Zenobi, R. Knochenmuss, *Mass Spectrom. Rev.* **1998**, *17*, 337–366.
- [203] T. M. Lovestead, G. Hart-Smith, T. P. Davis, M. H. Stenzel, C. Barner-Kowollik, *Macromolecules* **2007**, *40*, 4142–4153.
- [204] T. Gruending, G. Hart-Smith, T. P. Davis, M. H. Stenzel, C. Barner-Kowollik, *Macromolecules* **2008**, *41*, 1966–1971.
- [205] T. Gruending, S. Weidner, J. Falkenhagen, C. Barner-Kowollik, *Polym. Chem.* **2010**, *1*, 599–617.
- [206] K. L. Busch, *J. Mass Spectrom.* **1995**, *30*, 233–240.
-

- [207] H. Deutsch, K. Becker, S. Matt, T. D. Märk, *Int. J. Mass Spectrom.* **2000**, *197*, 37–69.
- [208] J. H. Gross, *Mass Spectrometry*, Springer, Heidelberg, **2017**.
- [209] M. Dole, L. L. Mack, R. L. Hines, R. C. Mobley, L. D. Ferguson, M. B. Alice, *J. Chem. Phys.* **1968**, *49*, 2240–2249.
- [210] M. Dole, L. L. Mack, R. L. Hines, R. C. Mobley, L. D. Ferguson, M. B. Alice, *J. Chem. Phys.* **1970**, *52*, 2240–2249.
- [211] M. Yamashita, J. B. Fenn, *J. Phys. Chem.* **1984**, *88*, 4451–4459.
- [212] S. J. Gaskell, *J. Mass Spectrom.* **1997**, *32*, 677–688.
- [213] S. H. Lomeli, S. Yin, R. R. Ogorzalek Loo, J. A. Loo, *J. Am. Soc. Mass Spectrom.* **2009**, *20*, 593–596.
- [214] P. Kebarle, L. Tang, *Anal. Chem.* **1993**, *65*, 972A–986A.
- [215] C. M. Whitehouse, R. N. Dreyer, M. Yamashita, J. B. Fenn, *Anal. Chem.* **1985**, *57*, 675–679.
- [216] J. Steinkoenig, H. Rothfuss, A. Lauer, B. T. Tuten, C. Barner-kowollik, *J. Am. Chem. Soc.* **2017**, *139*, 51–54.
- [217] E. Meyer, *Prog. Surf. Sci.* **1992**, *41*, 3–49.
- [218] G. Binnig, C. F. Quate, *Phys. Rev. Lett.* **1986**, *56*, 930–933.
- [219] F. J. Giessibl, *Rev. Mod. Phys.* **2003**, *75*, 949–983.
- [220] B. Cappella, G. Dietler, *Surf. Sci. Rep.* **1999**, *34*, 1–104.
- [221] M. Tortonese, R. C. Barrett, C. F. Quate, *Appl. Phys. Lett* **1993**, *62*, 834–836.
- [222] L. Howald, R. Lüthi, E. Meyer, P. Güthner, H.-J. Güntherodt, R. L. E. Meyer, H. Giintherodt, *Zeitschrift für Phys. B Condens. Matter* **1994**, *93*, 267–268.
- [223] J. Zhang, J. Tanaka, P. Gurnani, P. Wilson, M. Hartlieb, S. Perrier, *Polym. Chem.* **2017**, *8*, 4079–4087.
- [224] J. Jiang, S. Thayumanavan, *Macromolecules* **2005**, *38*, 5886–5891.



- 
- [225] A. E. Cherian, F. C. Sun, S. S. Sheiko, G. W. Coates, *J. Am. Chem. Soc.* **2007**, *129*, 11350–11351.
- [226] C. Li, Z. Ge, J. Fang, L. Shiyong, *Macromolecules* **2009**, *42*, 2916–2924.
- [227] J. Willenbacher, K. N. R. Wuest, J. O. Mueller, M. Kaupp, H.-A. Wagenknecht, C. Barner-Kowollik, *ACS Macro Lett.* **2014**, *3*, 574–579.
- [228] H. W. H. van Roekel, P. J. M. Stals, M. A. J. Gillissen, P. A. J. Hilbers, A. J. Markvoort, T. F. A. de Greef, *Chem. Commun.* **2013**, *49*, 3122.
- [229] E. Rabani, D. R. Reichman, P. L. Geissler, L. E. Brus, *Nature* **2003**, *426*, 271–274.
- [230] P. Chem, B. T. Tuten, D. Chao, K. Lyon, E. B. Berda, *Polym. Chem.* **2012**, *3*, 3068–3071.
- [231] P. Wang, H. Pu, M. Jin, *J. Polym. Sci. Part A Polym. Chem.* **2011**, *49*, 5133–5141.
- [232] X. Jiang, H. Pu, P. Wang, *Polymer* **2011**, *52*, 3597–3602.
- [233] P. A. Limacher, W. Klopper, *ChemPhysChem* **2017**, *18*, 3352–3359.
- [234] B. Neises, W. Steglich, *Angew. Chem. Int. Ed.* **1978**, *17*, 522–524.
- [235] J. Winsberg, S. Muench, T. Hagemann, S. Morgenstern, T. Janoschka, M. Billing, F. H. Schacher, G. Hauffman, J.-F. Gohy, S. Hoepfener, M. D. Hager, U. S. Schubert, *Polym. Chem.* **2016**, *7*, 1711–1718.
- [236] E. M. Simpson, Z. D. Ristovski, S. E. Bottle, K. E. Fairfull-Smith, J. P. Blinco, *Polym. Chem.* **2015**, *6*, 2962–2969.
- [237] J. Steinkoenig, M. M. Cecchini, S. Reale, A. S. Goldmann, C. Barner-Kowollik, *Macromolecules* **2017**, *50*, 8033–8041.
- [238] T. S. Fischer, J. Steinkoenig, H. Woehlke, J. P. Blinco, K. Fairfull-Smith, C. Barner-Kowollik, *Polym. Chem.* **2017**, *8*, 5269–5274.
- [239] M. Shibuya, M. Tomizawa, Y. Iwabuchi, K. C. Commun, *J. Org. Chem.* **2008**, *73*, 4750–4752.

- [240] M. A. Mercadante, C. B. Kelly, J. M. Bobbitt, L. J. Tilley, N. E. Leadbeater, *Nat. Protoc.* **2013**, *8*, 666–676.
- [241] X. Wei, W. Xu, M. Vijayakumar, L. Cosimbescu, T. Liu, V. Sprenkle, W. Wang, *Adv. Mater.* **2014**, *26*, 7649–7653.
- [242] C. Detrembleur, C. Jérôme, J. De Winter, P. Gerbaux, J. L. Clément, Y. Guillaeneuf, D. Gigmes, *Polym. Chem.* **2014**, *5*, 335–340.
- [243] J. Willenbacher, K. N. R. Wuest, J. O. Mueller, M. Kaupp, H. A. Wagenknecht, C. Barner-Kowollik, *ACS Macro Lett.* **2014**, *3*, 574–579.
- [244] M. Suguro, S. Iwasa, Y. Kusachi, Y. Morioka, K. Nakahara, *Macromol. Rapid Commun.* **2007**, *28*, 1929–1933.
- [245] G. D. Mendenhall, K. U. Ingold, *J. Am. Chem. Soc.* **1973**, *95*, 6390–6394.
- [246] P. Cimino, M. Pavone, V. Barone, *Chem. Phys. Lett.* **2006**, *419*, 106–110.
- [247] P. Dimitrov-Raytchev, S. Beghdadi, A. Serghei, E. Drockenmuller, *J. Polym. Sci. Part A Polym. Chem.* **2013**, *51*, 34–38.
- [248] O. Altintas, T. Josse, M. Abbasi, J. De Winter, V. Trouillet, P. Gerbaux, M. Wilhelm, C. Barner-Kowollik, *Polym. Chem.* **2015**, *6*, 2854–2868.
- [249] M. M. Obadia, B. P. Mudraboyina, A. Serghei, T. N. T. Phan, D. Gigmes, E. Drockenmuller, *ACS Macro Lett.* **2014**, *3*, 658–662.
- [250] T. K. Claus, J. Zhang, L. Martin, M. Hartlieb, H. Mutlu, S. Perrier, G. Delaittre, C. Barner-Kowollik, *Macromol. Rapid Commun.* **2017**, *38*, 1700264.
- [251] T. S. Fischer, *Orthogonally Triggered Unfolding of Single-Chain Polymeric Nanoparticles*, **2015**.
- [252] T. S. Fischer, D. Schulze-Sünninghausen, B. Luy, O. Altintas, C. Barner-Kowollik, *Angew. Chem. Int. Ed.* **2016**, *55*, 11276–11280.
- [253] M. Chen, G. Moad, E. Rizzardo, *J. Polym. Sci. Part A Polym. Chem.* **2009**, *47*, 6704–6714.
- [254] L. Chen, Y. K. Tian, Y. Ding, Y. J. Tian, F. Wang, *Macromolecules* **2012**, *45*, 8412–8419.

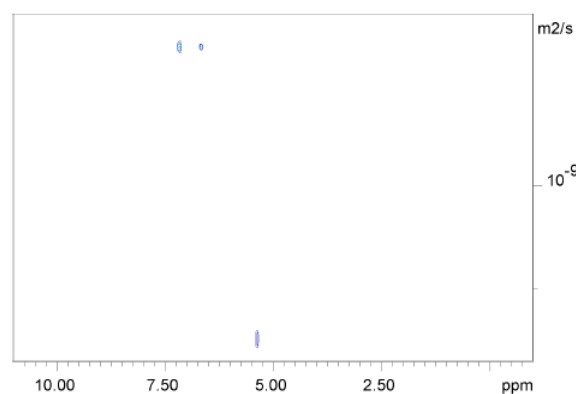
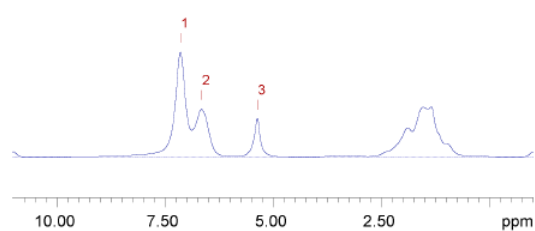
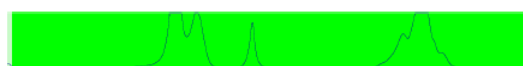
- [255] S. Dong, Y. Luo, X. Yan, B. Zheng, X. Ding, Y. Yu, Z. Ma, Q. Zhao, F. Huang, *Angew. Chem. Int. Ed.* **2011**, *50*, 1905–1909.
- [256] T. S. Fischer, S. Spann, Q. An, B. Luy, M. Tsotsalas, J. P. Blinco, H. Mutlu, C. Barner-Kowollik, *Chem. Sci.* **2018**, *9*, 4696–4702.
- [257] S. Hurre, A. Lauer, H. Gliemann, H. Mutlu, C. Woell, A. S. Goldmann, C. Barner-Kowollik, *Macromol. Rapid Commun.* **2017**, *38*, 1600598.
- [258] F. Mäsing, A. Mardyukov, C. Doerenkamp, H. Eckert, U. Malkus, H. Nüsse, J. Klingauf, A. Studer, *Angew. Chem. Int. Ed.* **2015**, *54*, 12612–12617.
- [259] A. Mardyukov, A. Studer, *Macromol. Rapid Commun.* **2013**, *34*, 94–101.
- [260] S. Jockusch, M. S. Landis, B. Freiermuth, N. J. Turro, *Macromolecules* **2001**, *34*, 1619–1626.
- [261] G. Delaittre, M. Dietrich, J. P. Blinco, A. Hirschbiel, M. Bruns, L. Barner, C. Barner-Kowollik, *Biomacromolecules* **2012**, *13*, 1700–1705.
- [262] B. A. Chalmers, J. C. Morris, K. E. Fairfull-Smith, R. S. Grainger, S. E. Bottle, *Chem. Commun.* **2013**, *49*, 10382–10384.
- [263] H. Mutlu, C. W. Schmitt, N. Jasinski, H. Woehlk, K. Fairfull-Smith, J. P. Blinco, C. Barner-Kowollik, *Polym. Chem.* **2017**, *8*, 6199–6203.
- [264] A. M. Hanlon, I. Martin, E. R. Bright, J. Chouinard, K. J. Rodriguez, G. E. Patenotte, E. B. Berda, *Polym. Chem.* **2017**, *8*, 5120–5128.
- [265] J. De-La-Cuesta, E. Gonzalez, J. A. Pomposo, *Molecules* **2017**, *22*, 1819.
- [266] A. Kuo, *CheM* **2011**, *1*, 40–51.
- [267] A. Kuo, *CheM* **2011**, *1*, 80–86.
- [268] K.-A. Hansen, K. E. Fairfull-Smith, S. E. Bottle, J. P. Blinco, *Macromol. Chem. Phys.* **2016**, *217*, 2330–2340.
- [269] W. Snipes, J. Cupp, G. Cohn, A. Keith, *Biophys. J.* **1974**, *14*, 20–32.
- [270] A. B. Eldrup, C. Christensen, G. Haaima, P. E. Nielsen, *J. Am. Chem. Soc.* **2002**, *124*, 3254–3262.

- [271] F. Osswald, E. Vogel, O. Safarowsky, F. Schwanke, F. Vogtle, *Adv. Synth. Catal.* **2001**, *343*, 303–309.
- [272] O. Altintas, T. Muller, E. Lejeune, O. Plietzsch, S. Bräse, C. Barner-Kowollik, *Macromol. Rapid Commun.* **2012**, *33*, 977–983.
- [273] H. Ihre, A. Hult, J. M. J. Fréchet, I. Gitsov, *Macromolecules* **1998**, *31*, 4061–4068.
- [274] A. Barnard, P. Posocco, S. Pricl, M. Calderon, R. Haag, M. E. Hwang, V. W. T. Shum, D. W. Pack, D. K. Smith, *J. Am. Chem. Soc.* **2011**, *133*, 20288–20300.
- [275] W. Xue, J. Wang, M. Wen, G. Chen, W. Zhang, *Macromol. Rapid Commun.* **2017**, *38*, 1600733.
- [276] L. Li, M. Yan, G. Zhang, C. Wu, *Macromolecules* **2013**, *46*, 8152–8160.
- [277] R. K. Pandey, G. G. Jarvis, P. S. Low, *Tetrahedron Lett.* **2012**, *53*, 1627–1629.
- [278] Y. Chen, G. L. Baker, *J. Org. Chem.* **1999**, *64*, 6870–6873.
- [279] Z. Yang, Y. Shi, W. Chen, F. Wang, *Polym. Chem.* **2015**, *6*, 5540–5544.
- [280] D. A. Leigh, A. R. Thomson, *Tetrahedron* **2008**, *64*, 8411–8416.
- [281] B. Zheng, M. Zhang, S. Dong, J. Liu, F. Huang, *Org. Lett.* **2012**, *14*, 1913–1916.

## 7

## APPENDIX

## A. Supporting Information for Chapter 3.1.1



|  |   |
|--|---|
| Fitted function:                       | $f(x) = I_0 \cdot \exp(-D \cdot x^2 \cdot \gamma^2 \cdot \Delta^2 / (3 \cdot \Delta^3) \cdot 10^4)$ |
| used gamma:                            | 26752 rad/(e*Gauss)   |
| used little delta:                     | 0.0030000 s   |
| used big delta:                        | 0.059900 s  |
| used gradient strength:                | variable  |
| Random error estimation of data:       | RMS per spectrum (or trace/plane)   |
| Systematic error estimation of data:   | worst case per peak scenario  |
| Fit parameter Error estimation method: | from fit using arbitray v uncertainties   |
| Confidence level:                      | 95%   |
| Used peaks:                            |   |
| Used integrals:                        | peak intensities  |
| Used Gradient strength:                | all values (including replicates) used  |

| Peak name | F2 [ppm] | D [m2/s] | error     |
|-----------|----------|----------|-----------|
| 1         | 7.147    | 3.92e-10 | 1.164e-11 |
| 2         | 6.650    | 3.90e-10 | 9.095e-12 |
| 3         | 5.367    | 2.81e-09 | 2.400e-10 |

**Figure 73.** Original Data of DOSY measurements of the folded polymer **P10**, recorded in DCM- $d_2$  at 298 K.

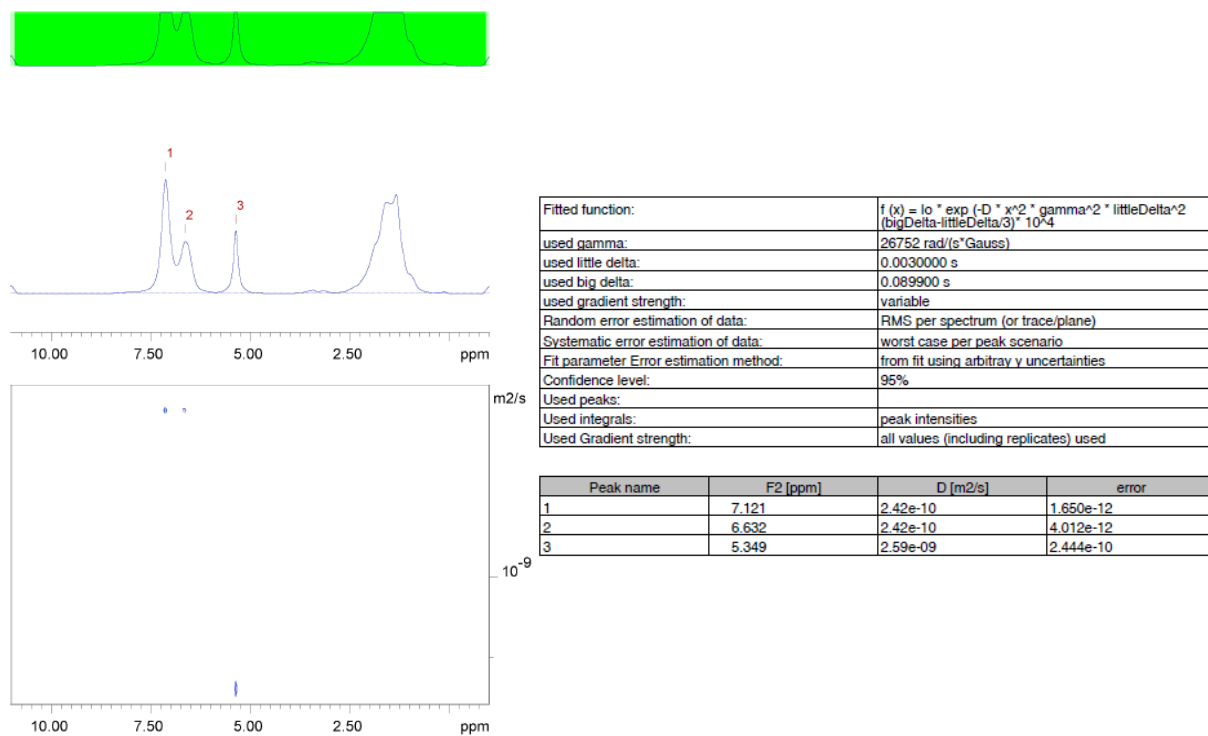


**Figure 74.** Original Data of DOSY measurements of the unfolded polymer **P10** after the addition of MeOH, recorded in DCM-*d*<sub>2</sub> at 298 K.

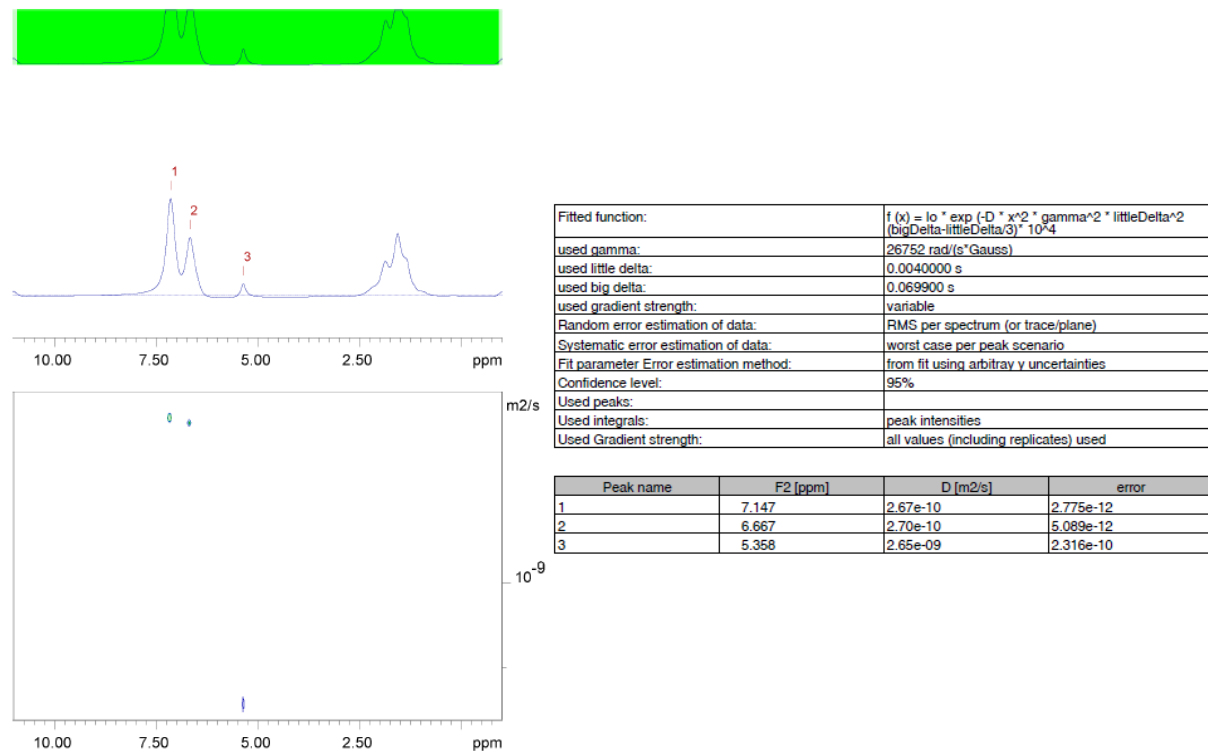


**Figure 75.** Original Data of DOSY measurements of the folded polymer **P11**, recorded in DCM-*d*<sub>2</sub> at 298 K.

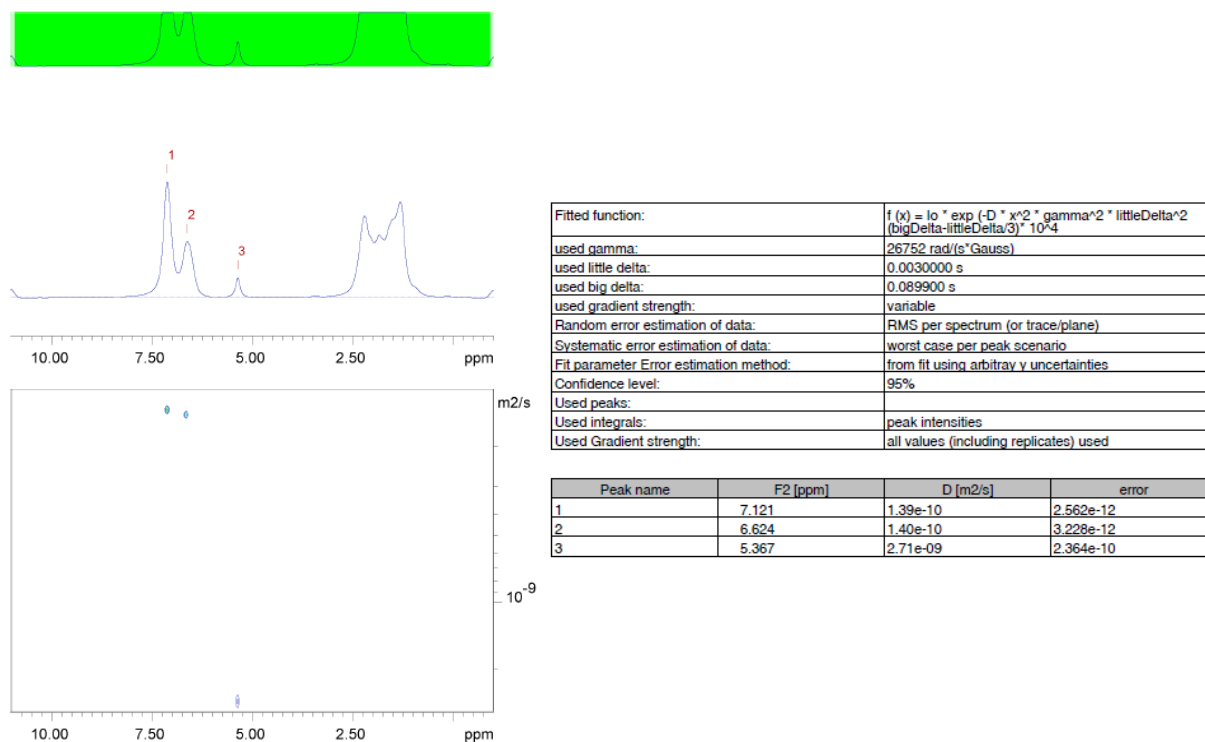


**Figure 76.** Original Data of DOSY measurements of the unfolded polymer **P11** after the addition of MeOH, recorded in DCM- $d_2$  at 298 K.

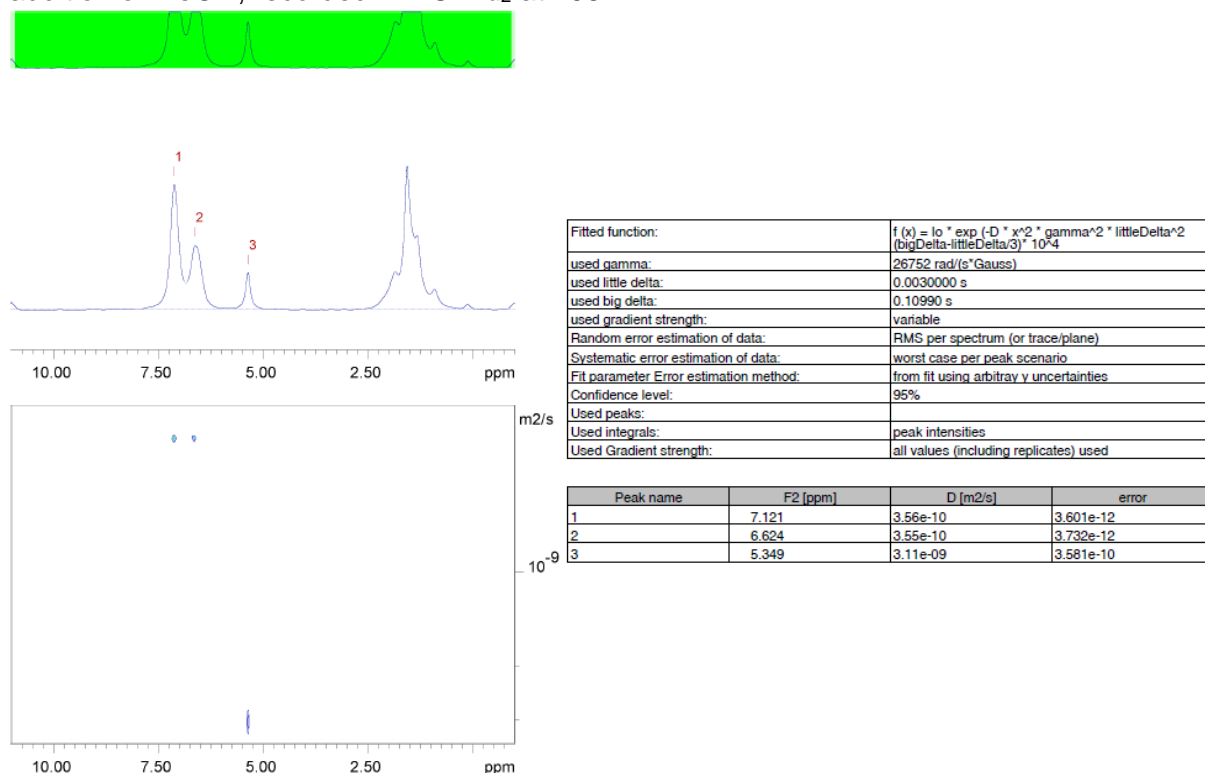


**Figure 77.** Original Data of DOSY measurements of the folded polymer **P12**, recorded in DCM- $d_2$  at 298 K.

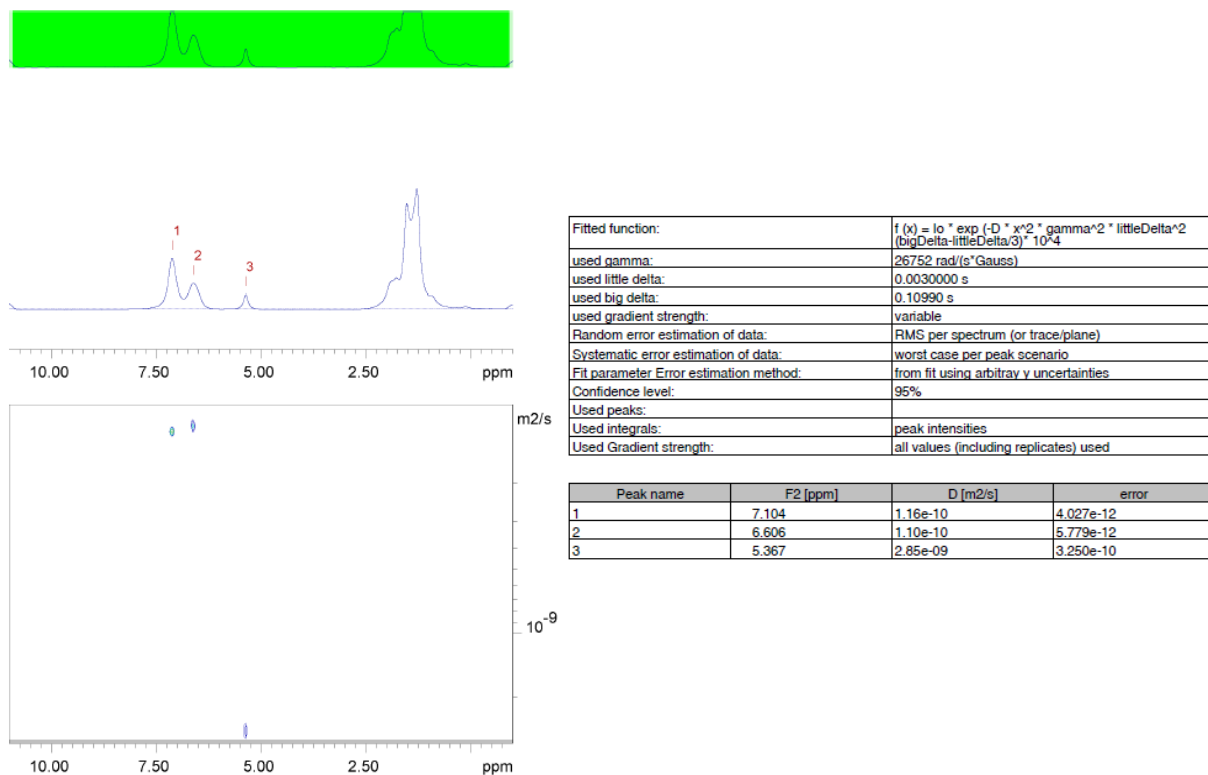


**Figure 78.** Original Data of DOSY measurements of the unfolded polymer **P12** after the addition of MeOH, recorded in DCM- $d_2$  at 298 K.

## B. Supporting Information for Chapter 3.1.2

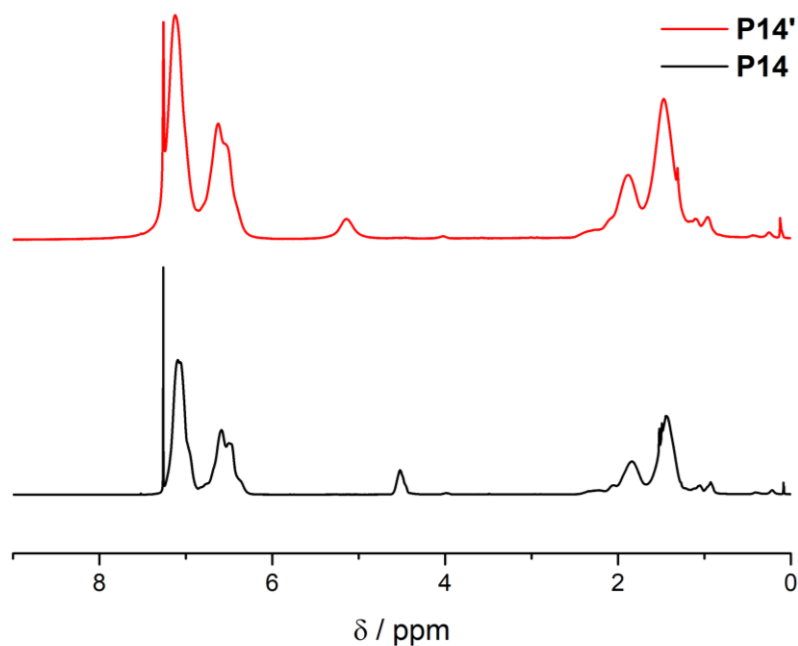


**Figure 79.**  $^1\text{H}$  NMR spectra of **P14** and **P14'** ( $\text{CDCl}_3$ , 298 K).



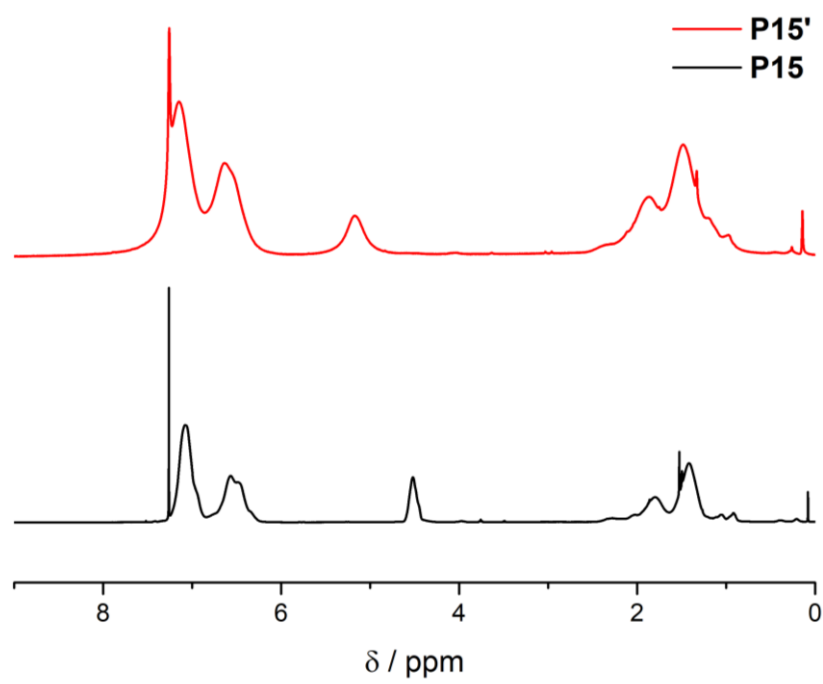


**Figure 80.** <sup>1</sup>H NMR spectra of **P15** and **P15'** (CDCl<sub>3</sub>, 298 K).

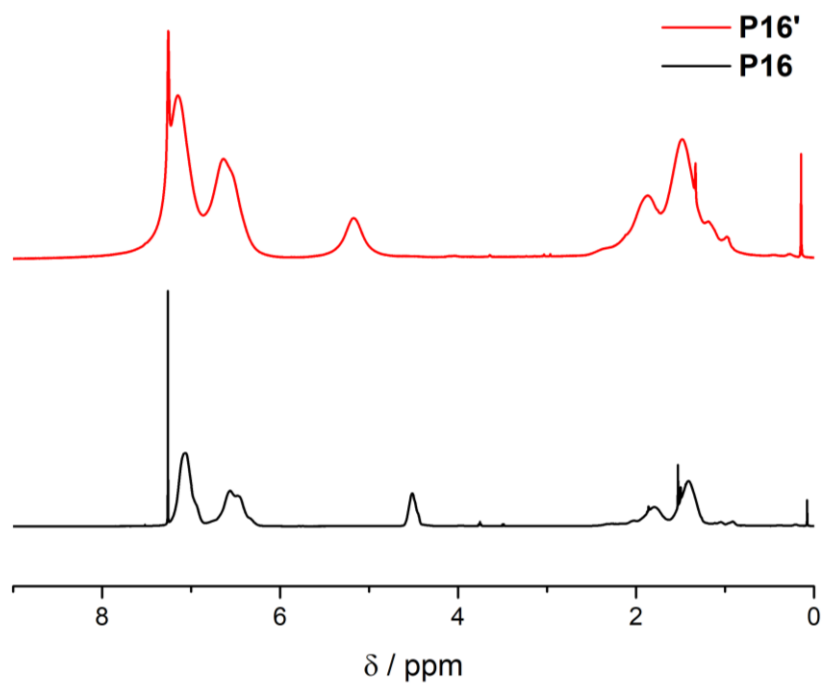


**Figure 81.** <sup>1</sup>H NMR spectra of **P16** and **P16'** (CDCl<sub>3</sub>, 298 K).

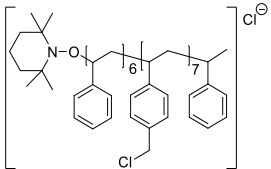
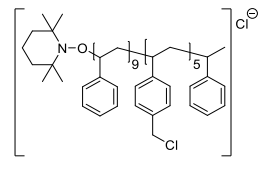
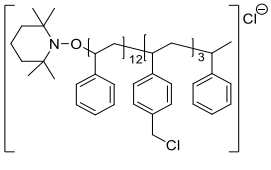
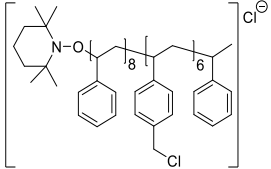
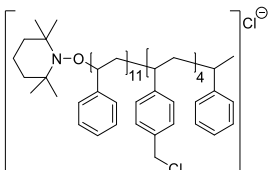
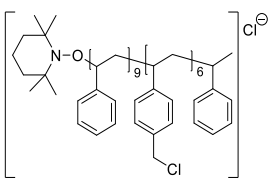
**Table A1.** Peak assignment of the ESI Orbitrap mass spectrum of **P13** showing the labels (corresponding to the species in Figure 17b, the resolution (obtained by the Xcalibur software), the experimental  $m/z$  and theoretical  $m/z$  values,  $\Delta m/z$  and the proposed chemical structures. Adapted from ref [238] with permission of the Royal Society of Chemistry.

| Label | Resolution | $m/z(\text{exp})$ | $m/z(\text{theo})$ | $\Delta m/z$ | Structure |
|-------|------------|-------------------|--------------------|--------------|-----------|
| ●     | 48000      | 2057.1311         | 2057.1336          | 0.0025       |           |
| ◆     | 46000      | 2065.2404         | 2065.2429          | 0.0025       |           |
| ○     | 49000      | 2105.1054         | 2105.1103          | 0.0049       |           |
| □     | 47000      | 2113.2169         | 2113.2195          | 0.0027       |           |

**Table A2.** Peak assignment of the ESI Orbitrap mass spectrum of **P14** showing the labels (corresponding to the species in Figure 17d, the resolution (obtained by the Xcalibur software), the experimental  $m/z$  and theoretical  $m/z$  values,  $\Delta m/z$  and the proposed chemical structures. Adapted from ref [238] with permission of the Royal Society of Chemistry.

| Label | Resolution | $m/z(\text{exp})$ | $m/z(\text{theo})$ | $\Delta m/z$ | Structure |
|-------|------------|-------------------|--------------------|--------------|-----------|
| ●     | 52000      | 2057.1330         | 2057.1336          | 0.0006       |           |
| ◆     | 46000      | 2065.2403         | 2065.2429          | 0.0026       |           |
| ❖     | 50000      | 2080.0675         | 2080.0704          | 0.0029       |           |
| ▲     | 47000      | 2084.1261         | 2084.1255          | 0.0006       |           |
| ○     | 49000      | 2105.1072         | 2105.1103          | 0.0031       |           |
| □     | 49000      | 2113.2167         | 2113.2195          | 0.0028       |           |
| ■     | 48000      | 2155.0838         | 2155.0884          | 0.0046       |           |
| □     | 47000      | 2209.1688         | 2209.1729          | 0.0041       |           |

**Table A3.** Peak assignment of the ESI Orbitrap mass spectrum of **P15** showing the labels (corresponding to the species in Figure 18b, the resolution (obtained by the Xcalibur software), the experimental  $m/z$  and theoretical  $m/z$  values,  $\Delta m/z$  and the proposed chemical structures. Adapted from ref [238] with permission of the Royal Society of Chemistry.

| Label | Resolution | $m/z(\text{exp})$ | $m/z(\text{theo})$ | $\Delta m/z$ | Structure   |
|-------|------------|-------------------|--------------------|--------------|---|
| ●     | 47000      | 1985.8391         | 1985.8326          | 0.0065       |    |
| ◆     | 51000      | 1992.9441         | 1992.9385          | 0.0056       |    |
| ○     | 51000      | 2002.0572         | 2002.0506          | 0.0065       |   |
| □     | 50000      | 2040.9210         | 2040.9151          | 0.0059       |  |
| ■     | 49000      | 2050.0337         | 2050.0278          | 0.0059       |  |
| □     | 49000      | 2145.9854         | 2145.9811          | 0.0043       |  |

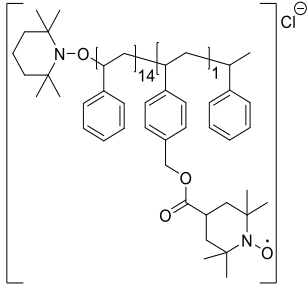
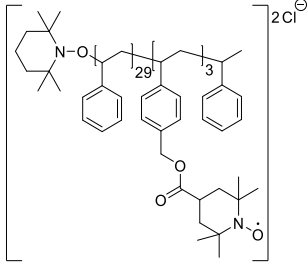
**Table A4.** Peak assignment of the ESI Orbitrap mass spectrum of **P16** showing the labels (corresponding to the species in Figure 18d, the resolution (obtained by the Xcalibur software), the experimental  $m/z$  and theoretical  $m/z$  values,  $\Delta m/z$  and the proposed chemical structures. Adapted from ref [238] with permission of the Royal Society of Chemistry.

| Label | Resolution | $m/z(\text{exp})$ | $m/z(\text{theo})$ | $\Delta m/z$ | Structure |
|-------|------------|-------------------|--------------------|--------------|-----------|
| ●     | 51000      | 1840.9000         | 1840.8992          | 0.0008       |           |
| ◆     | 49000      | 1994.9400         | 1994.9390          | 0.0010       |           |
| ○     | 50000      | 1897.9888         | 1897.9885          | 0.0003       |           |
| □     | 44000      | 1938.8505         | 1938.8525          | 0.0020       |           |

**Table A5.** Peak assignment of the SEC ESI Orbitrap mass spectrum of **P13'** showing the labels (corresponding to the species in Figure 21a), the resolution (obtained by the Xcalibur software), the experimental and theoretical  $m/z$ ,  $\Delta m/z$  and the proposed chemical structure. Reproduced from ref [238] with permission of the Royal Society of Chemistry.

| Label | Resolution | $m/z(\text{exp})$ | $m/z(\text{theo})$ | $\Delta m/z$ | Structure |
|-------|------------|-------------------|--------------------|--------------|-----------|
| ●     | 43000      | 2841.4822         | 2481.4933          | 0.0110       |           |
| ◆     | 44000      | 2511.4804         | 2511.4877          | 0.0073       |           |

**Table A6.** Peak assignment of the ESI Orbitrap mass spectrum of **P14'** showing the labels (corresponding to the species in Figure 21b), the resolution (obtained by the Xcalibur software), the experimental  $m/z$  and theoretical  $m/z$  values,  $\Delta m/z$  and the proposed chemical structures. Reproduced from ref [238] with permission of the Royal Society of Chemistry.

| Label | Resolution | $m/z(\text{exp})$ | $m/z(\text{theo})$ | $\Delta m/z$ | Structure  |
|-------|------------|-------------------|--------------------|--------------|--|
| ●     | 48000      | 2069.2441         | 2069.2463          | 0.0022       |   |
| ◆     | 45000      | 2148.7670         | 2148.7686          | 0.0016       |  |

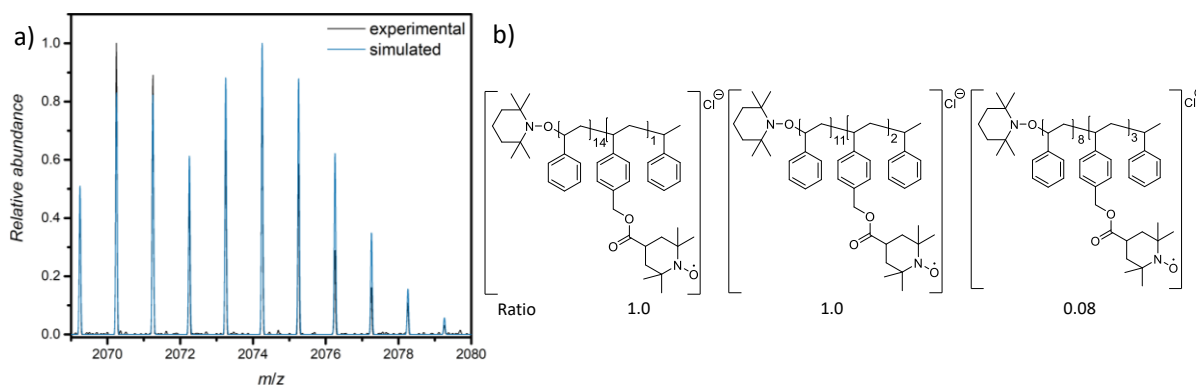


**Figure 82.** a) Isotopic simulation of a selected single charged pattern from  $m/z$  2069 to 2079 of **P14'** (●) comparing the experiment (black line) with the simulation (blue line) with a resolution of 49000. B) Identified structures and their ratio within the pattern. Adapted from ref [238] with permission of the Royal Society of Chemistry.

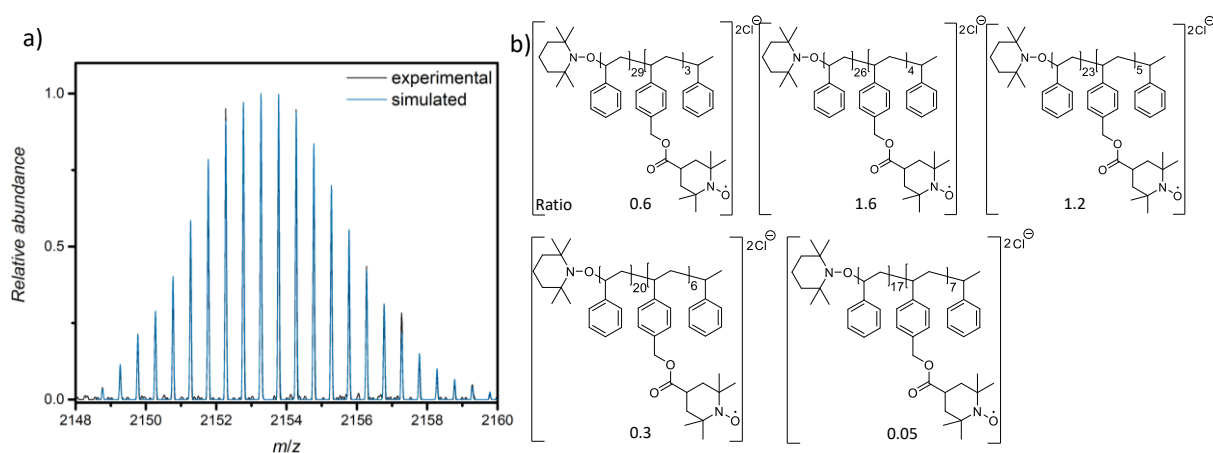


**Figure 83.** a) Isotopic simulation of a selected double charged pattern from  $m/z$  2149 to 2159 of **P14'** (◆) comparing the experiment (black line) with the simulation (blue line) with a resolution of 47000. B) Identified structures and their ratio within the pattern. Adapted from ref [238] with permission of the Royal Society of Chemistry.

**Table A7.** Peak assignment of the ESI Orbitrap mass spectrum of **P15'** showing the labels (corresponding to the species in Figure 21c), the resolution (obtained by the Xcalibur software), the experimental  $m/z$  and theoretical  $m/z$  values,  $\Delta m/z$  and the proposed chemical structures. Reproduced from ref [238] with permission of the Royal Society of Chemistry.

| Label | Resolution | $m/z(\text{exp})$ | $m/z(\text{theo})$ | $\Delta m/z$ | Structure |
|-------|------------|-------------------|--------------------|--------------|-----------|
| ●     | 42000      | 2493.4995         | 2493.5037          | 0.0042       |           |
| ◆     | 39000      | 2521.9906         | 2521.9976          | 0.0070       |           |

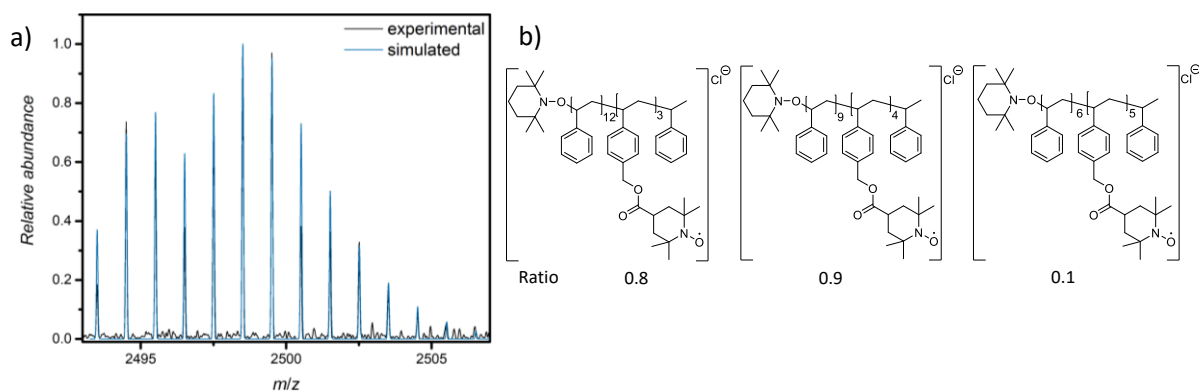


**Figure 84.** a) Isotopic simulation of a selected single charged pattern from  $m/z$  2491 to 2504 of **P15'** (●) comparing the experiment (black line) with the simulation (blue line) with a resolution of 43000. B) Identified structures and their ratio within the pattern. Adapted from ref [238] with permission of the Royal Society of Chemistry.

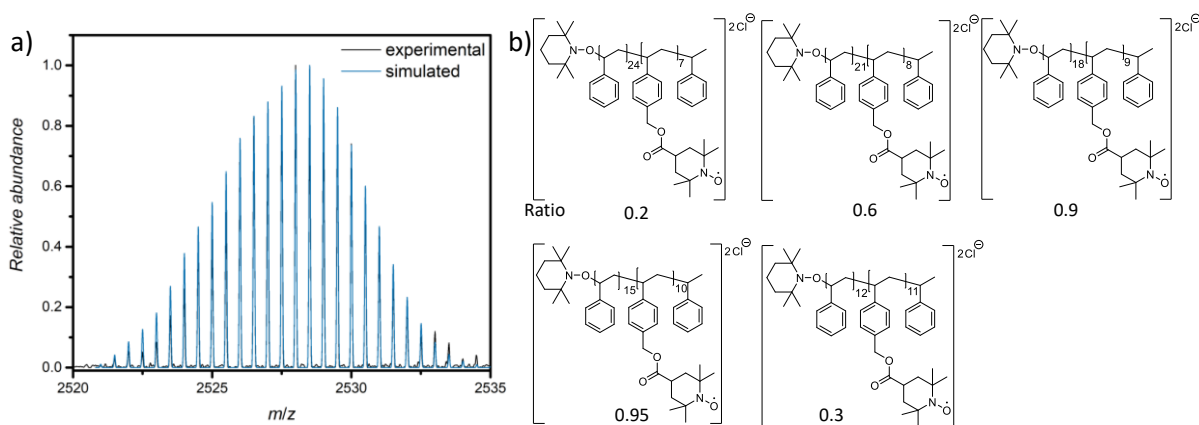


**Figure 85.** a) Isotopic simulation of a selected double charged pattern from  $m/z$  2521 to 2533 of **P15'** (◆) comparing the experiment (black line) with the simulation (blue line) with a resolution of 43000. B) Identified structures and their ratio within the pattern. Adapted from ref [238] with permission of the Royal Society of Chemistry.



**Table A8.** Peak assignment of the ESI Orbitrap mass spectrum of **P16'** showing the labels (corresponding to the species in Figure 21d), the resolution (obtained by the Xcalibur software), the experimental  $m/z$  and theoretical  $m/z$  values,  $\Delta m/z$  and the proposed chemical structures. Reproduced from ref [238] with permission of the Royal Society of Chemistry.

| Label | Resolution | $m/z(\text{exp})$ | $m/z(\text{theo})$ | $\Delta m/z$ | Structure |
|-------|------------|-------------------|--------------------|--------------|-----------|
| ●     | 33000      | 2469.4577         | 2469.4650          | 0.0073       |           |

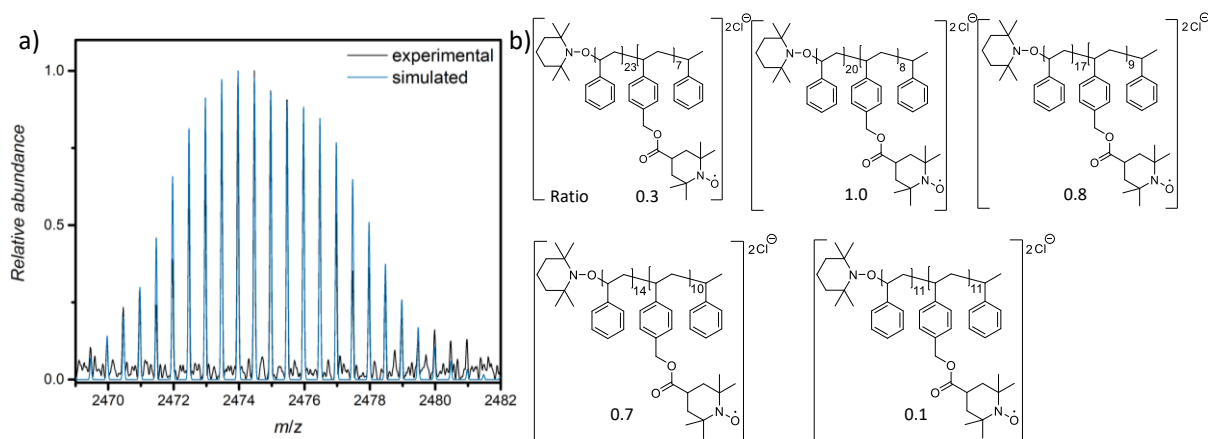


**Figure 86.** a) Isotopic simulation of a selected single charged pattern from  $m/z$  2470 to 2480 of **P16'** (●) comparing the experiment (black line) with the simulation (blue line) with a resolution of 42000. B) Identified structures and their ratio within the pattern. Adapted from ref [238] with permission of the Royal Society of Chemistry.

### C. Supporting Information for Chapter 3.1.3

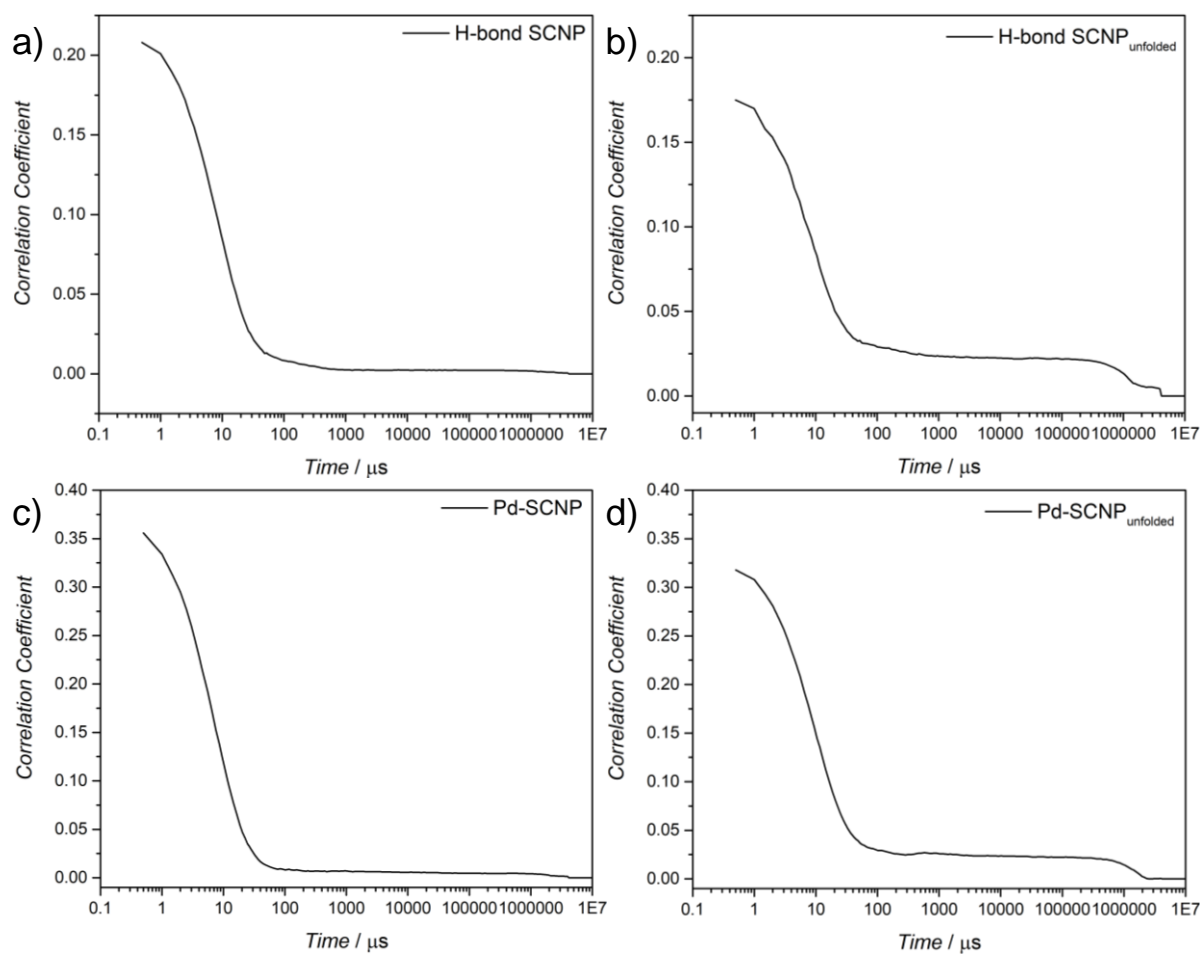


**Figure 87.** Autocorrelation curves for a) the **H-bond SCNP**, b) the unfolded **H-bond SCNP<sub>unfolded</sub>**, c) the folded **Pd-SCNP** and d) for the **Pd-SCNP<sub>unfolded</sub>**. All samples were measured in DCM at ambient temperature.

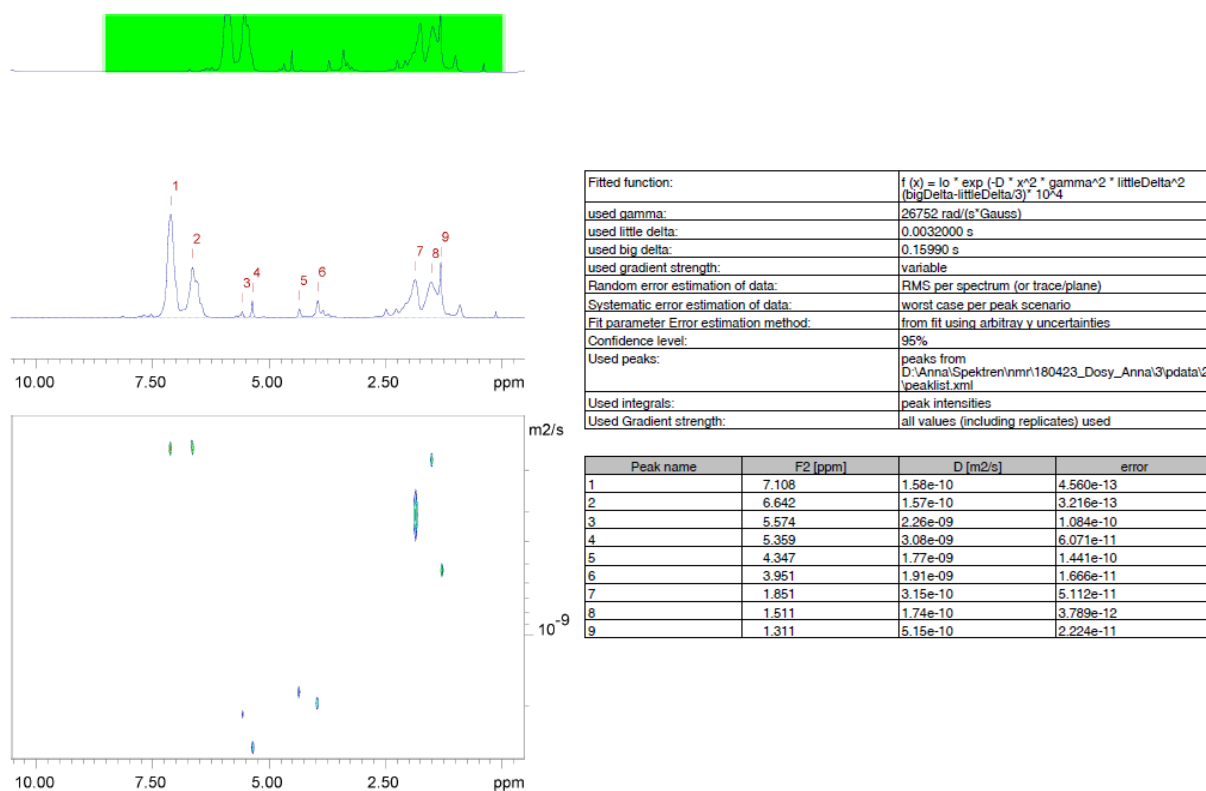


**Figure 88.** Original Data of DOSY measurements of the folded **H-bond SCNP**, recorded in DCM- $d_2$  at 298 K.

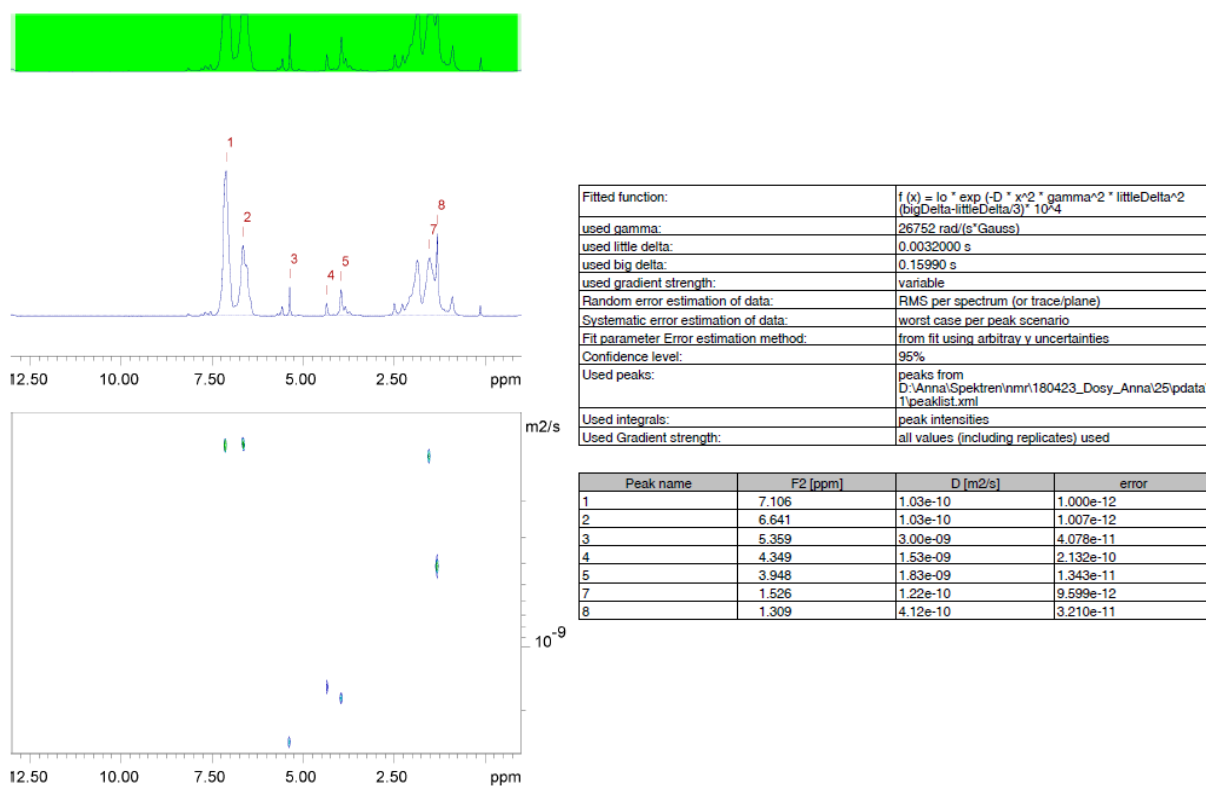


**Figure 89.** Original Data of DOSY measurements of the unfolded **H-bond SCNP<sub>unfolded</sub>**, recorded in DCM- $d_2$  at 298 K.

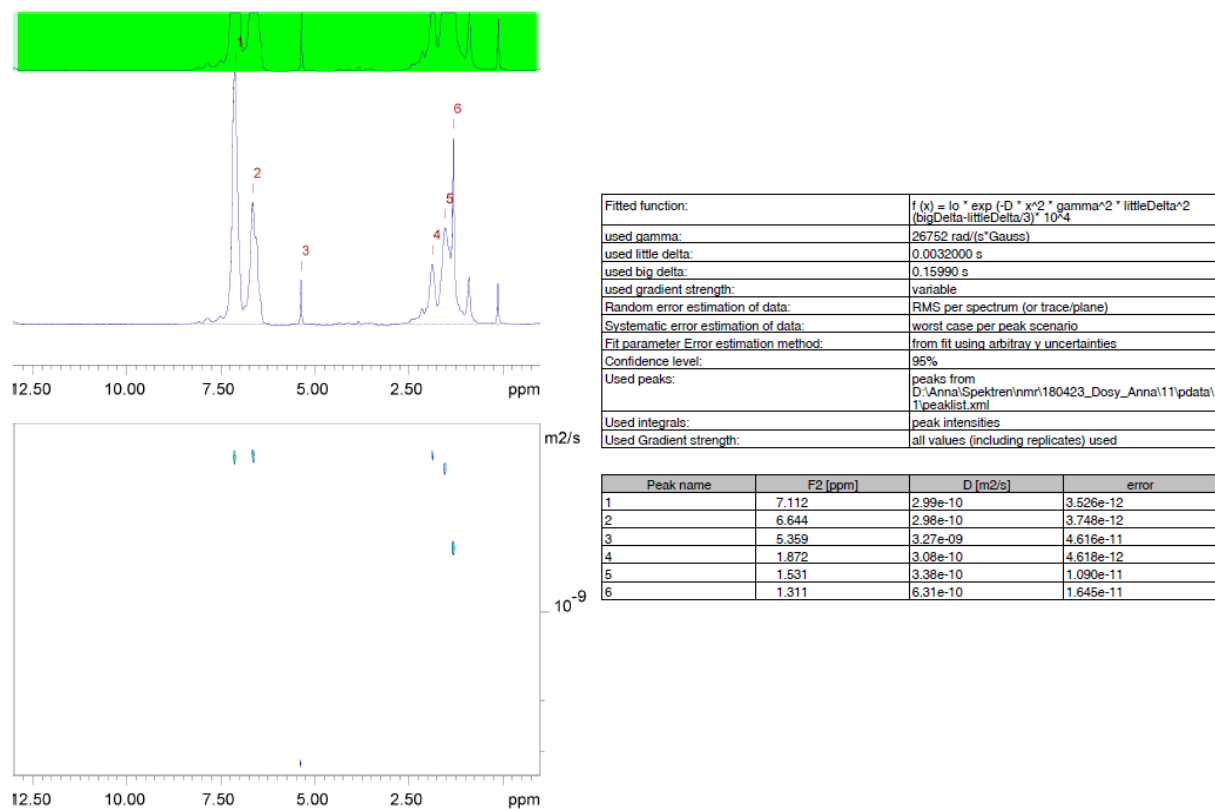


**Figure 90.** Original Data of DOSY measurements of the folded **Pd-SCNP**, recorded in DCM- $d_2$  at 298 K.

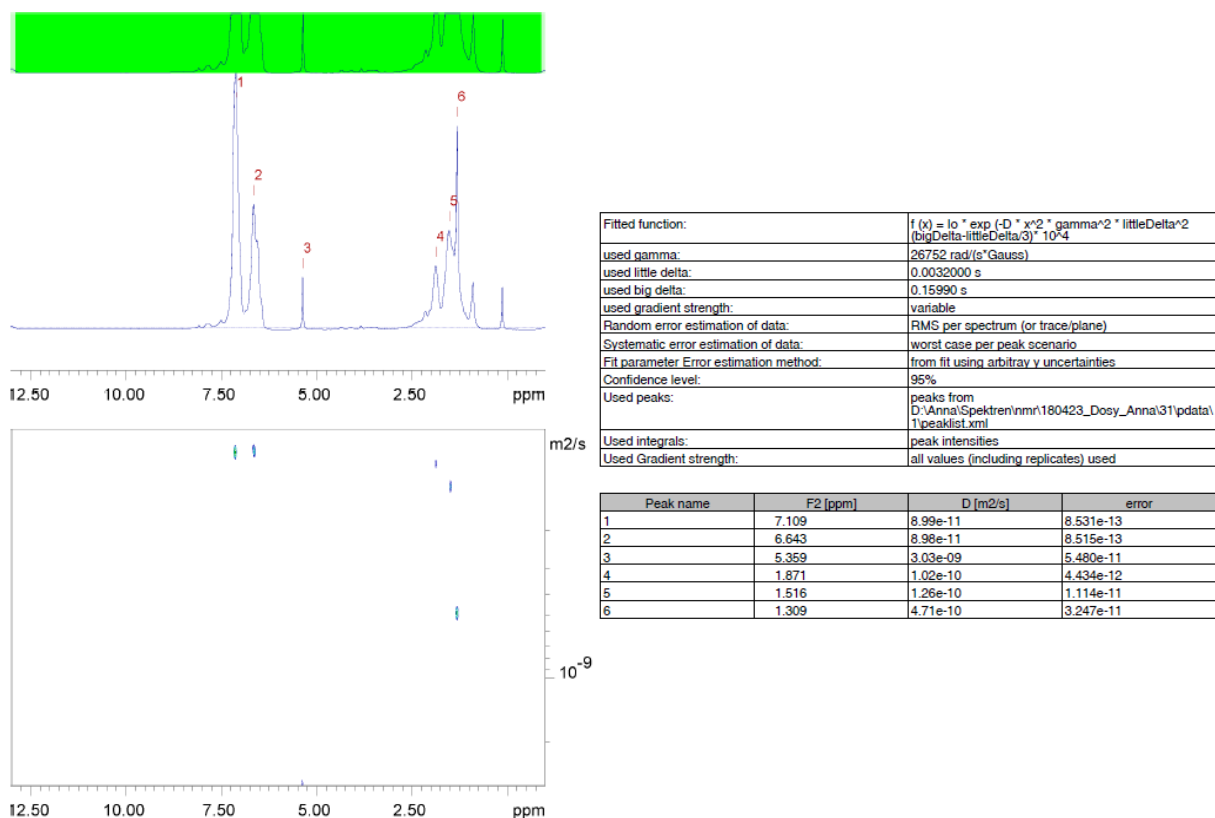


**Figure 91.** Original Data of DOSY measurements of the unfolded **Pd-SCNP<sub>unfolded</sub>**, recorded in DCM- $d_2$  at 298 K.

## D. Supporting Information for Chapter 3.2.1

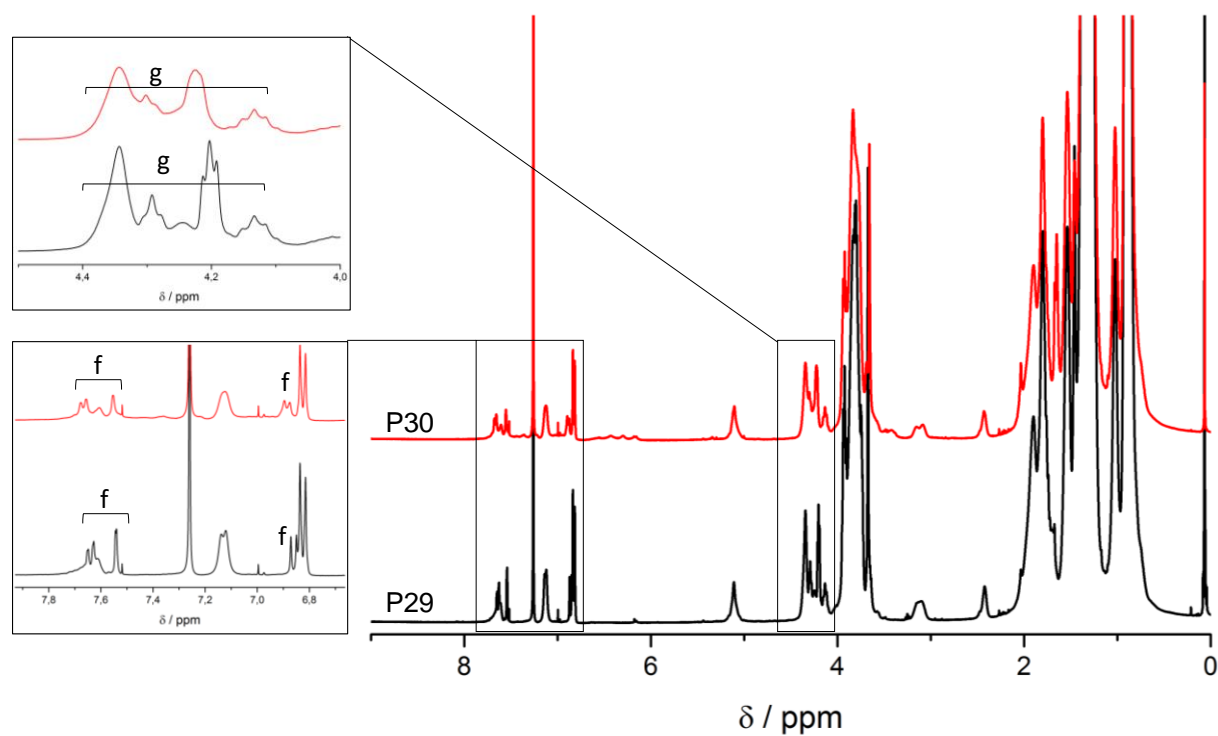


**Figure 92.** Full NMR spectrum of the protected polymer **P29** and the deprotected analogue **P30**, recorded in CDCl<sub>3</sub> (298 K). The assignments of the resonances can be found in Scheme 28. Adapted from ref [252] with permission from Wiley-VCH. © 2016 WILEY-VCH Verlag GmbH & Co. KgaA, Weinheim.

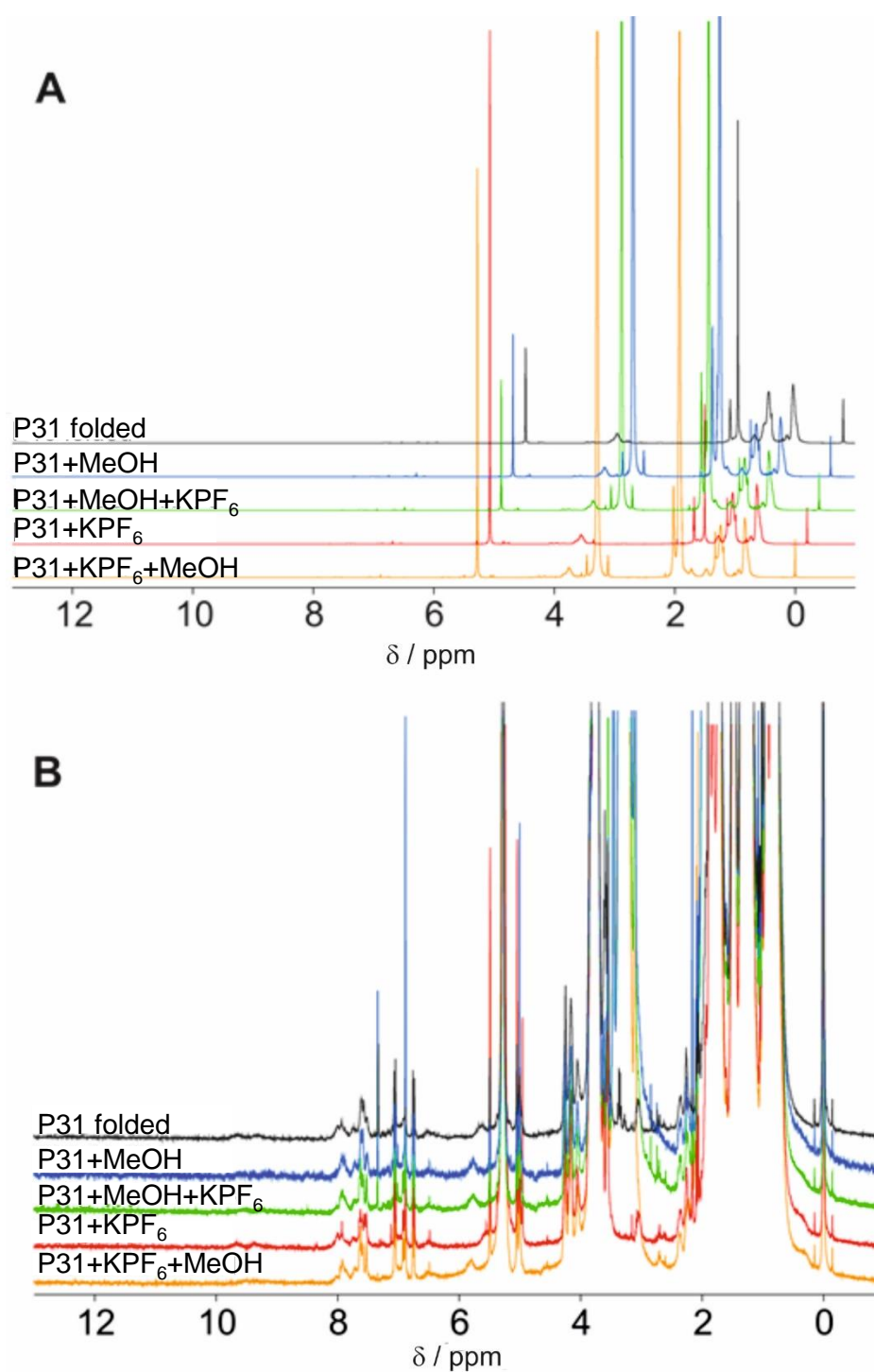


**Figure 93.**  $1D-^1H-NMR$  spectra of **P31** in the different folding and unfolding states. A and B show the same spectra, while B is scaled up for resonances near the baseline. All samples were recorded in  $DCM-d_2$  (298 K). Adapted from ref [252] with permission from Wiley-VCH. © 2016 WILEY-VCH Verlag GmbH & Co. KgaA, Weinheim.

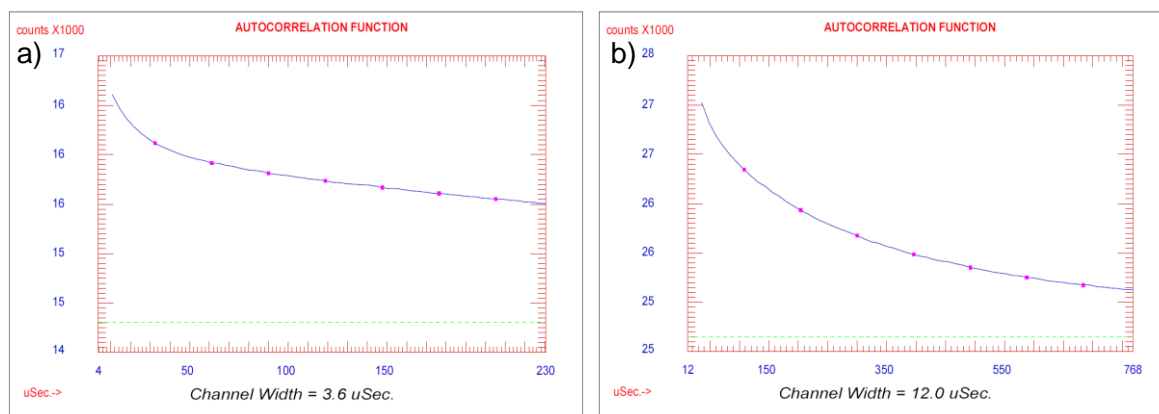


**Figure 94.** Autocorrelation functions of a) the folded **P30** and b) the unfolded polymer **P30** by addition of  $\text{KPF}_6$ . All samples were measured in a mixture of DCM/acetonitrile (9:1, v/v). Reproduced from ref [252] with permission from Wiley-VCH. © 2016 WILEY-VCH Verlag GmbH & Co. KgaA, Weinheim.

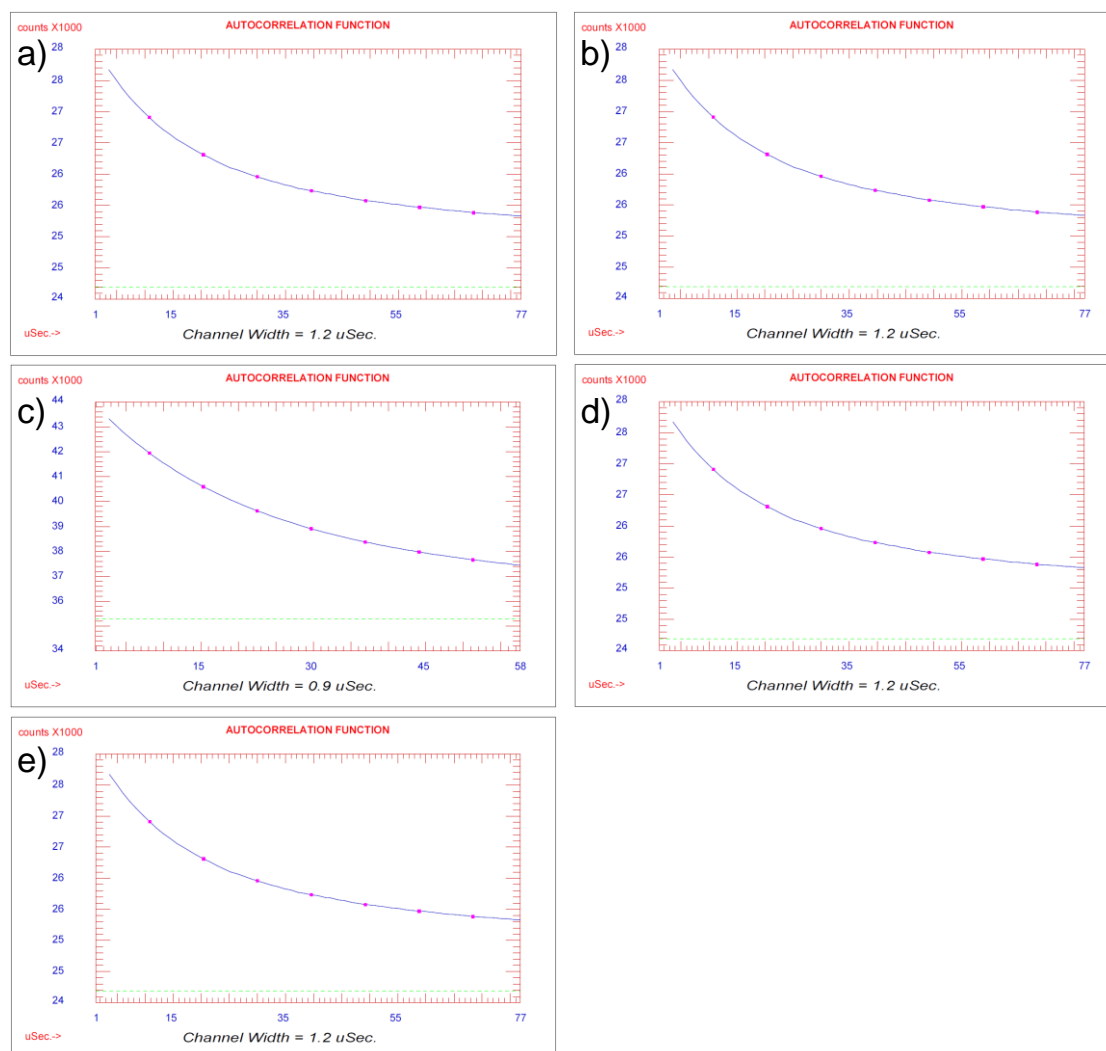


**Figure 95.** Autocorrelation functions of a) the folded **P31**, b) the polymer **P31** after the addition of MeOH to unfold the HW/CA motif, c) the unfolded polymer **P31** after addition of MeOH and  $\text{KPF}_6$ , d) the polymer **P31** after addition of  $\text{KPF}_6$  to unfold the B21C7/AS complex and e) the unfolded **P31** after the addition of  $\text{KPF}_6$  and MeOH. All samples were measured in a mixture of DCM/acetonitrile (9:1, v/v). Reproduced from ref [252] with permission from Wiley-VCH. © 2016 WILEY-VCH Verlag GmbH & Co. KgaA, Weinheim.

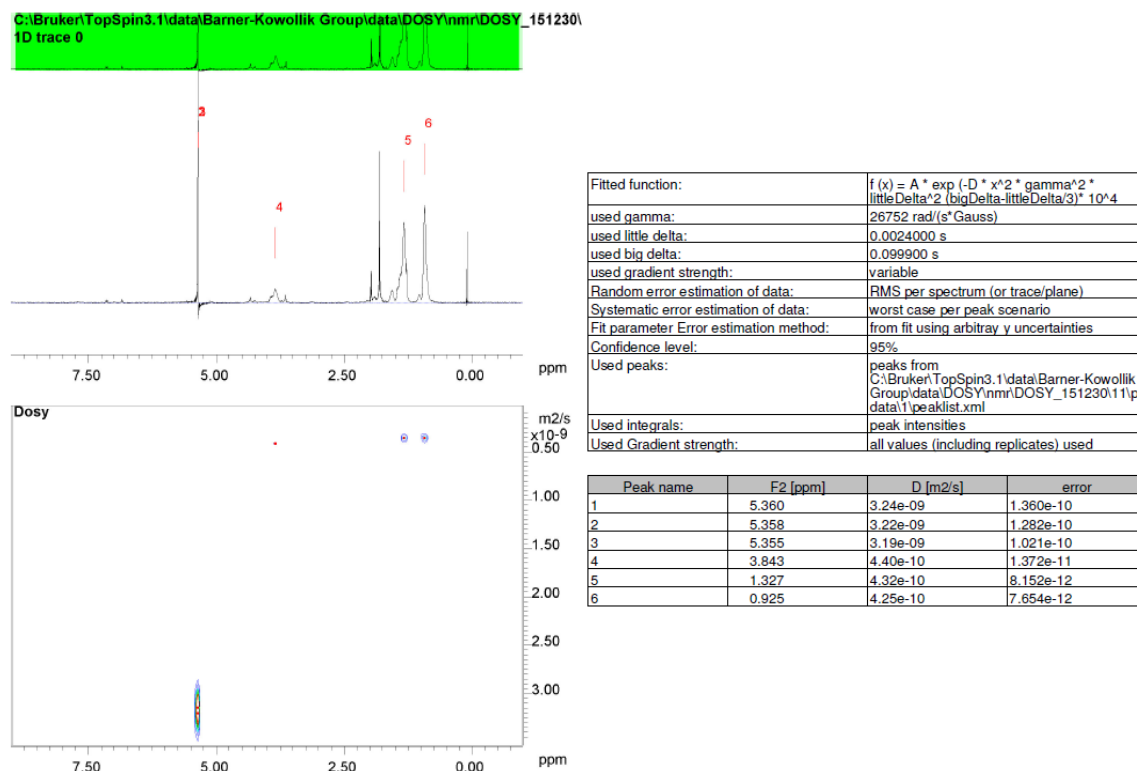


**Figure 96.** Original Data of DOSY measurements of the folded **P30**, recorded in DCM- $d_2$  at 298 K. Reproduced from ref [252] with permission from Wiley-VCH. © 2016 WILEY-VCH Verlag GmbH & Co. KgaA, Weinheim.

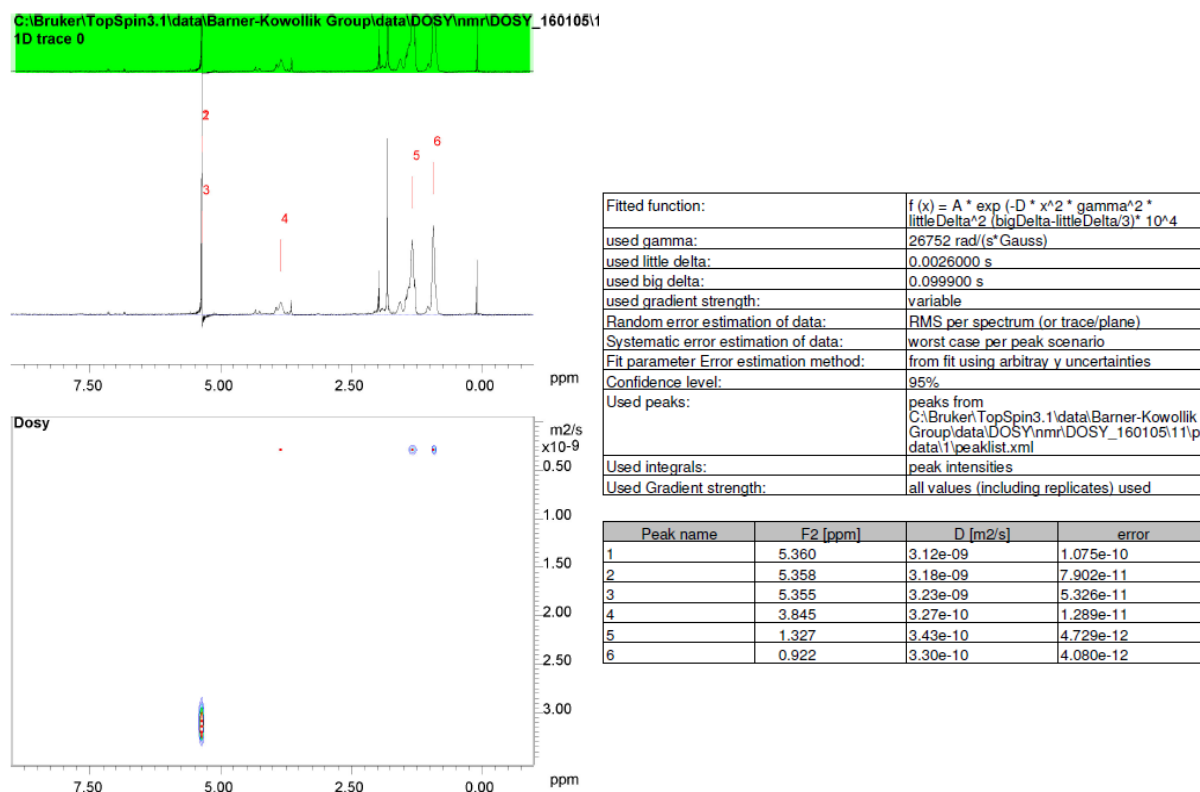


**Figure 97.** Original Data of DOSY measurements of the unfolded **P30** after addition of  $\text{KPF}_6$ , recorded in DCM- $d_2$  at 298 K. Reproduced from ref [252] with permission from Wiley-VCH. © 2016 WILEY-VCH Verlag GmbH & Co. KgaA, Weinheim.



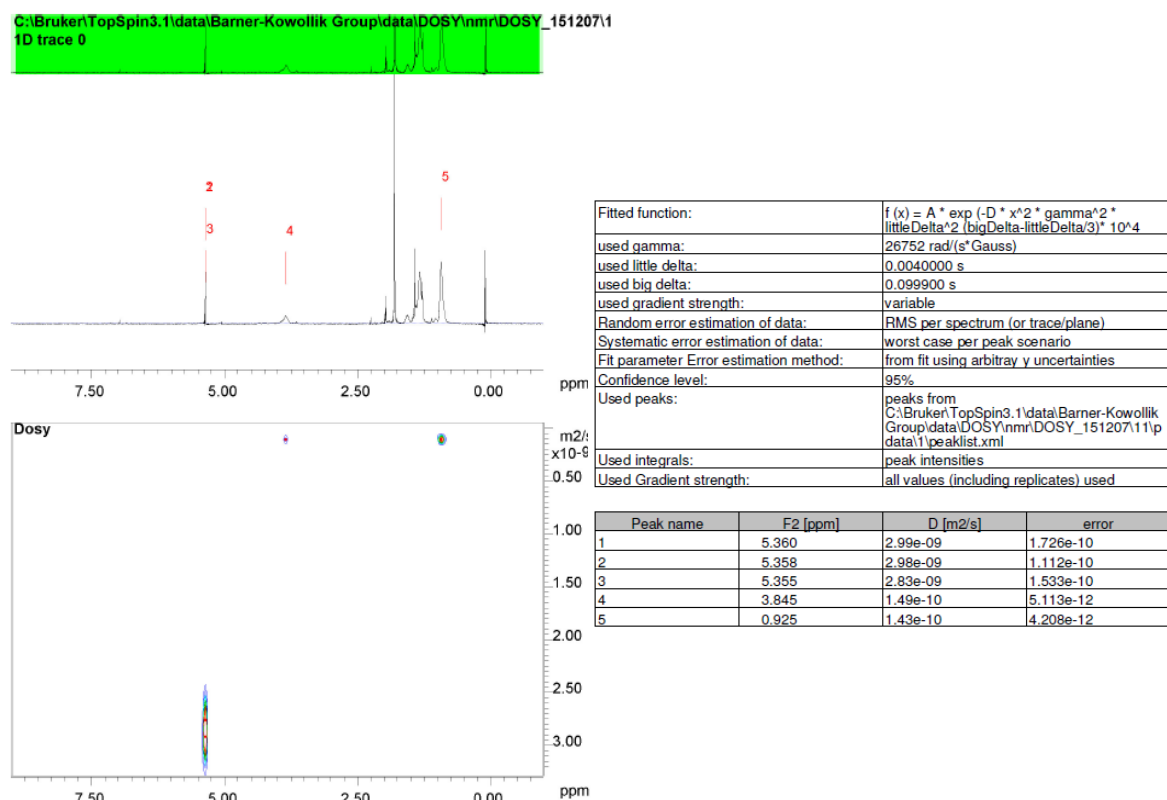


**Figure 98.** Original Data of DOSY measurements of the folded **P31**, recorded in DCM- $d_2$  at 298 K. Reproduced from ref [252] with permission from Wiley-VCH. © 2016 WILEY-VCH Verlag GmbH & Co. KgaA, Weinheim.

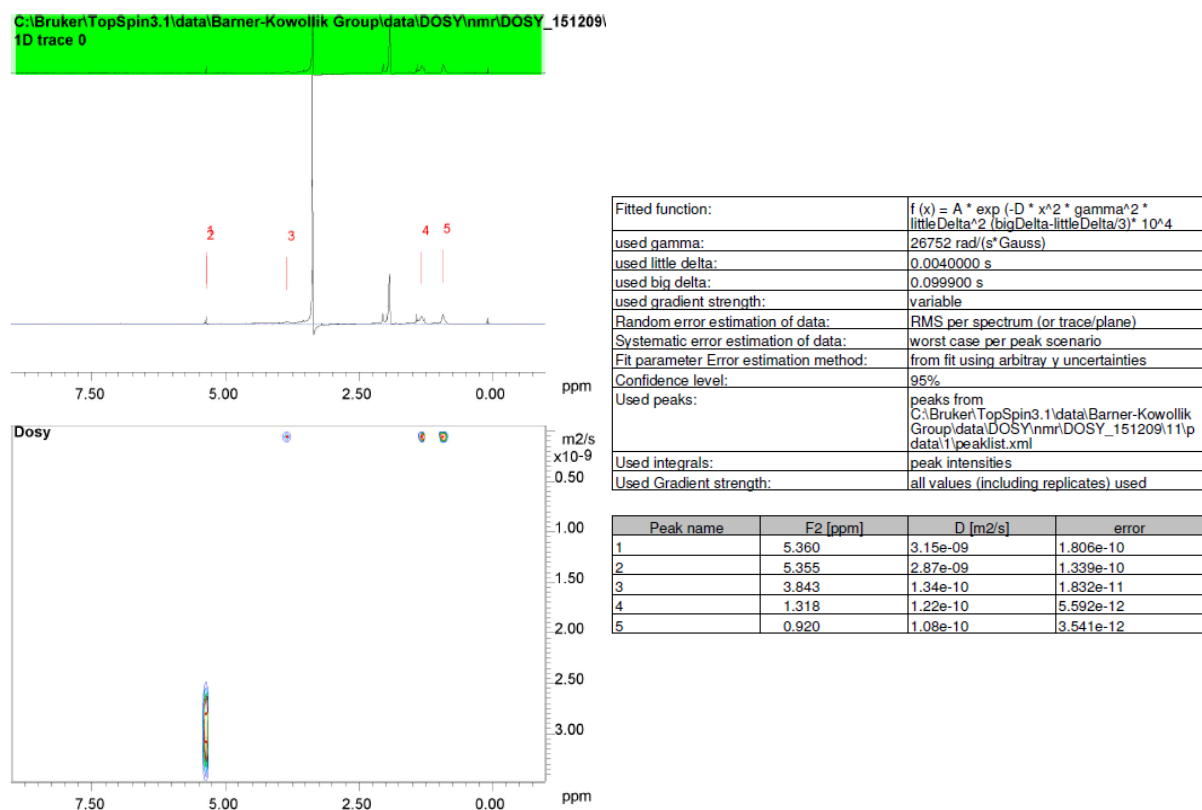


**Figure 99.** Original Data of DOSY measurements of the polymer **P31** after addition of MeOH to unfold the HW/CA motifs, recorded in DCM- $d_2$  at 298 K. Reproduced from ref [252] with permission from Wiley-VCH. © 2016 WILEY-VCH Verlag GmbH & Co. KgaA, Weinheim.

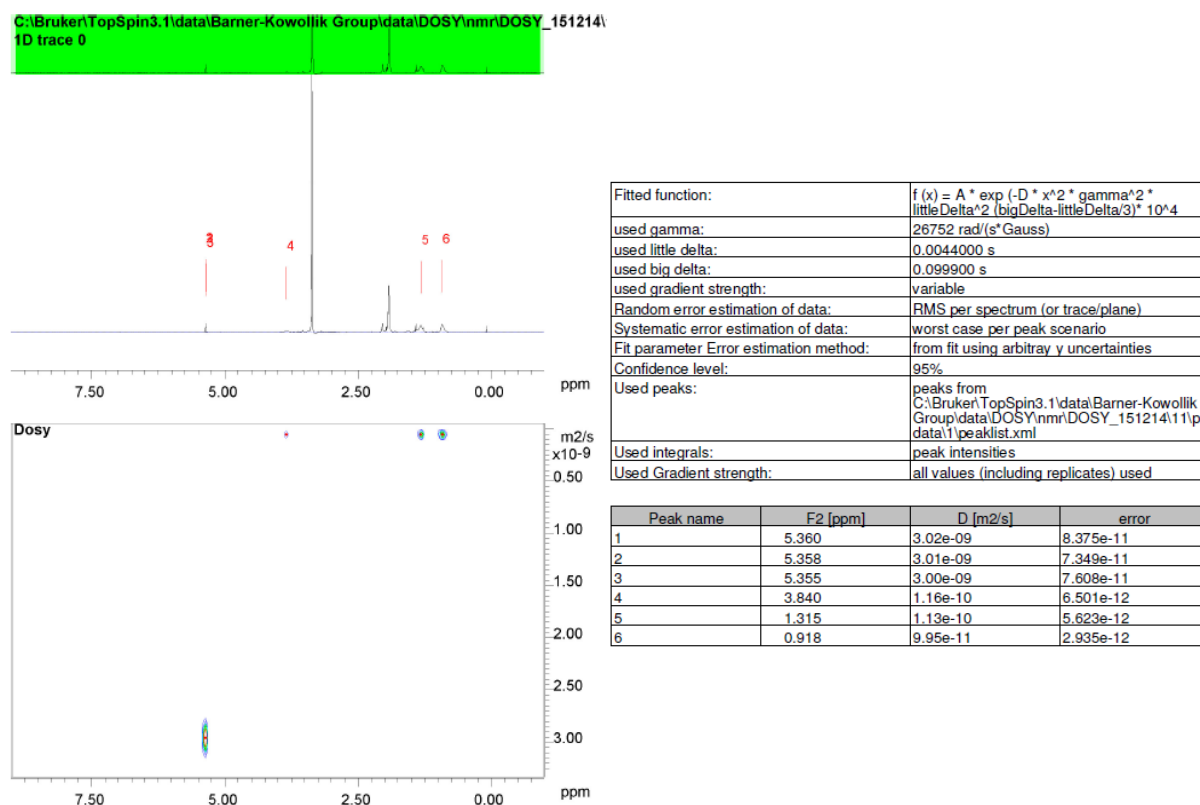


**Figure 100.** Original Data of DOSY measurements of the unfolded polymer **P31** after addition of MeOH and KPF<sub>6</sub>, recorded in DCM-*d*<sub>2</sub> at 298 K. Reproduced from ref [252] with permission from Wiley-VCH. © 2016 WILEY-VCH Verlag GmbH & Co. KgaA, Weinheim.

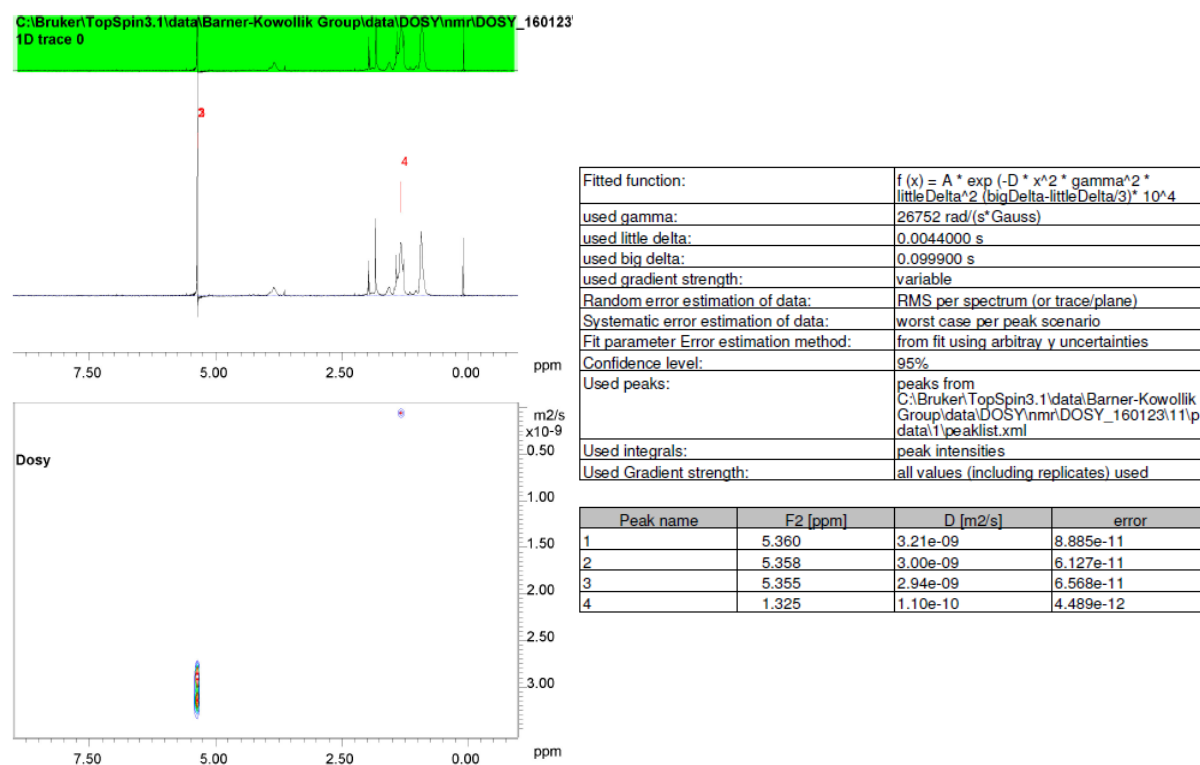


**Figure 101.** Original Data of DOSY measurements of the polymer **P31** after addition of KPF<sub>6</sub> to unfold the B21C7/AS complex, recorded in DCM-*d*<sub>2</sub> at 298 K. Reproduced from ref [252] with permission from Wiley-VCH. © 2016 WILEY-VCH Verlag GmbH & Co. KgaA, Weinheim.

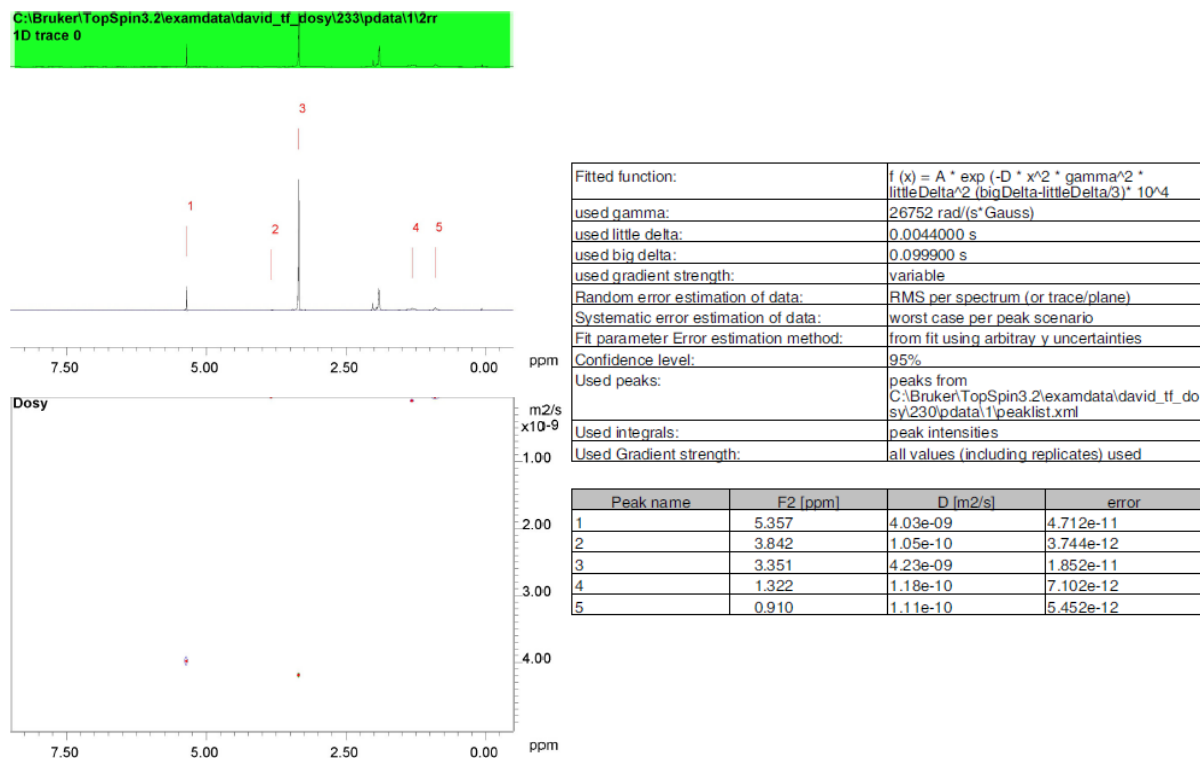


**Figure 102.** Original Data of DOSY measurements of the unfolded polymer **P31** after addition of  $\text{KPF}_6$  and MeOH, recorded in  $\text{DCM-d}_2$  at 298 K. Reproduced from ref [252] with permission from Wiley-VCH. © 2016 WILEY-VCH Verlag GmbH & Co. KgaA, Weinheim.

## Biexponential Fits to the DOSY Data of the P16+KPF6+MeOH Sample

Fitting of DOSY data using the equation

$$f(x) = b_1 e^{-a_1 x^2} + b_2 e^{-a_2 x^2}.$$

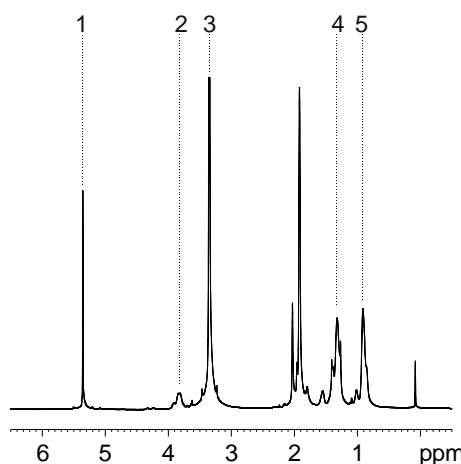


**Figure 103.** 1D  $^1\text{H}$  NMR spectrum of the **P31**+ $\text{KPF}_6$ +MeOH sample. For the signals 2, 4 and 5 a bi-exponential fit to the DOSY data was performed. Reproduced from ref [252] with permission from Wiley-VCH. © 2016 WILEY-VCH Verlag GmbH & Co. KgaA, Weinheim.

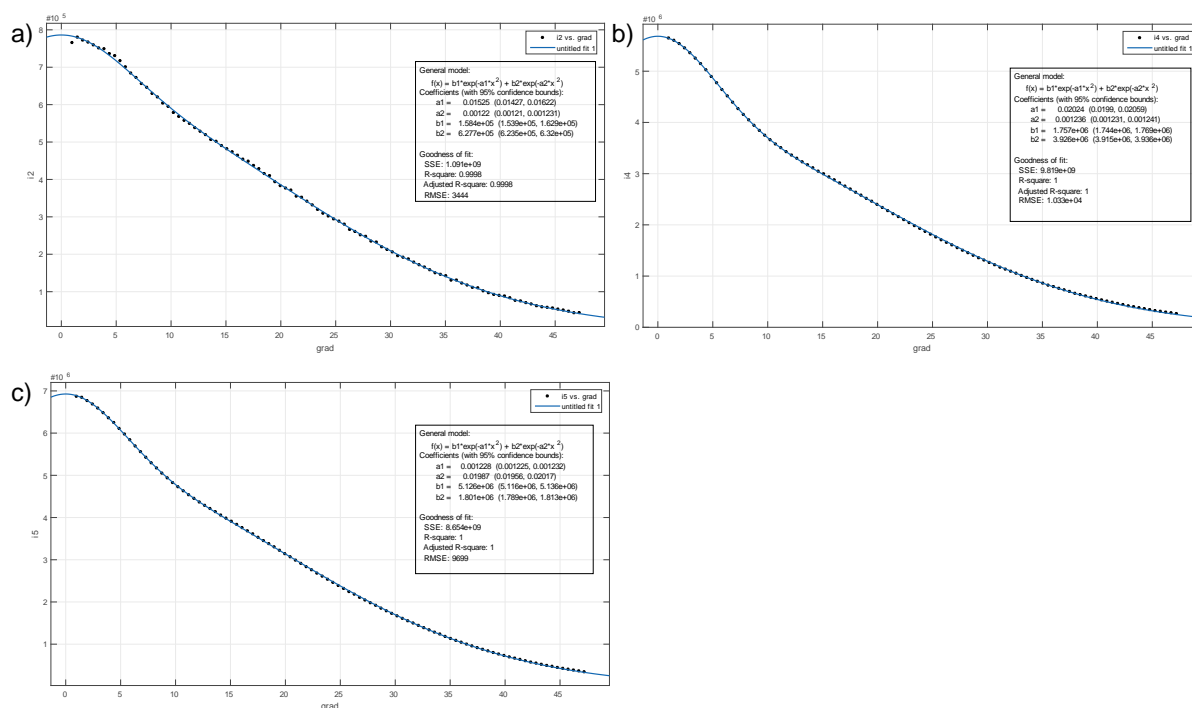


**Figure 104.** Bi-exponential fits to DOSY data of a) signal 2, b) signal 4 and c) signal 5. Reproduced from ref [252] with permission from Wiley-VCH. © 2016 WILEY-VCH Verlag GmbH & Co. KgaA, Weinheim.

The diffusion coefficients  $D$  can be calculated using

$$D_{1,2} = \frac{a_{1,2}}{\gamma_H^2 \delta^2 (\Delta - \delta)}$$

with the fit parameters  $a_1$  and  $a_2$ , which are given in Figure 104, the proton gyromagnetic ratio  $\gamma_H = 26752 \text{ rad}/(\text{s} \cdot \text{G})$ , the diffusion delay  $\Delta = 100 \text{ ms}$  and the length of the bipolar gradient pair  $\delta = 4.4 \text{ ms}$ . The results are shown in the chart below. Reproduced from ref [252] with permission from Wiley-VCH. © 2016 WILEY-VCH Verlag GmbH & Co. KgaA, Weinheim.

| Signal 2                  |                           | Signal 4                  |                           | Signal 5                  |                           |
|---------------------------|---------------------------|---------------------------|---------------------------|---------------------------|---------------------------|
| $D_1$ (m <sup>2</sup> /s) | $D_2$ (m <sup>2</sup> /s) | $D_1$ (m <sup>2</sup> /s) | $D_2$ (m <sup>2</sup> /s) | $D_1$ (m <sup>2</sup> /s) | $D_2$ (m <sup>2</sup> /s) |
| $1.12 \cdot 10^{-9}$      | $8.94 \cdot 10^{-11}$     | $1.50 \cdot 10^{-9}$      | $9.05 \cdot 10^{-11}$     | $8.99 \cdot 10^{-11}$     | $1.46 \cdot 10^{-9}$      |

## E. Supporting Information for Chapter 3.2.2

### NMR Data

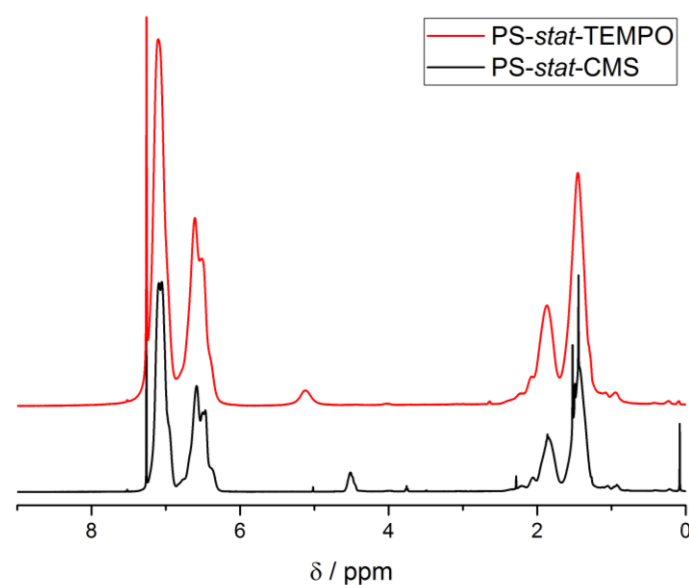


**Figure 105.** <sup>1</sup>H NMR spectra of the parent polymer **P32** (PS-*stat*-CMS) and the TEMPO functionalized **P32'** (PS-*stat*-TEMPO), measured in CDCl<sub>3</sub> (298 K). Adapted from ref [256] with permission of the Royal Society of Chemistry.

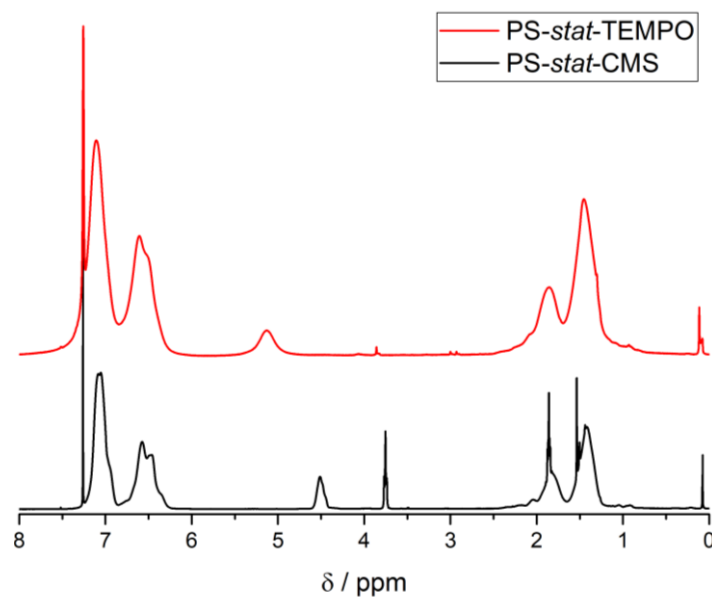


**Figure 106.** <sup>1</sup>H NMR spectra of the parent polymer **P33** (PS-*stat*-CMS) and the TEMPO functionalized **P33'** (PS-*stat*-TEMPO), measured in CDCl<sub>3</sub> (298 K). Adapted from ref [256] with permission of the Royal Society of Chemistry.

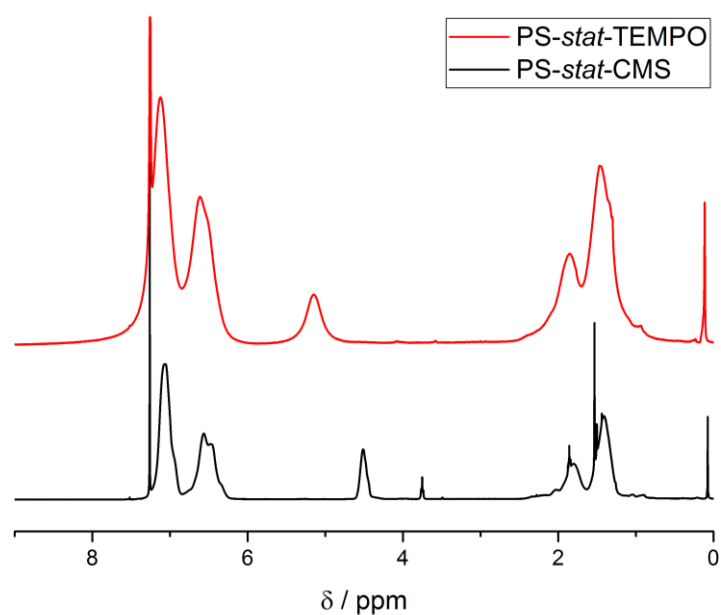


**Figure 107.** <sup>1</sup>H NMR spectra of the parent polymer **P34** (PS-*stat*-CMS) and the TEMPO functionalized **P34'** (PS-*stat*-TEMPO), measured in CDCl<sub>3</sub> (298 K). Adapted from ref [256] with permission of the Royal Society of Chemistry.

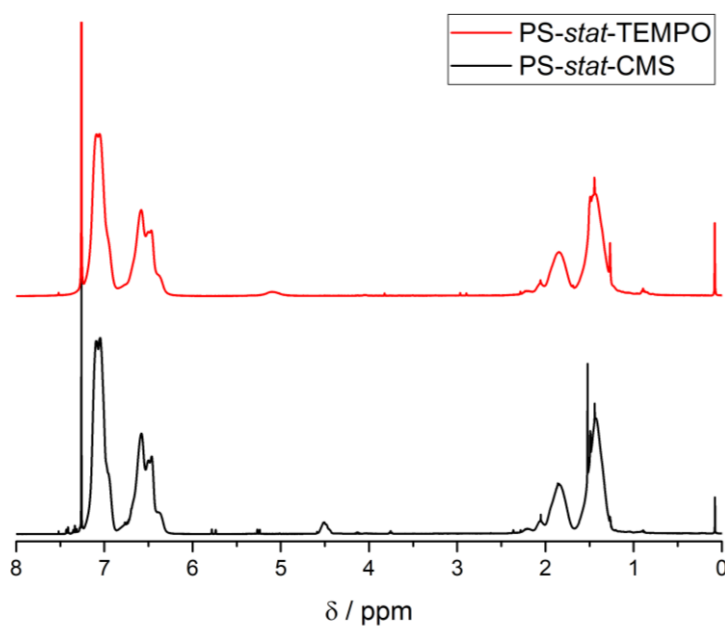


**Figure 108.** <sup>1</sup>H NMR spectra of the parent polymer **P35** (PS-*stat*-CMS) and the TEMPO functionalized **P35'** (PS-*stat*-TEMPO), measured in CDCl<sub>3</sub> (298 K). Adapted from ref [256] with permission of the Royal Society of Chemistry.

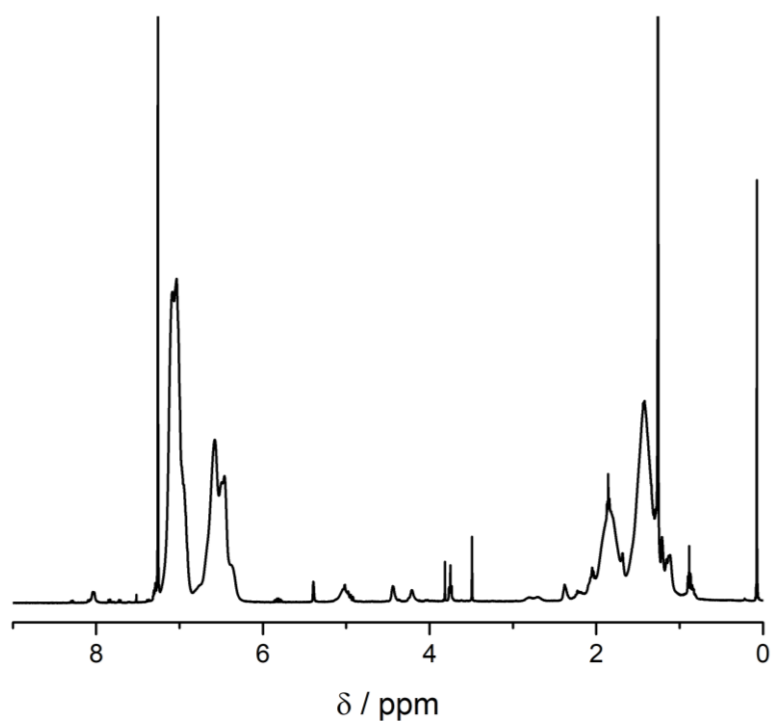


**Figure 109.** <sup>1</sup>H NMR spectrum of the SCNP **NP5** (CDCl<sub>3</sub>, 298 K). Adapted from ref [256] with permission of the Royal Society of Chemistry.

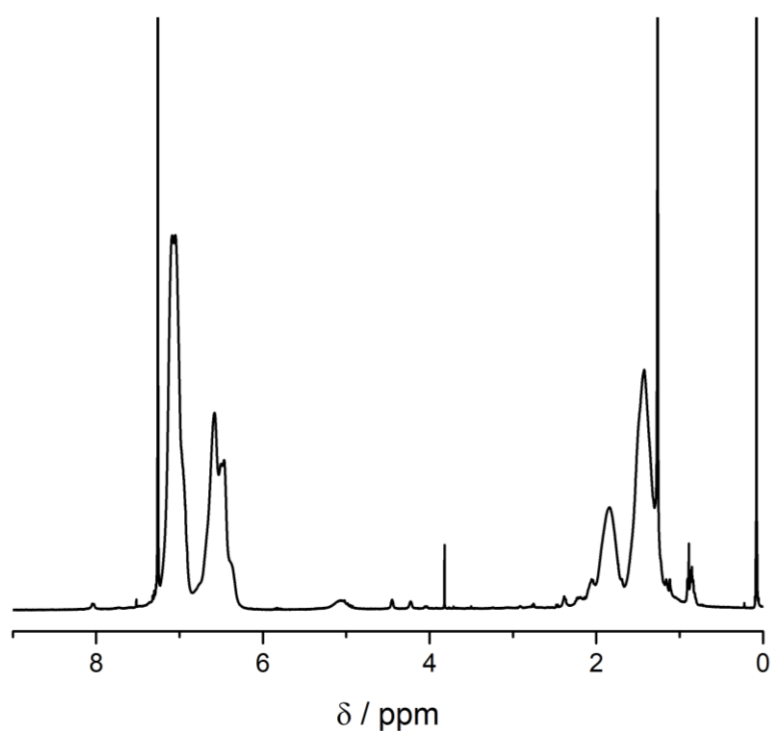


**Figure 110.** <sup>1</sup>H NMR spectrum of the SCNP **NP5<sub>unfolded</sub>** (CDCl<sub>3</sub>, 298 K). Adapted from ref [256] with permission of the Royal Society of Chemistry.

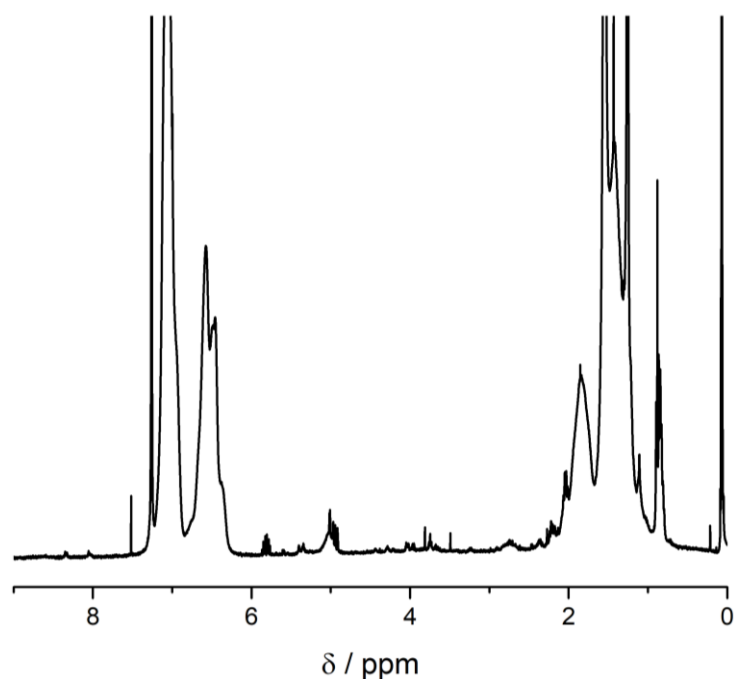


**Figure 111.**  $^1\text{H}$  NMR spectrum of the SCNP  $\text{NP5}_{\text{refolded}}$  ( $\text{CDCl}_3$ , 298 K). Adapted from ref [256] with permission of the Royal Society of Chemistry.

### UV-Vis Data

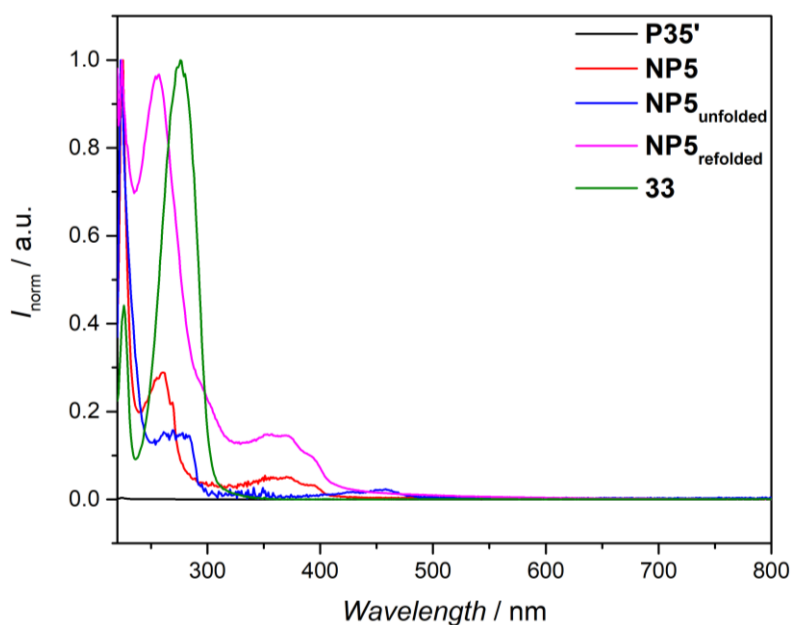


**Figure 112.** UV-Vis spectra of the parent polymer  $\text{P35}'$ , the folded SCNP ( $\text{NP5}$ ), the unfolded  $\text{NP5}_{\text{unfolded}}$ , the refolded  $\text{NP5}_{\text{refolded}}$  and the crosslinker  $\mathbf{33}$ . All samples were measured in DCM and at a concentration of  $c = 0.2 \text{ mg mL}^{-1}$ . Adapted from ref [256] with permission of the Royal Society of Chemistry.



**EPR Data**

The TEMPO density per polymer was calculated according to:

$$\frac{\text{Spin concentration}}{\text{Polymer concentration}}$$

**Table A9.** Material information used for the preparation of the EPR experiments and resulting concentrations. Adapted from ref [256] with permission of the Royal Society of Chemistry.

| ID         | M / g  | $M_n$ / g mol <sup>-1</sup> | n / mmol    | V / mL | $C_{\text{Polymer}}$ / mol L <sup>-1</sup> |
|------------|--------|-----------------------------|-------------|--------|--|
| <b>P4'</b> | 0.0027 | 33300                       | 8.10811E-05 | 0.5    | 0.000162                                   |
| <b>P9</b>  | 0.0034 | 18500                       | 0.000183784 | 1.13   | 0.000162                                   |
| <b>P10</b> | 0.0015 | 33400                       | 4.49102E-05 | 0.27   | 0.000166                                   |
| <b>P11</b> | 0.005  | 16200                       | 0.000308642 | 1.9    | 0.000162                                   |

**Table A10.** G-factors and hyperfine coupling constants ( $a_N$ ) for the parent polymer **P35'**, the folded **NP5**, the unfolded **NP5<sub>unfolded</sub>** and the refolded **NP5<sub>refolded</sub>** SCNPs. Reproduced from ref [256] with permission of the Royal Society of Chemistry.

|  | <b>P35'</b> | <b>NP5</b> | <b>NP5<sub>unfolded</sub></b> | <b>NP5<sub>refolded</sub></b> |
|--|-------------|------------|-------------------------------|-------------------------------|
| <b>g</b>   | 2.00725     | 2.00707    | 2.00727                       | 2.00697                       |
| <b><math>a_N</math> / G</b>                              | 15.24       | 15.51      | 15.24                         | 15.48                         |
| <b>Spin / mm<sup>3</sup></b>                             | 3.79E+14    | 4.21E+13   | 2.16E+14                      | 3.16E+12                      |
| <b><math>C_{\text{spin}}</math> / mol L<sup>-1</sup></b> | 3.79E-4     | 7.00E-5    | 3.59E-4                       | 5.25E-6                       |
| <b>Spin Count</b>  | 2.69E+16    | 2.98E+15   | 1.53E+16                      | 2.23E-14                      |
| <b>Microwave frequency / GHz</b>                         | 9.644       | 9.644      | 9.646                         | 9.645                         |
| <b>Magnetic field B / mT</b>                             | 343.34      | 343.34     | 343.34                        | 343.34                        |

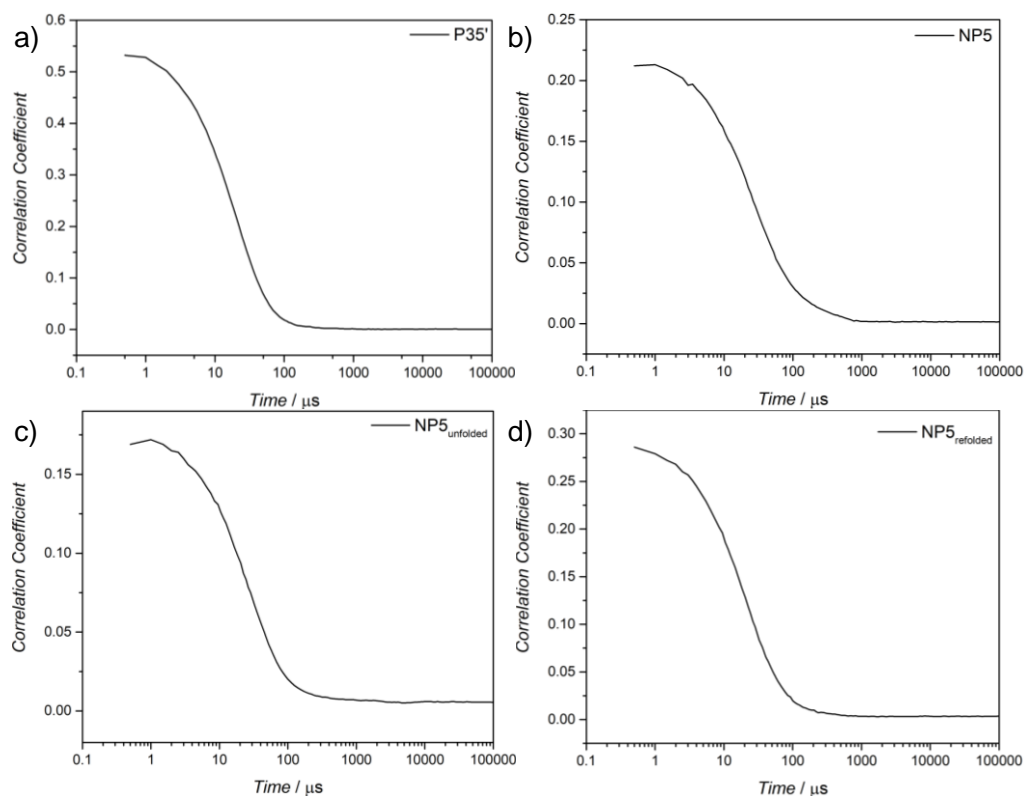
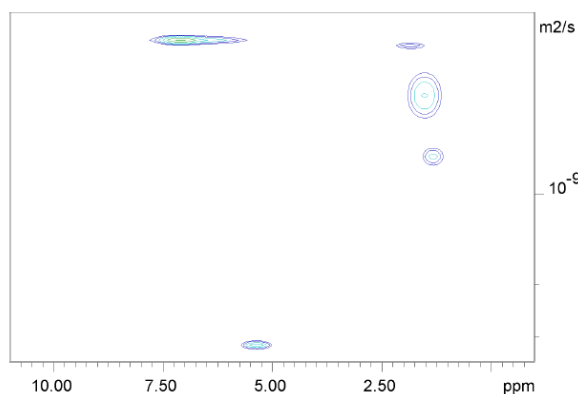
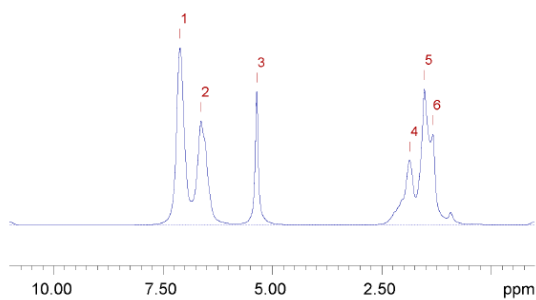
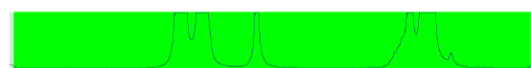


**Figure 113.** Autocorrelation curves for a) the precursor polymer **P35'**, b) the SCNP **NP5**, c) the unfolded **NP5<sub>unfolded</sub>** and d) the refolded **NP5<sub>refolded</sub>**. All samples were measured in DMAc + 0.3% LiBr. Adapted from ref [256] with permission of the Royal Society of Chemistry.



|  |   |
|--|---|
| Fitted function:                       | $f(x) = \text{lo} * \exp(-D * x^2 * \text{gamma}^2 * \text{littleDelta}^2 / (\text{bigDelta} - \text{littleDelta} / 3) * 10^4)$ |
| used gamma:                            | 26752 rad/(s*Gauss)   |
| used little delta:                     | 0.0030000 s   |
| used big delta:                        | 0.10990 s   |
| used gradient strength:                | variable  |
| Random error estimation of data:       | RMS per spectrum (or trace/plane)   |
| Systematic error estimation of data:   | worst case per peak scenario  |
| Fit parameter Error estimation method: | from fit using arbitrary uncertainties  |
| Confidence level:                      | 95%   |
| Used peaks:                            |   |
| Used integrals:                        | peak intensities  |
| Used Gradient strength:                | all values (including replicates) used  |

| Peak name | F2 [ppm] | D [ $\text{m}^2/\text{s}$ ] | error              |
|-----------|----------|-----------------------------|--------------------|
| 1         | 7.114    | $3.09\text{e-}10$           | $3.462\text{e-}12$ |
| 2         | 6.633    | $3.08\text{e-}10$           | $3.559\text{e-}12$ |
| 3         | 5.357    | $3.17\text{e-}09$           | $2.134\text{e-}11$ |
| 4         | 1.854    | $3.15\text{e-}10$           | $2.824\text{e-}12$ |
| 5         | 1.531    | $4.72\text{e-}10$           | $7.317\text{e-}11$ |
| 6         | 1.339    | $7.56\text{e-}10$           | $4.722\text{e-}11$ |

**Figure 114.** Original Data of DOSY measurements of **P35'**, recorded in  $\text{DCM-}d_2$  at 298 K. Adapted from ref [256] with permission of the Royal Society of Chemistry.

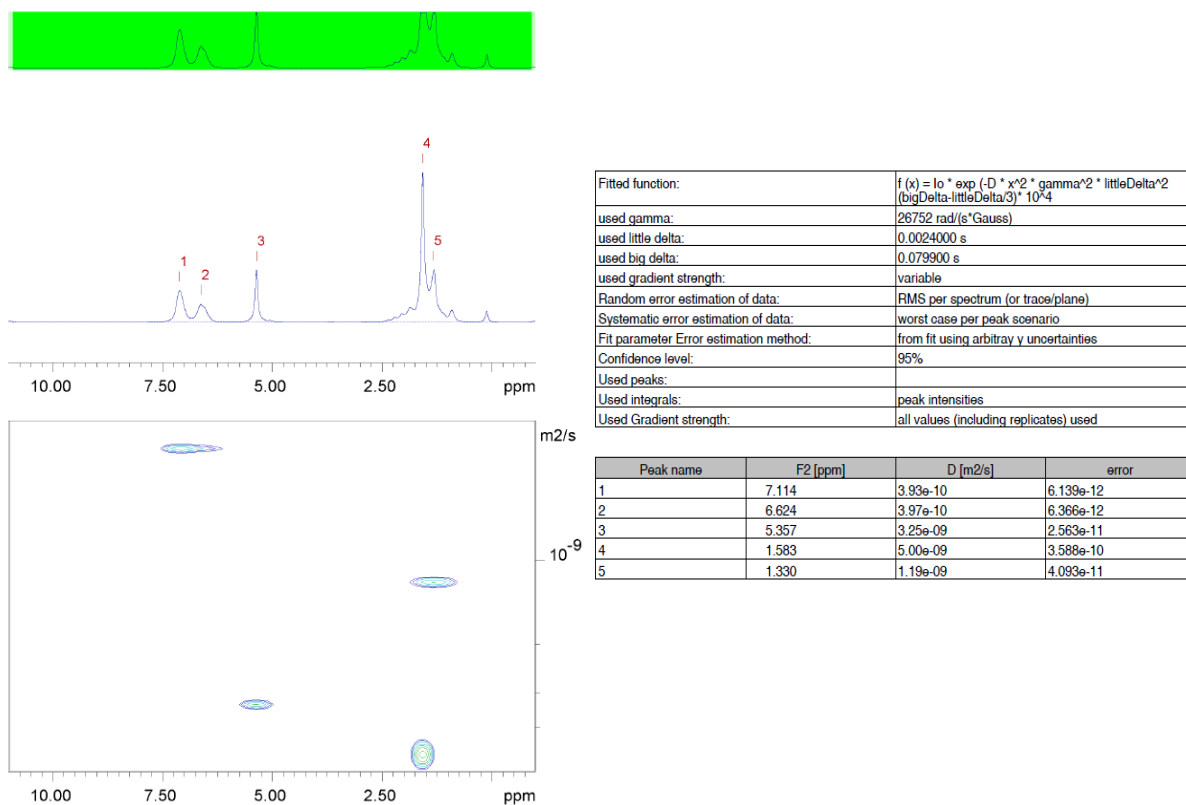


**Figure 115.** Original Data of DOSY measurements of **NP5**, recorded in DCM- $d_2$  at 298 K. Adapted from ref [256] with permission of the Royal Society of Chemistry.

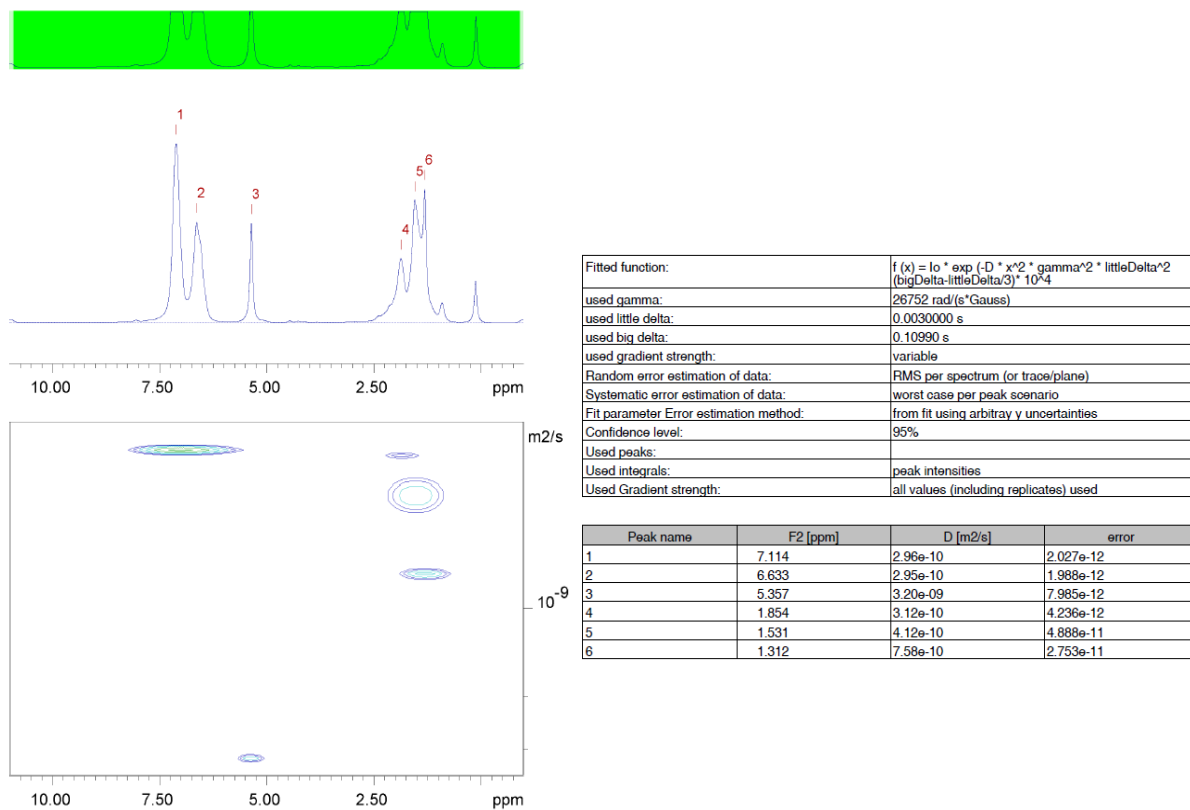
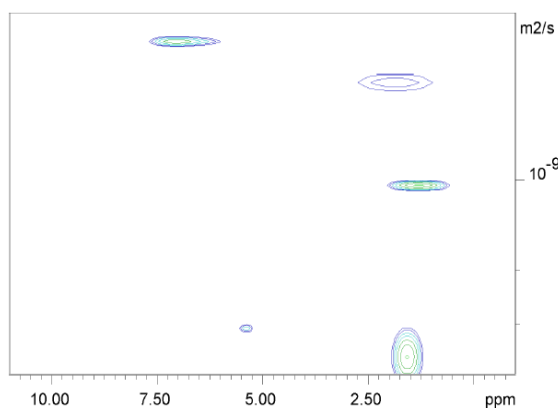
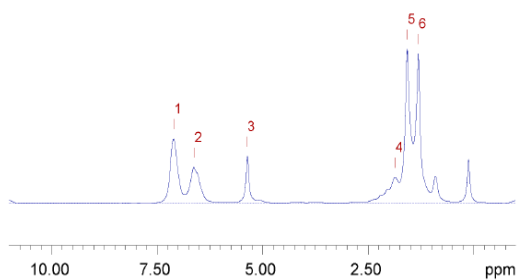
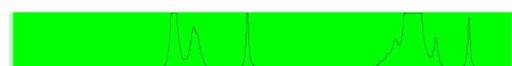


**Figure 116.** Original Data of DOSY measurements of **NP5<sub>unfolded</sub>**, recorded in DCM- $d_2$  at 298 K. Adapted from ref [256] with permission of the Royal Society of Chemistry.



|  |  |
|--|--|
| Fitted function:                       | $f(x) = I_0 \cdot \exp(-D \cdot x^2 \cdot \gamma^2 \cdot \Delta^2 \cdot (\Delta - \delta)^2 / 3) \cdot 10^4$ |
| used gamma:                            | 26752 rad/(e <sup>-</sup> Gauss)   |
| used little delta:                     | 0.0024000 s  |
| used big delta:                        | 0.079900 s   |
| used gradient strength:                | variable   |
| Random error estimation of data:       | RMS per spectrum (or trace/plane)  |
| Systematic error estimation of data:   | worst case per peak scenario   |
| Fit parameter Error estimation method: | from fit using arbitrary y uncertainties   |
| Confidence level:                      | 95%  |
| Used peaks:                            |  |
| Used integrals:                        | peak intensities   |
| Used Gradient strength:                | all values (including replicates) used   |

| Peak name | F2 [ppm] | D [m <sup>2</sup> /s] | error     |
|-----------|----------|-----------------------|-----------|
| 1         | 7.105    | 3.54e-10              | 4.073e-12 |
| 2         | 6.624    | 3.55e-10              | 3.911e-12 |
| 3         | 5.375    | 3.08e-09              | 4.530e-11 |
| 4         | 1.863    | 4.75e-10              | 3.392e-11 |
| 5         | 1.575    | 3.83e-09              | 5.387e-10 |
| 6         | 1.312    | 1.04e-09              | 2.106e-11 |

**Figure 117.** Original Data of DOSY measurements of **NP5<sub>unfolded</sub>**, recorded in DCM-*d*<sub>2</sub> at 298 K. Adapted from ref [256] with permission of the Royal Society of Chemistry.

---

## PUBLICATIONS ARISING FROM THIS THESIS

[1a] **Stepwise Unfolding of Single-Chain Nanoparticles by Chemically Triggered Gates**

T. S. Fischer, D. Schulze-Sünninghausen, B. Luy, O. Altintas, C. Barner-Kowollik, *Angew. Chem. Int. Ed.*, **2016**, *55*, 11276-11280.

[1b] **Chemisch gesteuerte schrittweise Entfaltung von Einzelketten-Nanopartikeln**

T. S. Fischer, D. Schulze-Sünninghausen, B. Luy, O. Altintas, C. Barner-Kowollik, *Angew. Chem.*, **2016**, *128*, 11446-11450.

[2] **High resolution mass spectrometric access to nitroxide containing polymers**

T. S. Fischer, J. Steinkoenig, H. Woehlk, J. P. Blinco, K. Fairfull-Smith, C. Barner-Kowollik, *Polym. Chem.*, **2017**, *8*, 5269-5274.

[3] **Synthetic Methods Towards Single-Chain Polymer Nanoparticles**

O. Altintas, T. S. Fischer, C. Barner-Kowollik, in **Single-Chain Polymer Nanoparticles: Synthesis, Characterization, Simulations and Applications**, Pomposo, J., Ed., ISBN: 978-3-527-34242-6, Wiley-VCH, **2017**, 1-45.

[4] **Self-Reporting Refoldable Fluorescent Single-Chain Nanoparticles**

T. S. Fischer, S. Spann, Q. An, B. Luy, M. Tsotsalas, J. P. Blinco, H. Mutlu and C. Barner-Kowollik, *Chem. Sci.*, **2018**, *9*, 4696-4702.

[5] **Chiral Monoborohydride Complexes of Scandium and Lutetium and their Catalytic Activity in Ring-Opening Polymerization of DL-Lactide**

T. P. Seifert, T. S. Brunner, T. S. Fischer, C. Barner-Kowollik, P. W. Roesky, *Organometallics*, **2018**, DOI: 10.1021/acs.organomet.8b00172

**ABBREVIATIONS**

|           |   |
|-----------|---|
| ACN       | acetonitrile                                |
| AEMA      | acetoacetoxy ethyl methacrylate             |
| Ada       | adamantyl                                   |
| AFM       | atomic force microscopy                     |
| AIBN      | Azobisisobutyronitrile                      |
| $a_N$     | hyperfine coupling constant                 |
| ARGET     | activator regenerated electron transfer     |
| AS        | secondary ammonium salt                     |
| ATRP      | atom transfer radical polymerization        |
| B         | B-field                                     |
| B21-C-7   | benzo-21-crown-7                            |
| BCB       | benzocyclobutene                            |
| BiPy      | bipyridine                                  |
| Boc       | <i>tert</i> -butylcarbonyl                  |
| BPLED     | bipolar longitudinal eddy current delay     |
| BPO       | benzoyl peroxide                            |
| BTA       | benzene-tricarboxamide                      |
| $c$       | concentration                               |
| CA        | cyanuric acid                               |
| CB        | cucurbit[n]uril                             |
| CD        | cyclodextrin                                |
| CD        | circular dichroism                          |
| CMS       | 4-(Chloromethyl)styrene                     |
| COD       | cyclooctadiene                              |
| Cp        | cyclo-pentadiene                            |
| CPBD      | 2-cyano-2-propyl-benzodithioate             |
| CTA       | chain-transfer agent                        |
| CuAAC     | copper catalysed azide-alkyne cycloaddition |
| $\bar{D}$ | dispersity index                            |
| $\delta$  | Chemical shift                              |

---

|          |   |
|----------|---|
| Da       | Dalton                                    |
| DA       | Diels-Alder                               |
| DAN      | diaminonaththyridine                      |
| DBP      | dibenzoyl peroxide                        |
| DCC      | <i>N,N'</i> -dicyclohexylcarbodiimid      |
| DCM      | dichloromethane                           |
| $D_h$    | hydrodynamic diameter                     |
| DIPEA    | diisopropylethylene amine                 |
| DLS      | dynamic light scattering                  |
| DMAP     | 4-dimethylaminopyridine                   |
| DMF      | dimethylformamide                         |
| DMA      | dimethylaniline                           |
| DOSY     | diffusion ordered NMR spectroscopy        |
| e.g.     | for example                               |
| EHMA     | ethylhexyl methacrylate                   |
| EI       | electron-impact ionization                |
| EPR      | electron paramagnetic resonance           |
| ESI      | electrospray ionization                   |
| FAB      | Fast atom bombardement                    |
| FMA      | furfuryl methacrylate                     |
| FRP      | free radical polymerization               |
| FT       | Fourier-transform                         |
| FT-ICR   | Fourier Transform Ion Cyclotron Resonance |
| FT-IR    | Fourier-transform infrared spectroscopy   |
| G        | Gauss                                     |
| <i>g</i> | <i>g</i> -factor                          |
| g        | gram                                      |
| GMA      | glycidyl methacrylate                     |
| h        | hour(s)                                   |
| HDA      | hetero Diels-Alder                        |
| HW       | Hamilton Wedge                            |
| Hz       | Hertz                                     |
| i.e.     | that is                                   |
| IC       | internal conversion                       |

## Abbreviations

---

|                   |  |
|-------------------|--|
| ISC               | intersystem crossing                               |
| K                 | Kelvin   |
| L                 | litre  |
| LED               | longitudinal eddy current delay                    |
| LPO               | lauroyl peroxide                                   |
| M                 | molar  |
| Mal               | maleimide  |
| MALDI             | Matrix-assisted laser desorption ionization        |
| MALLS             | multi-angle light scattering                       |
| <i>m</i> CPBA     | <i>meta</i> -Chlorperbenzoic acid                  |
| MeOH              | methanol   |
| mg                | milli gram   |
| min               | minute(s)  |
| MKHS              | Mark-Houwink-Sakurada parameter                    |
| mL                | milli liter  |
| MMA               | methyl methacrylate                                |
| $M_n$             | number average molecular weight                    |
| MONP              | metal-organic nanoparticle(s)                      |
| MWD               | molecular weight distribution                      |
| nm                | nanometer  |
| mT                | milli Tesla  |
| MS                | mass spectrometry                                  |
| NaOH              | sodium hydroxide                                   |
| NICAL             | nitrile imine- carboxylic acid ligation            |
| NITEC             | nitrile imine-mediated tetrazole-ene cycloaddition |
| NMP               | nitroxide-mediated polymerization                  |
| NMR               | nuclear magnetic resonance                         |
| NOESY             | nuclear Overhauser enhancement spectroscopy        |
| <i>ns</i> -CB[10] | <i>nor-seco</i> -CB[10]                            |
| OEGMA             | oligoethylene glycol methyl ether methacrylate     |
| PAA               | poly(acrylic acid)                                 |
| PEGMA             | poly(ethylene glycol)methyl ester methacrylate     |
| PFG               | pulsed field gradient                              |
| PFS               | pentafluoro styrene                                |



---

|           |   |
|-----------|---|
| PgA       | propargyl acrylate  |
| PMDETA    | <i>N,N,N',N'',N'''</i> -pentamethyldiethylenetriamine           |
| ppm       | parts per million   |
| PRE       | persistent radical effect                                       |
| PS        | polystyrene   |
| R         | resolution  |
| RAFT      | reversible addition-fragmentation chain transfer polymerization |
| RDRP      | reversible deactivation radical polymerization                  |
| rf        | radiofrequency  |
| $R_h$     | hydrodynamic radius   |
| ROP       | ring-opening polymerization                                     |
| ROMP      | ring-opening metathesis polymerization,                         |
| SAXS      | small angle X-ray scattering                                    |
| SCNP      | single-chain nanoparticle                                       |
| SEC       | size-exclusion chromatography                                   |
| STE       | stimulated echo   |
| STM       | scanning tunnelling microscopy,                                 |
| T         | Tesla   |
| TEA       | triethylamine   |
| TEY       | thiol-ene-coupling  |
| TEM       | transmission electron microscopy                                |
| TEMPO     | 2,2,6,6-tetramethylpiperidinyloxy                               |
| THF       | tetrahydrofuran   |
| TMEDA     | tetramethylethylenediamine                                      |
| TMS       | trimethylsilyl  |
| TOF       | time-of-flight  |
| TYC       | thiol-yne-coupling  |
| UG        | ureidoguanosine   |
| UPy       | 2-Ureido-pyrimidinon  |
| UV        | ultra violet  |
| $\mu$     | micro   |
| V         | Volt  |
| vs        | versus  |
| $\lambda$ | wavelength  |

---

## Abbreviations

---

|    |                |
|----|----------------|
| °  | degree         |
| °C | degree Celsius |
| %  | percent        |

## ACKNOWLEDGEMENTS

Zum Schluss dieser Arbeit möchte ich all denjenigen Personen danken, die mich während meiner Promotion begleitet und unterstützt haben und möchte den Personen hiermit meinen persönlichen Dank aussprechen.

Zu allererst gebührt mein Dank natürlich meinem Doktorvater Prof. Dr. Christopher Barner-Kowollik. Zum einen für die vielseitige, herausfordernde und spannende Thematik meiner Dissertation, zum anderen aber auch für die ausgezeichnete und angenehme Betreuung. Es hat mir viel Freude bereitet meine Arbeit unter deiner Betreuung anzufertigen. Ferner hattest du immer ein offenes Ohr, wenn es darum ging schwierige Situationen zu lösen und hast dabei immer dein bestmöglichstes gegeben. Hierfür nochmals ein herzliches Dankeschön.

Weiter bedanke ich mich bei meinen Kooperationspartnern David Schulze-Sünninghausen, dessen Nachfolger Sebastian Spann und Burkhard Luy für die angenehme Kooperation und die Messung zahlreicher DOSY Spektren und deren Interpretation. Es war stets angenehm mit euch zusammen zu arbeiten.

A special thanks goes to Dr. Özcan Altintas, Dr. Hatice Mutlu and Jan Steinkönig for your support in some of my projects. You contributed with your enormous knowledge to the success of the respective projects. In diesem Sinne gilt mein Dank Hendrik Wöhlk, Qi An und Manuel Tsotsalas, die mit ihrer jeweiligen Expertise innerhalb verschiedener Projekte ihren Teil zum Erfolg beigetragen haben.

Ein großes Dankeschön geht auch an Dr. Anja Goldmann, Dr. Dominik Voll, Evelyn Stühling, Maria Schneider, Vincent Schüler und Katharina Elies für die hervorragende administrative und technische Unterstützung in allen Belangen während meiner Zeit als Doktorand.

Des Weiteren danke ich Philipp Kamm, der seine Vertieferarbeit unter meiner Anleitung angefertigt hat, ich hoffe es hat dir genauso viel Freude bereitet wie mir. Nicht zu vergessen sind Christoph Frank, Christian Schmitt und Philipp Kamm für ihre Hilfe

und Arbeit im Rahmen als studentische Hilfskraft unter meiner Anleitung. Die Zusammenarbeit hat mir große Freude bereitet und ich wünsche euch für eure Promotion und Zukunft alles Gute.

I would like to thank the whole macroarc team and former members for the great working atmosphere and the warm welcome to the group. Special thanks goes to the AC team for the nice atmosphere and fruitful discussions.

Further, I would like to thank Dr. Anja Goldmann, Dr. Hatice Mutlu, Dr. Dominik Voll, Dr. Eva Blasco, Dr. Bryan Tuten and Dr. Charlotte Petit for proofreading parts of my dissertation.

Darüber hinaus gilt mein Dank meinen Kommilitonen und Freunden Aaron Schmidt, Tim Seifert, Thomas Feuerstein, Nicolai Knöfel und Andreas Boukis, für die unvergessliche studentische Zeit am KIT und darüber hinaus.

Zum Schluss, bedanke ich mich bei meinen Eltern und meiner Familie für ihre anhaltende Unterstützung nicht nur finanziell, sondern in jeder anderen erdenklichen Weise.

Besonderer Dank gilt hier natürlich meiner wundervollen Frau Sandra die mich zu jeder Zeit unterstützt, ermutigt und mir gleichzeitig „den Rücken frei gehalten“ hat. Ohne dich wäre diese Arbeit so nicht möglich gewesen. Dafür werde ich dir immer dankbar sein und freue mich schon darauf zu sehen, wohin uns unser gemeinsamer Weg noch hinführen wird.